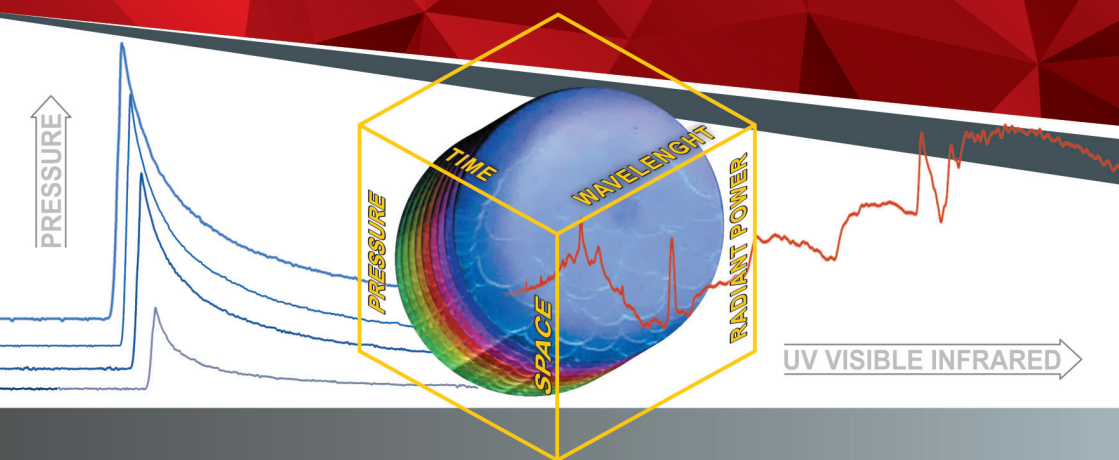




N. M. Rubtsov, M. I. Alymov, A. P. Kalinin,
A. N. Vinogradov, A. I. Rodionov, K. Ya. Troshin

Remote studies of combustion and explosion processes based on optoelectronic methods



Merzhanov Institute of Structural Macrokinetics and Materials Science RAS
Ishlinsky Institute for Problems in Mechanics RAS
“Reagent” Research & Development center, Joint-stock company
N.N. Semenov Federal Research Center for Chemical Physics RAS
Joint Institute for High Temperatures RAS

AUS PUBLISHERS
Melbourne, 2022

**Rubtsov Nikolai Mikhailovich, Alymov Mikhail Ivanovich,
Kalinin Alexander Petrovich, Vinogradov Alexey Nikolaevich,
Rodionov Alexey Igorevich, Troshin Kirill Yakovlevich**

Remote studies of combustion and explosion processes based on optoelectronic methods

AUS PUBLISHERS
Melbourne, 2022

Rubtsov N. M., Alymov M. I., Kalinin A. P., Vinogradov A. N., Rodionov A. I., Troshin K. Ya. Remote studies of combustion and explosion processes based on optoelectronic methods. – Melbourne: AUS PUBLISHERS, 2022. - 272p.

ISBN 978-1-922756-07-7

Rubtsov Nikolai Mikhailovich – Dr. of Chem. Sci., Merzhanov Institute of Structural Macrokinetics and Materials Science RAS, Joint Institute for High Temperatures RAS

Alymov Mikhail Ivanovich – full Professor, corr. mem. of RAS, Merzhanov Institute of Structural Macrokinetics and Materials Science RAS

Kalinin Alexander Petrovich – Dr. of Phys.-Math. Sci., Ishlinsky Institute for Problems in Mechanics RAS

Vinogradov Alexey Nikolaevich – Cand. of Phys.-Math. Sci., Head of the Laboratory of "Scientific and Technical Center "Reagent" JSC

Rodionov Alexey Igorevich – Cand. of Phys.-Math. Sci., N.N. Semenov Federal Research Center for Chemical Physics RAS.

Kirill Yakovlevich Troshin – Dr. of Phys.-Math. Sci., N.N. Semenov Federal Research Center for Chemical Physics RAS

Reviewers:

Arutyunov V.S. - *Professor, Doctor of Chemical Sciences, Head of the Laboratory of the Federal Research Center for Chemical Physics named after N.N.Semenov of the RAS, Professor of the Russian State University of Oil and Gas named after N.N. I.M. Gubkin*

Belyaev A.A. - *Leading Researcher, Candidate of Physical and Mathematical Sciences, Federal Research Center for Chemical Physics named after N.N.Semenov of the RAS*

The main objective of this book is to acquaint the reader with the main modern problems of the multisensor data analysis and opportunities of the hyperspectral shooting being carried out in the wide range of wavelengths from ultraviolet to the infrared range, visualization of the fast combustion processes of flame propagation and flame acceleration, the limit phenomena at flame ignition and propagation. The book can be useful to students of the high courses and scientists dealing with problems of optical spectroscopy, visualization, digital recognizing images and gaseous combustion.

The main goal of this book is to bring to the attention of the reader the main modern problems of multisensory data analysis and the possibilities of hyperspectral imaging, carried out in a broad wave-length range from ultraviolet to infrared by methods of visualizing fast combustion processes, propagation and flames acceleration, and limiting phenomena during ignition and flame propagation. The book can be useful for students of higher courses and experimental scientists dealing with problems of optical spectroscopy, visualization, pattern recognition and gas combustion.

CONTENTS

ABSTRACT.....	8
INTRODUCTION.....	15
CHAPTER 1. Methods and means of remote sensing in the optical range.....	18
Conclusions for Chapter 1.....	28
References for Chapter 1.....	28
CHAPTER 2. Optoelectronic devices and methods for studying combustion and explosion processes.....	29
Conclusions for Chapter 2.....	44
References for Chapter 2.....	44
CHAPTER 3. Investigation of the instabilities arising from the hydrogen and hydrocarbon flames propagation by the method of high-speed filming.....	46
§ 1. <i>Investigation of flame propagation modes of lean hydrogen-air mixtures in the presence of additives under conditions of central initiation by means of high-speed cinematography.....</i>	48
Experimental.....	49
Results and discussion.....	50
Appendix.....	59
§ 2. <i>The onset of the acoustic instability in hydrogen-air mixtures in a closed reactor upon central initiation by a spark discharge.....</i>	61
Experimental.....	62
Results and discussion.....	63
§ 3. <i>Interaction of spherical flames of hydrogen-air and methane-air mixtures with fine-mesh obstacles at central initiation by a spark discharge.....</i>	70
Experimental.....	71
Results and discussion.....	73
§4. <i>Thermal ignition in gas vortices.....</i>	79
Experimental.....	88
Results and discussion.....	89
Conclusions for Chapter 3.....	96
References for Chapter 3.....	98

CHAPTER 4. Detecting the regularities of propagation of an unstable flame front using optical 4D spectroscopy and color high-speed filming.....	103
Experimental.....	105
Results and discussions.....	108
Conclusions for Chapter 4.....	123
References for Chapter 4.....	123
CHAPTER 5. The use of high-speed optical multidimensional technique to determine the characteristics of ignition and combustion of 40% H₂ - air mix in the presence of platinum metal.....	126
Experimental.....	127
Results and discussion.....	133
Conclusions for Chapter 5.....	148
References for Chapter 5.....	149
CHAPTER 6. Determining the gas-dynamic and kinetic features of the penetration of methane-oxygen flames through obstacles by using 4D spectroscopy and high-speed filming.....	152
<i>§ 1. Gas-dynamic and kinetic features of the penetration of methane-oxygen flame through single holes and fine-meshed obstacles.....</i>	<i>153</i>
<i>§ 2. Peculiarities of penetration of flames of dilute mixtures of methane with oxygen through a single hole in a flat obstacle, diffuser, confuser and combined obstacles.....</i>	<i>163</i>
<i>§ 3. Factors determining a length of a flame jump after penetration through a small hole.....</i>	<i>181</i>
<i>§ 4. Spectral features of emission of methane-oxygen flames under conditions of penetration through obstacles. The possibilities of the 4D spectroscopy method.....</i>	<i>189</i>
Conclusions for Chapter 6.....	196
References for Chapter 6.....	197
CHAPTER 7. Study of the combustion of hydrogen-air and hydrogen-hydrocarbon (C₁- C₆) -air mixtures over the surface of palladium metal with the combined use of a hyperspectral sensor and high-speed color filming....	202
<i>§ 1. Study of the combustion of hydrogen-air and hydrogen-methane-air mixtures over the surface of palladium metal with the combined use of a hyperspectral sensor and high-speed color filming.....</i>	<i>203</i>
Experimental.....	204
Results and discussion.....	206

<i>§ 2. Ignition of hydrogen - hydrocarbon (C₁-C₆) - air mixtures over palladium surface</i>	212
Experimental	213
Results and discussion	215
<i>§ 3. Ignition of hydrogen-oxygen and hydrogen-methane-oxygen mixtures with heated wires at low pressure</i>	222
Conclusions for Chapter 7	231
References for Chapter 7	231
CHAPTER 8. Determination of the features of combustion of nanopowders and their compacted samples by the methods of visible and infrared filming	237
<i>§ 1. Combustion of copper nanopowders</i>	238
<i>§ 2. Combustion of tungsten nanopowders</i>	246
<i>§ 3. Combustion of compacted samples of iron nanopowders</i>	253
Experimental	253
Results and discussion	254
Conclusions for Chapter 8	258
References for Chapter 8	259
CONCLUSIONS	262

Some of the abbreviations used in the book:

FF - flame front, NG - natural gas, PSD - position sensitive detector

DDT - deflagration to detonation transition

HPC - high pressure chamber, ADC - data acquisition system

XPS - X-ray photoelectron spectroscopy, ADC - analog digital converter

BR - blocking ratio

RGB - abbreviation of the English words of Red, Green, Blue; an additive color model that describes a method of coding a color for color reproduction using three colors, which are commonly called primary

CS - Catalytic Stabilization - stabilization of the process using a catalyst

To, Po - initial temperature and pressure, θ – fraction of fuel in the gas mixture

BET - polymolecular adsorption according to Brunauer - Emmett - Teller

ABSTRACT

Nowadays, remote-sensing methods of studying various processes, for which various optoelectronic devices are used, are becoming more and more increasingly prevalent. In particular, multifrequency survey with the use of optoelectronic sensors for various wavelength ranges is of great interest. This book describes and analyzes some of the capabilities of optoelectronic devices for studying combustion and explosion processes in a wide wavelength range from ultraviolet to infrared range by methods of visualizing fast combustion processes, propagation and flames acceleration, limiting phenomena during ignition and flame propagation. Optoelectronic devices are understood as devices that convert an optical signal into an electrical signal, which is further processed by electronic devices. Optoelectronic devices, in particular, are digital cameras, digital video cameras, hyperspectrometers, UV sensors, etc. As a rule, the recorded radiation spectrum is limited for individual devices.

Therefore, two or more sensors are used for multisensory imaging; it is so-called multispectral analysis. The possibilities of unique UV sensors, which are developed at "Reagent" Research&Development center, Joint-stock company ("RDC "Reagent", JSC) and which have numerous applications in various fields of science and technology, are considered.

By numerous examples of the use of modern optoelectronic devices, the effectiveness of the use of multispectral multisensor imaging for studying combustion and explosion processes has been demonstrated.

The book considers the method of multispectral analysis of remote sensing data and assesses the capabilities of multisensory imagery carried out in a wide range of wavelengths from ultraviolet to infrared range. Various combinations of data made it possible to georeference images, to reveal the detailed structure of the analyzed scene, to study the spectral composition of the radiation of objects

and to distinguish point sources by it. It is especially important, for example, for detecting fire centers and determining their coordinates. One of the very promising optoelectronic devices is the hyperspectrometer. The relevance of the work carried out in Russia on the creation of new types of hyperspectral modules is determined by their ability to extract the maximum information from optical radiation ascending from remotely probed objects. Besides, it is determined by the lagging of domestic developments outlined in the 90s of the last century from developments carried out abroad. The hyperspectral modules developed at "RDC "Reagent", JSC by their technical characteristics are not inferior to and even surpass modern foreign aviation imaging spectrometers. In particular, this concerns the spatial resolution and the number of spectral channels of the modules. "RDC "Reagent", JSC has mastered the industrial production of hyperspectral modules in the UV, visible and near-infrared range. Full-scale tests of the developed and manufactured devices confirmed the correctness of the design solutions incorporated in them and the ability to confidently determine the type and state of probed natural and anthropogenic objects based on hyperspectral sensing data in the interests of solving many scientific, industrial and other problems. In particular, it is shown that the joint analysis of data from different sensors can achieve a significant synergetic effect. This book examines some hyperspectrometers developed at "RDC "Reagent", JSC, as well as a very interesting development - the UV-C sensor. A good deal of the book is devoted to describing the results of remote sensing of combustion and explosion processes in laboratory conditions.

As a result of a series of works on the study of combustion and explosion processes in laboratory conditions, which included remote sensing methods using multi-sensor analysis, it was experimentally established that during central ignition, the flame of lean (6-15% H_2) hydrogen-air mixtures has a cellular structure. In the mixtures containing 10-15% of H_2 , the flames at the initial stage near the lower concentration limit propagate spherically symmetrically. In mixtures containing 6-10% of H_2 , the flames at the initial stage near the lower concentration limit propagate spherically symmetrically; then the gravity field distorts the shape of the combustion front, while the flames of mixtures containing 10-15% of H_2 propagate spherically symmetrically. It is shown that the Boussinesq approximation is applicable to obtain cells with a concentration of $H_2 < 10\%$, taking into account the gravity force. Calculations by the Boussinesq model in the absence of gravity do not give the formation of cells. The use of the Navier-Stokes equations for a compressible medium makes it possible to describe the spherically symmetric mode of propagation of a cellular flame under microgravity conditions. It has been found that the analysis of experimental data on flame propagation in lean mixtures does not make it possible to distinguish the calculation results using a two-dimensional model with and without convection. It has been shown experimentally that additions of isobutene C_4H_8 in amounts below the lower concentration limit (up to 1.5%) lead to an increase, and additions of CO_2 to 15% - to a decrease in the flame

propagation rate in lean hydrogen-air mixtures. The reasons for the acceleration of combustion in the presence of a hydrocarbon additive are considered.

It is shown that the detected luminescence instabilities can be associated with the presence of acoustic waves by the example of the combustion of hydrogen-air mixtures (30% and 15% H₂). It was found that the flame propagation velocities in a stoichiometric hydrogen-air mixture with central spark initiation do not depend on the material of the inner surface of the reactor (stainless steel, TiO₂, Ta, Pt), but depend on the shape of the inner surface of the reactor.

It is shown that spark-initiated flames of lean hydrogen mixtures (8% -15% H₂ in air) pass through aluminum mesh spheres with a cell size of 0.04-0.1 mm², while the flame of the mixture of 15% of H₂ in air accelerates after passing through an obstacle. In the presence of an obstacle during the flame propagation in mixtures with an H₂ concentration of 10% and 15%, acoustic oscillations of the gas appear in the reactor. With a decrease in the diameter of the sphere, the oscillations appear earlier in time. The flame of the mixture with a concentration of 7.5% of H₂ in air does not pass through the mesh spheres. It was found that the flame of a mixture of 8% of natural gas with air passes through the mesh spheres, but after the obstacle, the flame velocity remains the same. In this case, acoustic oscillations are not observed. It is shown that the active centers of combustion of methane and hydrogen, which determine the propagation of the flame, have a different chemical nature.

In a static bypass installation with a tangential inlet of the mixture under study, the effect of thermal ignition of combustible mixtures at reactor temperatures significantly lower than the thermal ignition temperature was experimentally discovered. In this case, the difference between the temperature of the reactor and the temperature of thermal ignition can reach more than 150 K. This effect is caused primarily by the presence of centripetal forces, which inevitably arise during the formation of a vortex gas flow. The result of the action of these forces on the flow is the radial stratification of the gas in terms of density and, therefore, in terms of temperatures. In the central region, the hottest and least mobile gas is formed and, in addition, it is well insulated from the walls of the reactor. The possibility of mixing it with fresh cold masses of gas is excluded. The pressure increase in the reactor caused by the mixture puffing leads to adiabatic compression and additional heating of the gas. The centripetal forces contribute to the fact that the heat, which begins to release with the onset of a chemical reaction, accumulates in the central region of the reactor, thus creating favorable conditions for thermal ignition.

It is shown that the phenomena due to the instability of a flat flame occur when the flame front (FF) propagates from spherical shape to propagation in a tube by the example of combustion of stoichiometric mixtures of n-pentane (C₅H₁₂) with air, diluted with carbon dioxide (CO₂) and argon (Ar) at total atmospheric pressure. It is shown that, upon deceleration of the FF near the end wall of the reactor,

a smooth FF acquires a cellular structure. It is shown that qualitative modeling of the results obtained is possible when analyzing the Navier-Stokes equations for a compressible medium in the low Mach number approximation. Using the methods of 4D optical spectroscopy and color high-speed filming, the features of combustion in flame cells caused by hydrodynamic instability have been experimentally established for the first time. It is shown that each combustion cell is essentially a separate "chemical reactor", in each of which the process of complete chemical transformation is carried out. The results obtained on the spectral study and visualization of the propagation of unstable flames fronts are important in solving the issues of explosion safety for volumes of complex geometry.

A cellular mode of combustion of the 40 % mixture of hydrogen with air in the presence of platinum wire and foil in the range of 270-350 °C at atmospheric pressure was found. Using the methods of traditional and 4D optical spectroscopy, which makes it possible to record the intensity of the optical spectrum simultaneously depending on the wavelength, time and coordinate, and high-speed color filming, combustion cells caused by catalytic instability have been experimentally detected for the first time. It was found that the cellular mode is determined by the catalytic combustion of hydrogen on Pt particles formed during the decomposition of unstable platinum oxide in the gas phase. It is shown that the temperature dependence of the hydrogen ignition delays on a platinum wire and foil in both stationary and rotating gases corresponds to the activation energy of 19 ± 3 kcal/mol, which is close to the activation energy of branching of the reaction chains of hydrogen oxidation. The impurity origin of the 552 nm emission band, which is often recorded during the gas combustion and heterogeneous mixtures, has been established. The results obtained are of direct importance for the development of Catalytic Stabilization (CS) technology and the development of catalysts with increased activity. The results are also important for verification of theoretical concepts of the propagation of dust and gas flames.

It has been shown experimentally that in the case of flame penetration through an obstacle, gas-dynamic factors, for example, flame-generated turbulence, can determine the kinetics of the process, including the transition of low-temperature combustion of a hydrocarbon to a high-temperature regime.

It was found that the flame front after a single obstacle does not arise in the immediate vicinity of the obstacle. The first nucleation site for ignition can be observed relatively far from the surface of the obstacle. It is shown that the use of a mesh sphere as an obstacle leads to an increase in the length of the flame "jump" behind the obstacle in comparison with a round hole. It has been demonstrated that two or more obstacles, both spherical and planar, noticeably suppress the propagation of the flame, which can be associated with both heat losses from the flame front and with heterogeneous termination of reaction chains on the obstacle. It has been shown experimentally that below the limit of the flame penetration of a diluted methane-oxygen mixture through a flat obstacle with one hole, the flame does

not penetrate from the side of the funnel mouth, but penetrates from the side of the funnel nose for an obstacle in the form of a funnel. Numerical model based on the Navier-Stokes equations for a compressible medium in the low Mach number approximation with the representation of a chemical process as a single reaction and the simplest chain mechanism made it possible to describe qualitatively the experimental laws. Within the framework of an approximate consideration using the Navier-Stokes equations in a compressible reacting medium, the features of flame propagation through a conical obstacle with additional holes on the converging generatrix are qualitatively described. The flame does not penetrate through the central hole of the converging tube, but only penetrates through the central hole of the diffuser, even if there are holes in the generatrix of the cone. The simulation carried out in small volumes suggests that in the event of an emergency situation, the flame will not penetrate through the open valve located in the center of the confuser located in the pipe. In this case, the most effective two-sided obstacle to the flame propagation in the pipe can be a system of two confusers, the funnels of which are located on the pipe axis along the gas flow and against it. It is necessary since an emergency situation can occur before and after the obstacle. A hole or valve can be located in the middle.

Using color filming and visualization of a gas flow, the features of the penetration of the flame front through rectangular holes in comparison with round holes are experimentally investigated. It is shown that the length of the “flame jump” after the hole in the obstacle is mainly determined by the time of occurrence of the laminar-turbulent transition, and not by the ignition delay period.

Using 4D spectroscopy combined with high-speed color filming, it was found that C_2 radicals in detectable amounts and the main heat release in the process of chemical transformation are observed after the flame passes the first obstacle, i.e. after turbulization of the gas flow. The obtained result means that the used experimental technique allows separating “cold” and “hot” flames in time and space in one experiment. The obtained results is also important for the verification of numerical models of methane combustion. In addition, the results obtained are important for solving explosion safety problems for volumes with complex geometry.

It was found that the ignition temperature of 40% of H_2 - air mixture in the presence of metallic palladium (70 °C, 1 atm) is ~ 200 °C lower than over the platinum surface (260 °C, 1 atm). In addition, Pd initiates the ignition of mixtures (30-60% H_2 + 70-40% CH_4)_{stoich} + air; Pt foil does not initiate combustion of these mixtures up to 450 °C. The effective activation energy of ignition over Pd is estimated as ~ 3.5 kcal/mol.

It was found that the temperature of the ignition limit of mixtures of 30% methane + 70% hydrogen + air ($\theta = 0.9$, $T = 317$ °C) and 30% propane + 70% hydrogen + air ($\theta = 1$, 106 °C) above the surface of palladium at 1.75 atm, measured by the “approach from below” method in temperature, decreases during subsequent ignitions. It is 270 °C for a mixture containing hydrogen-methane and 32

°C for a mixture containing hydrogen-propane. The flammability limit returns to the initial value after the reactor is treated with oxygen or air, i.e. hysteresis takes place. The temperature of the ignition limit of mixtures of 30% (C₂, C₄, C₅, C₆) + 70% H₂ + air ($\theta = 0.6, 1.1, 1.2, 1.2$, respectively) over the palladium surface is 19 ÷ 35 °C at 1.75 atm; there is no hysteresis. It is shown that the lean ($\theta = 0.6$) mixture of 30% ethane + 70% hydrogen + air has the lowest temperature of the ignition limit: 24 °C at 1 atm. The effective activation energy for the ignition of mixtures over palladium is estimated as $\sim 2.4 \pm 1$ kcal / mol. It was found that the separation of the CH and Na emission bands in time during the combustion of a mixture of 30% propane + 70% H₂ + air ($\theta = 1$), found in this work, is due to the occurrence of hydrodynamic instability of the flame when it touches the end of the cylindrical reactor.

It was found that the ignition temperatures of hydrogen - oxygen and hydrogen - methane - oxygen mixtures with heated wires of palladium, platinum, nichrome and kantal (fechral) at a total pressure of 40 Torr increase during a decrease in the hydrogen content in the mixture. Only heated palladium wire has a noticeable catalytic effect. A qualitative numerical calculation made it possible to reveal the role of the additional branching reaction $H + HO_2 \rightarrow 2OH$ in the process of ignition initiation by a heated wire.

The regularities of the combustion of copper and tungsten nanopowders have been established. Copper nanopowders are obtained by the method of hydrogen reduction (chemical and metallurgical method) and thermal decomposition of copper citrate and formate. It was shown that copper nanopowder synthesized from copper citrate is not pyrophoric. Combustion of this copper nanopowder can be initiated by an external source, with the combustion wave velocity being 1.3 ± 0.3 mm/s. The nanopowder has a ~ 4 times larger specific surface (45 ± 5 m²/g) than the nanopowder obtained by the hydrogen reduction method, practically does not contain oxides and is stable in atmospheric air. Copper nanopowder obtained by the chemical and metallurgical method is pyrophoric and therefore requires passivation, but its passivation leads to the formation of noticeable amounts of copper oxides. The combustion velocities of passivated and non-passivated copper nanopowder obtained by the chemical and metallurgical method are the same and amount to 0.3 ± 0.04 mm/s. The dynamics of temperature fields during the ignition and combustion of copper nanopowders obtained by various methods has been investigated.

Tungsten nanopowders W were synthesized by reduction of tungsten trioxide with hydrogen (chemical metallurgy method) at 440 ÷ 640 °C from samples with different specific surface: 2 m² / g (1), 11 m² / g (2), 0.8 m² / g (3). It is shown that the W nanopowder synthesized at 640 °C for all three precursors used is non-pyrophoric α -W. Its combustion can be initiated by an external source. Combustion develops in a spatially non-uniform regime. Nanopowder synthesized at 480 °C from tungsten oxide grades 1 and 2 is a mixture of α -W, β -W and WO_{2,9}; this

powder is pyrophoric. It was found that the passivated W nanopowder synthesized at 480 °C from grade 3 tungsten oxide is β -W with traces of WO_3 and $\text{WO}_{2.9}$. The temperature range of the synthesis β -W obtained in this work is very small: 470 ÷ 490 °C. The specific surface area of α -W nanopowders is $10 \pm 2 \text{ m}^2/\text{g}$. For the β -W mixture with traces of WO_3 and $\text{WO}_{2.9}$, it is $18 \pm 1 \text{ m}^2/\text{g}$. The dynamics of temperature fields during the ignition and combustion of tungsten nanopowders obtained at different temperatures has been investigated.

Experimental studies of the combustion features of compact samples made of unpassivated iron nanopowders and the effect of the porosity of these compact samples on the dynamics of their heating in air are described. It was found that the propagation velocity of the combustion front and the maximum combustion temperature of compacted samples made of unpassivated iron nanopowders decrease with increasing compact density.

INTRODUCTION

Optical methods have two indisputable advantages: *contact free and panoramic view*. In other words, they do not affect the "object - air" system and in many cases make it possible to obtain data in the form of an image at once over the entire flow field or, for example, a flame front. Among the optical methods, one can single out the methods of *visualizing* the flow, which are no less important than measuring its parameters, because they give a visual representation of the general picture of the flow process in a certain medium or the propagation of the combustion front. It is clear that it is important to visualize the flows and fronts of chemical reactions in liquids or gases that arise spontaneously or under the influence of external sources initiated by various physical factors (ultrasound, laser radiation, magnetic and electric fields, etc.). In flows of liquids and gases, the fields of velocities, pressure and temperature are usually visualized. Visualization of chemical processes in flow conditions by means of a variety of methods and means is used to establish their qualitative characteristics: observation of the optical spectrum of a chemical reaction, streamlines, boundary layer separation regions, vortices and shock waves, flow states (laminar or turbulent, stationary or unsteady, etc.). Visualization of the fronts of chemical reactions and flows is carried out by both non-optical and optical methods. Non-optical (direct) visualization of gas and liquid flows includes: the method of introducing rags of smoke (for gas) or colored liquid (for hydrodynamic flows) into the flow, the method of tracing particles. It includes also the method of applying drops or films of a specific liquid (colored, with solid impurities or fluorescent), the use of a thin light sheet (laser sheet) to illuminate particles, etc. Optical methods make it possible to visualize flows using optical instruments and installations. These methods provide visualization of inhomogeneous flows of reacting gas and liquid, qualitative analysis of the state and structure of the flow, non-contact and inertialess measurement simultaneously within the entire visualized section of the flow of the flux density.

The first experiments with chronophotography, which made it possible to record the movement of an object by photographing its individual phases at short equal intervals of time, and which became the prototype of cinema, were carried out for the same purposes. They allowed studying the imperceptible phenomena. Modern equipment allows you to shoot from several thousand to tens of millions of frames per second, making it possible to observe very fast processes. High-speed digital devices are used to analyze many fast-moving phenomena, in particular, to analyze the processes of flame propagation, transition of combustion to detonation, spark discharges and other phenomena. The frames obtained in laboratory conditions make it possible to measure the parameters of the medium flows, the velocity and structure of the combustion fronts, and ultimately present the visualization results in a form that is convenient for understanding and mod-

eling. Modern electronic recording devices, as a rule, do not contain moving parts that limit performance. CCD-matrices allow registering fast processes with a frequency of up to 1000 frames per second. The CMOS sensors made it possible to shoot millions of frames per second and completely replace cine film. The speed level reached at the beginning of the decade at 0.6 trillion frames per second made it possible to record the movement of the light front of a pulsed laser. Even some digital compact cameras, such as the Casio Exilim series, are equipped with high-speed video recording at up to 1200 frames per second at reduced frame sizes. For accelerated filming, special digital cinema cameras are used, the most famous of which are Phantom devices capable of shooting up to a million frames per second, infrared video cameras (for example, Xeva-2.35-320) are already capable of recording radiation with an acceptable resolution of up to 400 frames per second.

At present, along with the above visualization methods, remote sensing methods for studying various processes using the latest optoelectronic devices are becoming more and more widespread. This book focuses on the use of hyperspectrometers, the domestic line of which is being intensively developed, unique UV-C sensors, as well as the combined use of hyperspectrometers and high-speed color filming. Hyperspectrometers are devices that allow remote registration of reflected, scattered and upward radiation to obtain its spectrum in a wide range of wavelengths. Measurements in the range from several hundred to a thousand spectral channels are called hyperspectral, and a hyperspectral image sensor is a device that simultaneously measures spectral and spatial coordinates. This book examines domestic lines of hyperspectrometers, which at one point in time register a narrow band of emitting, reflecting or scattering radiation surface (the so-called push broom systems). Registration is carried out on a two-dimensional matrix, along one coordinate of which the spatial coordinate x is fixed (along a narrow strip of the recorded surface), and along the other - the spectral one. As a rule, the third coordinate y is formed due to the movement of the hyperspectrometer by some kind of carrier (airplane, helicopter, car, satellite), or this movement is carried out using a rotary device. In addition to the two standard coordinates x and y , the spectral coordinate and the intensity of the spectral line are added, which provides a 4D dimension of the data space. If the hyperspectrometer is in the state of rest, then since the data is read from the recording device of the hyperspectrometer in frames accumulated on the recording device for a certain time, in this case (instead of the y coordinate) the t -time coordinate appears. It becomes possible to study the temporal characteristics of the processes occurring on a narrow strip of the surface, i.e. the 4D dimension is formed by the x coordinate, the spectral coordinate - by the wavelength λ , the intensity of the spectral line I and the time t .

In the first Chapter of this book, methods and means of remote shooting in the optical range are considered. The advantages of using multispectral multisensory imaging, which significantly increase the efficiency of remote analysis of both images and combustion and explosion processes, are demonstrated. In the

second Chapter, optoelectronic devices are considered, such as the domestic line of hyperspectral sensors of the optical range and the UV-C sensor, developed and created at "RDC "Reagent", JSC. The following Chapters are devoted to the results of studying combustion and explosion processes, including the help of optoelectronic devices. In the third Chapter, a study of instabilities arising from the propagation of hydrogen and hydrocarbon flames by the method of high-speed filming is carried out. The regimes of flame propagation during combustion of lean hydrogen-air mixtures in the presence of additives under conditions of central initiation by the method of high-speed filming are considered. The onset of acoustic instability in hydrogen-air mixtures in a closed reactor with central initiation by a spark discharge is analyzed. The regularities of the interaction of spherical flames of hydrogen-air and methane-air mixtures with fine-mesh obstacles at central initiation by a spark discharge have been established. The features of thermal ignition in gas vortices are investigated. The fourth Chapter presents the results of studying the patterns of propagation of an unstable flame front using optical 4D spectroscopy and color high-speed filming. The fifth Chapter describes the use of a high-speed optical multidimensional technique to establish the characteristics of ignition and combustion of 40% H_2 - air mixture in the presence of platinum metal. In the sixth Chapter, 4D spectroscopy and high-speed filming are used to establish the gasdynamic and kinetic features of the penetration of methane-oxygen flames through obstacles. The gasdynamic and kinetic features of the penetration of a methane-oxygen flame through single holes and fine-mesh obstacles have been investigated. The regularities of the penetration of flames of dilute mixtures of methane with oxygen through a single hole in a flat obstacle, diffuser, confuser and combined obstacles have been established. The factors determining the length of the flame jump after penetration through a small hole are revealed. The spectral features of the emission of methane-oxygen flames under the conditions of penetration through obstacles have been established.

The seventh Chapter describes the establishment of the basic features of combustion of mixtures of hydrogen-air and hydrogen-hydrocarbon ($C_1 - C_6$) -air above the surface of palladium metal with the combined use of a hyperspectral sensor and high-speed color filming. The combustion of mixtures hydrogen-air and hydrogen-methane-air over the palladium surface, the ignition of mixtures hydrogen - hydrocarbon (C_1-C_6) - air over the palladium surface at pressures of 1÷2 atm is investigated. Regularities are established and numerical simulation of the ignition of hydrogen-oxygen and hydrogen-methane-oxygen mixtures by heated wires at low pressure is carried out. The eighth Chapter is devoted to the establishment of the laws governing the combustion of copper, tungsten and iron nanopowders and compacted samples of iron nanopowders by the methods of visible and infrared filming.

CHAPTER 1. Methods and means of remote sensing in the optical range

Methods and means of remote sensing in the optical range are considered. The advantages of using multisensor sensing, which significantly increase the efficiency of remote analysis of both images and combustion and explosion processes, are demonstrated.

Keywords: *video camera, hyperspectrometer, thermal imager, UV sensor, remote sensing, image, alignment*

Since the seventies of the last century, remote sensing methods in the optical range have undergone significant changes. In particular, such effective means of remote sensing as spectrozonal, multispectral and hyperspectral survey have appeared. Accordingly, adequate processing methods were developed, taking into account the spectral features of the interaction of waves of various ranges with the material of the probed objects and their morphological structure. We will point out here only the methods of spectral synthesis, neural network algorithms and the method of principal components.

At the same time, all these methods related only to the processing of data obtained by one sensor. However, an approach based on the processing of multispectral data obtained by different sensors when they simultaneously shoot the same scene is of certain interest. It is obvious that sensors can have different spatial resolution, different angular field of view, sensitivity, etc.

This approach is a development of the principle of multispectral sensing, since the creation of a single device that would cover the entire optical range from ultraviolet to far infrared and would have high values of spatial and spectral resolution seems to be very problematic.

In this regard, the purpose of this Chapter is to demonstrate the capabilities of multisensory imaging aimed at improving the efficiency of vision systems through the joint analysis of images obtained in different wavelength ranges. In particular, it is shown that the joint analysis of data from different sensors can achieve a significant synergistic effect and create a basis for the so-called extended vision system [1].

Initially used in aerial and space imaging of the Earth, as well as in laboratory experiments, panchromatic imaging made it possible to obtain images with a high spatial resolution (due to the higher sensitivity of black-and-white photographic film) (Fig. 1), but it did not provide the necessary distinguishability of the objects with color (spectral) differences.

In point of fact, the image contrast was formed by adding spectral contrasts in quadrature (by "power") without taking into account their phase relationships during panchromatic, since different spectral contrasts could even be opposite and, when added, compensate each other. Of course, full compensation could not be

due to their different weight ratios, but the result was a decrease in the total contrast.

So, it was necessary to "sweep" the radiation received by the sensor along the wavelength. The first intuitive solution to this problem was first the use of color and then multispectral photography, in which the photographic film was sensitized to different spectral zones. Finally, the so-called multi-zone method was developed, in which a camera was used with several lenses equipped with filters with different spectral transmission bands.

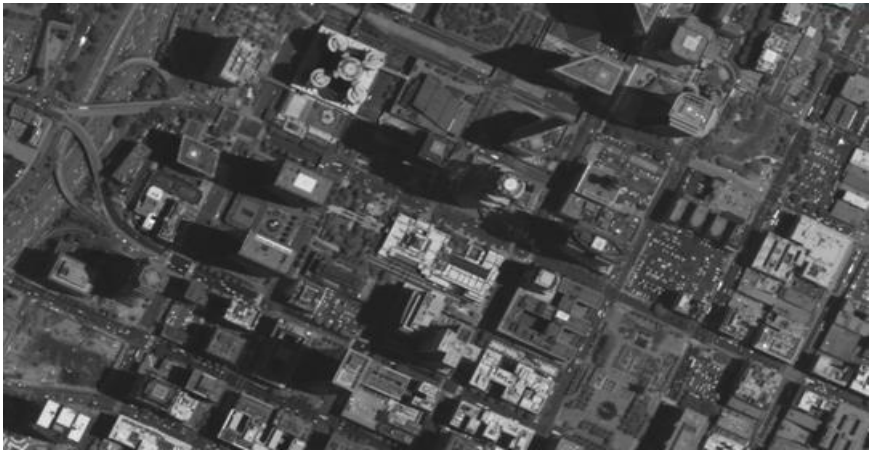


Figure 1. City of Los Angeles (USA). The picture was taken by domestic optoelectronic equipment with a resolution of 1 m from an altitude of 475 km in the panchromatic range from the "Resurs-P" spacecraft in June 2013

The solar radiation reflected from the sensing object passed through such a filter fell on a highly sensitive black-and-white film, forming a spectrozonal image on it. The black-and-white negatives (positives) obtained then were illuminated by light sources with real or conventional colors with the help of special devices and projected onto a common screen. At the same time, it was possible to interactively project on the screen both the negatives and the positives of the images in order to produce their in-phase summation, as well as to give each of them its own weight. This procedure is called "image synthesis".

The most famous of such space sensors is the MKF-6 multispectral space camera, which has successfully passed field tests on the "Soyuz-22" spacecraft. Even the first experiments with multispectral images have shown their high efficiency in recognizing objects in images (Fig. 2).

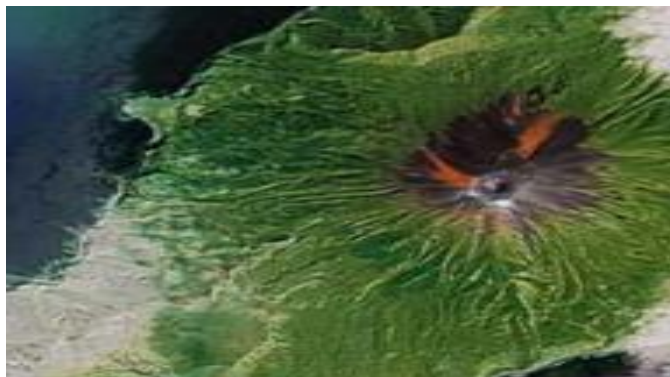


Figure 2. *Synthesized image in false colors of the territory of the "Mir" diamond quarry, obtained by the MKF-6 camera*

A further development of multispectral imaging was the appearance of opto-electronic multispectral MSS scanners on the ERTS-1 satellites AS (Landsat), "Meteor", SPOT, etc. (see Fig. 3).

As the number of spectral channels of sensors increased and the methods of their processing were improved, the information content of the data obtained with their help enhanced. In particular, it was found that the maximum contrast of the probed objects occurs in the images corresponding to the first principal component of the original multispectral data.



Figure 3. *Synthesized image of the territory of Northern Ukraine in false colors, obtained on the basis of imagery with a multispectral MSS scanner from the ERTS-1 AS (Landsat)*

Spectrometers used on board aircraft and satellites, which possessed up to several hundred spectral channels (for example, "Spectr-256"), provided only path survey and did not allow obtaining spectral images of the terrain and, therefore, could not compete with multispectral scanners. The situation has changed dramatically with the advent of laboratory and onboard hyperspectral sensors, which provide simultaneous acquisition of several hundred spectral images recorded on a photodetector matrix. One of the first representatives of the line of hyperspectrometers developed at "RDC "Reagent", JSC [2] VID-IK3 is shown in Fig. 4. Its main technical characteristics are shown below.

Spectral range, nm	400 – 1000
Spectral resolution, nm	1 – 10
Angular spatial resolution, rad	$1 \cdot 10^{-3}$
Number of independent spectral channels	224
Signal-to-noise ratio	more than 100

To demonstrate the possibilities of using such sensors, we present a hyperspectral image of the fire zone (Fig. 5), obtained with a VID-IK3 hyperspectrometer



Figure 4. Photo of a VID-IK3 hyperspectrometer

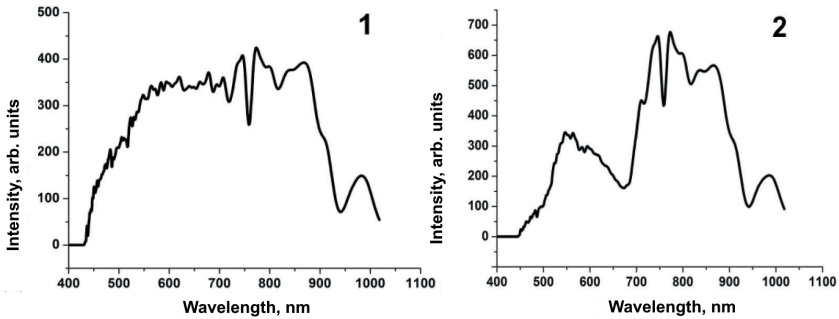


Figure 5. RGB image of a fire obtained by a hyperspectrometer:
1-area affected by fire; 2-area, not affected by fire.

At the bottom of Fig. 5, the emission spectra corresponding to the pixels highlighted on it (points 1 and 2) are shown. For these spectra, the absorption of solar radiation was not taken into account, therefore, the most characteristic peaks associated with the absorption of solar radiation in the atmosphere are clearly visible on them. Spectrum 1 clearly shows a peak in the region of 450-700 nm associated with chlorophyll. In Fig. 6, an image obtained on the basis of the first main component of this hyperspectral image is shown. It is interesting because the boundaries of objects are more clearly visible on it than on the RGB image due to the higher contrast of the depicted objects.



Figure 6. The first principal component of the hyperspectral image

Thus, the hyperspectral image obtained using the first principal component algorithm has the highest possible contrast achieved by a single sensor.

A detailed description of the product of hyperspectral sensors created at "RDC "Reagent", JSC, some of which were used to obtain the results described in the following Chapters, is given in Chapter 2. Naturally, the question of using a hyperspectrometer to study combustion and explosion processes in laboratory conditions has arisen. Thus, in [3, 4], the prospects for such a study were demonstrated and experimental results were presented that cannot be obtained by traditional emission optical spectroscopy.

For this, a laboratory hyperspectrometer was created for remote sensing of reflected, scattered and emitted light from a distance of 3 m (Fig. 7).



Figure 7. The laboratory hyperspectrometer

It was shown that the created hyperspectrometer can be effectively used to control and study combustion and explosion processes. The possibility of studying the processes occurring during combustion and explosion simultaneously in a wide range of wavelengths turned out to be especially interesting. In addition, the hyperspectrometer provides measurement of the time dependence of the light emission that occurs during combustion and explosion (see Fig. 8).

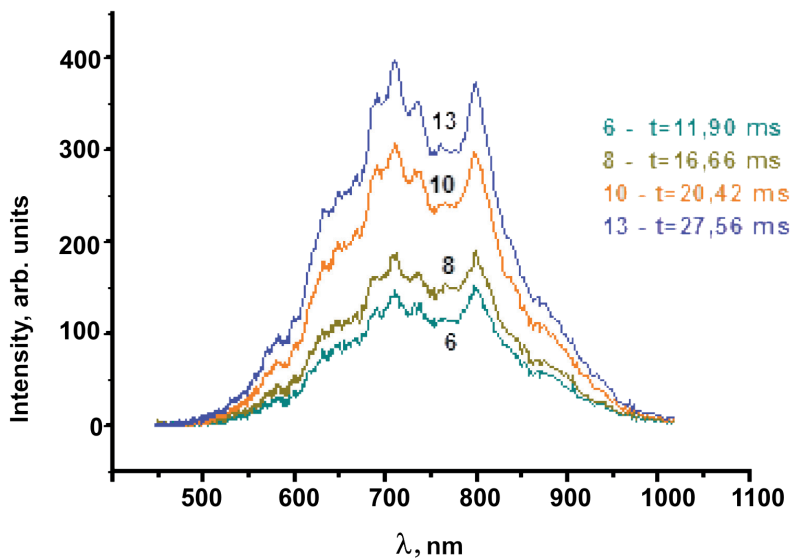


Figure 8. Spectra of explosion radiation versus time

As mentioned in the introduction, digital compact-size cameras are capable of high-speed video recording at up to 1200 frames per second at reduced frame sizes. Such measurements make it possible to visualize the combustion and explosion processes (in particular, to register the movement of the flame front in time), but do not make it possible to determine the chemical composition of the products. Therefore, it turned out to be interesting to combine the simultaneous use of high-speed color filming [5] and hyperspectral measurements for studying combustion and explosion processes.

Another promising optoelectronic sensor is an ultraviolet sensor in the UV-C range (UV-C sensor). Several versions of this device have been developed at "RDC "Reagent", JSC. In Fig. 9 the "Corona" sensor is shown [6]. A more detailed description and operation of the UV sensor is given in Chapter 2. This sensor detects radiation in the UV range of 250-280 nm. The UV range is interesting because solar UV radiation is absorbed by the ozone layer and the "Corona" sensor can register object radiation in sunlight.

To illustrate the possibility of detailing such catastrophic phenomena as fire when using various sensors: the UV-device "Corona", a hyperspectrometer and a thermal imager, the fire centers were recorded.



Figure 9. "Corona" UV-C sensor

So, in Figs. 10 and 11 a video image of the area with a fire in the background is shown. The "Corona" sensor is visible in the foreground.



Figure 10. Video image of a scene with a fire that does not fall within the visible area of the "Corona" device



Figure 11. Video image of a scene with a fire falling into the viewing field of the "Corona" device

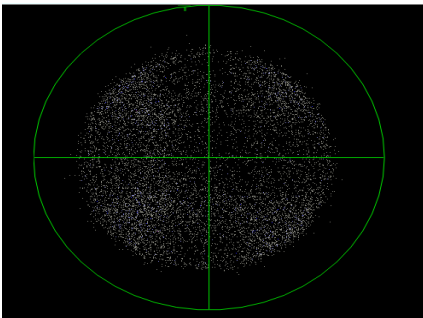


Figure 12. The image obtained by the "Corona" device for the case when the fire zone did not get into its viewing field (see Fig. 10)

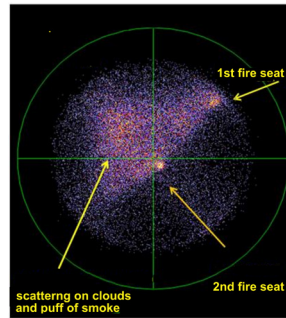


Figure 13. The image obtained by the "Corona" device for the case when the fire zone got into its field of viewing (see Fig. 11)

Analysis of the images in Figs. 10-13 allows us to conclude that the joint use of video and UV-C data makes it possible to accurately georeference the fire centers and study their structure. In addition, the UV image allows one to identify several local fire sources and determine its front. So, video filming gives a general view of the scene, while the UV image allows one to identify the fires inside the smoke plume.

The next step was to study the possibilities of combining video and thermal photography when they probe the same scene with a fire (Figs. 14 and 15, respectively). As in the previous case, Fig. 14 gives an overview description of the

fire pattern and reveals the geometry of the smoke plume well. However, the thermal imaging image (Fig. 15) demonstrates the internal structure of the fire and allows one to highlight the open fire zone and, thus, to show latent information hidden from the eye. Joint consideration of both images provides an informational synergistic effect that cannot be obtained separately by each sensor.



Figure 14. Video image of the fire zone

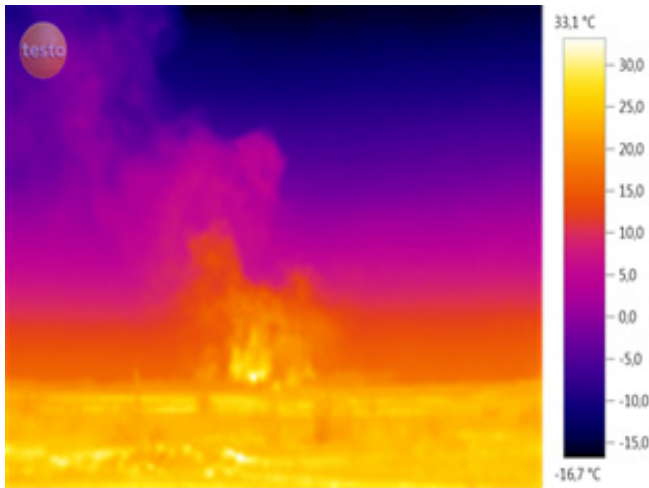


Figure 15. Image of the fire zone, obtained with a thermal imager in the range of 8-14 μm

Conclusions for Chapter 1

This Chapter discusses a method for multispectral analysis of remote sensing data using various sensors and assesses the capabilities of multisensor imagery carried out in a wide range of wavelengths from ultraviolet to infrared. Various combinations of data make it possible to reveal the detailed structure of the analyzed scene, to study the spectral composition of the radiation of objects and to distinguish point sources by it. The prospects of using various sensors for studying combustion and explosion processes are shown. The results of using different sensors are demonstrated in subsequent Chapters.

References for Chapter 1

1. *Vision system overview, C&PS Flight Technical Services. 2013. https://www.mygdc.com/assets/public_files/gdc_services/pilot_services/presentations/Vision_Systems_Overview.pdf*

2. *Rodionov I. D., Rodionov A. I., Vedeshin L. A. Vinogradov A.N., Egorov V. V., Kalinin A. P. Airborne hyperspectral systems for solving remote sensing problems. Izvestiya Atmospheric and Oceanic Physics. 2014. Vol. 50. No. 9. pp. 989-1003. DOI: 10.1134/S0001433814090175*

3. *Kalinin A. P., Orlov A. G., Rodionov A. I., Troshin K. Ya. Demonstraciya vozmozhnosti izucheniya processov goreniya i vzryva s pomoshch'yu distancionnogo giperspekttral'nogo zondirovaniya (Demonstration of the possibilities to study combustion and explosion processes on the base of hyperspectral remote sensing). Physical-Chemical Kinetics in Gas Dynamics. 2009. Vol. 8. <http://chemphys.edu.ru/issues/2009-8/articles/202/> (in Russian)*

4. *Kalinin A. P., Troshin K. Ya. Orlov A. G. Rodionov A. I. Giperspektrometr kak sistema kontrolya i izucheniya processov goreniya i vzryva (Hyperspectrometer as a system for monitoring and studying combustion and explosion processes). Sensors & Systems. 2008. No. 12. pp.19-21. (in Russian)*

5. *Vinogradov A. N., Kalinin A. P., Rodionov I. D., Rodionov A. I., Rodionova I. P., Rubtsov N. M., Chernysh V. I., Tsvetkov G. I., Troshin K. Ya. Ustrojstvo dlya distancionnogo izucheniya processov goreniya i vzryva s ispol'zovaniem giperspektrometrii i skorostnoj fotos"emki (Device for remote study of combustion and explosion processes using hyperspectrometry and high-speed filming), Patent RF No. 158856. 2016. (in Russian)*

6. *Belov A. A., Egorov V. V., Kalinin A. P., Korovin, Rodionov A. I., Rodionov I. D., Stepanov S. N. Ultraviolet Monophoton Sensor "Korona". Automation and Remote Control. 2014. Vol. 75. No. 12. pp. 345-349, DOI:10.1134/S0005117914080116*

CHAPTER 2. Optoelectronic devices and methods for studying combustion and explosion processes

Optoelectronic devices such as the domestic line of hyperspectral sensors of the optical range and the UV-C sensor, developed and created at "RDC "Reagent", JSC are considered. A photo-integrated CMOS sensor performs registration of hyperspectral images. The main technical characteristics of the sensors and examples of hyperspectral RGB images obtained during the tests are presented.

Keywords: *hyperspectrometer, objective, diaphragm bundle, dispersing device, photo-integrated matrix, prism, resolution, sensor*

The optoelectronic devices that are discussed in this chapter include hyperspectrometers and ultraviolet sensors in the wavelength range of 250-280 nm (UV-C sensors). As mentioned in Chapter 1, modern hyperspectrometers provide detailed spatial and spectral information about the type and state of probed natural and anthropogenic objects on the earth's surface. It also gives information about various dynamic processes, for example, combustion and explosion processes, which are discussed below. The interest to in such devices is explained by the fact that due to the Gaussian distribution of the instantaneous values of the electromagnetic field entering the sensor lens. All the useful information contained in the optical signal is displayed in the spectrum.

The more accurately the spectrum envelope of the received radiation is reproduced, the more information can be extracted from it [1]. It is no coincidence, therefore, that the developers strive to increase the number of spectral channels and higher spectral resolution of sensors from units of spectral channels of multi-spectral devices to several hundred and thousands of channels in hyperspectrometers.

Hyperspectrometers can be used with aircraft (aircraft, helicopters, unmanned aerial vehicles), satellites, in ground and laboratory research. The data of hyperspectral measurements are especially useful for solving such complex problems as detecting small objects, identifying the composition of the objects under study and dynamic processes, differentiating closely related classes of objects, assessing biochemical and geophysical parameters, etc. Only hyperspectral measurements can reveal small spectral differences between individual elements of an object.

A hyperspectrometer is an optoelectronic sensor that allows simultaneous measurement of spectral and spatial coordinates. This chapter deals with push broom hyperspectrometers, which measure a narrow strip of emitting, reflecting or scattering surfaces. Registration is carried out on a two-dimensional area array detector, along one coordinate of which the spatial coordinate x is fixed (along a narrow strip of the recorded surface), and along the other - the spectral one. As a rule, the third coordinate y is formed due to the movement of the hyperspectrom-

eter by some kind of carrier (airplane, helicopter, car, satellite), or this movement is carried out using a rotating device. In Fig. 1, the process of hyperspectral remote sensing using a delivery aircraft is demonstrated.

The basic concept of hyperspectral imaging is the "hypercube" shown in Fig. 2.

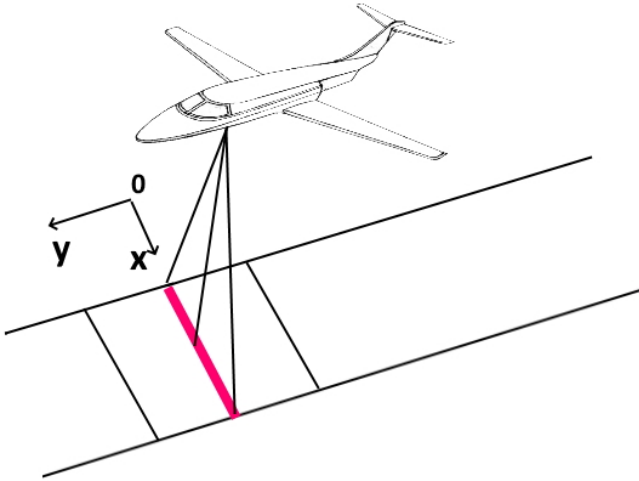


Figure 1. Remote sensing of the Earth by a push broom hyperspectrometer

This is the name of the set of data formed by the values of the intensity of light emitted or reflected from the investigated two-dimensional surface, conventionally divided into image elements - the pixels of the emitted light signal

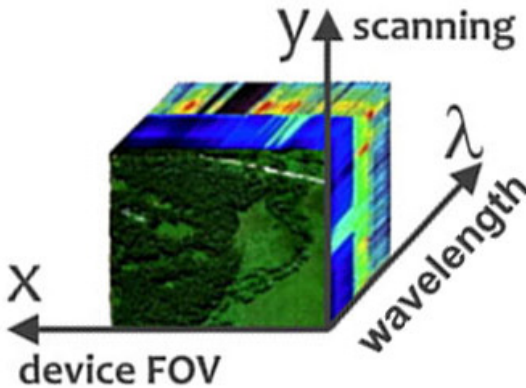


Figure 2. Hyperspectral cube

In addition to the two standard coordinates X and Y, the spectral coordinate λ and the intensity of the spectral line are added, which provides the 4D dimension of the data space. If the hyperspectrometer is at rest (for example, when registering combustion and explosion processes), then, since the data sampling from the hyperspectrometer's recording device occurs in frames accumulated on the hyperspectrometer's recording device for a certain time, in this case (instead of the Y coordinate) coordinate t - time occurs. In other words, it becomes possible to study the temporal characteristics of the processes occurring on a narrow strip of the surface. In this case, the 4D array is formed by the x coordinate, the spectral coordinate - by the wavelength λ , the intensity of the spectral line I and the time t.

Unfortunately, this branch of technology in Russia has a time lag behind the advanced countries. Significant efforts are being made to create promising hyperspectral sensors to correct radically the current situation in Russia. In particular, the team of employees of "RDC "Reagent", JSC, the Space Research Institute RAS, the Ishlinsky Institute for Problems in Mechanics RAS has been developing hyperspectral sensors of the optical range for many years [2-5]. The experience accumulated in the course of these developments made it possible to create a line of hyperspectrometers of the 0.2 - 2.5 μm range in terms of their main technical characteristics, which are not inferior to similar foreign models.

When designing a line of hyperspectrometers, special attention was paid to the calculation of their optical schemes, the choice of dispersive devices and detectors. In this regard, the purpose of this Chapter is to describe the developed line of hyperspectral modules operating in the specified range, their tactical and technical characteristics, the results of field experiments performed with their help, as well as possible areas of application of a scientific and applied nature, in particular, for remote sensing of combustion and explosion processes.

The selection of a narrow strip of the probed object, which is necessary for the operation of the hyperspectrometer in the push broom mode, is performed by means of a slit located in the diaphragm assembly. The diaphragm bundle is placed in the best image plane of the input lens (focal plane). When designing hyperspectral modules of the 0.2 - 2.5 μm range, the developers were tasked with obtaining the maximum possible values for the spatial and spectral resolution at the given values of the field of viewing. In this regard, an approach was used based on the search for various kinds of compromise solutions, which made it possible to find the optimal design option for which the optical system of hyperspectral modules was calculated. In particular, it was decided to create several hyperspectral modules with the ability to cover the entire specified spectral range.

In the course of model experiments, using Zemax optical design software, ray tracing were performed to determine optical system performance of the hyperspectral devices. Based on these calculations, the designs of the hyperspectral modules were selected. In Fig. 3 the path of rays in one of the hyperspectral modules (which was later called VID-IK3) is shown. In Fig. 4 an example of calculat-

ing the spot diagrams for the same module at different viewing angles of a point source (0° , 6.3° , 9.0° , 12.6° and 18° - points 1-5) and for two wavelengths (450 and 900 nm) is presented. It follows from an analysis of Fig. 4 that the sizes of the spots lie in the range from 8 to 16 μm , which with a focal length of the module of 17 mm correspond to the dimensions of a pixel on the earth's surface from a height of exposure of 1 km - from 0.3 to 0.6 m.

Based on the calculations performed, an experimental series of hyperspectrometers was manufactured. Various dispersive elements can be used in hyperspectrometers: a diffraction grating, a holographic grating, a prism, a combination of prisms, a combination of optical wedges and a diffraction grating, etc. A prism-based design was used in this case.

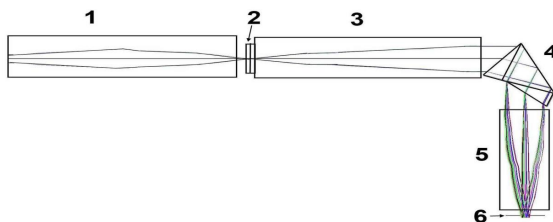


Figure 3. Calculated ray path in the VID-IK3 hyperspectral module

- 1 - entrance lens, 2 - diaphragm unit with a slit, 3 - collimator,
- 4 - dispersive element, 5 - camera lens, 6 - photodetector array

For spectral instruments, prisms are made from flints and heavy flints, since these glasses have high-refractive indices and dispersion. Both 60° refractive angle prisms and a constant deflection prism were used.

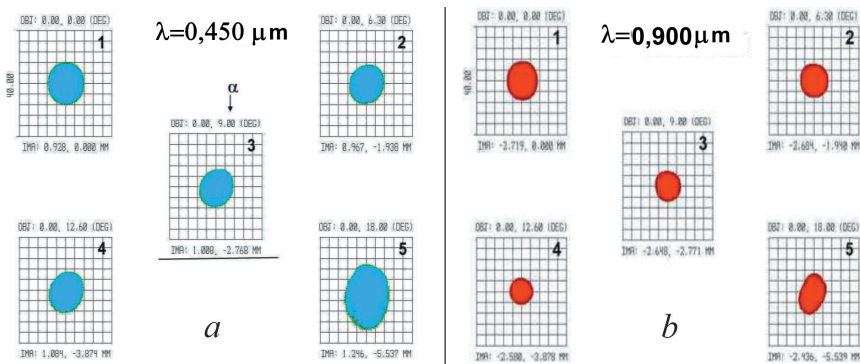


Figure 4. Spot diagrams in the image plane:

- a) - for a wavelength of 450 nm; b) - for a wavelength of 900 nm

In the case of a prism with a refractive angle of 60° , there is still no total in-

ternal reflection from the second surface and a high dispersion is achieved. In one of the hyperspectral modules, in order to reduce its size, a prism of constant deflection angle of 90° (Abbe prism) was used (see Fig. 3, structural element 4). All hyperspectral modules have the same functional diagram (see Fig. 5). Each module of the line is made in the form of a monoblock without a single fixing plate.

Measurements of the spectral resolution of the hyperspectral modules were carried out.

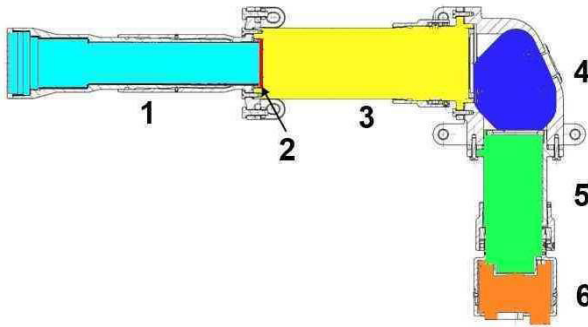


Figure 5. Functional diagram of hyperspectral modules (correspondence of numbers to elements coincides with Fig. 3)

In Fig. 6, digit 1 shows the measured dependence of the spectral bandwidth $\Delta\lambda$ of the VID-IK3 module on the wavelength, and digit 2 $\Delta\lambda \sim \lambda^{-3}$ shows the fitting, where λ is the wavelength, which corresponds to theoretical calculations for a prism hyperspectrometer.

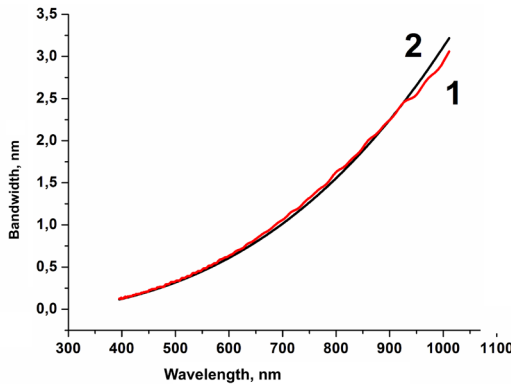


Figure 6. Dependence of the spectral bandwidth of the IK-VID3 module on the wavelength: 1 - measured; 2 - fitting $2 \Delta\lambda \sim \lambda^{-3}$

The hyperspectral modules of the product line have variations in the values

of the spectral range and differ significantly in the magnitude of the field of view. Therefore, the choice of their specific version should be determined by the complex of tasks to be solved. Different values of the field of view of hyperspectral modules are achieved by changing the focal length of their optical systems. In addition, the VID-IK1 module, unlike the other three modules, is equipped with a thermal stabilization system, which led to an increase in its weight up to 11 kg. The technical characteristics part of the product line of the hyperspectral modules are shown in Table 1, and their photographs are shown in Fig. 7.

Table 1.
Characteristics of hyperspectral modules

No.	Characteristics	Hyperspectral modules			
		UF-VID	VID-IK1	VID-IK2	VID-IK3
1.	Spectral range, μm	0.35-0.55	0.45-1.0	0.45-0.9	0.4-1.0
2.	Field of view, degrees	60	60	20	35
3.	Spatial resolution from a height of 1 km, m	up to 0,3			
4.	Number of channels	up to 500			
5.	Frame rate, 1/s	up to 70			
6.	Weight, kg	6.6	11	1.95	3.2
7.	Dimensions (LxWxH), mm ³	590x310x102	575x315x135	400x180x80	425x230x84

All hyperspectral modules can be equipped with a compact processing system (preprocessing, including calibration, as well as thematic processing) and data storage in real time. In the case of using the developed airborne hyperspectrometers, they are integrated with the on-board navigation system and provide data transfer to communication channels. These systems can be adapted at the request of the consumer to specific media and purpose.

"RDC "Reagent", JSC has also developed hyperspectrometers for the wavelength range 900-1700 nm (BIK1) and 900-2500 nm (BIK2). For the sake of brevity, we report only the aircraft hyperspectral device - BIK1. The BIK1 hyperspectrometer, the optical system of which is shown in Fig. 9, contains an entrance objective lens 1, a diaphragm bundle 2, a collimator 3, consisting of two sections 4 and 5. These sections are installed at an angle to each other, the optimal value of the rotation angle is 90° .

A mirror 6 is placed between the collimator sections 4 and 5. A dispersing unit made in the form of a diffraction grating 7 is installed behind the collimator section 5. Further, along the path of the beams, the lens 8 and the photodetector array 9 are installed.

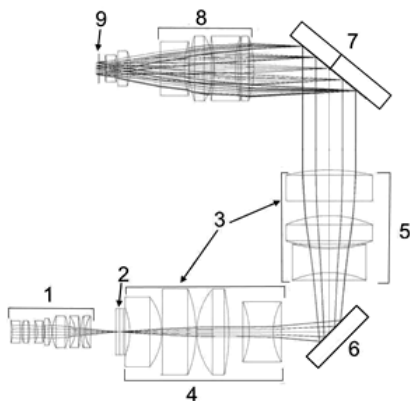


Figure 9. *Optical system of the BIK1 hyperspectrometer*

In the course of model experiments, using Zemax optical design software, ray tracing were performed to determine optical system performance of the hyperspectral device BIK1.

An example of calculating the spot diagrams for sighting a point source is shown in Fig. 10, and in Fig. 11 - coordinates of beams for different wavelengths in the image plane of the hyperspectrometer.

It follows from analysis of Figs. 10 and 11 that the sizes of the spot diagrams are in the range from 1.7-10 μm , depending on the wavelength λ and the angular field 2ω along the transverse strip of the viewing area (see the table in the upper right part of Fig. 10). Thus, the spot is significantly smaller than the pixel size of the used photodetector array (30 μm x 30 μm). For an effective focal length of 15 mm, the size of a pixel on the earth's surface from a shooting height of 1 km will be 2 m (i.e., the angular resolution will be $2 \cdot 10^{-3}$ rad). The optimal design of the BIK1 hyperspectrometer was chosen after taking into account these calculations.

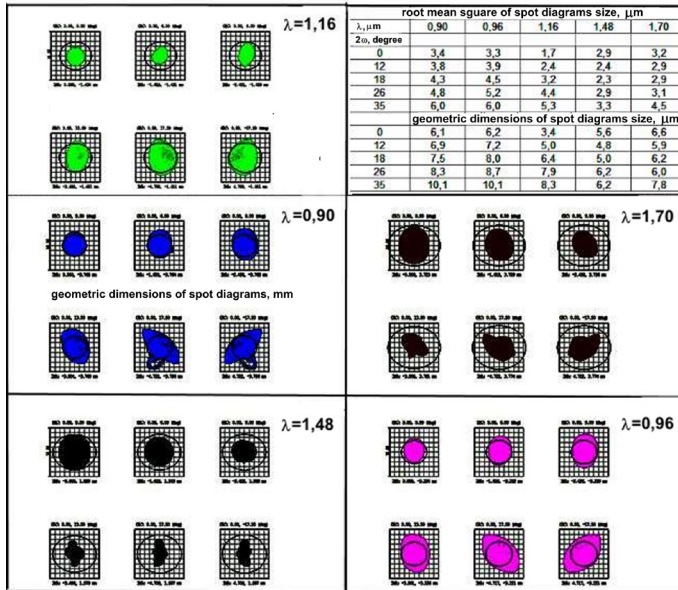


Figure 10. Spot diagrams for the instantaneous field of view of the BIK1 device

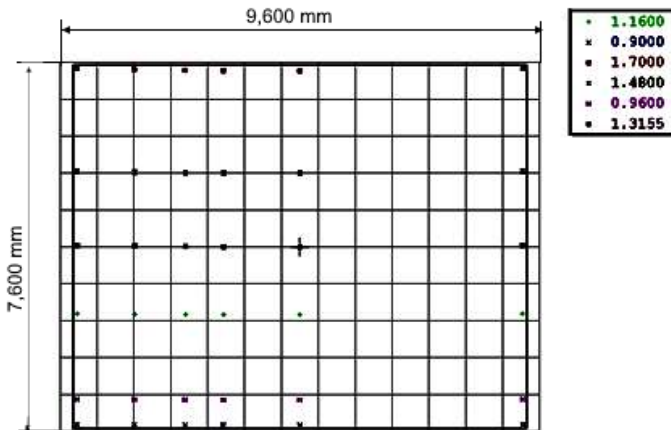


Figure 11. Coordinates of beams for different wavelengths in the image plane of the hyperspectrometer

Spectral calibration of the BIK1 hyperspectrometer was carried out using a monochromator according to the correspondence of the array pixel number to the wavelength (black squares in Fig. 12).

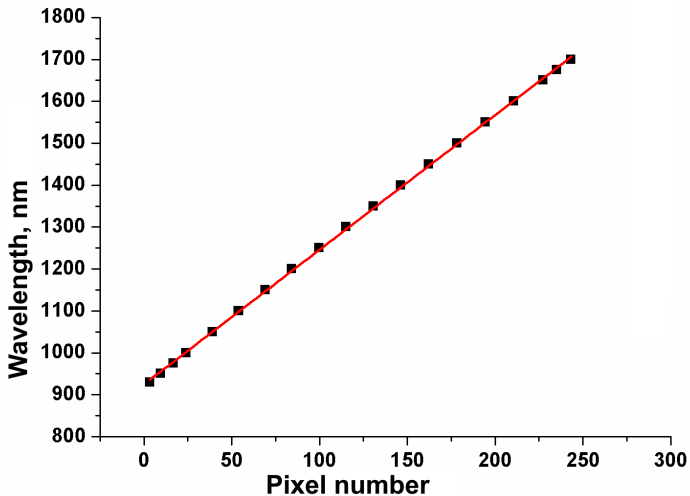


Figure 12. Graph of correspondence of the pixel number of the matrix and the wavelength of the light beam

The red line in Fig. 12 shows a linear approximation of the measurement results. It can be stated that the measurements and the linear dependence are in good agreement, which indicates the efficiency of the calculations of the hyperspectrometer design.

Technical characteristics of the BIK1 module are given in Table 2, and its appearance in Fig. 13.

Table 2.
Basic technical characteristics of the BIK1 module

Parameter	Value
Spectral range, nm	900 - 1800
Angle of field of view, degrees	35
Width of spectral channels within the specified spectral range, nm	3.2
Number of spectral channels	250
Number of pixels in a spatial coordinate	320
Angular resolution, rad	2×10^{-3}
Weight, kg	8



Figure 13. External view of the BIK1 hyperspectrometer

In laboratory conditions, the spectral resolution of hyperspectrometers has been studied. Thus, the spectra of a mercury lamp for the VID IK3 sensor in Fig. 14a and in Fig. 14b for BIK1 is shown. These measurements indicate a good resolution of the sensors under study.

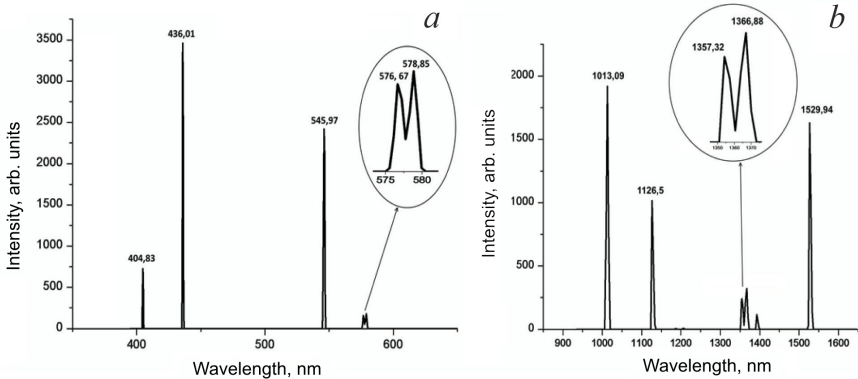


Figure 14. Spectra of a mercury lamp measured with a VID-IK3 (a) hyperspectrometer and BIK1 (b)

In some experiments to measure radiation used an assembly of two sensors. So when studying ignition and combustion of a mixture of 40% H_2 - air in the presence of platinum metal were applied hyperspectrometers – VID-IK3 and VID-IK3 modified (the ability to programmatically reduce the linear field of view with increasing frame rate). Assembly appearance shown in Fig. 15. Here the number 1 stands for hyperspectrometer VID-IK3, digit 2 is hyperspectrometer VID-IK3 modified and number 3 is rotary scanning device. The use of two devices at once allowed reveal new features of the combustion process.



Figure 15. Assembly of two hyperspectrometers VID-IK3 and VID-IK3 modified on a rotary scanning device

It should be emphasized that it is difficult to find a field of science, technology, and the national economy where hyperspectrometers could not be used with great success. So in work [6], about 30 possible applications are noted only in remote experimental studies of regional and global processes in the terrestrial environment using space hyperspectral and infrared sensors.

Let us consider the possibility of one of the very interesting applications of hyperspectrometers in the simultaneous use of both a hyperspectrometer and high-speed color filming for laboratory study of combustion and explosion processes.

A experimental design laboratory with the combined use of a hyperspectral sensor and a high-speed camera is shown in Fig. 16. Here 1 is a reactor, in which a combustion or explosion occurs; 2 is an optical sapphire window that allows radiation to pass in the wavelength range of 200 - 6000 nm. And 3 is a narrow strip recorded by a hyperspectrometer. Fig. 16 demonstrates the process of hyperspectral imaging of combustion and explosion in laboratory conditions using a VID-IK3 hyperspectrometer. The ray propagation scheme in the hyperspectrometer is shown in Fig. 17a (the object numbers correspond to the numbers in Fig. 5.)

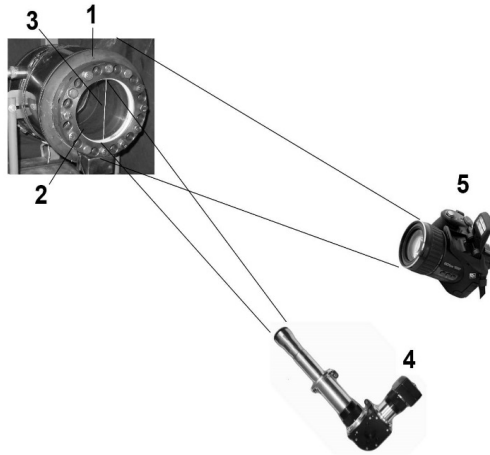


Figure 16. Scheme of an experiment on the combined use of a hyperspectrometer and high-speed filming to study combustion and explosion processes

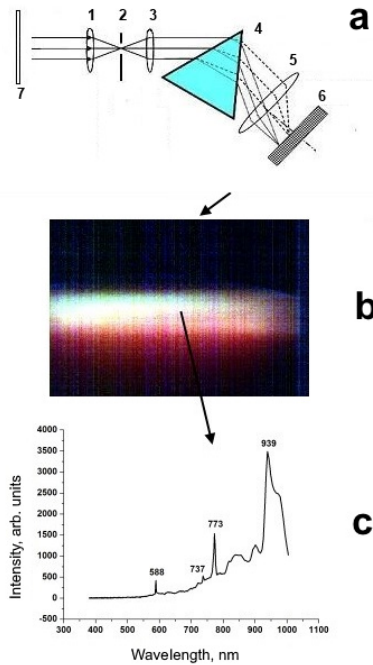


Figure 17. Stages of the process of hyperspectral imaging of combustion and explosion in laboratory conditions

The spectrometer field of view provides a view of a narrow strip along the reactor window (strip 3 in Fig. 16). In Fig. 17b hyperspectral data (hypercube) in pseudo-RGB colors (horizontal - spatial coordinates of the red stripe, and vertical - dependence on shooting time) are shown. In Fig. 17c, the emission spectrum corresponding to one of the points of the hypercube and depending on the position on the survey strip and time is demonstrated. The use of a high-speed cine camera makes it possible to compare the recorded spectrum of the video frame of the combustion mode under study at the same moment in time, which provides unique information about the peculiarities of the process in the given volume elements. Chapters 4-7 of this book discuss in detail the combined application of hyperspectral measurements in conjunction with high-speed color filming to various modes of the combustion process: laminar, cellular and turbulent flames.

Let us consider a promising development of "RDC "Reagent", JSC, which was mentioned in Chapter 1, an ultraviolet sensor for the wavelength range of 250-280 nm (UV-C sensor). Several variants of such a sensor have been developed. The UV-C sensor "Corona 30" is discussed below.

The interest in the 250-280 nm region is due to the fact that this range has a relatively low level of background noise. Solar radiation is the main source of natural interference in the optical range. However, thanks to the planet's ozone layer, as well as the atmosphere, the bulk of solar radiation in the 250-280 nm region is blocked. The solar radiation that reaches the earth's surface is concentrated in the regions of visible and infrared radiation (Fig. 18).

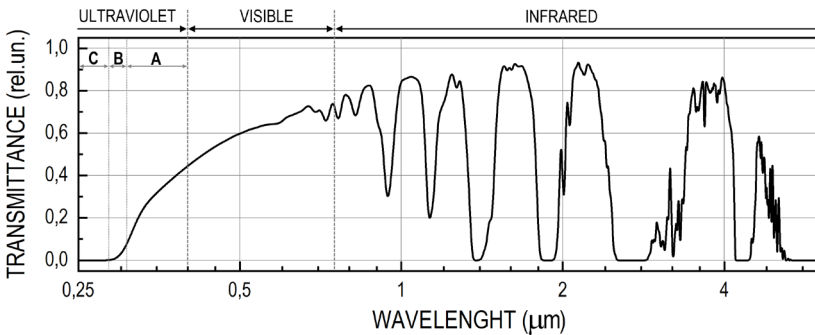


Figure 18. The transmittance of solar radiation through the Earth's atmosphere

It can be seen from this figure that the spectral range below 280 nm can be characterized as free from solar radiation (solar-blind).

The absence of natural interference caused by solar radiation, the low level of background interference in the UV range, makes the solar-blind range very attractive for the creation of photodetector equipment that solves various technical problems. The peculiarities of UV sensors developed by "RDC "Reagent", JSC are

the ability to determine the coordinates of a detected photon, work in a monophotonic mode and determine the time of arrival of a photon. This provides the sensor with a unique ability to measure the time dependence of the detected radiation and analyze this dependence. Thus, the created sensor acquires an innovative quality i.e. the determination of the characteristics of the UV radiation source, which radically increases the potential of the created sensor in comparison with the existing counterparts. One of such developed UF-C devices is "Korona 30" sensor.

Some of the characteristics of this sensor are indicated in Table 3.

Table 3.
Features of "Corona 30" sensor

Characteristic	Value
Spectral range, nm	250 – 280
Field of view, degrees	30
Spatial resolution, mrad	1
Time resolution, ns	1

The design and operation of the UV sensor is shown in Fig. 19.

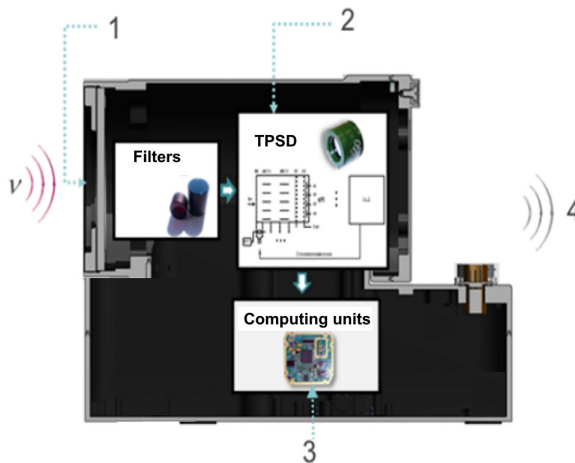


Figure 19. Figure explaining the device and principle of operation of the "Corona 30" sensor

The device consists of (Fig. 19): entrance lens 1, Time Position Sensitive Detector (TPSD) 2 with electronic tracts, computing unit 3, number 4 corresponds to the output data - coordinates and time of arrival of the registered photon. The entrance lens consists of a lens system made of crystals with good transmission of the selected UV range while suppressing other wavelengths and UV filters. Thanks to the entrance lens, a solar-blind mode of registration of UV radiation is provided, and the sensor can work in conditions of intense solar radiation. The transmitted photon ν enters the photocathode of the PSD detector. The suppression factor of photons with wavelengths other than the range of 250-280 nm after passing through the lens and detector can reach 10^{-14} . PSD provides determination of the angular coordinates of photon reception and determination of the time of its arrival. More details about the operation of UV sensors can be found in [7-9].

The developed sensor is applicable in various fields of science and technology. Chapter 1 demonstrated the use of UV sensors for fire detection. One of the practically important applications is the use of this sensor for remote diagnostics of high voltage alternating current electrical installations and, in particular, power transmission lines [10]. This is because a corona discharge occurs on such electrical installations, and especially on electrical insulators of power transmission lines, accompanied by UV radiation. Also, this sensor is promising for optical location, providing good spatial resolution and the ability to operate at any time of the day. The UV sensor can be used in aircraft landing systems [11] and in many other applications.

Conclusions for Chapter 2

Optoelectronic devices such as the domestic line of hyperspectral sensors of the optical range and the UV-C sensor, developed and created at ""RDC "Reagent", JSC, are considered. A schematic diagram of a laboratory experiment to study combustion and explosion processes with the combined use of a hyperspectral sensor and a high-speed cine camera is presented.

References for Chapter 2

1. *Ishimaru A. Wave propagation and scattering in random media. Vol. 1. New York (NY, USA): Academic Press. 267 p. <https://doi.org/10.1016/B978-0-12-374701-3.X5001-7>*
2. *Nepobedimiy S. P., Rodionov I. D., Vorontsov D. V., Orlov A. G., Kalashnikov S. K., Kalinin A. P., Ovchinnikov M. Yu., Rodionov A. I., Shilov I. B., Lyubimov V. N., Osipov A. F. Hyperspectral remote sounding of the ground. Doklady Physics. 2004. Vol. 49. No. 7. pp. 411-414. DOI: 10.1134/1.1784854*

3. Rodionov I. D., Rodionov A. I., Vedeshin L. A., Vinogradov A. N., Egorov V.V., Kalinin A. P. Airborne hyperspectral systems for solving remote sensing problems. *Izvestiya Atmospheric and Oceanic Physics*. 2014. Vol. 50. No. 9. pp. 989-1003. DOI: 10.1134/S0001433814090175

4. Egorov V. V., Kalinin A. P., Rodionov I. D., Rodionova I. P., Orlov A. G. *Giperspektrometr – kak element sistemy intellektual'nogo tekhnicheskogo zreniya (Hyperspectrometer - as an element of an intelligent technical vision system)*. *Sensors & systems*. 2007. No. 8. pp. 33-35. (in Russian)

5. Vinogradov A. N., Egorov V. V., Kalinin A. P., Rodionov A. I., Rodionov I. D. *Bortovoj giperspektrometr vidimogo i blizhnego infrakrasnogo diapazona s vysokim prostranstvennym razresheniem (On board visual and near UV-band hyperspectrometer with high spatial resolution)*. *Current problems in remote sensing of the Earth from space*. 2012. Vol. 8. Number 2. pp. 101-107. (in Russian)

6. Akim E.L., Behr P.Bries., K., Egorov V.V., Fedunin E.Yu., Kalinin A.P., Kalashnikov S.K., Kolk K.-H., Montenegro S., Rodionov A.I., Rodionov I.D., Ovchinnikov M.Yu., Orlov A.G., Pletner S., B.R.Shub, Vedeshin L.A., Vorontsov D.V. *The fire infrared-hyperspectral monitoring (Russian – Germany Proposals for an International Earth Observation Mission)*. Preprint of the Keldysh Institute of Applied Mathematics. Russian Academy of Sciences. 2004. № 32. 36 pp.

7. Belov A. A., Egorov V. V., Kalinin A. P., Korovin N. A., Rodionov A. I., Rodionov I. D., Stepanov S. N. *Monofotonnyj sensor ul'trafiioletovogo diapazona «Korona» (Ultraviolet monophotonic sensor "Corona")*. *Sensors and systems*. 2012. No. 12. pp. 58-60. (in Russian)

8. Belov A. A., Egorov V. V., Kalinin A. P., Korovin, Rodionov A. I., Rodionov I. D., Stepanov S. N. *Ultraviolet monophoton sensor "Corona"*. *Automation and Remote Control*. 2014. Vol. 75. No. 12. pp. 345-349. DOI:10.1134/S0005117914080116

9. Belov A. A., Egorov V. V., Kalinin A.P., Krysiuk I. V., Osipov A. F., Rodionov A. I., Rodionov I. D., Stepanov S. N. *Universal'nyj monofotonnyj sensor ul'trafiioletovogo diapazona (Universal ultraviolet monophotonic sensor)*. Preprint IPMech RAS. 2010. No. 935. 48 p. (in Russian)

10. Belov A. A., Egorov V. V., Kalinin A. P., Korovin N. A., Rodionov I.D., Stepanov S. N. *Primenenie monofotonnogo sensora «Korona» dlya distancionnogo monitoringa sostoyaniya vysokovol'tnogo oborudovaniya (Application of the monophotonic sensor "Corona" for remote monitoring of the state of high-voltage equipment)*. *Chief Power Engineer*. 2012. No. 6. pp. 12-17. (in Russian)

11. Belov A. A., A.N. Vinogradov, Egorov V. V. et al. Zavalishin O. I., Kalinin A. P., Korovin N. A., Rodionov A. I., Rodionov I. D. *Vozmozhnosti ispol'zovaniya koordinatno-chuvstvitel'nykh monofotonnykh UF-S datchikov dlya navigacii vozdushnykh sudov v zone aerodroma (Possibilities of using position-sensitive monophotonic UV sensors for aircraft navigation in the airfield area)*. 2014. *Sensors & systems*. No. 1. pp. 37-42. (in Russian)

CHAPTER 3. Investigation of the instabilities arising from the hydrogen and hydrocarbon flames propagation by the method of high-speed filming

The method of high-speed filming was used to study the instabilities arising from the propagation of hydrogen and hydrocarbon flames. The regimes of flame propagation during combustion of lean hydrogen-air mixtures with additives under conditions of central initiation by the method of high-speed filming are considered. The onset of acoustic instability in hydrogen-air mixtures in a closed reactor with central initiation by a spark discharge is analyzed. The regularities of the interaction of spherical flames of hydrogen-air and methane-air mixtures with fine-mesh obstacles at central initiation by a spark discharge have been established. The features of thermal ignition in gas vortices are studied.

Keywords: *instability, hydrogen, hydrocarbon, spherical flames, cellular obstacle, thermal ignition, gas vortice.*

Every day, at home or in the workplace, we meet with devices which use combustion, or in which combustion occurs. In this case, the combustion process can be useful, for example, a primitive fire, cooking ovens, various technological processes, including an internal combustion engine. This process can be extremely harmful, in particular, forest fires, mine fires, etc. Such a wide application and significance of combustion in our life requires knowledge of the laws of this phenomenon. If ignition has occurred, the flame spreads through the combustible mixture. Under certain conditions, the flame can accelerate and detonation occurs - a complex consisting of a shock wave fed by the energy released during combustion and a combustion zone that propagates at a supersonic speed. Obviously, such processes leading to the destruction of industrial and residential premises and the death of people should be excluded. Combustion must be strictly controlled; reliable methods of preventing combustion should be available.

Combustion suppression methods can be divided into chemical (using active additives that break the reaction chains) and physical (flame arresters). Methods for extinguishing with foam and aerosol formulations are intermediate, since the substances introduced into the flame zone are usually reactive. Active additives that suppress combustion (inhibitors) have many disadvantages, despite their apparent ease of use, for example, the possibility of mixing with a combustible gas in advance. Hydrogen combustion inhibitors, such as unsaturated hydrocarbons, are flammable themselves and are effective only in stoichiometric and rich mixtures. These inhibitors accelerate, on the contrary, combustion in lean mixtures. Metal carbonyls are poisonous and cannot be used in the presence of human personnel. Practically safe freons in case of an abnormal fire lead to the formation of toxic fluorophosgene. Physical methods such as barriers and grids can also serve as combustion turbulators along with a suppressive effect. Under certain conditions,

they can lead to an acceleration of the combustion front with undesirable consequences.

On the other hand, many combustion devices require complete combustion (diesel engines) or accelerated combustion (detonation engine). This is ensured by the use of nozzles, turbulators and other obstacles to accelerate the flame, which, on the contrary, is desirable in this situation. The presentation of the foundations of the theory of combustion was not included in the tasks of the authors of this book. However, the authors draw the reader's attention to the fact that the modern theory of combustion is given in a number of references to the fundamental works and monographs for each subsequent Chapter, and the reader can get acquainted with the fundamentals of this field of science with their assistance.

As far as is known, the processes of gaseous combustion proceed under conditions of unsteady flows, fluctuations in density and pressure, i.e. are nonstationary in nature. Sound vibrations are a manifestation of these instabilities. It is known that there is a significant acceleration of various heat-and-mass transfer processes (mixture formation, evaporation, heat transfer from gas to walls, heat transfer when the flow interacts with heated bodies, etc.) in unsteady flows. Particle agglomeration and coagulation of aerosols is improved. In addition, during vibration combustion, the level of emission of toxic substances NO_x decreases.

Acoustic vibrations during combustion are caused by the instabilities arising from the propagation of the flame front. These instabilities manifest themselves in combustion processes in various forms and can be classified as thermal diffusion instability, hydrodynamic one, and thermoacoustic one.

Thermal-diffusion instability is observed in flames in which the rates of heat transfer and diffusion are different, i.e. $Le \neq 1$ (Lewis number $Le = D / a$, where D is the diffusion coefficient of the component that determines the combustion process, and a is the thermal diffusivity). This instability leads, for example, to the cellular nature of the propagation of flames in hydrogen-lean combustible mixtures.

Hydrodynamic instability is determined by the difference in the densities of the burnt and unburned gas associated with the thermal expansion of the reaction products and also, under certain conditions, can lead to the appearance of cellular flames.

Thermoacoustic instability is determined by the resonant relationship between the unsteady combustion mode and the acoustic modes of the reactor. Non-stationary heat release leads to the generation of acoustic vibrations, which, reflecting from the walls of the reactor, interact with the combustion process. Since combustion is sensitive to changes in gas flow conditions, if the phase between acoustic oscillations and unsteady combustion satisfies certain conditions, feedback and, accordingly, combustion instability can occur. The criterion for the occurrence of this instability was proposed by Rayleigh and consists in the fact that acoustic oscillations are maintained if maximum heat is imparted to the oscillating gas at the moment of its maximum compression.

It is known that a flat flame is unstable from a hydrodynamic point of view. For a spherical FF, its stability was explained by the fact that the radius and, accordingly, the surface of the flame front grow so rapidly that instability does not have time to develop against this background. Therefore, at the initial stage of combustion, when the flame front has a spherical shape, hydrodynamic instability should not manifest itself. However, after the flame front touches the walls of the reactor, it propagates in the cylindrical channel. At this stage of combustion, the conditions for the rapid growth of the FF surface disappear and the hydrodynamic instability of the flame should occur.

Recently, much attention has been paid to the use of hydrogen-containing fuels in the automotive industry and power plants, including the combustion of the most ecological lean hydrogen-air mixtures, accelerated by the addition of hydrocarbons. The expected results on FF visualization are important both for the experimental verification of theoretical concepts of the propagation of gas flames and for solving the issues of explosion safety.

Let us note in conclusion that in the modern scientific literature there is no systematic information about the conditions leading to the unstable propagation of the FF of mixtures of hydrogen and hydrocarbons with air in a cylindrical reactor with a central spark ignition.

§ 1. Investigation of flame propagation modes of lean hydrogen-air mixtures in the presence of additives under conditions of central initiation by means of high-speed cinematography

As indicated above, in the absence of special conditions, gas-phase combustion processes proceed under conditions of unsteady flows, fluctuations in density and pressure, i.e. are nonstationary ones [1-3]. For example, lean hydrogen-air mixtures are characterized by the inhomogeneity of combustion front caused by thermal-diffusive instability, which leads to the appearance of flame cells [3-5]. For the first time, flame cells during the combustion of lean (up to 10% H₂) hydrogen-air mixtures were observed in [6]. It was shown in [1, 7] that flame cells in lean mixtures of hydrogen with air are also observed under microgravity conditions. In other words, the gravity field is not a prerequisite for the formation of flame cells.

When studying the propagation of flames in lean mixtures of hydrogen with air in narrow vertical pipes, it was found that the propagation of the flame “upward” is accompanied by the underburning of the fuel. In addition, in this case, the concentration of the fuel at the limit of propagation is less than in the “downward” direction [4, 8].

In two-dimensional simulations of the combustion of hydrogen-lean mixtures, convection and gravity were neglected [9]. However, the calculated burning velocities turned out to be close to the experimental ones. The analytical theory of a

cellular flame, based on the representation of a flame as a dense flat structure of hexagonally packed flame balls [2], also gives good agreement with experiment on the values of combustion velocities with a good selection of parameters. It is of interest to find out the limits of applicability of hydrogen flame models that do not take into account convection and compressibility of the medium for describing the experimentally observed flame velocities [2, 4, 5, 7, 9, 10] in comparison with models that take into account convection [2, 11] and medium compressibility.

For this purpose, in this section, a study of the structure of flames of lean mixtures of hydrogen with air in a bomb of constant volume at atmospheric pressure is carried out by the method of high-speed filming. The obtained results are compared with numerical calculations and experimental data known from the literature.

Experimental

The experiments were carried out with lean mixtures of hydrogen (6-15%) with air at initial atmospheric pressure and temperature $T_0 = 298$ K.

A horizontally located cylindrical stainless steel reactor 15 cm long and 13 cm in diameter was used as a setup. At one of the ends, the reactor was equipped with an optical quartz window. In the center of the reactor, spark ignition electrodes were placed, the distance between which was 0.5 mm. The experiments were carried out in the following sequence. If necessary, carbon tetrachloride CCl_4 , and then hydrogen and air, were fed into the reactor up to atmospheric pressure. The reactor was pumped out to 10^{-2} Torr beforehand. It should be noted that an inert additive of CCl_4 up to 4% is used to visualize a hydrogen flame [12]. The mixture was kept for 15 min for complete mixing, and the ignition was initiated with a spark (the discharge power was 1.5 J). The dynamics of the ignition and propagation of the FF was recorded through the optical window using a Casio Exilim F1 Pro color high-speed film camera (frame rate - 60 - 1200 s^{-1}). The resulting video file was written into the computer memory and then processed frame-by-frame.

The change in pressure during combustion was recorded using a piezoelectric sensor, the signal from which was fed to S9-8 digital storage oscilloscope. The pressure in the reactor during the composition of the gas mixture was monitored with vacuum gauge. Before each experiment, the reactor was evacuated using a 2NVR-5D foreline pump. Gas H_2 , carbon tetrachloride CCl_4 were used of chemically pure grade. The degree of expansion of combustion products ε_T was determined by the value of the maximum pressure developed during the combustion of the P_b mixture [7]:

$$P_b/P_0 = 1 + \gamma(\varepsilon_T - 1) \quad (1.1)$$

The value of the normal velocity of flame propagation in the initial section Un was determined from the relation [13]:

$$Un = Vv/\varepsilon_T \quad (1.2)$$

In expressions (1), (2) P_b is the maximum pressure, P_0 is the initial pressure, γ is the adiabatic index of the initial mixture, V_v is the apparent flame velocity in the initial section.

Results and discussion

As is seen in Fig. 1, the flame front at the initial stage of development has a spherical shape. Cells are well visualized at the flame front, and the diameter of the sphere can be measured experimentally. For mixtures with H_2 concentration $<10\%$, the flame front has a spherical shape only at the initial stage after initiation (Fig. 1a).

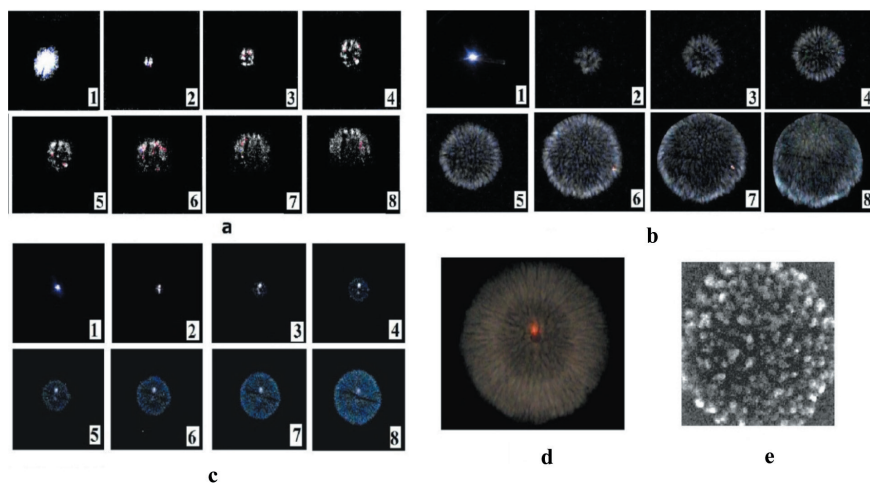


Figure 1. The result of high-speed filming

a) - the process of propagation of a cellular flame front 4% CCl_4 + 8% H_2 + 88% air, $T_0 = 298$ K, initiation energy is 1.5 J. Frame rate 60 s^{-1} [9];

b) - the process of propagation of a flame front illuminated with 4% CCl_4 in a mixture of 10% H_2 + 86% air at atmospheric pressure. Film speed 60 frames/s;

c) - the process of propagation of a flame front illuminated with 4% CCl_4 in a mixture of 15% H_2 + 81% air at an initial atmospheric pressure. Film speed is 600 frames/s. The number on the frame corresponds to the frame number when shooting. The first frame corresponds to the occurrence of a spark discharge;

d) - a frame from high-speed filming of the propagation of the flame front illuminated with 2% CCl_4 in a mixture of 12.5% H_2 + 87.5% air at atmospheric pressure [8]. Film speed is 60 frames/s;

e) - a frame from high-speed filming of the flame front propagation under microgravity conditions, 7.0% H_2 in air, addition of 0.4% CF_3Br . 1.18 s after initiation has passed [7].

Further, in the combustion process, the effect of gravity is manifested. The flame front takes the form of a hemispherical segment moving upward (Fig. 1a, b). For mixtures containing $H_2 > 10\%$, the flame front velocity increases so much that the effect of gravity does not have time to manifest itself, and the flame propagates spherically symmetrically (Fig. 1c, d). The flame front remains cellular, while the size of the flame cells decreases with an increase in hydrogen content up to 15%.

It can be seen in Fig. 1a, that for 8% H_2 in air at the initial stage, the combustion front is spherical (Fig. 1a, frames 2-6). Figure 1b shows the results of high-speed shooting for flame propagation in a mixture of 10% H_2 in air, illustrating the sphericity of the flame front. The apparent flame velocity V_v measured by us for a mixture of 4% $CCl_4 + 10.0\% H_2 + 86.0\%$ air (Fig. 1a) is 36 cm/s, while the normal velocity U_n calculated by formula (1.2) is 21 cm/s taking into account the experimental value of εT for this mixture is 1.6.

The apparent flame velocity V_v for a mixture of 4% $CCl_4 + 15.0\% H_2 + 81.0\%$ air (Fig. 1c) is 2.4 m/s, while the normal velocity U_n calculated by formula (1.2) is 60 cm/s, taking into account that for this mixture the experimental value of εT is 4. As is seen in Fig. 1c, combustion is cellular in nature at this hydrogen concentration. These values of the normal velocity agree with the value of U_n known from the literature data. They are also close to the results of the numerical calculation of U_n obtained using the laminar flame model without taking into account convection [9], i.e. without taking into account the cellular structure of the flame. This means that the perturbations of a thermodiffusion nature observed in the flame front at the initial stage of combustion do not have a significant effect on the propagation velocity of the lean mixture flame.

It is possible to indicate the concentration boundaries of various modes of propagation of a cellular flame in lean hydrogen-air mixtures from Fig. 1 and the data [4, 8]:

a) "gravitational" with the content of $H_2 < 10\%$, which corresponds to different velocities of propagation of the flame front "up" and "down" in narrow tubes [4, 8] and a spherically symmetric regime at the initial section of combustion;

b) spherically symmetric with an H_2 content in the range of $10\% \div 15\%$, while there is no difference between the "up" and "down" propagation velocities.

The literature also describes a spherically symmetric mode of propagation of a cellular flame under microgravity conditions at a hydrogen concentration of less than 10% [1, 7]. It should be noted also that under zero gravity there is also a little-studied mode of the appearance of separate isolated stationary combustion cells during the combustion of lean mixtures [1].

We point out that the experimental values of the lower concentration limit of flame propagation in microgravity (C_{micro}) have a noticeable scatter, which does not allow us judging with certainty whether its value is close to the "upward" or "downward" propagation limit. According to [7], this concentration limit is close to the value of the limit when the flame propagates upward in the gravity field and

is 5.5% H₂ in air. However, according to [1], (C_{micro}) is 7% H₂ and according to [7] (C_{micro}) is 7% H₂ in presence of 2.5% CF₃Br.

From the above, we can conclude that the spherical shape is inherent in the propagation of cellular flames of lean mixtures at the initial stage. The gravity field only then distorts the shape of the combustion front for mixtures near the lower concentration limit of flame propagation (Fig. 1a, b). However, we point out that a careful approach is required to the concept of sphericity or the degree of sphericity of flames in reaction volumes of different shapes and sizes. In this work, a two-dimensional projection of the FF onto the end plane of a cylindrical reactor is used for conclusion on the sphericity.

Let us consider some of the results obtained in the numerical simulation of cellular flames. A two-dimensional plane problem was considered in [10, 14] and the model of thermal convection was used in the Boussinesq approximation for analyzing the combustion front in lean hydrogen-air mixtures. The reduced kinetic scheme of the hydrogen oxidation reaction, which included 13 reactions, as well as the thermochemical parameters, was taken from [8]. However, in the absence of gravity, but taking into account convection associated with gas expansion during combustion, the cellular regime was missing in the calculations. Thus, the calculation in the Boussinesq approximation does not allow simulating the experimentally observed propagation of a cellular flame under microgravity conditions.

In order to establish, which physical processes should be taken into account when describing the propagation of a cellular flame under microgravity conditions, a numerical analysis by the finite element method was carried out using the FlexPde 6.0 software package [15]. At the same time, since it was shown in [11, 14] that, within the Boussinesq approximation, the features of propagation of lean hydrogen flames do not depend on the nature of the most rapidly diffusing intermediate product, but are determined by the diffusion coefficient of the initial component that is in lack [4, 8], the chemical reaction was set by one equation in the Arrhenius form. The authors note that such a simplified approximation can introduce uncertainties associated with the replacement of the combustion mechanism by one activated reaction.

The results of calculating the propagation of the combustion zone in the Boussinesq approximation is shown in Fig. 2. These results are demonstrated at a) $g = 0$ (g is the acceleration of gravity), b) $g = 980 \text{ cm/s}^2$, c) - calculation of the propagation of the combustion zone at $g = 0$ based on the analysis of the Navier–Stokes equations for a compressible medium [16] (see Appendix).

It can be seen in Fig. 2 that taking into account the convection associated with gas expansion during combustion does not lead to the appearance of a cellular combustion mode in the absence of gravity in a leanly compressible medium (Fig. 2a). In this case, one of the possibilities to describe the cellular regime in the absence of gravity is to take into account the compressibility of the medium in the Navier–Stokes equations (Fig. 2c). We point out that when analyzing the sys-

tem of equations in the Boussinesq approximation, which takes into account the reduced kinetic mechanism of hydrogen oxidation from 12 elementary reactions [10, 14] in the absence of gravity, the cellular combustion mode is also missing, as in Fig. 2a. This means that the simplified approximation used (replacing the reaction mechanism with one activated reaction) does not noticeably affect the results of the qualitative calculation.

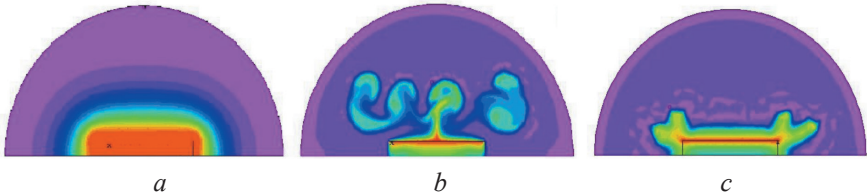


Figure 2. Calculation by the finite element method [16] (see Appendix) of the propagation of the combustion zone in the Boussinesq approximation
 a) - $g = 0$, b) $g = 980 \text{ cm/s}^2$,
 c) - calculation of the propagation of the combustion zone at $g = 0$, solving the Navier–Stokes equations for a compressible medium, $\zeta = 16$

Thus, the Boussinesq approximation is applicable to simulate cells in the gravitational ($\text{H}_2 < 10\%$) mode of flame propagation in lean hydrogen-air mixtures [11]. The Navier–Stokes equations for a compressible medium should be used to describe a spherically symmetric regime under microgravity conditions.

Clarifying the limits of applicability of hydrogen flame models that do not take into account convection and compressibility of the medium for calculating the experimentally observed flame velocities [2, 4, 5, 7, 9, 10, 13] in comparison with models that take into account convection [2, 11] and compressibility of the medium is of interest. Let us compare the data available in the literature on measuring and calculating the combustion velocities of lean hydrogen-air mixtures, taking into account our results. A large set of publication data is presented in [2]. We also use the data from [13], which presents the results of several groups of authors. A comparison of the measured and calculated normal flame velocities for lean hydrogen-air mixtures at 1 atm and an initial temperature of 298 K, depending on the fuel content in the mixture (θ is the excess ratio of fuel in a mixture with air: $\theta\text{H}_2 + 0.5(\text{O}_2 + 3.76\text{N}_2)$) is shown in Fig. 3.

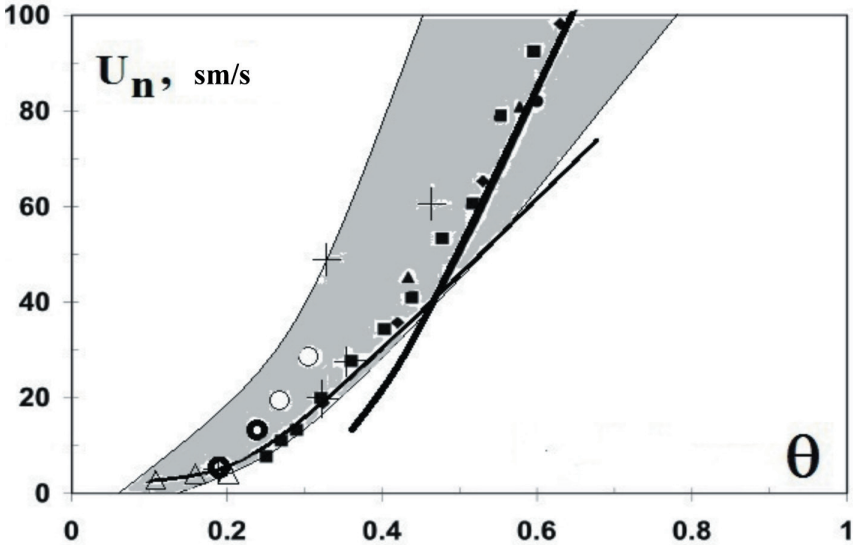


Figure 3. Comparison of measured and calculated normal flame velocities for lean hydrogen-air mixtures at 1 atm and initial temperature of 298 K depending on the fuel content in the mixture (θ is the excess ratio of fuel in a mixture with air: $\theta H_2 + 0.5 (O_2 + 3.76N_2)$). The bold curve is the calculation of the one-dimensional problem [2], the thin curve is the calculation by the analytical relation [2], the points are the data of experimental studies cited in [2] (see Fig. 1 from [2]). The crosses are the experimental data [10, 11], thin circles - data of two-dimensional calculation without taking into account convection [9], bold circles - data of two-dimensional calculation taking into account convection and gravity [10], triangles - experimental data in the absence of gravity [7]. The area in which the experimental values of the propagation velocities of hydrogen-air flames are located according to [13], which contains the data of several groups of authors, are highlighted gray

The bold curve represents the simulation results within the framework of the one-dimensional problem [2], the thin curve is the calculation using the analytical relationship obtained in [2]. The dots in the figure represent the experimental data cited in [2] (see Fig. 1 from [2]), crosses — experimental data [10], thin circles — two-dimensional calculation data without convection (Fig. 2 from [9]), bold circles - data of two-dimensional calculation taking into account the velocity field

(Fig. 3 and Fig. 4 from [10]), triangles - experimental data in the absence of gravity [7]. The area in which the experimental values of the propagation velocities of the flame of hydrogen-air flames from [13] are found is highlighted gray.

As is seen in Fig. 3 the results obtained in [9] using a two-dimensional model without taking into account convection (crosses) are in the range of experimental values of the propagation velocities of the flame of hydrogen-air flames from [13]. It follows from Fig. 3 that the error in experimental data on flame propagation in lean mixtures does not make it possible to consider in detail the kinetic mechanism of hydrogen combustion and even take apart the results of a two-dimensional model with and without convection. In other words, a good selection of parameters allows one to obtain agreement with a specific experience. It should be noted that even the calculations according to the one-dimensional model (the bold curve in Fig. 3), which agree very much with the experiment, are also in the region of the experimental values of the propagation velocities of hydrogen-air flames.

It should be noted that the above discussion applies only to hydrogen-air mixtures in the absence of other combustible additives, for example, hydrocarbons. It is known that the addition of hydrogen to hydrocarbon fuels is promising for increasing the level of environmental safety of combustion products [1]. Combustion of lean hydrogen mixtures in this aspect is the most environmentally friendly, but the burning velocities of such mixtures are low. The combustion velocity can be increased by adding a small amount of hydrocarbon to the lean mixture (see, for example, [18]). The foregoing determines the relevance of the below experimental study of the rates and dynamics of combustion of lean hydrogen mixtures in the presence of a small additive of hydrocarbon, isobutene in this work. The results of high-speed filming of combustion of lean mixtures of hydrogen with the addition of C_4H_8 , the content of which in all cases does not exceed the lower concentration limit of ignition, which is 1.8% [12] are shown in Fig. 4a-f.

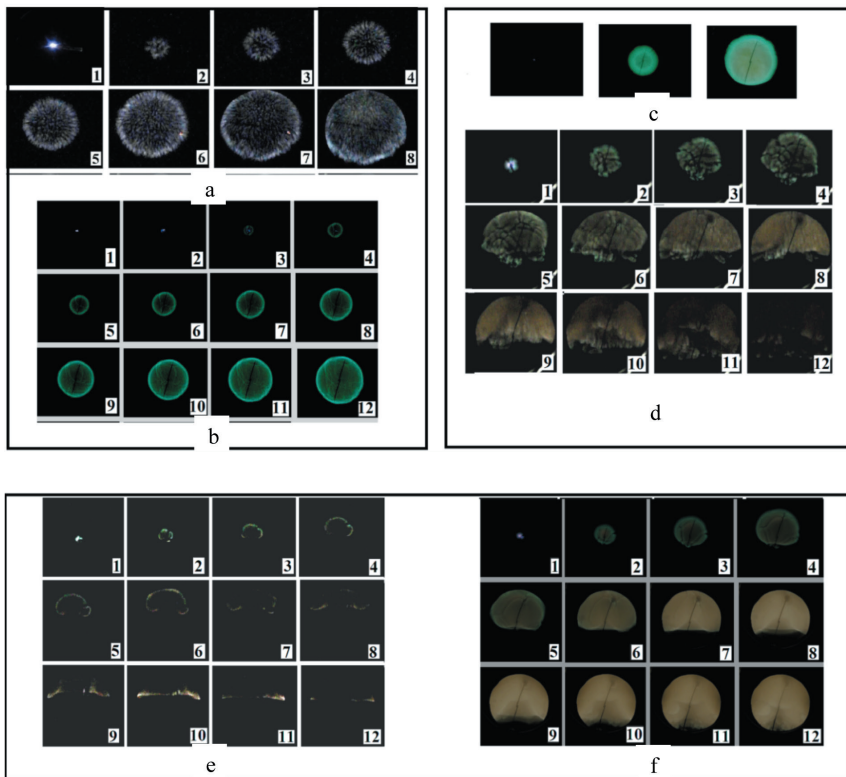


Figure 4. *The result of high-speed filming*

a) - the process of propagation of a flame front illuminated with 4% CCl_4 in a mixture of 10% H_2 + 86% air at atmospheric pressure. Filming speed is 60 frames/s;

b) - the result of high-speed filming of the propagation of the flame front in a mixture of 1.5% C_4H_8 + 10% H_2 + 88.5% air at atmospheric pressure. The speed of filming is 300 frames/s.

c) - the result of high-speed filming of the propagation of the flame front in a mixture of 1.5% C_4H_8 + 7.5% H_2 + 91% air at the initial atmospheric pressure. Filming speed is 60 frames/s;

d) - the result of high-speed filming of the propagation of the flame front, in a mixture of 0.5% C_4H_8 + 7.5% H_2 + 92% air at the initial atmospheric pressure.

e) - the result of high-speed filming of the propagation of the flame front, in a mixture of 1% C_4H_8 + 5.8% H_2 + 93.2% air at atmospheric pressure. The number on the frame corresponds to the frame number when shooting. Filming speed is 60 frames/s.

f) - the result of high-speed filming of the propagation of the flame front, in a

mixture of 1% C_4H_8 + 6.5% H_2 + 92.5% air at atmospheric pressure. Filming speed is 60 frames/s. The number on the frame corresponds to the frame number when shooting. The first frame corresponds to the occurrence of a spark discharge.

From a comparison of the video sequences shown in Fig. 4a-f, it can be seen that in the presence of this additive, the combustion of mixtures containing two combustible components is noticeably accelerated. In other words, in accordance with [18], isobutene accelerates the additive of hydrogen, which burns faster than in the absence of isobutene; the additive of isobutene C_4H_8 , in such quantities, is not combustible.

Indeed, it follows from Fig. 4a, b that a 1.5% addition of isobutene accelerates the combustion of 10% H_2 in air by several times as compared to 10% H_2 in air without an addition. Figure 4c, d shows that an increase in isobutene additive by a factor of 3 accelerates the combustion of 7.5% hydrogen with air also approximately by a factor of 3. Even near the combustion limit, the addition of isobutene significantly accelerates the combustion of hydrogen, see Fig. 4e, f.

In addition, as can be seen in Fig. 4b, c, f, the gas-dynamic features of the propagation of the combustion front of lean hydrogen mixtures in the presence of a hydrocarbon additive also qualitatively change. With an increase in the content of the hydrocarbon additive, inhomogeneities appear no longer in the form of cells, but in the form of “folds” on the surface of the flame front, which are not observed during combustion of lean hydrogen-air mixtures in the absence of a hydrocarbon additive. This means that the stability of the combustion front increases.

Note that the chemical mechanism of combustion of combined fuels based on lean hydrogen mixtures in the presence of hydrocarbons has not been considered in the literature. At the same time, the solution of this issue is necessary for correct numerical simulation of combustion of lean binary mixtures of hydrogen and hydrocarbon with air. The normal flame propagation velocities of hydrogen-air mixtures in the presence of isobutene and CO_2 additives, measured at the initial stage of the combustion process (from the first video frames, when the flame front still retains a spherical shape) using equations (1.1) and (1.2) are shown in Fig. 5.

Normal combustion velocities in the absence of additives (0% isobutene (iso) in Fig. 5) measured in this work are consistent with [12]. As is seen in Fig. 5 the 1.5% addition of isobutene is the most effective and provides an increase in the normal flame velocity of the combined fuel in comparison with the combustion of a lean hydrogen mixture in air by more than 5 times. Addition of CO_2 that phlegmatizes combustion [12] leads to a decrease in the flame velocity (Fig. 5).

It can also be seen in Fig. 5 that to achieve the same flame propagation velocity, for example, 5.8% hydrogen in air requires either 1% C_4H_8 or 2% H_2 (dashed lines in Fig. 5).

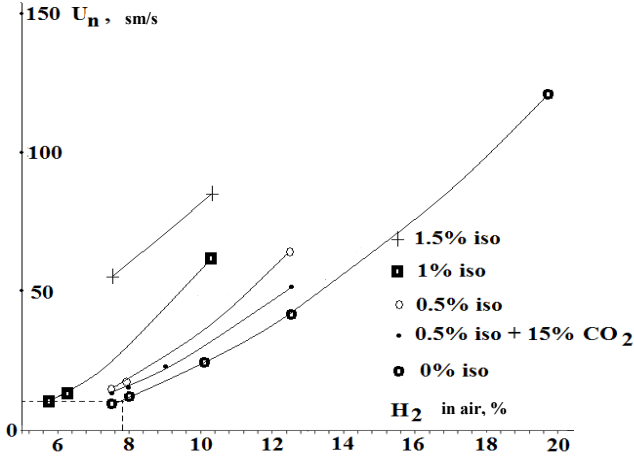


Figure 5. Normal combustion velocities of hydrogen-air mixtures in the presence of isobutene and CO₂ additives

One of the reasons for the observed efficiency of the hydrocarbon additive may be associated with the fact that the thermal effect of oxidation of isobutene is 2549.7 kJ/mol, and of hydrogen - 242.9 kJ/mol [12] and, accordingly, when the hydrocarbon additive burns, heat is released 10 times more than in the combustion of hydrogen. This provides an increase in flame velocity by increasing the adiabatic combustion temperature. Another reason may be a change in the kinetics of combustion in the presence of a hydrocarbon additive. It is important at the initial stage of the flame propagation process, when initiation by a spark discharge leads to the appearance of active centers that initiate combustion, both with the participation of hydrogen and hydrocarbon.

We note in conclusion that in lean hydrogen-air mixtures, in contrast to rich ones [18], the additive of hydrocarbon burns completely in an excess of oxidizer (which is accompanied by light emission, see Fig. 4b-e. Therefore, it is necessary to introduce an effective process with the participation of a hydrocarbon and subsequently take into account the most important elementary reactions of combustion of a hydrocarbon to calculate the flame velocity in the presence of a hydrocarbon additive, along with the mechanism of hydrogen oxidation.

We briefly summarize the results obtained. It was found that cellular flames of lean hydrogen-air mixtures propagate spherically symmetrically at the initial stage of combustion. Therefore, it is possible to use the change in the visible radius of a spherical flame to calculate the rate of cellular combustion of lean hydrogen-air mixtures. Only after that the gravity field distorts the shape of the combustion front for mixtures near the lower concentration limit of flame propagation. It is shown that the Boussinesq approximation is applicable to describe the appear-

ance of cells in a gravity field with an H_2 content $<10\%$. The involvement of the Navier-Stokes equations for a compressible medium makes it possible to describe the spherically symmetric mode observed during the combustion of lean mixtures under microgravity conditions. It is shown that the error in experimental data on flame propagation in lean hydrogen-air mixtures does not make it possible to carry out reliable verification of various calculation models and, all the more, to detail the kinetic mechanism of hydrogen combustion, which is necessary to describe the combustion of lean hydrogen-air mixtures. It was shown that the additives of isobutene C_4H_8 in amounts less than the lower concentration limit of ignition (up to 1.5%) lead to an increase, and the addition of CO_2 leads to a decrease in the flame velocity using the method of color high-speed filming. It was found that the gas-dynamic features of the propagation of the combustion front of lean hydrogen mixtures in the presence of a hydrocarbon additive also change qualitatively. With an increase in the content of the hydrocarbon additive, inhomogeneities appear no longer in the form of cells, but in the form of “folds” on the surface of the flame front, which are not observed in combustion of lean hydrogen-air mixtures in the absence of a hydrocarbon additive. This indicates an increase in the stability of the combustion front. One of the reasons for the increase in the flame front velocity may be an increase in the adiabatic combustion temperature. Another reason may be a change in the combustion kinetics in the presence of a hydrocarbon additive.

Appendix

We use the example BUOYANT.PDE from the software package of the finite element method FlexPde 6.0 [15] to solve a two-dimensional problem for a qualitative consideration of the conditions for the emergence of cellular structures. A reactor of circular cross-section with firing by a step on the horizontal axis is considered. The calculation is carried out in the upper half of the area (Fig. 2). The chemical process is represented by a single reaction in the form of Arrhenius. In the Boussinesq approximation [17], we assume that the medium is incompressible, except for the thermal effects of expansion. The form of the Navier-Stokes equations for an incompressible medium:

$$\text{grad}(\mathbf{U}) = 0, \partial \mathbf{U} / \partial t + \mathbf{U} \text{grad}(\mathbf{U}) + \text{grad}(p) = \nu \text{div}(\text{grad}(\mathbf{U})) + \mathbf{F}$$

where \mathbf{U} is the velocity vector, p is the pressure, ν - the kinematic viscosity, \mathbf{F} - the vector of mass forces.

The first equation expresses conservation of momentum, while the second one expresses conservation of mass.

We obtain the momentum equation using the relations $\text{grad}(\mathbf{U}) = 0$ and $\text{grad}(\text{rot}(\mathbf{U})) = 0$, and the definition of $\mathbf{w} = \text{rot}(\mathbf{U})$:

$$\partial \mathbf{w} / \partial t + \mathbf{u} \partial \mathbf{w} / \partial x + \mathbf{v} \partial \mathbf{w} / \partial y = \nu \text{div}(\text{grad}(\mathbf{w})) - \mathbf{g} \partial \rho / \partial x$$

taking into account the fact that in two dimensions the velocity has only two components, u and v , and the vortex has only one, represented as w .

Let us now consider the continuity equation. If we define a scalar function φ in such a way that $u = \partial\varphi/\partial y$, $v = -\partial\varphi/\partial x$, then $\text{grad}(U) = \partial^2 \varphi / \partial x \partial y - \partial^2 \varphi / \partial y \partial x = 0$, and the continuity equation is satisfied exactly, then $\text{div}(\text{grad}(\varphi)) = -w$

If F – is the force of gravity, then $F = (0, -g \rho)$ and $\text{rot}(F) = -g \partial \rho / \partial x$ where ρ - the density and g - the acceleration of the gravity. If the liquid expands linearly with temperature T , then

$$\rho = \rho_0 (1 + \alpha (T - T_0)) \text{ и } \text{rot}(F) = -g \rho_0 \alpha \partial T / \partial x$$

temperature - $\text{div}(\lambda \text{grad}(T)) = \rho_0 C_p (\partial T / \partial t + u \partial T / \partial x + v \partial T / \partial y)$, λ – coefficient of thermal conductivity, C_p – thermal heat capacity at constant pressure.

The Arrhenius law gives the first order reaction rate

$\text{RC}(C, \text{Temp}) = (1 - C) \exp[\zeta (1 - 1/T)]$. Taking diffusion into account, the system of equations takes the form:

$$\begin{aligned} \partial w / \partial t + u \partial w / \partial x + v \partial w / \partial y &= v \text{div}(\text{grad}(w)) - g \partial \rho / \partial x \\ \text{div}(\text{grad}(\varphi)) &= -w \end{aligned}$$

$$\begin{aligned} \text{div}(\lambda \text{grad}(T)) + \beta_2 \text{RC} &= \rho_0 C_p (\partial T / \partial t + u \partial T / \partial x + v \partial T / \partial y) \\ \text{div}(D \text{grad}(C)) + \beta_1 \text{RC} &= \partial C / \partial t + u \partial C / \partial x + v \partial C / \partial y \end{aligned}$$

and the state equation

$$p = \rho T$$

The temperature of the walls of the outer cylinder is T_0 , the concentration C on the wall of the outer cylinder is zero, the boundary condition of the second kind is specified for the density on the wall of the outer cylinder. Boundary conditions of the second kind for temperature, concentration and density are specified on the segment of the abscissa axis separating the upper and lower halves of the cylinder. The initial temperature of flame initiation at the step is $5T_0$, the initial temperature in the volume is T_0 , the initial concentration is $C_0 = 0$; other parameters are set equal to $T_0 = 1$, $D = 1$, $\lambda = 0.01$, $\alpha = 0.009$, $\rho_0 = 10^{-2}$, $\zeta = 16$, $v = 0.001$, $\beta_2 = 0.3$, $\beta_1 = 0.2$, $g = 0$ (Fig. 2a), $g = 980$ (Fig. 2b).

For a compressible medium, the Navier-Stokes equations in the absence of gravity are written as follows [16]:

$$\partial U / \partial t + U \text{grad}(U) + \text{grad}(p) = v \text{div}(\text{grad}(U)) + \mu \sigma (\sigma \cdot U) + F, \quad \partial \rho / \partial t + \text{grad}(\rho U) = 0$$

When introducing the function w , the moment equation taking into account the identical relation

$$\text{rot}(\text{rot}(w)) = \sigma (\sigma \cdot w) - \text{div}(\text{grad}(w)) \text{ becomes:}$$

$$\partial w / \partial t + u \partial w / \partial x + v \partial w / \partial y = v \text{div}(\text{grad}(w)) + \mu (\text{rot}(\text{rot}(w)) - \text{div}(\text{grad}(w)))$$

along with the equations of continuity, temperature and concentration:

$$\partial \rho / \partial t + \text{grad}(\rho U) = 0$$

$$\begin{aligned} C_p / (\rho \text{Re} \text{Pr}) \text{div}(\text{grad}(T)) + \beta_2 \text{RC} - (\partial T / \partial t + u \partial T / \partial x + v \partial T / \partial y) &= \\ C_p (C_p - 1) / (\rho \text{Re}) ((\partial u / \partial y + \partial v / \partial x)^2 + \frac{2}{3} ((\partial u / \partial x + \partial v / \partial y)^2) + (\partial v / \partial y)^2 + (\partial u / \partial x)^2) & \\ \text{div}(D \text{grad}(C)) + \beta_1 \text{RC} = \partial C / \partial t + u \partial C / \partial x + v \partial C / \partial y & \end{aligned}$$

In the calculation, we used the same initial and boundary conditions that are given above. We also assumed $Re = 10^5$, $Pr = 1$, $\mu = \nu/3$ (Fig. 2d). The scales for dimensioning were chosen as follows [16]: L - length, T_0 - initial temperature, pressure $R\rho_0T_0$, speed - $(\gamma RT_0)^{1/2}$, time - $L/(\gamma RT_0)^{1/2}$. Dimensionless parameters $\gamma = C_p/C_v$, $Pr = \mu C_p / \lambda = 0.72$ [16] (λ - coefficient of heat conduction), $Re = \rho_0 (\gamma RT_0)^{1/2} L/\nu$.

§ 2. The onset of the acoustic instability in hydrogen-air mixtures in a closed reactor upon central initiation by a spark discharge

As is known, combustion is a source of sound vibrations. The sound generated by combustion plays an important role in ensuring the stable operation of engines, turbines, etc. [19]. In particular, intense pressure fluctuations lead to undesirable additional loads on the walls of the combustion device. On the other hand, it is known [20] that in oscillating flows, there is a significant acceleration of various heat and mass transfer processes (mixture formation, evaporation, heat transfer from gas to walls, heat transfer when the flow interacts with heated bodies, etc.), particle agglomeration and coagulation of aerosols are improved. In addition, in vibration combustion, the level of NOx decreases [21].

Acoustic vibrations during combustion are caused by instabilities arising from the propagation of the flame front [20, 22]. These instabilities manifest themselves in combustion processes in various forms and can be classified as follows (see the beginning of this Chapter)). Thermal diffusion instability is observed in flames in which the rates of heat transfer and diffusion are different, i.e. $Le \neq 1$ (Lewis number $Le = D/\alpha$, where D - where D is the diffusion coefficient of the component that determines the combustion process, α - is the thermal diffusivity) [23, 24]. The hydrodynamic instability is determined by the difference in the densities of the burnt and unburnt gas associated with the thermal expansion of the reaction products [22, 25]. Thermoacoustic instability is determined by the resonant relationship between the unsteady combustion mode and the acoustic modes of the reactor [20, 22, 25]. The criterion for the occurrence of this instability was proposed by Rayleigh [26]. In [27] this hypothesis is formulated as follows: if the phase shift between pressure fluctuations and fluctuations in the rate of heat supply is less than $\pi/2$ in absolute value, the oscillations are getting excited; if the phase shift is in the range from $\pi/2$ to π , the oscillations are damped.

Pressure fluctuations accompanied by sound during combustion in closed vessels are usually associated with thermoacoustic instabilities that occur during spontaneous ignition, detonation, etc. [28]. Until now, the nature of this phenomenon is not completely clear [28]. In [29], fluctuations in the sound range were recorded in rich mixtures of pentane with air. However, in the same mixtures of benzol with air, fluctuations were not observed. In [12], sound vibrations were recorded during the combustion of a hydrogen-air mixture with $\theta = 0.42$. However,

during the combustion of a hydrogen-air mixture ($\theta = 0.60$), there were no sound vibrations. The possibility of self-ignition in the process of flame propagation in explosive bombs was pointed out in [30]. A sufficiently high rate of change in heat release during combustion with such self-ignition or with acceleration of the flame [29] can induce pressure oscillations and thermoacoustic oscillations. In turn, that can lead to an increase in the rate of heat release. Experiments carried out in [42] showed that during the ignition of rich mixtures of isooctane and lean mixtures of hydrogen with air, strong pressure fluctuations arise. The appearance of acoustic oscillations in [42] was associated with the development of hydrodynamic instability during the propagation of flames. However, during combustion of a stoichiometric mixture of hydrogen with air, pressure oscillations were not observed in [42]. Although it is known that the combustion of a stoichiometric mixture of hydrogen with air in cylindrical reactors is accompanied by a characteristic sound [12].

In the literature, for modeling thermoacoustic phenomena, the analysis of the inhomogeneous wave equation for acoustic pressure with a thermoacoustic source is used [21, 31, 32]:

$$\frac{1}{c_0^2} \frac{D^2 P(x, y, z, t)}{D t^2} - \nabla^2 P(x, y, z, t) = \frac{\partial}{\partial t} \left[\frac{\gamma - 1}{c_0^2} Q_t \right] \quad (2.1)$$

where c_0 - sound velocity, P - acoustic pressure, γ - the ratio of heat capacities at constant pressure, Q_t - the rate of heat release [W/m^3].

If we assume the feedback mechanism as a linear function - Q_t of P [32], then it can be shown [36] that equation (2.1) is an acoustic oscillator that is excited or attenuated depending on whether the Rayleigh criterion is met or not.

This section presents the results of experiments on the observation of acoustic instabilities arising from the ignition of mixtures of hydrogen with air in a cylindrical bomb of constant volume with a central ignition.

Experimental

Stoichiometric mixtures of hydrogen with air were used at total atmospheric pressure and initial temperature $T_0 = 298$ K. The experiments were carried out in a horizontal cylindrical stainless steel reactor 15 cm long and 13 cm in diameter. The reactor was equipped with an optical quartz window at one of the ends. In the center of the reactor, spark ignition electrodes were placed, the distance between them was 0.5 mm. In order to change the material and shape of the inner surface of the reactor in various experiments, titanium foil 0.1 mm thick was introduced into the reactor, covering the entire inner side surface of the reactor, tantalum foil 0.1 mm thick, covering $\frac{1}{4}$ of the inner side surface of the reactor, and platinum foil 12x6 cm with a thickness of 0.3 mm. In a number of experiments, a titanium foil

0.1 mm thick was introduced into the reactor, which covered 1/3 of the inner side surface of the reactor with three longitudinal corrugations 12 cm long, protruding into the reactor by 1 cm and located at a distance of 4 cm from each other. We point out that the introduction of Ti foil can be considered as the treatment of the inner surface of the reactor with titanium dioxide TiO_2 , since titanium metal is always covered with a thin oxide layer. In a number of experiments, filming was carried out through NS-1 filters to reduce the illumination intensity of the camera matrix. For the same purpose, in some experiments, optical glass was covered with a thin layer of talc.

The experiments were carried out in the following sequence. If it is necessary, CCl_4 was fed into the reactor, then hydrogen, air were added to atmospheric pressure so that the H_2 content in the mixture was 30% and 15%, kept for 15 min in the reactor for complete mixing. After that spark initiation was carried out. The registration of the ignition and propagation of the FF was carried out through the optical window with a color high-speed camera Casio Exilim F1 Pro (frame speed - 60 - 1200 s^{-1}). The resulting video file was recorded into the computer memory and then processed frame-by-frame. To visualize the hydrogen flame, 2-3% carbon tetrachloride (CCl_4) was added to the mixture. It should be noted that the addition of less than 3% CCl_4 for this mixture is inert and does not have a noticeable inhibitory effect on the combustion of hydrogen with air [12].

The change in pressure during combustion was recorded using a piezoelectric sensor, the signal from which was fed through an ADC to a computer. Before each experiment, the reactor was evacuated using a 2NVR-5D foreline pump. The pressure in the reactor was also monitored with a vacuum gauge. The gases H_2 , carbon tetrachloride CCl_4 , were of chemically pure grade, the purity of the used foils was: Ti - 99.9%, Ta - 99.99%, Pt - 99.99%.

Results and discussion

The experiments have shown that the features of the light emission during the afterburning of a stoichiometric hydrogen-air mixture under conditions of central spark initiation do not depend on the material of the inner surface of the reactor (stainless steel, TiO_2 , Ta, Pt) but depend on its shape. The normal velocity of a spherical flame is also independent of the surface material. Experiments have also shown that acoustic oscillations during combustion of hydrogen-air mixtures in a cylindrical reactor at atmospheric pressure are excited differently than in a spherical reactor.

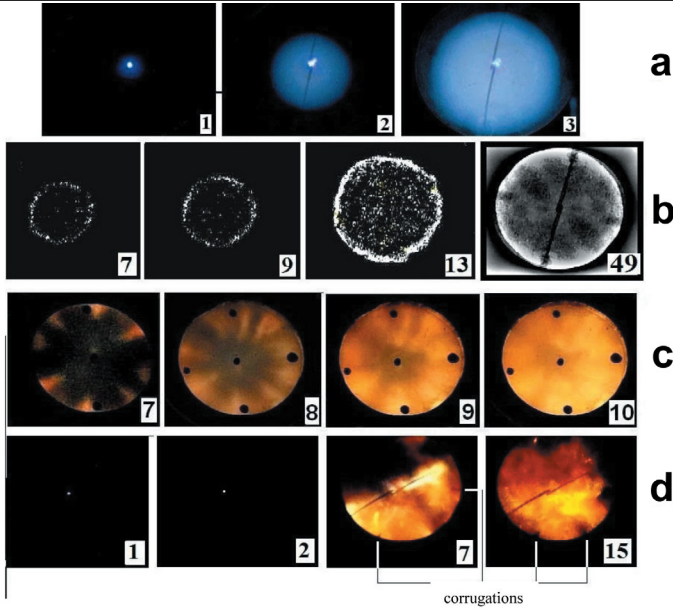


Figure 6. Filming of the process of propagation of a spherical flame front. The number on the frame corresponds to the number of the frame when shooting, $T_o = 298\text{ K}$, $E_o = 1.5\text{ J}$

- a) - $(\text{H}_2 + \text{air})_{\text{stoich}} + 5\% \text{ CCl}_4$, frame speed 600 s^{-1}
- b) - $14.5\% \text{ H}_2 + \text{air} + 3\% \text{ CCl}_4$, frame speed 300 s^{-1}
- c) - $(\text{H}_2 + \text{air})_{\text{stoich}}$, NS⁻¹ filter, optical window treated with talcum powder, surface - stainless steel, frame speed 600 s^{-1} ,
- d) - $(\text{H}_2 + \text{air})_{\text{stoich}}$, 2 NS⁻¹ filters, Ti foil with corrugations (marked on frames 7 and 15) is located in the lower part of the reactor, the frame speed is 600 s^{-1} .

The results of filming of a spherical front propagation process of a stoichiometric hydrogen-air flame with a frame speed of 600 s^{-1} is demonstrated in Fig. 6a. The frames of FF development in a stoichiometric hydrogen-air mixture containing $+ 5\% \text{ CCl}_4$ is demonstrated in Fig. 6a. It is seen that the front of the developing flame has a spherical shape without disturbances. The results of filming of process of flame propagation in a mixture of $15\% \text{ H}_2 + \text{air} + 3\% \text{ CCl}_4$ is indicated in Fig. 6b. It can be seen that the FF consists of small cells, while in the process of its propagation, long-wave disturbances arise. Figure 7 shows oscillograms of pressure changes during the ignition of combustible mixtures of $30\% \text{ H}_2 + \text{air}$ and $15\% \text{ H}_2 + \text{air} + 3\% \text{ CCl}_4$.

Figure 7 shows that acoustic oscillations are excited after reaching the maximum pressure. In 15% of the mixture these oscillations are excited later than in the stoichiometric mixture, in contrast to [28]. In [28], acoustic oscillations in a

spherical reactor were observed only in lean hydrogen-air mixtures and before reaching the maximum pressure, and in mixtures close in composition to stoichiometric ones, they were not observed at all (Fig. 3 [28]).

Perturbations of the spherical FF in a lean mixture burning in a cylindrical reactor caused by thermal diffusion instability [23, 24] and indicated in Fig. 7b develop until the flame front touches the side walls of the reactor. However, these perturbations do not lead to the excitation of acoustic oscillations during the propagation of a spherical FF. Obviously, the perturbations did not have time to develop and ensure the excitation of acoustic oscillations due to the smaller diameter of the reactor used in this work (13 cm) compared to [28], in which the diameter of the spherical bomb was 38.4 cm (see Figs. 3 from [28], curve $\theta = 0.4$). In our reactor, thermoacoustic instabilities, as can be seen from Fig. 6 a, b and 7, are excited noticeably later than the moment the flame front touches the side walls of the reactor. The data obtained are an argument in favor of the existence of a scale effect when this type of instability occurs.

It should be noted that in [25], cellular flames that arise in dilute stoichiometric hydrocarbon-air mixtures after the flame front touches the walls of a cylindrical reactor were discovered and are caused by the occurrence of gas-dynamic instability (see also Chapter 4). This means that the nature of the pressure fluctuations observed by us (Fig. 7) can also be caused by the gas-dynamic instability arising after the flame touches the side walls of the reactor [27]. It is due to the fact that both instabilities, gas-dynamic and acoustic ones, are experimentally observed in the same time interval. Verification of this assumption requires further research.

The results of video recording of the combustion of a stoichiometric hydrogen-air mixture in the time interval corresponding to the appearance and development of pressure oscillations for various materials of the reactor surface are demonstrated in Fig. 6c, d and Fig. 8a, b (stainless steel, TiO_2 with corrugations, Fig. 6; Pt and Ta, Fig. 8).

\

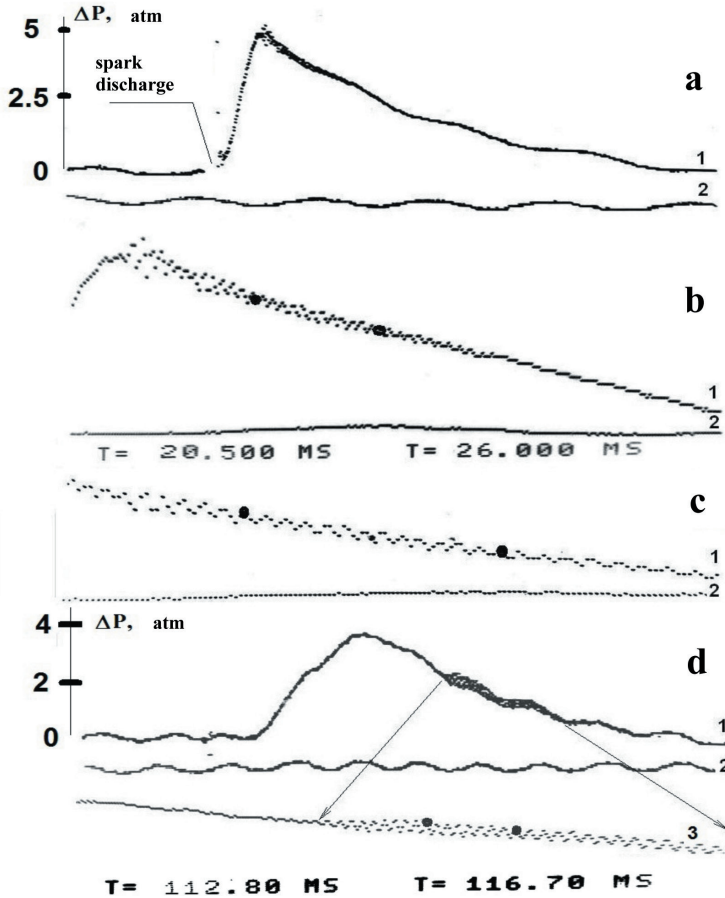


Figure 7. Oscillograms of pressure changes during ignition of combustible mixtures,

- 1 - signal at initiated ignition, 2 - comparison signal, bold points - time interval:
 a, b, c - $(\text{H}_2 + \text{air})_{\text{stoich}}$, different time intervals;
 d - $15\% \text{H}_2 + \text{air} + 3\% \text{CCl}_4$, 3 - extended time interval.

The figures show that after the flame touches the side wall of the reactor, the afterburning of the combustible mixture occurs unevenly in the vertical section of the reactor, while the symmetric picture of the afterburning corresponds to the realization of longitudinal gas oscillations in the reactor. This means that the high-speed filming method makes it possible to visualize the longitudinal vibrations of the after-burning gas.

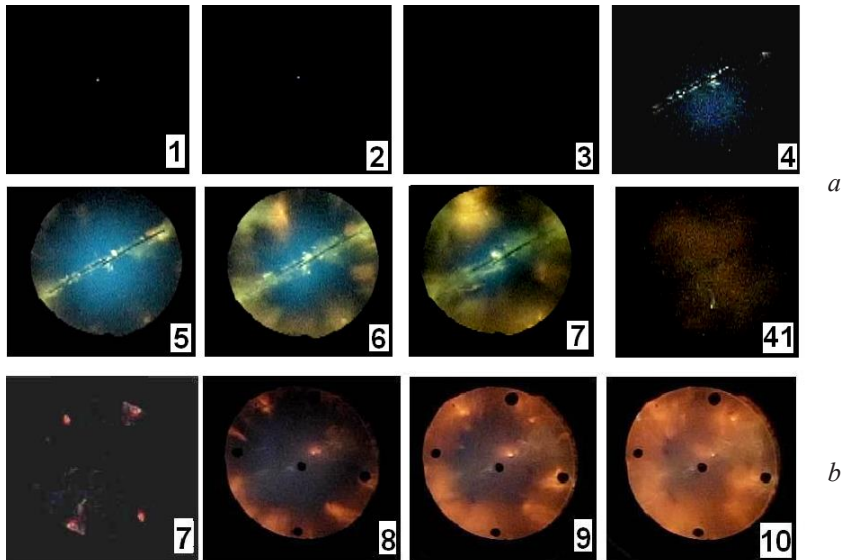


Figure 8. Filming of the process of propagation of a spherical flame front with a frame rate of 600 s^{-1} . The number on the frame corresponds to the frame number during shooting, $T_0 = 298 \text{ K}$, $E_0 = 1.5 \text{ J}$.

- a) - $(\text{H}_2 + \text{air})_{\text{stoich}}$, 1 filter HC-1, Pt foil is located in the lower part of the reactor,
 b) - $(\text{H}_2 + \text{air})_{\text{stoich}}$, 2 filters HC-1, Ta foil is located in the lower part of the reactor.

It can be seen from these figures that in the case of a smooth inner surface of the reactor, the observed character of the afterburning of the combustible mixture (compare frame 8 in Fig. 6c, frame 6 in Fig. 8a, frame 8 in Fig. 1b) does not depend on the material of the reactor surface.

In the next series of experiments, non-uniform gas flows were provided by introducing into the reactor a titanium foil with three longitudinal corrugations protruding 1 cm deep into the reactor (see Experimental). It was found (Fig. 6d, TiO_2 foil with corrugations) that in the case of a nonsmooth inner surface of the reactor, the most intense afterburning of the combustible mixture occurs in the region of inhomogeneous gas flows, namely, in the region of corrugations.

Comparing the oscillation frequencies observed directly on the pressure oscillograms (Fig. 7) and the natural frequencies of the longitudinal oscillations of the cylinder filled with gas (Fig. 6c, Fig. 8), observed visually from different spatial intensities of the afterburning of the combustible mixture is of interest.

To determine the longitudinal modes of a cylindrical reactor, it is sufficient

to set the right-hand side of equation (2.1) equal to zero. If $P(x,y,z,t)=\exp(i \omega t) v(x,y,z)$ we obtain the well-known [15, 32] eigenvalue equation:

$$\nabla^2 v(x,y,z) = -\frac{\omega^2}{c_0^2} v(x,y,z) \quad (2.2)$$

Where ω - the frequency of the gas vibration mode.

The solution of this problem by the finite elements method for the natural frequencies of longitudinal vibrations of a cylinder filled with an inert gas with fixed walls and a height equal to the diameter was carried out. It was performed using the software package (FlexPDE 6.08, A Flexible Solution System for Partial Differential equations, 1996-2008 PDE Solutions inc. [15]), in which this problem appears as an example.

Since combustion takes place under conditions close to adiabatic, it is possible to estimate the temperature in the reactor at a given time from the relation

$$\frac{\Delta P}{P} = \frac{\Delta T}{T} \text{ on the pressure oscillogram. For the moment of time 21 ms in Fig. 7b}$$

$\Delta P = 4$, $P=1$, and, accordingly, $\Delta T = 273 \cdot 4 \approx 1000$ °C for this temperature $c_0 \approx 1000$ m/s [33], and for the moment of time 27 ms $\Delta P = 3.5$, $P=1$, and, accordingly, $\Delta T = 273 \cdot 3.5 \approx 900$ °C; for this temperature $c_0 \approx 900$ m/s [33]. The video frame 7 from Fig. 6 and frame 41 from Fig. 7 and the calculated modes of air oscillations in the cylinder is demonstrated in Fig. 9: mode 36 and mode 4. It is seen that the calculated vibrational modes correlate well with the visually observed afterburning pattern for a stoichiometric hydrogen-air mixture.

Taking into account the cylinder length of 0.15 m for the 36th vibration mode, we obtain $\omega = 1.11$ KHz, at $c_0 = 900$ m/s ($T \approx 900$ °C) we obtain $\omega = 0.7$ KHz for the 4th mode. We obtain an oscillation frequency of ~ 1.9 KHz, which agrees with the value $\omega = 1.11$ KHz, calculated from equation (2.2) according to the algorithm [15] from Fig. 7b in the time interval 20.5 ms - 26 ms and Fig. 7d in the time interval 112.5 ms - 116.7 ms from the pressure oscillograms.

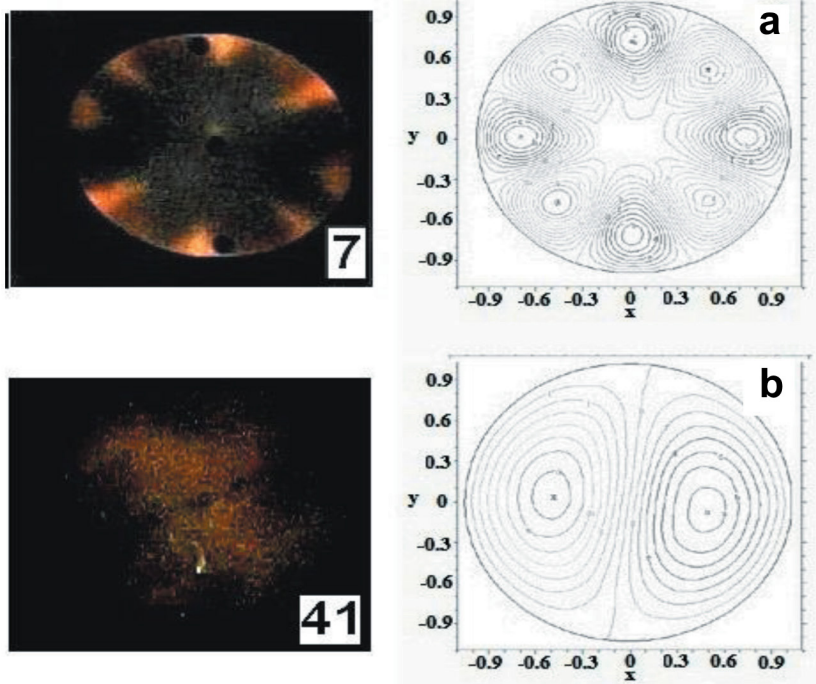


Figure 9. Video shots from Fig. 6 and Fig. 7 and the calculated modes of air oscillations in the cylinder, a - 36th mode, b - 4th mode

It can also be seen from Fig. 7 that at the end of the afterburning process of the combustible mixture in the final sections of the pressure oscillograms corresponding to the cooling reactor, the oscillation frequency decreases noticeably and reaches 1 kHz in oscillogram 3 in Fig. 7. It also agrees with the calculation performed for the lower mode of longitudinal vibrations $w = 0.7$ kHz.

The above comparison is illustrative and does not allow, for example, to interpret the more complex mode structure of oscillations observed for a 15% hydrogen-air mixture (Fig. 6b, frame 49).

We briefly summarize the results obtained.

Using the combustion of hydrogen-air mixtures (30% and 15% H_2) as an example, it is shown that the high-speed filming method allows visualizing the longitudinal oscillations of the after-burning gas. It was found that the features of flame propagation in a stoichiometric hydrogen-air mixture with central spark initiation do not depend on the material of the inner surface of the reactor (stainless steel, TiO_2 , Ta, Pt) but depend on the degree of its roughness. It was found that thermoacoustic oscillations during the combustion of hydrogen-air mixtures

in a cylindrical reactor at atmospheric pressure are getting excited differently than in a spherical reactor, and at the same time depend on the size of the reactor.

§ 3. Interaction of spherical flames of hydrogen-air and methane-air mixtures with fine-mesh obstacles at central initiation by a spark discharge

The influence of obstacles located in different volumes filled with a reactive mixture on the propagation of the flame front has been studied for a long time. These studies are carried out in order to clarify the dependence of the nature of combustion on the type of obstacles and the possibility of influencing the intensity of combustion by varying the geometrical arrangement of the obstacle. We point out that this issue will also be discussed in Chapter 6.

It is known that if the combustible mixture is at a sufficient distance from the concentration limits of ignition, then the velocity of flame propagation in the presence of obstacles can rapidly increase to supersonic values [34, 35]. However, the velocity of the supersonic combustion wave in the presence of obstacles is significantly lower than the Chapman-Jouguet velocity [36, 37]. Therefore, from a practical point of view, the most important aspect in the study of accelerating flames is due to explosion safety problems and is mainly associated with the transition of fast combustion to nonstationary (detonation-like) one, the destructive effect of which is stronger than the steady-state Chapman – Jouguet wave [38]. It should be noted that the effect of obstacles, can manifest itself both in maintaining a detonation wave as a result of reflections of shock waves, and in damping and of a detonation wave a detonation wave as a result of heat and momentum losses according to [34].

The foregoing can be attributed to the initial stage of flame acceleration, namely, to the moment when the laminar flame meets an obstacle in the form of a mesh, which is the subject of this study. In this case, the development of flame instability occurs, which contributes to its acceleration [12]. On the other hand, upon contact of the flame with the surface, one should expect an increase in the contribution of heterogeneous reactions, in particular, the termination of reaction chains [39], which should contribute to the deceleration and extinction of the flame. Such a dual mechanism of action of obstacles causes the fact that physical methods of suppressing detonation (nets, nozzles, etc.) [40] are not always effective.

In [35], the effect of turbulizing obstacles (grids and perforated spheres with minimum cells of 2x2 mm and a hole diameter of 4 mm) located inside a combustible gas mixture on the apparent combustion velocity of stoichiometric hydrogen-air and hydrogen-oxygen mixtures was studied. In experiments, combustion acceleration was always observed by a factor of 1.5–2.5 after obstacles. For hydrogen-oxygen mixtures, a transition from combustion to detonation was observed, which depended on the initiation energy [35].

However, information on the interaction of flames of lean hydrogen-air mix-

tures with mesh obstacles is practically missing in the literature. Although such experiments are of interest for establishing the influence of oppositely acting factors accelerating the development of instability and slowing down the flame (termination of active centers on the obstacle surface).

The purpose of this section was to study the dynamics of propagation of flames of lean hydrogen-air mixtures and a stoichiometric mixture of natural gas with air inside the mesh sphere, passing through the mesh sphere and further propagation outside the mesh sphere.

Experimental

The experiments were carried out with lean mixtures of hydrogen (7.5-15%) with air and a stoichiometric mixture of natural gas (NG) with air at initial atmospheric pressure and temperature $T_0 = 298$ K. A horizontally located cylindrical stainless steel reactor 15 cm long and 13 cm in diameter was used. The reactor was equipped with an optical quartz window at one of the ends (Fig. 10). In the center of the reactor, spark ignition electrodes 6 were placed, the distance between which was 0.5 mm. On partially insulated electrodes 6, a sphere 5 with cut-out slots for electrodes, made of a mesh, consisting of two hemispheres and fastened by a spring 7 was fixed. In this case, the volume enclosed in the mesh sphere and the external reaction volume were in contact only through the mesh cells. We used mesh spheres with a diameter of $d = 3$ cm (wire diameter 0.2 mm, cell size 0.04 mm²), $d = 4$ cm (wire diameter 0.25 mm, cell size 0.08 mm²), $d = 6$ cm (wire diameter 0.3 mm, cell size 0.1 mm²). The mesh material was aluminum wire. As is known, the surface of aluminum is always coated with its oxide. Consequently, the surface of the mesh was aluminum oxide Al_2O_3 , which effectively terminates the reaction chains [12].

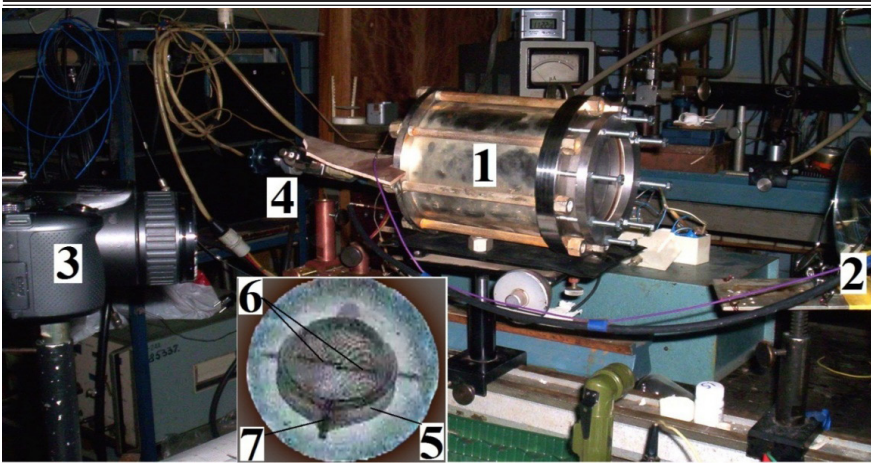


Figure 10. Photo of the experimental setup

1 - stainless steel reactor, 2 - folding mirror,
 3 - high-speed color film camera Casio Exilim F1 Pro,
 4 - vacuum valve for gas inlet and evacuation, 5 - mesh sphere $d = 6$ cm,
 6 - ignition electrodes, 7 - spring. The inset shows a view of the interior of the reactor with a mesh sphere

The experiments were carried out in the following sequence. If necessary, CCl_4 , then hydrogen, or natural gas (NG) was poured into the reactor, then air was added to atmospheric pressure. The mixture was kept for 15 min for complete mixing, and then spark initiation was performed (the discharge energy was 1.5 J). The dynamics of ignition and the propagation of the flame front (FF) was studied through the optical window using a Casio Exilim F1 Pro color high-speed film camera (frame speed - $60 \div 1200 \text{ s}^{-1}$). The resulting video file was recorded into the computer memory and then processed frame-by-frame. To visualize the hydrogen flame, 4% carbon tetrachloride (CCl_4) was added to the mixture. It should be noted that the additive of up to 4% CCl_4 for these mixtures is inert [12].

The change in pressure during combustion was recorded using a piezoelectric sensor, the signal from which was fed to an S8-2 digital storage oscilloscope. The pressure in the reactor during the composition of the gas mixture was monitored with a vacuum gauge. Before each experiment, the reactor was evacuated using a 2NVR-5D forvacuum pump. Gases H_2 , carbon tetrachloride C were used of chemically pure grade, PG contained 2% propane and butane according to the data of chromatographic analysis. The value of the degree of expansion of the combustion products ε_r was determined from the value of the maximum pressure developed during the combustion of the P_b [23], as in §1:

$$P_b/P_0 = 1 + \gamma(\varepsilon_r - 1) \quad (3.1)$$

The magnitude of the normal flame propagation velocity U_n was determined from the relation [23]:

$$U_n = V_v/\varepsilon_r \quad (3.2)$$

In expressions (3.1), (3.2) P_b – maximum pressure, γ – adiabatic index of the initial mixture, V_v - visible flame velocity.

Results and discussion

In all experiments, the flame initiated inside the mesh sphere passed through the mesh cells (except for a mixture of 4% CCl_4 + 7.5% H_2 with air). This means that the interaction of a relatively slowly spreading flame (the normal flame velocity in a mixture of 15% H_2 with air is ~ 6 times less than in a stoichiometric mixture (≈ 50 cm/s) in a mixture of 10% H_2 with air and ~ 15 times less than in a stoichiometric mixture (≈ 20 cm/s) [12]) with a surface providing effective termination of reaction chains (Al_2O_3) does not lead to flame-out. Thus, the effect of heterogeneous termination of active combustion centers on flame propagation under our conditions is not sufficient to blow off the flame.

It was found that mixtures of 4% CCl_4 + 7.5% H_2 with air do not pass through the nets. However, individual flame cells are observed inside the mesh. In the absence of a mesh, the cellular flame of this mixture, as in [13], rises up to the reactor wall. Under our conditions, there is a critical concentration of hydrogen at which the flame does not pass through the mesh. This is consistent with the results of calculation work [9], where it was shown that the effect of heterogeneous termination on flame propagation should be observed in the immediate vicinity of the lower concentration limit of flame propagation (which for a hydrogen-air mixture is $\sim 5\%$ H_2 [12]).

A sequence of video images of the propagation of a flame front illuminated with 4% CCl_4 in mixtures of 10% H_2 and 15% H_2 with air, respectively, illustrating the effect of the mesh sphere on the dynamics of flame propagation is shown in Fig. 11. It can be seen that, after passing through the obstacle, the flame front in these mixtures is noticeably disturbed in comparison with the flame propagation in the absence of the obstacle. It can be seen from Fig. 11 IIa, b that the FF consists of small cells, while in the process of its propagation, long-wave disturbances arise.

Figure 11c shows the dynamics of an increase in the radius of the flame front in the absence and in the presence of a mesh sphere. It can be seen from the figure that the flame slows down when approaching the mesh, but after passing the obstacle it noticeably accelerates, in agreement with the results of [35]. Then, flame retardation is again observed at the reactor wall, associated with a change in the conditions for the expansion of combustion products [12, 23].

Worthy of note is the appearance of streams of hot glowing gas from the volume bounded by the grid, which appears after the flame reaches the walls of the

reactor (frames 17-19 Fig. 11 IIb). In accordance with the existing ideas about the combustion mechanism of hydrogen - air mixtures, there should be no secondary exothermic reactions in this mixture [12]. The presence of the mesh should also lead to a faster cooling of the gas inside it. Therefore, the gas flow must be directed towards the inside of the mesh.

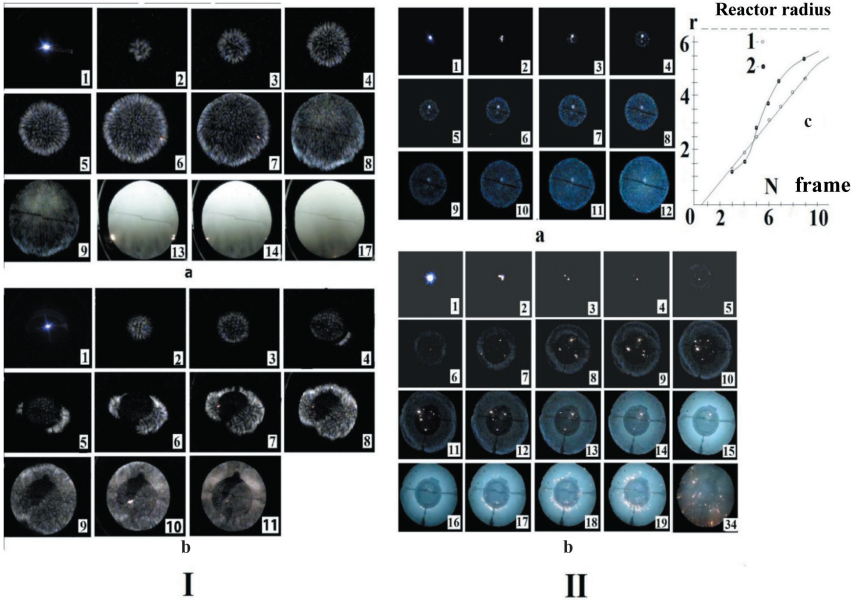


Figure 11. I - the result of high-speed filming of the propagation of the flame front illuminated with 4% CCl₄ in a mixture of 10% H₂ + 86% air at atmospheric pressure. The number on the frame corresponds to the frame number when shooting. Filming speed is 60 frames/s

a) - in the absence of a mesh; b) - in the presence of a mesh sphere $d = 6$ cm.

II - the result of high-speed filming of the propagation of the flame front illuminated with 4% CCl₄ in a mixture of 15% H₂ + 81% air at the initial atmospheric pressure. The number on the frame corresponds to the frame number when shooting. The first frame corresponds to the occurrence of a spark discharge. Filming speed is 600 frames/s.

a) - in the absence of a mesh; b) - in the presence of a mesh sphere $d = 4$ cm;

c) - dynamics of an increase in the radius of the flame front in the absence (1) and in the presence (2) of a mesh sphere $d = 4$ cm (15% H₂, II a, b).

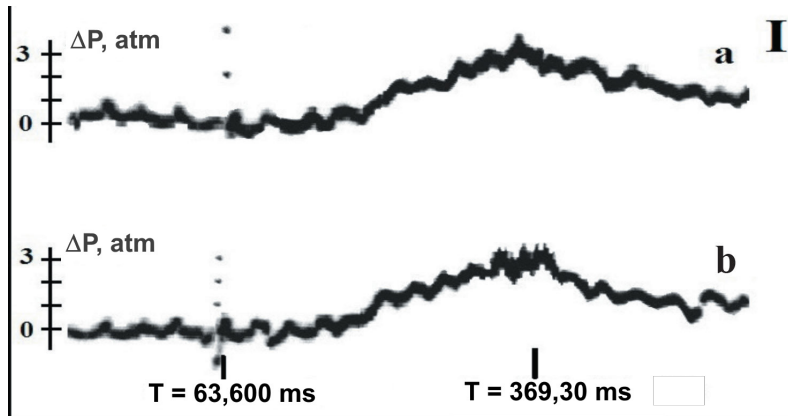
However, the gas flow is directed outside the mesh sphere. Identification of the cause of this phenomenon requires a more detailed study.

It was also found that in the presence of a mesh sphere, flame propagation of

both 10% H_2 and 15% H_2 in the air is accompanied by a characteristic sharp sound, i.e. acoustic vibrations of gas. It should be noted that the propagation of a flame in a mixture of 10% H_2 with air in the absence of obstacles inside the reactor is not accompanied by a sound effect. Figure 12 shows the dependences of the total pressure change on time for the indicated mixtures during flame propagation in the presence of a mesh.

It follows from Fig. 12 Ib that, in the presence of a mesh in a 10% mixture of H_2 and air, acoustic oscillations are excited, and the rate of pressure rise becomes higher compared to the process in the absence of a mesh, in accordance with [35].

Figure 12 II shows that in a 15% mixture of H_2 with air in the absence of a mesh, acoustic oscillations are excited after reaching the maximum pressure. In the presence of a mesh with $d = 3$ cm, acoustic vibrations occur much earlier than the pressure maximum is reached. The presence of a mesh leads to a more rapid development of instability and provides an intensification of the combustion process. It should be noted that in a spherical bomb 38.4 cm in diameter, i.e. larger than that used in this work (see Fig. 3 from [28], curve $\theta = 0.4$), acoustic oscillations appear before the pressure maximum is reached. Attention should be paid to the fact that the larger the diameter of the mesh sphere, the later the acoustic vibrations occur, recorded by the pressure sensor (cf. Fig. 12 IIb and IIc, ~ 10 ms and ~ 25 ms, respectively). This means that the presence of a mesh barrier leads to the development of instabilities at the combustion front and the appearance of acoustic vibrations. In the next series of experiments, it was shown that the process of chemical conversion in a stoichiometric mixture of NG with air for all mesh spheres used in this work completely covers the volume of the reactor.



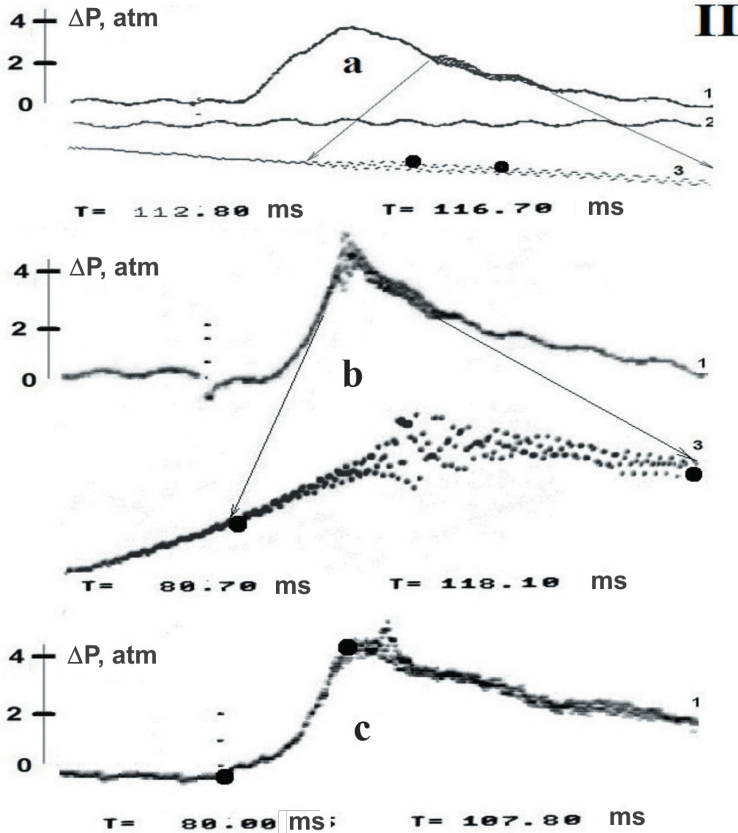


Figure 12. Oscillograms of pressure changes during ignition of combustible mixtures

I - 4% CCl_4 + 10% H_2 in air; a) - in the absence of a mesh; b) - in the presence of a mesh $d = 6$ cm.

II - 4% CCl_4 + 15% H_2 in air; a) - in the absence of a mesh; b) - in the presence of a mesh $d = 3$ cm; c) - in the presence of a mesh $d = 4$ cm; 1 - signal at initiated ignition, 2 - comparison signal, bold points - time interval; 3 - extended time interval.

However, the flame actually stops with the disappearance of the light emission in contrast to the combustion of hydrogen-air mixtures, near the inner surface of the mesh (Fig. 13).

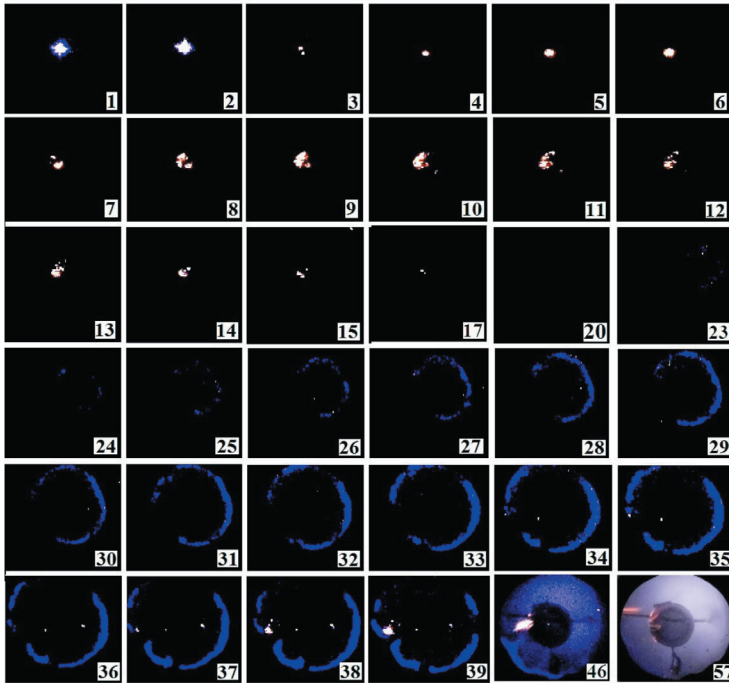
This means that the mechanism for the penetration of such a flame through an obstacle is different from the mechanism for hydrogen-air mixtures. Figure 13a shows a sequence of video images when the flame of a mixture of NG with air

propagates through a mesh obstacle. In Fig. 13b dynamics of an increase in the radius of the flame front in the presence of a mesh sphere is demonstrated. It can be seen from the figure that when the flame front approaches the mesh sphere, the flame is practically extinguished. After the onset of combustion outside the mesh obstacle, the flame front is not accelerated, but propagates at an almost constant speed. Therefore, the excitation of acoustic vibrations due to the acceleration of the flame during the combustion of this mixture is not observed. There is an estimation of the normal velocity of flame propagation outside the mesh obstacle using relations (1) and (2) gives ~ 27 cm/s - a value close to the normal velocity of a spherical flame for this mixture composition (35 cm/s [12]). It can be assumed that the extinction of the NG - air flame is associated with the intense heterogeneous termination of active intermediate combustion products on the mesh material. However, stable intermediate combustion products (for example, hydroperoxides) diffuse through the mesh cells and initiate flame propagation outside the mesh sphere.

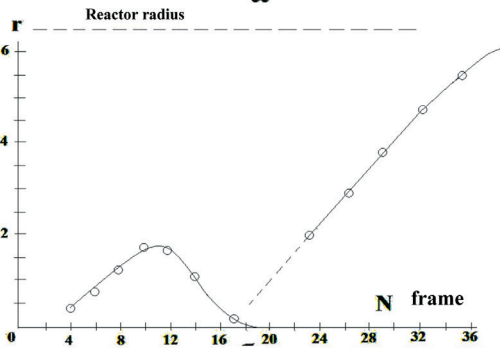
The absence of acoustic vibrations during the combustion of this mixture supports this assumption, i.e. the presence of a mesh barrier does not lead to turbulence of the combustion front and the appearance of acoustic vibrations.

We point out that the normal flame velocities of mixtures of 10% H₂ and 15% H₂ with air are, respectively, 21 and 45 cm/s according to [13], which presents the data of several groups of authors on the definition of Un and the curve of the average values of this value.

It should be noted that the normal flame propagation velocity in the NG-air mixture is 35 cm/s, i.e. the Un values for the three mixtures under consideration are close to each other.



a



b

Figure 13.

a) - the result of high-speed filming of the propagation of a flame front, a stoichiometric mixture of a steam generator with air at atmospheric pressure in the presence of a mesh sphere $d = 4$ cm. The number on the frame corresponds to the number of the frame during shooting. Filming speed is 600 frames/s

b) - dynamics of an increase in the radius of the flame front in the presence of a mesh sphere.

In this case, the molar heat of combustion of natural gas is much higher than that of hydrogen [12]. Thus, according to only the thermal theory [23], the stopping of the NG-air flame near the mesh obstacle has no explanation. This means that the work obtained direct evidence that the active centers of combustion of methane and hydrogen, which determine the propagation of the flame, have a different chemical nature [41, 42]. The reason for the stopping of the NG-air flame is that hydrogen atoms easily penetrate through the mesh obstacle, and the carriers of the chains in the combustion of methane, on the contrary, actively die on Al_2O_3 .

Let us summarize the results obtained.

It is shown that spark-initiated flames of lean hydrogen mixtures (8% -15% H_2 in air) pass through mesh spheres with a mesh size of 0.04-0.1 mm^2 , while the flame of a mixture of 15% H_2 in air accelerates after passing through an obstacle. In the presence of an obstacle during the propagation of flame in mixtures of 10% and 15% H_2 in air, acoustic oscillations of the gas are initiated the earlier, the smaller the diameter of the mesh sphere. The flame of 7.5% H_2 in air does not pass through mesh spheres. It is shown that the process of chemical conversion in a stoichiometric mixture of NG with air for all mesh spheres used in this work covers the entire volume of the reactor, but is not accompanied by acoustic vibrations. The appearance of streams of hot glowing gas from the volume bounded by the mesh, which appear after the flame reaches the walls of the reactor, is found. It is shown that the active centers of combustion of methane and hydrogen, which determine the propagation of the flame, have a different chemical nature.

§ 4. Thermal ignition in gas vortices

In laboratory [36, 37, 43, 44] and in large-scale experiments [45, 46], it was demonstrated that obstacles located in the path of a propagating flame can provide a rapid acceleration of the flame. Under these conditions, the detailed kinetic mechanism of the process falls by the wayside and the representation of the gross process by the effective Arrhenius reaction is sufficient. Thus, the gas-dynamic features of the process are of paramount importance.

Qualitatively, the mechanism of this acceleration of the flame is well understood. Thermal expansion of the hot reaction products causes the unburned gas to move. In the presence of obstructions, turbulence can occur in this flow. Turbulence increases the local combustion velocity by increasing the surface area of the flame and the velocity of transfer of mass and energy. The increasing velocity of combustion provides, in turn, a higher flow rate in the unburnt gas. This feedback leads to continuous acceleration of flame propagation. Under appropriate conditions, this can lead to a transition to detonation.

Depending on the sensitivity of the mixture, high intensity turbulence can reduce the overall combustion rate when the flame is highly distorted and the

combustion products and cold unburnt mixture rapidly mix. If the temperature of the reaction zone is lowered to a value, at which the flame cannot propagate, the flame can be extinguished locally. Turbulent quenching plays a role when the velocity of the unburnt gas increases. For some leanly initiated mixtures, this can destroy the described positive feedback mechanism and lead to extinguishing the flame in general. Consequently, both the degree of flame acceleration and the final result (the maximum achieved flame velocity) depend on the competing effects described above due to gas turbulization [47].

Let us consider the main control parameters of processes in reacting gas streams and some features of the modern approach to the theory of turbulence. In a laminar flame of a premixed mixture, changes in the shape of the flame are described in terms of flame extension, which is a combination of its deformation and curvature. Flame expansion is caused by hydrodynamic effects in the flow, which disturb the flame front and local curvature of the flame. We point out that the main types of instability of subsonic flames can be classified for reasons that cause them as thermodiffusion, thermoacoustic, and gas-dynamic ones [48]. Flame expansion can have a positive or negative effect on the flame propagation velocity, depending on the directions of deformation and curvature, as well as the Lewis number, which is the ratio of the thermal diffusivity (α) and diffusion (D) coefficients [12, 24, 49]:

$$Le = \alpha/D = \lambda/\rho C_p D \quad (4.1)$$

Figure 14 shows possible examples of stress and curvature at the flame front, which is built according to the Huygens principle [23]. As the flame spreads in the area of diverging streams (Fig. 14a), the flame is deformed so as to accelerate the diffusion of unreacted gas into the reaction zone, but also to cool the reaction zone. If $Le > 1$, then such a deformation will lead to a decrease in the flame propagation velocity, since the reaction zone cools faster than the diffusion rate increases. On the contrary, with the same deformation, the flame propagation velocity will increase for mixtures with $Le < 1$.

Figure 14b shows a flame propagating into a converging flow, which leads to an increase in the flame velocity for $Le > 1$ and a decrease in the flame velocity for $Le < 1$. For a Lewis number of the order of unity, the curvature practically does not affect the propagation velocity. In areas of a convex flame (Fig. 14c, peak), the flame surface increases while the reaction zone cools. The opposite happens in areas with a concave flame (Fig. 14c, bottom).

Figure 15 illustrates the stabilizing and destabilizing effects associated with the Lewis number. For $Le > 1$, the heat propagation rate is higher than the diffusion rate. This stabilizes the flame as concave areas spread faster than convex areas. As a result, initial disturbances along the flame surface tend to level down, stabilizing the flame.

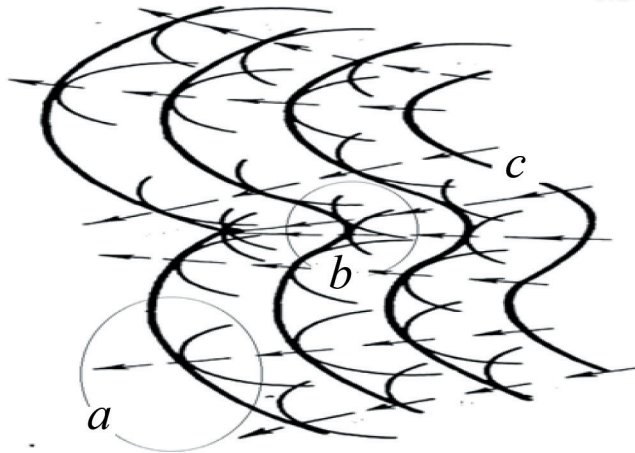


Figure 14. Disturbances and curvature of the flame front: a) disturbance in the direction of propagation of the flame front, b) disturbance in the opposite direction, c) curvature and propagation [23, 50]

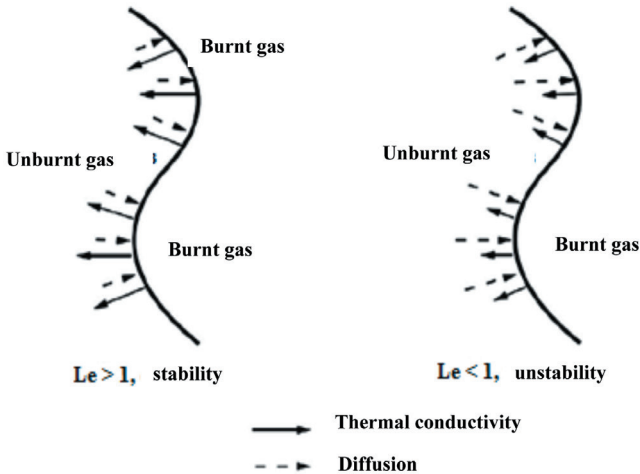


Figure 15. Stabilizing and destabilizing effects determined by the Lewis number

For $Le < 1$, the disturbances of the flame structure are intensified as the concave regions slow down relative to the convex regions, and this leads to flame instability. For $Le = 1$, the diffusion and heat transfer rates are balanced and do not affect the flame structure. The hydrodynamic effects associated with convection can increase if the gas flow is accelerated. For example, in a partially closed channel (hole), the expansion of combustion products leads to the propagation of compression waves ahead of the flame to the open end. That causes the flow of unburnt gas. This ultimately leads to an increase in the velocity of the S_f flame, which is the sum of the unburnt gas speed and the laminar velocity of the S_L flame. As the flame further spreads into the unburnt gas, it is accelerated due to the additional flame region created initially by the axial velocity profile along the width of the hole.

Turbulence leads to a wrinkled flame, whereby the surface of the flame increases from the level of laminar combustion A to the level of turbulent combustion A_T . The consequence of an increase in the flame area is an increase in the volumetric combustion rate up to the so-called turbulent combustion rate S_T . Since the products are mixed with reagents during turbulence in case of turbulence-accelerated transfer processes, the laminar flame thickness δL increases to the thickness of the turbulent flame brush δT .

There is, obviously, an inverse relationship between the flame propagation process and the turbulence of the gas medium. As the unburnt gas is consumed by the flame, baroclinic vortex flow [51] can occur, which is the result of changes in density and pressure. This process is viewed as turbulence generated by a flame. In this case, an increase in the kinematic viscosity in the flame due to an increase in temperature leanens the local turbulence.

Historically, the study of turbulent combustion was initially focused on predicting the control parameters of turbulence such as S_T and δT [49]. Unfortunately, S_T and δT depend on local flow conditions, and therefore predictions are not as easy as in the case of a turbulent flame. Instead, it is wise to focus on the various turbulent combustion regimes that exist and make certain simplifications for the analysis of each regime. For a given mixture, the effect of turbulence on flame propagation will vary with the intensity and scale of the turbulence. When the flame accelerates in an obstructed channel, leading to a deflagration-to-detonation (DDT) transition, the entire spectrum of turbulent combustion modes is likely to be passed through. It should be noted that the main dimensionless criteria in the analysis of the phenomena associated with turbulence, in addition to the Reynolds number, are the Karlovitz and Damköhler numbers [49]:

$$Ka = \tau_c / \tau_\eta = (\delta / S_L) / (\eta / u_\eta) \quad (4.2)$$

$$Da = \tau_T / \tau_c = (l / T / u'T) / (\delta / S_L) \quad (4.3),$$

where τ_c is the time scale of chemical transformations. Integral time, length and scales of turbulence velocities, designated as τ_T , l/T and $u'T$, characterize the high-

est energy containing eddies that exist in a turbulent flow. These scales are often determined by the geometry of the structure that restricts the flow. Energy is transferred along the turbulence scale to smaller and smaller eddies through a cascade process that ends on the so-called Kolmogorov scale. In other words, any turbulent flow includes a continuous spectrum of the structures of the eddies. Large eddies are created due to the instability of the mean flow, then they transfer their energy to smaller eddies, which in turn transfer their energy to even smaller ones.

The flow in the mixing layer as is shown in Fig. 16 where one can see a cascade of eddies (Fig. 17) from the largest eddies to the smallest ones.

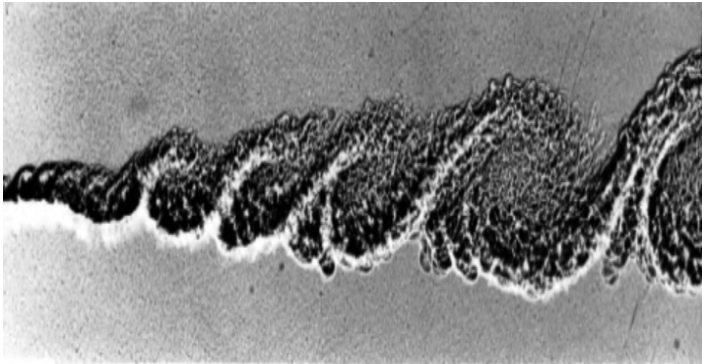


Figure 16. Flow in the mixing layer. Vortex Cascade [51]

The kinetic energy is dissipated only at the last stages of this process, when the vortex structures become so small that the Reynolds number, determined by the size of small eddies, becomes of the order of unity $Re = \rho ul/\mu \sim 1$. In this sense, viscosity plays a rather passive role.

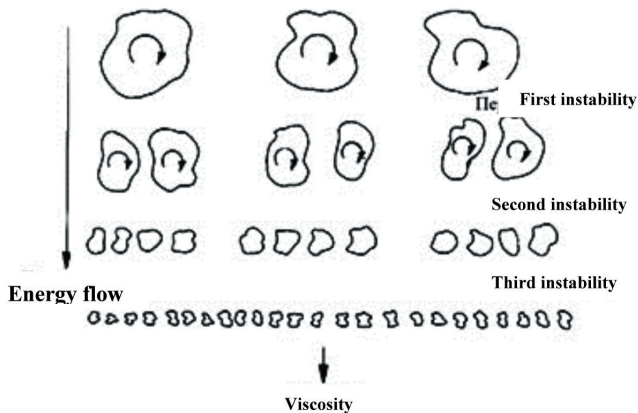


Figure 17. Energy cascade

Let us determine the characteristic size of the smallest eddies in a turbulent flow (Kolmogorov scale). Suppose u and v represent the characteristic velocities associated with the largest and smallest eddies sizes, respectively. In addition, suppose l and η be the characteristic dimensions of the largest and smallest structures that is, eddies transfer most of their energy to smaller eddies during a characteristic time $\sim l/u$. Therefore, the speed, with which energy (per unit mass) is transferred down the cascade of eddies from the largest eddies is defined as $\Pi \sim u^2/(l/u)$. When conditions are statistically stationary, the rate, at which the energy of the largest eddies is transferred down the cascade must match the rate of energy dissipation at the level of the smallest eddies. If this were not so, then in this case the energy would accumulate at some intermediate stage of the eddies cascade. We exclude this possibility, since we are considering the case when the statistical structure of the turbulent flow does not change over time. The rate of energy dissipation at the level of the smallest eddies is defined as $\varepsilon \sim \nu S_{ij} S_{ij}$, where S_{ij} is the velocity-strain tensor, which in a turbulent flow (due to the presence of a wide range of eddy scales) is associated precisely with the smallest eddies, since the local velocity gradients are determined precisely by the smallest eddies. $S_{ij} = \frac{1}{2} (\partial u_i / \partial x_j + \partial u_j / \partial x_i) \sim v / \eta$. This leads to the estimate $\varepsilon \sim \nu (v / \eta)^2$.

Since the dissipation of turbulence energy ε must coincide with the production of turbulence Π , we have $u^3/l \sim \nu (v / \eta)^2$. We also know that the Reynolds number, determined from the characteristic values of the velocity and the size of the smallest eddies, must be of the order of unity: $v\eta/v \sim 1$. Combining the last two relations, we find $\eta/l \sim 1/Re^{3/4}$ or $\eta = (v^3/\varepsilon)^{1/4}$, as well as $v/u \sim 1/Re^{1/4}$, or $v = (v^3/\varepsilon)^{1/4}$, where Re is the Reynolds number calculated from the size of the largest vortices, $Re = ul/v$. In a conventional wind tunnel experiment, the Reynolds number can be of the order of $Re=10^3$ at $l=1$ cm. From the above formulas, one can easily estimate the size of the smallest eddies, we obtain $\eta \sim 0.06$ mm. Suppose most of the energy of the global flow dissipate at the level of the smallest eddies, which have a size less than a millimeter. Obviously, the turbulent flow at the level of small eddies has a very fine structure, and the larger the value of the Reynolds number, the smaller the size of the smallest eddies is. Two turbulent jets at two different Reynolds numbers are shown in the Fig. 18. As the Reynolds number increases, the size of the smallest eddies decreases.

Thus, the larger the Reynolds number is, the finer the turbulent flow at the level of the smallest eddies is. The characteristic size of the smallest eddies η and velocities v is called the Kolmogorov scale, l is the integral scale. It should be noted that all of the above estimates appear to agree surprisingly with experimental data. In fact, these results appear to be the most reliable in the theory of turbulence.

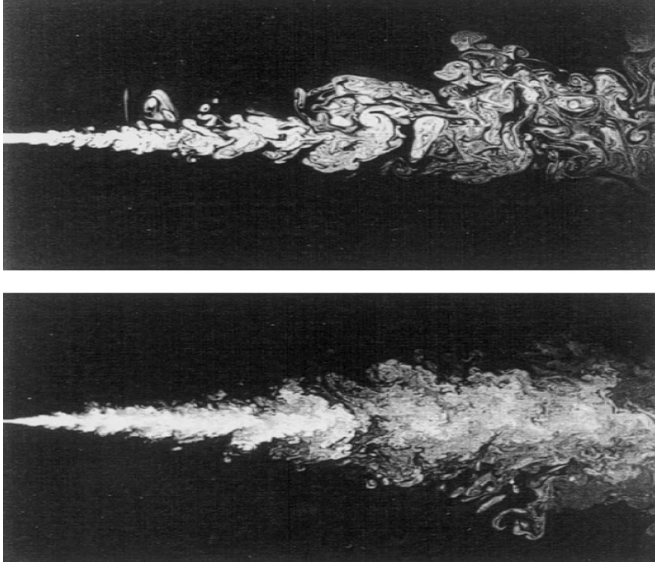


Figure 18. Influence of the Reynolds number on the structure of turbulent jets [52]. The lower jet has a higher Reynolds number

So, Kolmogorov time, length and scale of velocities are indicated as τ_η , u_η' , and η , and are defined as [54]:

$$\tau_\eta = (v/\varepsilon)^{1/2}; \quad \eta = (v^3/\varepsilon)^{1/4}; \quad u_\eta' = (v\varepsilon)^{1/4} \quad (4.4)$$

According to Kolmogorov, the directions of displacement of large scales disappear in the chaotic process of scale reduction, when energy is transferred to successively smaller eddies. Kolmogorov hypothesis of local isotropy indicates that at sufficiently high Re , small-scale turbulent flows are statistically isotropic. Here, the term "local isotropy" means small scale isotropy. Large-scale turbulence can still be anisotropic. The first Kolmogorov similarity hypothesis indicates that in every turbulent flow in a sufficiently high Reynolds number, the statistics of small-scale motions have some universal form, which is exclusively determined ε and v through three equations (4.4) and:

$$u_\eta'/\eta = 1/\tau_\eta; \quad Re_\eta = u_\eta'\eta/v = 1$$

The fact that, according to Kolmogorov, $Re = 1$ is consistent with the statement that the cascade of eddies continues to smaller and smaller scales until Re decreases sufficiently for the dissipation to be effective.

Initially, the flame acceleration is responsible for the geometric increase in the flame area caused by large-scale structures in the flow, which arose, for example, due to the interaction of the FF with obstacles. At the same time, when the acceleration of the flame continues and the flow of unburnt gas is turbulized, the

processes of mass and momentum transport into the flame are accelerated. An increase in the combustion rate further contributes to the acceleration of the flame.

The structure of a turbulent flame (flame brush) is highly dependent on the intensity of the turbulence and the characteristic scales of combustion and turbulence. If the time scale of combustion is less than the turnover time of the turbulent eddy, the flame brush can be modeled by a structure consisting of a large number of different laminar flamelets. If the combustion is slow compared to the eddy turnover time, then the reaction zones in the “flame brush” become dispersed and require the use and comparison of different model approaches.

A scheme of turbulent combustion regimes, known as the Borchi diagram (Fig. 19), illustrates the influence of the Karlovitz and Damköhler criteria on turbulent combustion. When the fluctuations of the unburnt gas u' are less than the laminar combustion rate S_L , the final effect of turbulence is to distort the shape of the laminar flame without disturbing the internal structure of the flame.

The different zones in Fig. 19 are based on conditional dimensions of coordinates and only give an estimate of the order of magnitude of the transition limits. The transitions between combustion modes within these limits do not occur abruptly. This is an area of intensive research devoted to the establishment of new criteria in order to more accurately characterize and describe the transitions between combustion modes. In this case, we point out that in most practical calculations of turbulent combustion, combustion models are valid only for a certain combustion mode. It follows directly from the above that the experimental values measured using a particular setup may not necessarily be reproduced under the conditions of another setup, even if both devices are of the same type, for example, in a static fast admission reactor.

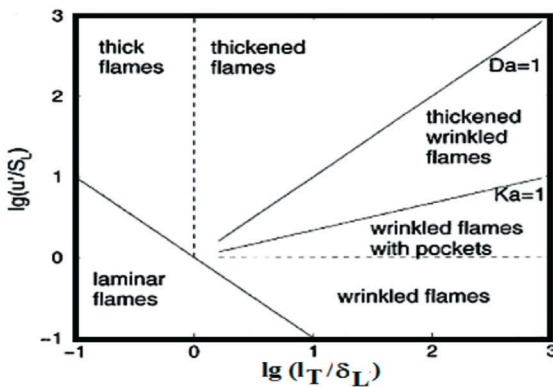


Figure 19. Borchi diagram. Combustion areas [55].

Obviously, the experimental results (for example, ignition delay times) relate only to the installation, by which they were obtained, since the behavior of gas flows arising in a reactor when a gas mixture is poured into it can differ significantly even for installations of the same type.

This situation was described by one of the authors in [56], and the main results of this work are presented below. It should be noted that the combustion distributed in eddies was investigated in [57] to determine the effect of such flows on the environmental issues and combustion efficiency in a gas turbine with ultra-low NOx emissions. The authors of [57] have shown that the eddy flow provides a high speed regime in the core of the combustion chamber and, accordingly, better mixing of components. In [56], a deeper understanding of the effect of tangential gas admission was demonstrated, both on the regularities of gas combustion and on the interpretation of experimental results.

As is clear from the above, the study of the propagation and stabilization of a flame in a rotating combustible gas is of interest both for a deeper understanding of the laws of turbulent combustion and thermal ignition in turbulent flows implemented in various technical devices. The specific effects of the eddy flow observed during the propagation of a flame in rotating flows can also manifest themselves in the modes of thermal ignition in eddy gas flows. The problem of flame propagation and stabilization in a separate eddy flow has received considerable attention from researchers [57–61]. The experiments carried out in [57] showed that when the mixture is ignited at the maximum distance from the axis of rotation, the resulting flame source in the form of an irregular segment moves to the axis of rotation. Having reached the center, the source of the flame is transformed into a rotational body. The flame propagation velocity is approximately equal to or less than the apparent speed in the medium at rest. The movement of the flame to the center of the reactor is easily explained by the presence of centripetal forces leading to the appearance of a radial convective flow in a system, in which there are regions with markedly different densities (initial mixture and combustion products).

In [60], flame extinguishing in a rotating gas was studied. The mixtures of methane and air were used. The mixture was ignited with an electric spark in the center of the vessel. Experiments have shown that the flame propagates only up to a certain critical radius r_{cr} and diminishes. The authors of the work explain the flame extinguishing effect by the fact that the processes of combustion and cooling of the rotating gas are accompanied by complex radial movements of fresh gas and combustion products, which, in turn, lead to gradients of the gas rotation speed along the radius. This gradient can cause turbulence or flame extinguishment. The most detailed review of the publication on the problem of combustion in eddies can be found in [61]. Thus, it follows from the publication that the propagation of flame in eddy flows of combustible mixtures has a number of specific effects due to the presence of centripetal forces in the rotating gas. Unfortunately, their effect on the self-ignition of gas eddies arising in real flows, including flows with devel-

oped turbulence, under conditions with strongly differing temperatures in different regions of the flow has hardly been studied.

The radial stratification of the eddy flow in terms of density and the arising convective flows during the eddy flow of gas and two-phase mixtures should affect both the appearance of points of origin of thermal ignition and the development of the process of flame propagation from them (including the induction mechanism of Ya. B. Zeldovich [61]). These flows significantly change the temperature field and heat-exchange conditions. In a number of technical installations, for example, a hypersonic ramjet, these effects can turn out to be very important from the point of view of improving the ignition conditions and intensifying the combustion of fuel in the air flow. Therefore, their study seems to be practically valuable.

In this regard, in [56, 61], the task was posed to fill the gaps in the understanding of ignition processes in difficult conditions of a eddy flow. In other words, it is also necessary to study experimentally the effect of radial stratification of a eddy flow on self-ignition and the resulting combustion of fuel-air mixtures.

Experimental

The peculiarity of the experimental setup consisted in the method of creating a rotating eddy of the gas mixture. In [57, 60], a rotating gas flow was formed due to the rotation of the reactor around its axis. This technique makes it difficult for the long-term heating of the reactor, which is necessary for the study of thermal ignition, and cannot provide high velocities of tangential flow. In [15], the rotation of the combustible mixture was carried out in a stationary heated reactor due to the swirling of the gas flow with tangential admission into the evacuated vessel. The installation diagram is shown in Fig. 20.

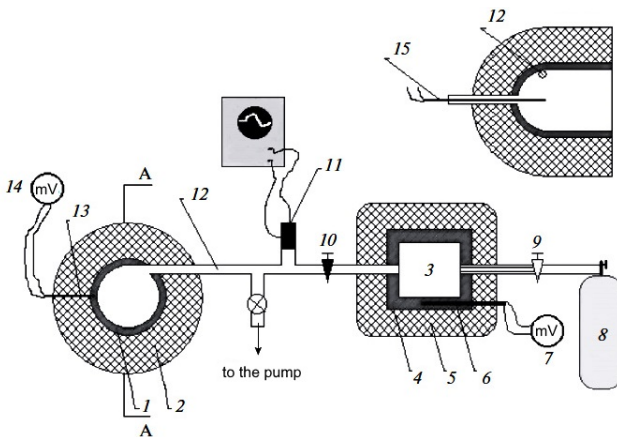


Figure 20. Installation diagram:

1 - reactor, 2 - electric furnace and thermal insulation, 3 - high pressure chamber (HPC), 4, 5, 6 - electric heater, thermal insulation and thermocouple, measuring the HPC temperature, 7 – voltmeter. 8 - mixing chamber, 9 - valve, 10 - electromagnetic valve, 11 - pressure sensor and registration system, 12 - inlet port, 13 - thermocouple, 14 - voltmeter, 15 - thin thermocouple made of tungsten and rhenium wires with a diameter of 30 μm

The bypass vessel, heated reactor and supply communication lines were made of stainless steel. Both vessels were connected by a communication equipped with an electromagnetic valve. The time, during which the valve can be open is set from 50 ms to several seconds. The inner diameter of the reactor was 14 cm. The reactor could be used in two modifications: as a spherical chamber, in this case, only pressure registration is possible, and as a spherical-cylindrical vessel. In this version, high-speed video filming was carried out through a quartz window 14 cm in diameter and 2 cm thick. The experimental technique and measurement of the ignition delays did not differ from the technique adopted for a conventional bypass installation. The ignition was registered with a pressure sensor, thermocouple, or photodiode. The reactor was evacuated and heated to a predetermined temperature. A pre-prepared mixture was fed into the bypass vessel from the mixer, the time for mixing the gases was at least 48 hours. During the experiment, pressure was recorded with a "Courant DI" pressure sensor and an information collection system based on an analog-to-digital converter. The sampling frequency in all experiments was 1000 Hz.

Results and discussion

Experiments carried out with well-studied mixtures, such as air stoichiometric mixtures of methane, propane, pentane and rich mixtures of hydrogen with air, showed a discrepancy between the measurement results and the known experimental data. First of all, the ignition delays turned out to be much shorter than those expected at a given temperature of the reactor walls. The results also showed that the minimum reactor temperatures, at which autoignition occurs are significantly lower than their literature values. For example, an air mixture containing 40% hydrogen ignited at a reactor temperature of only 558 K (285 °C) instead of 773 K (500 °C) at a pressure of about 1.0 atm. The stoichiometric air mixture of propane ignited at a reactor temperature of 630 K (357 °C), while, according to the literature data given in [15], this temperature is 743 K (470 °C). The corresponding oscillograms of ignition are shown in Fig. 21.

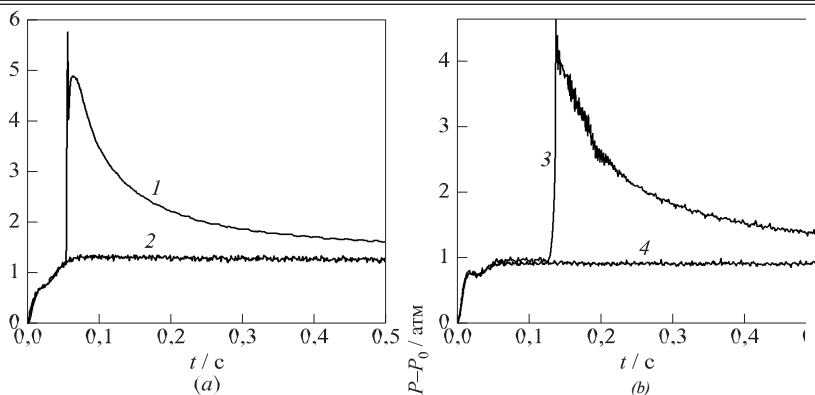


Figure 21. Oscillograms of pressure obtained by passing a mixture of 40% H_2 and 60% air (a) and stoichiometric air mixture of propane (b) into a heated reactor. Wall temperature: 1 - 558 K, 2 - 552 K; 3 - 630 K; 4 - 620 K

The obtained effect of lowering the temperature of thermal ignition in an eddy flow is not consistent with the existing concepts of self-ignition of combustible gases and requires an explanation of its mechanism.

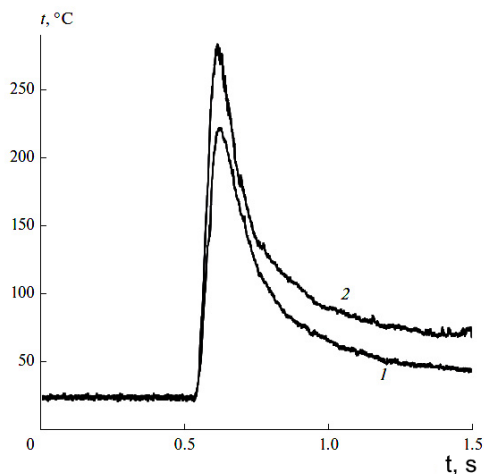


Figure 22. Records of thermocouple signals recorded in the center of the reactor at different pressures P in the HPC. Reactor and HPC temperature - room temperature; 1 - $P = 0.3$ MPa, 2 - $P = 1.0$ MPa. The valve opening time is 0.05 s

Figure 22 shows the temperature-time relationship recorded in experiments in which air was introduced into an evacuated reactor at room temperature. The pressure in the HPC is, 0.3 MPa. As you can see, the higher the pressure in the HPC, the higher the temperature peak in the center of the reactor is. It was shown that the absolute value of the temperature peak in the heated reactor is, significantly higher than its value in the reactor at room temperature. The ratio of the temperature at the peak to the initial temperature of the reactor (in degrees K) decreases slightly with an increase in the temperature of the reactor. Experiments show that temperature peaks are also observed when the high pressure gas is injected not into an evacuated reactor, but into the reactor containing the low pressure gas. Thus, the tangential injection of gas into the reactor leads to the formation of an unsteady vortex flow, the temperature distribution in which reaches a maximum in the center of the eddy (see below).

To obtain additional information on the processes occurring during the filling of a combustible mixture into a heated reactor and its spontaneous combustion, a series of experiments was carried out using high-speed video filming. The shooting was carried out with a Casio Exilim EXFH25 camera with a frequency of 1000 fps and a high-speed FANTOM camera with a speed of 10,000 fps. Examples of such video filming in the form of several separate frames are shown in Fig. 23 and 24.

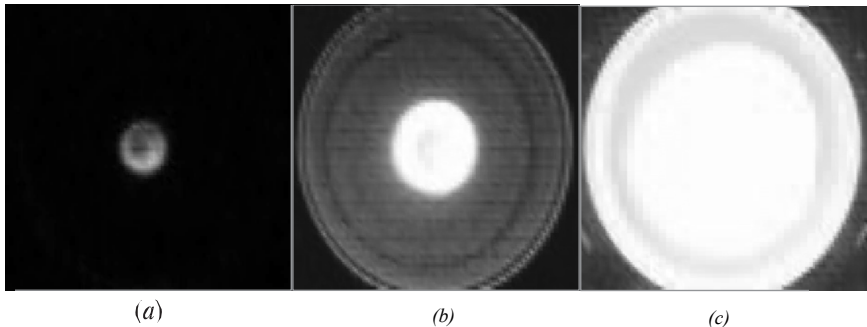


Figure 23. Development of a point of origin of thermal ignition in time. Mixture - air + 4% C_3H_8 . The temperature of the walls of the reactor is 630 K (357 °C): (a) $t = 2$ ms; (b) 5; (c) $t = 9$ ms.

High-speed footage of the central region of the reactor is demonstrated in Fig. 24. It turned out that in the case of tangential admission of the mixture into a heated reactor and the formation of a swirling vortex flow, ignition always occurs in the central region, and only then the flame propagates throughout the volume of the vessel. In contrast to the results of work [60], in which spark ignition of the mixture was carried out in a rotating reactor, flame extinguishing was not observed. In all the mixtures considered, once having appeared in the center of the reactor,

the flame spread throughout the entire volume without extinguishing. Obviously, a certain radial temperature distribution is established in the reactor by the time of ignition: in the central region, the highest temperature, at which self-ignition occurs; at the periphery, in the near-wall region, the temperature corresponds to the temperature of the walls of the reactor

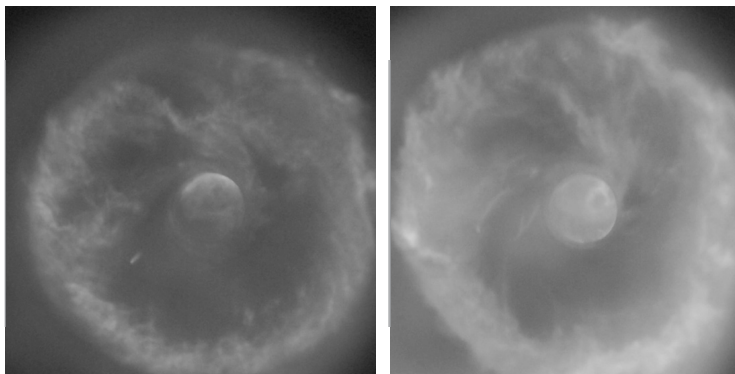


Figure 24. *The center of thermal ignition in the central region of the reactor at different moments in time. The difference between frames is 0.1 ms. Mixture - 40% H₂ + 60% air. Reactor wall temperature is 558 K (285 °C)*

This suggests that the radius of the region heated enough to create conditions providing the induction mechanism of flame propagation proposed by Ya. B. Zeldovich [61] is greater than the critical radius r_{cr} [60].

The glow of the cooling products confirms the fact of the vortex flow in the reactor. Shooting the central region of the reactor with a high-speed camera showed that at the moment of thermal ignition, the gas in it is practically stationary. Such a picture of thermal ignition differs significantly from that observed in a static setup with an axial filling of the mixture under study [48, 64], i.e. in the absence of rotation of the gas mixture. The experiments carried out on the high-speed registration of thermal ignition without rotation showed that the primary ignition source arises on the surface of the reactor. At the same time, the place of origin of the focus changes in each subsequent experiment under the same conditions (Fig. 25a).

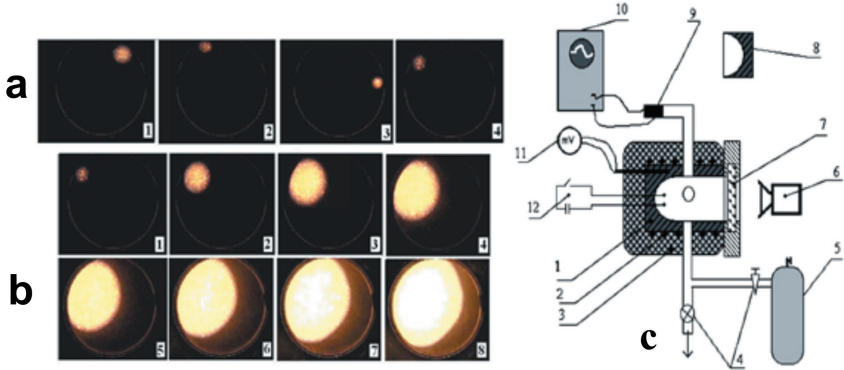


Figure 25.

a) - Video images of primary ignition centers in stoichiometric mixtures of n-pentane - air in four successive experiments at a wall temperature of 1 - 650 K; 2 - 643 K; 3-645 K; 4-649 K. 600 frames/s, $P = 1$ atm. The numbers in each image correspond to the sequential number of the experiment

b) - Sequences of video images of the spatial development of thermal ignition in stoichiometric mixtures of n-pentane - air at a reactor wall temperature of 649 K, 600 frames/s. $P = 1$ atm. The numbers on the frames correspond to the sequential number of the video image.

c) Diagram of the experimental setup: (1) reactor, (2) electric heater, (3) thermal insulation, (4) valves, (5) mixer, (6) digital video camera, (7) optical window, (8) hemispherical insert, (9) pressure transducer, (10) ADC data acquisition system, (11) digital voltmeter, and (12) spark ignition circuit.

This means that the reactivity of different parts of the surface changes from one experiment to the next one. Obviously, the observed character of the onset of combustion corresponds to the mode of ignition by a heated surface [50, 64]. The main feature of the ignition process is that ignition occurs in separate areas of the surface, at the same temperature of the reactor surface. Figure 25b shows video sequences of the spatial development of ignition recorded at 600 frames/s in a stoichiometric mixture of pentane with air at a reactor wall temperature of 620 K, which correspond to the development of one of the point of origin shown in Fig. 25a. It can be seen that, first, a hemispherical flame develops from the point of origin, which loses its symmetrical shape as new combustion centers appear. In the presented series of experiments, the induction period was at least 7 s. Therefore, steady heating of the combustible mixture, according to direct measurements [56, 61], was practically ensured, since the rapid filling of the mixture and the resulting turbulization reduce the heating time of the mixture. Consequently, the combustion process begins on the surface of the steel reactor even under conditions of practically steady heating of the combustible mixture.

Thus, the ignition of combustible mixtures in a heated reactor in a rotating flow is completely homogeneous. If there is no vortex flow, or there is a different flow structure, then in the installation shown in Fig. 25c, thermal ignition is not uniform, i.e. thermal ignition modes are qualitatively different. These regimes are obviously not determined by the kinetics of the reaction, which remains the same. They are only related to gas dynamics. It should be noted that, after studies carried out by the high-speed filming method, thermal ignition in a heated reactor, which was considered as a steady ignition in volume, turned out to be in fact the propagation of a flame from a primary focus of a chemical or thermal nature, depending on the experimental conditions.

In the case of tangential admission, the flow of the reacting gas outflowing from the bypass vessel at the speed of sound (at the initial moment of time) flows around the heated spherical wall of the reactor. According to estimates [56, 61], overloads of more than 100 g occur in the rotating gas. The appearance of centripetal forces inevitably leads to radial stratification of the reacting gas flow in terms of density. The first portions of the inflowing gas are heated very quickly (high flow velocity and low pressure, i.e., a very high thermal diffusivity). The warmest, that is, the least dense, gas masses appear in the center of the eddy [61], and the coldest ones - on the periphery, where fresh cold portions of gas continue to flow.

Together with the radial stratification of the gas in terms of density, the temperature distribution is also observed. In the central region of the reactor, a slow-moving gas is collected, initially heated to the temperature of the reactor wall. Heat outflow from this area is difficult due to its remoteness from the reactor walls and low convective heat transfer. A further increase in the pressure in the reactor due to the continued admission of a fresh mixture into it will lead to adiabatic compression and, consequently, heating of the combustible mixture in the central part to a temperature exceeding the wall temperature.

Let us estimate this value of the gas temperature in the central region, at which thermal ignition occurs. Based on the condition of adiabatic compression, we have: $T_k/T_i = (P_k/P_i)^{(\gamma-1)/\gamma}$. Here, the index *i* indicates the initial state of the gas in the reactor, and the index *k* indicates the final state, γ is the ratio of the heat capacities. The available experimental data make it possible to make a reasonable estimate of the ratio of the P_k/P_i values.

We will assume that the combustion of the mixture in the reactor will be complete if the central region of the reactor, in which self-ignition occurs, has a radius *R* not less than the critical flame extinguishing radius r_{cr} , $R \geq r_{cr}$ [60]. Therefore, as the initial pressure P_i of the mixture in the reactor, we will take the pressure of that amount of the mixture, which, being compressed to the final pressure P_k , will occupy the volume of the central region of the reactor, limited by the radius r_{cr} . The temperature will correspond to the minimum temperature of thermal ignition taken from the literature sources.

We will numerically estimate the P_k/P_i value using the example of a stoichiometric mixture of propane and air and a rich mixture of hydrogen and air. Oscillograms of pressure during spontaneous ignition of these mixtures for various wall's temperatures are shown in Fig. 21a, b. It is known from the reference literature that the minimum temperature of thermal ignition of propane in air is $T = 743 \text{ K}$ (470°C). In accordance with [23], we take the ratio of the specific heat capacities for this mixture $\gamma = 1.369$. Thus, taking into account that the minimum reactor temperature at which ignition occurs is 630 K (357°C), it is easy to estimate the value of $P_k/P_i \approx 1.84$.

Arguing in the same way, let us numerically estimate the P_k/P_i value for a rich mixture of hydrogen and air. Proceeding from the fact that at atmospheric pressure the minimum temperature of thermal ignition of hydrogen is 773 K (500°C), and the value of the ratio of specific heat capacities $\gamma = 1.396$, according to the data of [63], it is easy to estimate $P_k/P_i \approx 3.15$.

This local adiabatic heating of the gas under investigation in the central region of the reactor causes the gas to ignite at a low temperature.

To make sure that the observed effect was caused by the eddy rotation of the gas, control experiments were carried out, in which the formation of the eddy motion of the gas was suppressed at the moment the mixture was poured into the reactor. For this, an annular rib was installed in the reactor in the transverse direction to the gas flow outflowing from the bypass vessel. The outer diameter of the ring was equal to the inner diameter of the reactor and was 14 cm , and the inner diameter was 11 cm . This barrier excluded the swirling of the reacting gas flow, without interfering with the turbulent movement of the medium and providing rapid mixing of heated and cold layers of gas, as well as convective heat exchange with the walls of the reactor. The suppression of the flow swirling of the combustible mixture led to the disappearance of the effect under consideration.

The results of this series of experiments have convincingly shown that the effect of ignition of combustible mixtures at a low temperature is associated precisely with the eddy nature of the flow that occurs in the bypass installation with tangential filling of the mixture under study.

Let us summarize the results obtained.

The effect of thermal ignition of combustible mixtures at reactor temperatures significantly lower than the thermal ignition temperature was experimentally observed in a static bypass installation with a tangential inlet of the mixture under study. In this case, the difference between the temperature of the reactor and the temperature of thermal ignition can reach more than 150 K .

This effect is primarily caused by the presence of centripetal forces that inevitably arise during the formation of a eddy gas flow. The result of the action of these forces on the flow is the radial stratification of the gas in terms of density and, therefore, in terms of temperatures. The rotational motion of the gas in a flow with a temperature gradient leads to the formation in the center of the eddy of a

region with an increased temperature relative to the peripheral layers of the gas. In the central region, the hottest and least mobile gas is formed. In addition, it is well insulated from the walls of the reactor. Depending on the average temperature of the gas and the degree of pressure increase in it, this difference can reach several hundred degrees, which is confirmed by a significant decrease in the autoignition temperature of combustible mixtures in comparison with the values known from the literature sources.

The pressure increase in the reactor caused by the mixture admission leads to adiabatic compression and additional heating of the gas. The centripetal forces contribute to the fact that the heat, which begins to generate with the onset of a chemical reaction, is accumulated in the central region of the reactor, thus creating favorable conditions for thermal ignition.

The study of the discovered effect can be important for understanding the mechanism of thermal ignition of turbulent flows in various technical devices. This effect can be used in a hypersonic ramjet to improve ignition conditions and intensify combustion. In addition, an emergency situation with the formation of eddy flows of combustible mixtures under conditions that would seem to exclude the possibility of their thermal ignition is possible in industry.

The discovered effect of local adiabatic heating of the mixture under study can be used to measure ignition delays in the so-called intermediate temperature range and ignition delays of fuel-air mixtures, namely, between temperatures and delays characteristic of experiments in shock tubes and in bypass installations for initial pressures ≤ 1 atm. This range is practically not covered in the literature source, since the results of experiments in installations of adiabatic compression refer to pressures significantly higher than atmospheric, and the results of measurements in jet installations are very rare.

Conclusions for Chapter 3

Experiments proved that spherical flames of lean (6–15% H₂) hydrogen-air mixtures have a cellular structure. In mixtures containing 6–10% H₂, flames propagate spherically symmetrically at the initial stage near the lower concentration limit. Then the gravity field distorts the shape of the combustion front. Flames of mixtures containing 10–15% H₂ propagate spherically symmetrically. It is shown that the Boussinesq approximation is applicable to obtain cells with H₂ < 10%, taking into account the force of gravity. Calculations by the Boussinesq model in the absence of gravity do not allow the formation of cells. The use of the Navier-Stokes equations for a compressible medium makes it possible to describe the spherically symmetric mode of propagation of a cellular flame under microgravity conditions. It is shown that the analysis of experimental data on flame propagation in lean mixtures does not make it possible to distinguish between the calculation results using a two-dimensional model with and without convection. It has

been shown experimentally that additions of isobutene C_4H_8 in amounts below the lower concentration limit (up to 1.5%) lead to an increase, and additions of CO_2 to 15% - to a decrease in the flame propagation rate in lean hydrogen-air mixtures. The reasons for the acceleration of combustion in the presence of a hydrocarbon additive are considered.

It is shown that the detected light emission inhomogeneities can be associated with the presence of acoustic waves by using the combustion of hydrogen-air mixtures (30% and 15% H_2) as an example. It was found that the flame propagation velocities in a stoichiometric hydrogen-air mixture with central spark initiation do not depend on the material of the inner surface of the reactor (stainless steel, TiO_2 , Ta, Pt) but depend on the shape of the inner surface of the reactor.

It is shown that spark-initiated flames of lean hydrogen mixtures (8% - 15% H_2 in air) pass through aluminum mesh spheres with a cell size of 0.04-0.1 mm², while the flame of a mixture of 15% H_2 in air is accelerated after passing through an obstacle. In the presence of an obstacle during the propagation of flame in mixtures of 10% and 15% H_2 , acoustic oscillations of the gas arise in the reactor. The onset of oscillations occurs earlier in time in the presence of a sphere of a smaller diameter. The flame of a mixture of 7.5% H_2 in air does not pass through the mesh spheres. It was found that the flame of a mixture of 8% natural gas with air passes through the mesh spheres. However, after the obstacle, the flame velocity remains the same, while acoustic oscillations are not observed. It is shown that the active centers of combustion of methane and hydrogen, which determine the propagation of the flame, have a different chemical nature.

In a static bypass installation with a tangential inlet of the mixture under study, the effect of thermal ignition of combustible mixtures at reactor temperatures is found to be significantly lower than the thermal ignition temperature. In this case, the difference between the temperature of the reactor and the temperature of thermal ignition can reach more than 150 K. This effect is caused primarily by the presence of centripetal forces, which inevitably arise during the formation of a vortex gas flow. The result of the action of these forces on the flow is the radial stratification of the gas in terms of density and, therefore, in terms of temperatures. In the central region, the hottest and least mobile gas is formed and in addition, it is well insulated from the walls of the reactor. The possibility of mixing it with fresh cold masses of gas is excluded. The pressure increase in the reactor caused by the mixture puffing leads to adiabatic compression and additional heating of the gas. The centripetal forces contribute to the fact that the heat, which begins to generate with the onset of a chemical reaction, is accumulated in the central region of the reactor, thus creating favorable conditions for thermal ignition.

References for Chapter 3

1. Ronney P. D. *Premixed-Gas Flames. Microgravity Combustion: Fires in Free Fall* (H. Ross, Ed.). Academic Press, London. U.K. 2001. pp. 35-82.
2. Williams F. A., Grear J. F. *A hypothetical burning-velocity formula for very lean hydrogen-air mixtures. Proc. of the Combustion Institute. 2009. Vol. 32. No. 1. pp. 1351-1360.*
3. *Nonsteady flame propagation* (ed. by George H. Markstein). Perg. Press. Oxford. London. 1964. Vol. 75. 328 p.
4. Zeldovich Ya. B. *Selected Works. Vol. 1: Chemical Physics and Hydrodynamics* (Princeton Legacy Library, 140). 1992. 490 p.
5. Chen Z., Ju Y. *Theoretical analysis of the evolution from ignition kernel to flame ball and planar flame. Combustion Theory and Modelling. 2007. Vol. 11. No. 3. pp. 427-453. DOI:10.1080/13647830600999850*
6. Coward H. F., Brinsley F. *Influence of additives on flames. J. Chem. Soc. 1914. (105) pp. 1859-1866.*
7. Ronney P. D. *Near-limit flame structures at low Lewis number. Combustion and Flame. 1990. Vol. 82. pp. 1-14.*
8. Zeldovich Ya. B., Drozdov N. P. *Diffusion phenomena at the limits of flame propagation. Journal of Physical Chemistr. 1943. Vol. 17. No. 3. pp. 134-144.*
9. Rubtsov. N. M., Seplyarsky B. S., Tsvetkov G. I., Chernysh V. I., *Numerical investigation of the effects of surface recombination and initiation for laminar hydrogen flames at atmospheric pressure. Mendelevov Communications. 2008. Vol. 18. pp. 220-222.*
10. Rubtsov N. M., Seplyarsky B. S., Troshin K. Ya., Chernysh V. I., Tsvetkov G. I. *Features of the propagation of laminar spherical flames initiated by a spark discharge in mixtures of methane, pentane, and hydrogen with air at atmospheric pressure. Russian Journal of Physical Chemistry A. 2011. Vol. 85. No. 10. pp. 1707-1716.*
11. Rubtsov N. M., Kotelkin V. D., Seplyarskii B. S., Tsvetkov G. I., Chernysh V. I. *Investigation into the combustion of lean hydrogen-air mixtures at atmospheric pressure by means of high-speed cinematography. Mendelevov Communications. 2011. Vol. 21. No. 5. pp. 215-217.*
12. Lewis B., Von Elbe G. *Combustion, Explosions and Flame in Gases. New York. London. Acad. Press. 1987. 566 p.*
13. Dahoe A. E. *Laminar burning velocities of hydrogen-air mixtures from closed vessel gas explosions. Journal of Loss Prevention in the Process Industries. 2005. Vol. 18. pp. 152-169.*

14. Rubtsov N. M., Kotelkin V. D., Seplyarskiy B. S., Tsvetkov G. I., Chernysh V. I. *Issledovanie osobennostey iniciirovannogo goreniya bednyh vodorodno-vozdushnyh smesey pri atmosfernom davlenii metodom skorostnoj fotos"emki.* (Study of the Features of Initiated Combustion of Poor Hydrogen-Air Mixtures at Atmospheric Pressure by High-Speed filming). *Chemical physics and mesoscopy.* 2011. Vol. 13. No. 3. pp. 331-339. (in Russian)

15. Backstrom G. *Simple Fields of Physics by Finite Element Analysis* (Paperback), GB Publishing. 2005. 324 p.

16. Polezhaev V., Nikitin S. *Thermoacoustics and heat transfer in an enclosure induced by a wall heating.* 16th International Congress on Sound and Vibration. Kraków. Poland. 5–9 July 2009. pp. 2-8.

17. Rayleigh J. W. *On convection currents in a horizontal layer of fluid, when the higher temperature is on the under side.* *Phil. Mag.* 1916. Vol. 32. pp. 529-546.

18. Rubtsov N. M., Azatyan V. V., Baklanov D. I., Tsvetkov G. I., Chernysh V. I. *Effect of chemically active additives on the detonation wave velocity and the detonation limits in lean mixtures.* *Theoretical foundations of Chemical Engineering.* 2007. Vol. 41. No. 2. pp. 154-163.

19. Lieuwen T. C. *Experimental investigation of limit-cycle oscillations.* *Journal of Propulsion and Power.* 2002. Vol. 18. pp. 61-67.

20. Larionov V. M., Zaripov R. G. *Avtokolebaniya gaza v ustanovkah s goreniiem* (Gas self-oscillations in combustion installations. Kazan: Publishing House of Kazan State Tech. Univer. 2003. 227 p. (in Russian)

21. van Kampen J. *Acoustic pressure oscillations induced by confined turbulent premixed natural gas flame.* PhD thesis. University of Twente. Enschede. The Netherlands. March 2006. 260 p.

22. Williams F. A. *Combustion Theory (The Fundamental Theory of Chemically Reacting Flow Systems).* 2nd Ed. The Benjamin Cummings. Pub. Co. Menlo Park. Ca. 1985. 665 p.

23. Zeldovich Ya. B., Barenblatt G. I., Makhviladze G. M., Librovich V. B., *The Mathematical Theory of Combustion and Explosion.* Consultants Bureau. New York. 1985.

24. Zeldovich, Ya. B. *Structure and stability of steady laminar flame at moderately large Reynolds numbers.* *Combustion and Flame.* 1981. Vol. 40. pp. 225–234.

25. Rubtsov N. M., Seplyarskiy B. S., Troshin K. Ya., Chrenysh V. I., Tsvetkov G. I. *Initiation and propagation of laminar spherical flames at atmospheric pressure.* *Mendeleev Communications.* 2011. Vol. 21. No. 4 pp. 218-221. <https://doi.org/10.1016/j.mencom.2011.07.016>

26. Rayleigh J. W. S. *The theory of sound.* New York: Dover. 1945.

27. Putnam A. A., Dennis W. R. *Organ-pipe oscillations in a burner with deep ports.* *JASA.* 1956. Vol. 28. pp. 260-268.

28. Al-Shahrany A.S., Bradley D, Lawes M, Liu K, Woolley R. Darrieus-Landau and thermo-acoustic instabilities in closed vessel explosions. *Combustion Science and Technology*. 2006. Vol. 178. No. 10-11. pp. 1771-1802.

29. Maxwell G. B. ,Wheeler R. V. Some flame characteristics of motor fuels. *Ind. Eng. Chem*. 1928. Vol. 20. pp. 1041-1044.

30. Megalchi M., Keck J.C. Burning velocities of mixtures of air with methanol, isooctane and indolene at high pressure and temperature. *Combust. Flame*. 1982. Vol. 48. pp. 191-210.

31. Clane C., Searb G. First experimental study of the Darrieus Landau instability. *Phys. Rev. Lett*. 1998. Vol. 2. pp. 3867-3870.

32. Clavin P. Premixed combustion and gasdynamics. *Ann. Rev. Fluid Mech*. 1994. Vol. 26. pp. 321-352.

33. Solovyanova I. P., Shabunin I. S. Teoriya volnovykh processov (Theory of wave processes). *Acoustic Waves*. Yekaterinburg: SEI HVE USTU-UPI, ISBN 5-321-00398 X. 2004. 142 p. (in Russian)

34. Teodorczyk A., Lee J. H. S., Knystautas R. The Structure of Fast Turbulent Flames in Very Rough, Obstacle-Filled Channels. *Twenty-Third Symposium (Int.) on Combustion*. The Combustion Institute. 1990. pp. 735-741.

35. Gorev V. A., Miroshnikov S. N. Uskoryayushcheesya gorenje v gazovykh ob'emakh (The accelerating combustion in gas volumes). *Khimicheskaya fizika*. Chemical Physics. 1982. No. 6. pp. 854-858. (in Russian)

36. Moen I. O., Donato M., Knystautas R., Lee J. H., Wagner H. G. Turbulent Flame Propagation and Acceleration in the Presence of Obstacles. *Gasdynamics of Detonations and Explosions*. Progress in Astronautics and Aeronautics. 1981. No. 75. pp. 33-47.

37. Wagner H. Gg. Some Experiments about Flame Acceleration. *Fuel-Air Explosions*. University of Waterloo Press. 1982. pp. 77-99.

38. Nikolayev Yu. A., Topchiyan M. E. Raschet ravnovesnykh techenij v detonacionnykh volnah v gazakh (Calculation of equilibrium flows in detonation waves in gases). *Physics of Combustion and Explosion*. 1977. Vol. 13. No. 3. pp. 393-404. (in Russian)

39. Sokolik A. S. Samovosplamnenie, plama i detonaciya v gazakh (Self-ignition, flame and detonation in gases). M: Publishing house of the Academy of Sciences of the USSR. 1960. 470 p. (in Russian)

40. Fischer V., Pantow E, Kratzel T. Propagation, decay and reignition of detonations in technical structures. in "Gaseous and heterogeneous detonations: Science to applications". Moscow: ENASH Publishers. 1999. 197 p.

41. Rubtsov N. M., Tsvetkov G. I., Chernysh V. I. Razlichnyy kharakter deystviya malykh aktivnykh dobavok na vosplamneniye vodoroda i metana (Different nature of the action of small active additives on the ignition of hydrogen and methane). *Kinetics and catalysis*. 2007. Vol. 49. No. 3. pp. 363-370. (in Russian)

42. Rubtsov N. M., Seplyarsky B.S., Tsvetkov G. I., Chernysh V. I. *Vliyanie parov metalloorganicheskikh soyedineniy na protsessy vosplamneniya i goreniya vodoroda, propilena i prirodnogo gaza* (Influence of vapors of organometallic compounds on the processes of ignition and combustion of hydrogen, propylene and natural gas). *Theoretical Foundations of Chemical Technology*. 2009. Vol. 43. No. 2. pp. 187–193. (in Russian)

43. Lee J. H. S., Knystautas R., Chan C. K. *Turbulent Flame Propagation in Obstacle - Filled Tubes* ". 20th Symposium (International) on Combustion. 1985. pp. 1663-1672.

44. Chan C. K., Lee J. H. S., Moen I. O., Thibault P. *Turbulent Flame Acceleration and Pressure Development in Tubes*. In *Proc. of the First Specialist Meeting (International) of the Combustion Institute*. Bordeaux. France. 1981. p. 479.

45. Van Wingerden C. J. M., Zeeuwen J. P. *Investigation of the Explosion Enhancing Properties of a Pipe-Rack-Like Obstacle Array*. *Progress in Astronautics and Aeronautics*. 1986. Vol. 106. 53 p.

46. Cummings J. C., Torczynski J. R., Benedick W. B. *Flame Acceleration in Mixtures of Hydrogen and Air*. Sandia National Laboratory Repor. SAND- 86-0173. 1987.

47. Breitung W., Chan C., Dorofeev S., Eder A., Gelfand B, Heitsch M., Klein R. Malliacoss A., Shepherd E., Studer E., Thibault P. *State-of-the-Art Report On Flame Acceleration and Deflagration-to-Detonation Transition In Nuclear Safety*. Nuclear Safety NEA/CSNI/R 2000. OECD Nuclear Energy Agency. [http:// www. nea.fr](http://www.nea.fr).

48. Rubtsov N. M. *The Modes of Gaseous Combustion*. Springer International Publishing Switzerland. 2016. 294 p.

49. Poinso T., Veynante D. *Theoretical and Numerical Combustion*. R.T. Edwards Inc.; 2nd edition. 2005. 540 p.

50. Zeldovich Ya. B. *Izbrannyye trudy. Khimicheskaya fizika i gidrodinamika* (Selected Works. Chemical Physics and Hydrodynamics, ed. Khariton Yu. A. M: Publishing house "Nauka". 1984. 379 p. (in Russian)

51. Brown G. L. *On density effects and large structure in turbulent mixing layers*. *Journal of Fluid Mechanics* , Vol. 64. No. 4. pp. 775 - 816. <https://doi.org/10.1017/S002211207400190X>

52. Dimotakis P. E., Miake-Lye R. C., Papantoniou D. A. *Structure and dynamics of round turbulent jets*. *Phys. Fluids* 1983. Vol. 26. pp. 3185–3196. <https://doi.org/10.1063/1.864090>

53. Joly L., Chassaing P., Chapin J. N, Chassing P., Chapin V., Reinaud J. N., Micalief J., Suarez J., Bretonnet L., Fontane J. *Baroclinic Instabilities*. ENSICA - Département de Mécanique des Fluides., *Variable Density Turbulent Flows – Villanova i la Geltru – 2003*. https://oatao.univ-toulouse.fr/2366/1/Joly_2366.pdf.

54. Pope. S. B. *Turbulemt premixed Flames. Ann. Rev. Fluid Mech. 1987. Vol. 19. p. 237. DOI:10.1007/3540101926_10*

55. Bray K. *Turbulent flows with premixed reactants. Turbulent reacting flows. 980. pp. 115-183. 1. DOI: 10.1007/3540101926_10*

56. Borisov A. A., Smetanyuk V. A., Troshin K. Ya., Shamshin I. O. *Samovosplamneniye v gazovykh vikhryakh (Selfignition in gas vortices). Gorenje i vzryv (Moskva). Combustion and explosion. 2016. Vol. 9. No. 1. p. 219. (in Russian)*

57. Khalil A. E. E., Gupta A. K. *Fuel Flexible Distributed Combustion With Swirl For Gas Turbine Applications. Applied Energy. 2013. Vol. 109. p. 2749.*

58. Khalil A. E. E., Gupta A. K. *Swirling Flow field for Colorless Distributed Combustion. Applied Energy. 2014. Vol. 113. p. 208.*

59. Margolin A. D., Karpov V. P. *Combustion of rotating gas. Dokl. AN USSR. 1974. Vol. 216. p. 346.*

60. Babkin V. S., Badalyan A. M., Borisenko A. V., Zamashchikov V. V. *Flame extinction in rotating gas. Combustion Explosion and Shock Waves. 1982. Vol. 18. p. 272.*

61. Ishizuka S. *Flame propagation along a vortex axis. Progress in Energy and Combustion Science. Vol. 28. pp. 477-542.*

62. Zel'dovich Ya. B., Gelfand B. E., Tsyganov S. A., Frolov S. M., Polenov A. N. *Concentration and temperature nonuniformities of combustible mixtures as reason for pressure waves generation. Dynamics of explosions. Eds. A. Borisov, A. L. Kuhl, J.R. Bowen, J.-C. Leyer. 1988. Progress in astronautics and aeronautics ser. Washington. D.C. AIAA. Vol. 114. p. 99.*

63. Troshin K. Ya., Shamshin I. O., Smetanyuk V. A., Borisov A. A. *Selfignition and combustion of gas mixtures in a medium with vortex Flow. Russian Journal of Physical Chemistry B. 2017. Vol. 11. No. 6. pp. 952-962.*

64. Borisov A. A., Rubtsov N. M., Skachkov G. I., Troshin K. Ya. *Gas-phase spontaneous ignition of hydrocarbons. Russ. J. Phys. Chem. B. 2012. Vol. 6. pp. 517-522 DOI: 10.1134/S1990793112080040*

CHAPTER 4. Detecting the regularities of propagation of an unstable flame front using optical 4D spectroscopy and color high-speed filming

It is shown by the example of combustion of stoichiometric mixtures of n-pentane (C_5H_{12}) with air, diluted with carbon dioxide (CO_2) and argon (Ar), at total atmospheric pressure that during the propagation of the FF flame front from spherical to propagation in a pipe, the phenomena caused by instability of a flat flame occur. It is shown that, upon deceleration of the FF near the end wall of the reactor, a smooth FF acquires a cellular structure. It is shown that qualitative modeling of the results obtained is possible when analyzing the Navier-Stokes equations for a compressible medium in the approximation of a small Mach number. Using the methods of 4D optical spectroscopy and color high-speed filming, the features of combustion in flame cells caused by hydrodynamic instability have been experimentally observed for the first time. It is shown that any combustion cell is essentially a separate "chemical reactor", in each of which the process of complete chemical transformation is carried out.

Keywords: *flame front, hydrodynamic instability, flat flame, cellular structure, hyperspectrometer, color high-speed filming*

Let us recall that in real conditions, the processes of gas-phase combustion proceed under conditions of unsteady flows, fluctuations in density and pressure, i.e. have nonstationary character [1]. As shown by L. D. Landau, from a hydrodynamic point of view, a flat flame should be unstable [2]. This Chapter is devoted to the consideration of combustion in unsteady and unstable modes. The main attention is paid to the use of the methods of color high-speed filming and 4D optical spectroscopy, which makes it possible to register the intensity of the optical spectrum simultaneously depending on the wavelength, time and coordinate to establish the features of these processes.

Unstable modes manifest themselves in combustion processes in various forms and can be classified as thermal diffusion, hydrodynamic and thermoacoustic ones [3-9], see also Chapter 3.

Determining the nature of the chemical transformation during unstable combustion is an urgent problem both from the point of view of theory and in practical applications related to both the intensification of combustion and the issues of explosion safety. Experimentally, this issue was solved for the case of thermal diffusion instability, for which it was necessary to carry out experiments under zero gravity on the International space station. In [10], it was experimentally shown for the first time that in the presence of instabilities of a thermodiffusion nature (lean mixtures of hydrogen with oxygen), in zero gravity, there is a mode of formation of separate isolated stationary combustion cells. In other words, there are separate "chemical reactors" in a combustible environment. In this regard, we note that more than 50

years ago Zeldovich [4] showed that stationary heating and mass conservation equations admit a solution corresponding to a stationary spherical flame, although the same governing equations in plane geometry admit a solution in the form of a combustion wave. In the simplest case of spherical geometry, the solutions of the stationary equations of free convection for temperature T and chemical particles C : $\nabla^2 T = 0$ and $\nabla^2 C$ in polar coordinates have the form $c_1 + c_2/r$, where c_1 and c_2 – constants. This form satisfies the requirement that T and Y are bounded as $r \rightarrow \infty$. For cylindrical and planar geometries, the corresponding solutions have the form $c_1 + c_2 \ln(r)$ and $c_1 + c_2 r$, respectively, which are obviously not bounded as $r \rightarrow \infty$. For this reason, the theory allows stable solutions for a ball of flame, but not, say, a "cylinder of flame". It is these stable balls of flame predicted by Ya. B. Zeldovich that were observed in [10].

Despite the fact that the internal hydrodynamic instability of a flat flame has been recognized for almost a century, and that the first attempts at an analytical description were made more than fifty years ago, data on experimental measurements of the growth rates of flat flame perturbations began to appear in the literature relatively recently. One of the reasons for this is the experimental difficulty of controlling the initially flat front of the flame of premixed mixtures, in a regime, in which the flat front is unstable. A direct experimental test of Landau's hypothesis was carried out in [11]. Note that the FF is not characterized by only one characteristic frequency, but by a set of frequencies, which leads to the existence of regions of flame instability, often manifested in the appearance of cellular structures during combustion [2-5]. An important feature is that the boundaries of the instability region shift with an increase in the acoustic amplitude, i.e. it is possible to stabilize a planar phase transition with respect to hydrodynamic instability using an external acoustic field. In [11], an experiment was described in which the growth rate of cellular structures at the boundary of a plane flame was directly measured. The flat shape of the unstable laminar flame front was maintained by imposing an acoustic field. The growth rate of two-dimensional disturbances in time was observed after the acoustic field was turned off. Thus, Landau's hypothesis was verified by imposing an external factor i.e. an acoustic field. This experiment also illustrates the relationship between the main factors causing the instability of hydrodynamic and acoustic flames [9].

In experiments with a spherical FF, conditions are possible, under which an unperturbed regime can be realized at a certain stage of FF propagation, since perturbations of a spherical FF develop more slowly than those of a flat flame [12]. The instability of a spherical flame has a specific character associated with the fact that its front surface area is continuously growing. If the disturbances on the spherical FF increase more slowly than according to the linear law when the radius of the sphere as a whole grows, the FF smoothes out over time, despite the increase in the absolute value of the amplitude of the curvatures. The properties of the flame in this case approach the properties of an undisturbed spherical FF

[12]. Thus, in a spherical flame, disturbances grow in time more slowly than in a flat flame [12]. However, after the phase transition loses its spherical shape, for example, during propagation in a cylindrical channel, the conditions for the rapid growth of the phase transition surface disappear and the instability predicted by L. D. Landau [2]. In such an experiment, no external flame stabilization is required, since the initial spherical FF is initially undisturbed until it touches the reactor walls.

In this Chapter, using the example of the combustion of mixtures of n-pentane with air, the spatial propagation of a FF in a reactor of constant volume is investigated under conditions when the FF loses its spherical shape and the hydrodynamic instability of a plane flame front according to Landau is manifested. We assumed that the deceleration of the FF and the reaction products upon touching the FF wall would be accompanied by the onset of combustion instability. In this case, an additional reason for the instability of combustion under our conditions will be the splash of cold gas from the mains and its ignition, as well as the amplification of acoustic vibrations that repeatedly pass through the FF.

In order to find out the features of the described unstable combustion regime in this Chapter, the spatial propagation of the FF of stoichiometric mixtures of n-pentane with air in the presence of inert gas additives, at 1 atm and an initial temperature of 298 K in a constant-pressure bomb was investigated by methods of high-speed color photography and optical 4D spectroscopy. It should be noted that in stoichiometric flames of mixtures diluted with an inert gas, one should not expect the appearance of instabilities of either a thermodiffusion (there is no large difference in the transfer coefficients) or a thermoacoustic nature (the normal flame propagation velocity is low).

Experimental

The experiments were carried out in a cylindrical reactor with a volume of 2826 cm³ made of stainless steel, 25 cm long and 12 cm in diameter, equipped with removable covers and an optical quartz window at the end. In Fig. 1a a photograph of a setup for studying combustion is shown where: 1- stainless steel reactor, 2- optical quartz glass, 3- strip, along which the hyperspectral survey was carried out, the width of which is about 1 mm (see Chapter 2). Figure 1b shows a diagram of this installation where: 1- reactor, 2- electric heater, 3- thermal insulation, 4- valves, 5- mixer, 6- optical window, 7- digital film camera, 8- hyperspectrometer, 9- pressure sensor, 10 - information recording system based on ADC and computer, 11- digital millivoltmeter, 12- spark ignition system. In the center of the reactor, spark ignition electrodes were located, the distance between which was 0.5 mm.

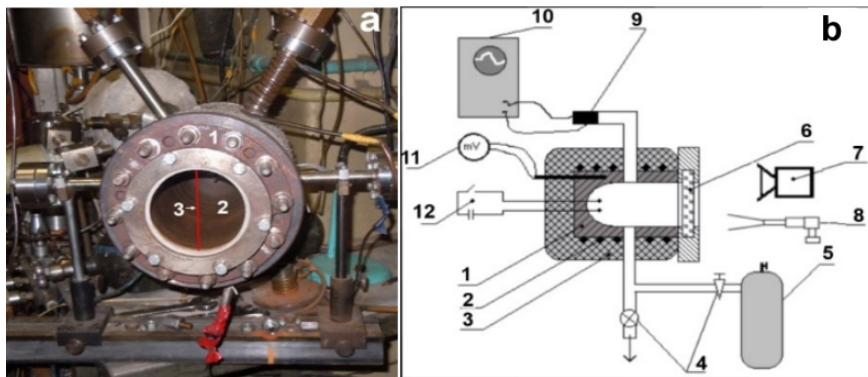


Figure 1.

- a) - photograph of the installation for studying combustion;
- b) - block diagram of the experimental installation

The experiments were carried out in the following sequence. A combustible mixture of a given composition prepared in advance in a cylinder was admitted into the reactor to the required pressure, and then ignition was initiated with a spark (1.5 J). Registration of the FF ignition and propagation was carried out through the optical window with a hyperspectrometer and a color high-speed film camera (Fig. 2) Casio Exilim F1 Pro (frame rate - 60 - 1200 s⁻¹). The data obtained were recorded into the computer memory and then processed.

Chapter 2 details the experimental setup using a hyperspectrometer and high-speed video (see Fig. 16 in Chapter 2). Let us briefly recall that spectroscopic measurements were carried out using a 4D spectrometer (hyperspectrometer), which allows performing simultaneous measurements of spectral and spatial coordinates [13, 14]. A hyperspectrometer (of the *push broom* type) registers a narrow strip on the sensed object at the same time. Registration is carried out on a two-dimensional photodetector matrix, according to one coordinate of which the spatial coordinate is measured, and according to the other - the spectral one (wavelength). Two more (up to 4D dimensions) are signal intensity and time.



Figure 2. The location of the high-speed video camera for filming the combustion process

Since the data are taken from the photodetector matrix of the hyperspectrometer at a frame rate of up to 300 Hz, the time dependence of the emission spectra of the combustion process is thus recorded. In this work, both video recording of the combustion with a video camera and registration of the combustion process with a hyperspectrometer were carried out, and then the obtained data were compared. The measurements were performed using a VID-IK3 hyperspectrometer [14] (see Chapter 2).

Before each experiment, the reactor was evacuated using a 2NVR-5D forevacuum pump. The pressure in the reactor was monitored with an exemplary pressure gauge and a vacuum gauge. Gases H_2 , n-pentane ($n-C_5H_{12}$), Ar, CO_2 , CCl_4 were of the "chemically pure" grade. Carbon tetrachloride CCl_4 was used as a combustion inhibitor for n-pentane.

Experiments in a stainless steel reactor were carried out with pre-prepared mixtures of 40% H_2 + air + (0 ÷ 1%) CCl_4 and stoichiometric mixtures of n-pentane ($n-C_5H_{12}$) with air diluted with argon (Ar) or carbon dioxide (CO_2) at total atmospheric pressure. Ar additions to the previously prepared stoichiometric mixture of 2.5% C_5H_{12} - 97.5% air were 15%, CO_2 - 10%, CCl_4 additions to a diluted stoichiometric mixture of n-pentane with air were up to 2%.

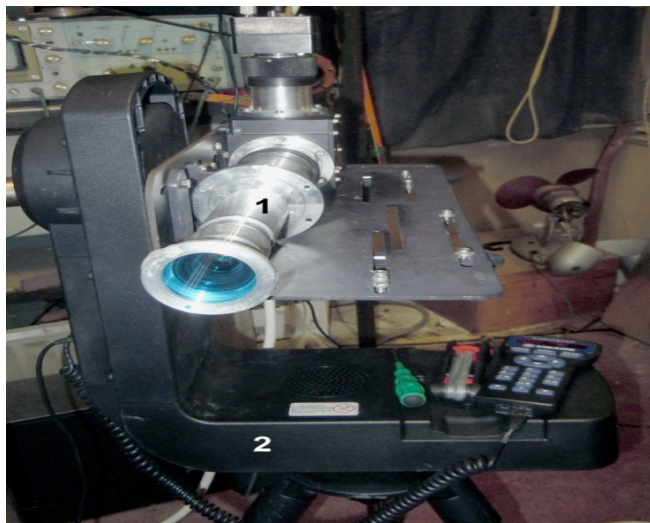


Figure 3. Location of the IR-VID3 hyperspectrometer (1) on the rotating device (2)

Results and discussion

It was found in preliminary experiments with mixtures of 40% H_2 with air that, in accordance with [5], additions of CCl_4 in an amount of up to 2% to this mixture do not noticeably affect either the flame front propagation velocity or the FF emission spectrum in the visible region. Therefore, for the presentation in this work, we have chosen the most illustrative pair “film - spectrum” for a hydrogen – air mixture. The results of video recording of the combustion of a mixture of 40% H_2 with air and the addition of 1% CCl_4 at a pressure of 1 atm in a stainless steel reactor with a frame rate of 600 s^{-1} is shown in Fig. 4. The number on the frame corresponds to the frame number when shooting. Combustion was initiated by a spark in the geometric center of the reactor. The frames of high-speed filming with a frame rate of 600 s^{-1} of the propagation of FF of mixtures of n-pentane with air for various compositions of combustible mixtures is shown in Fig. 5-7. In these frames, after the moment of initiation, stationary propagation of the FF is observed until the moment it touches the side surface of the reactor. The number on the frame corresponds to the number of the frame during filming. It can be seen that the FF is deformed near the openings of the gas supply lines (Fig. 4, frame 31; Fig. 7, frame 50). Further propagation of the FF continues in the cylindrical part of the reactor in the direction of the end. In this case, the injection of a cold combustible mixture from the volume of the mains into the combustion products in the reactor is observed (Fig. 6).

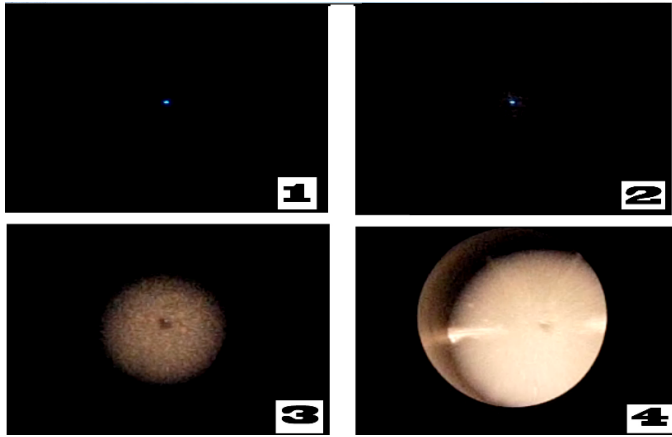


Figure 4. Result of frame-by-frame processing of filming of initiated ignition of the mixture of 40% H_2 with air and 1% CCl_4 addition

It can be seen that the FF is deformed near the openings of the gas supply lines (Fig. 5, frame 31; Fig. 7, frame 50).

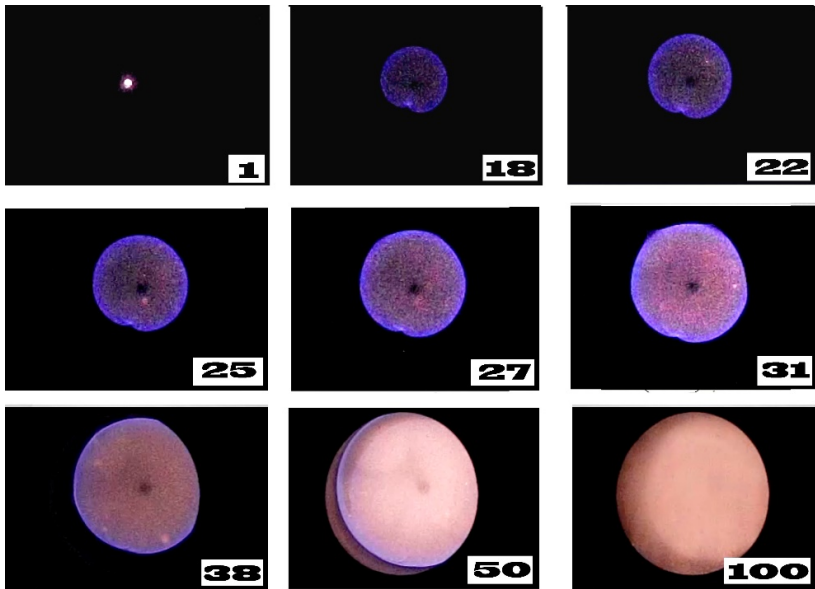


Figure 5. The result of time-lapse processing of filming of the process of propagation of a spherical flame front of a stoichiometric mixture of pentane with air and 10% CO_2

Further propagation of the FF continues in the cylindrical part of the reactor in the direction of the end. In this case, the injection of a cold combustible mixture from the volume of the mains into the combustion products in the reactor is observed (Fig. 6). When passing to the combustion regime in a cylinder in diluted by Ar or $\text{CO}_2 + \text{CCl}_4$ mixtures, disturbances in the form of cells appear on the FF surface.

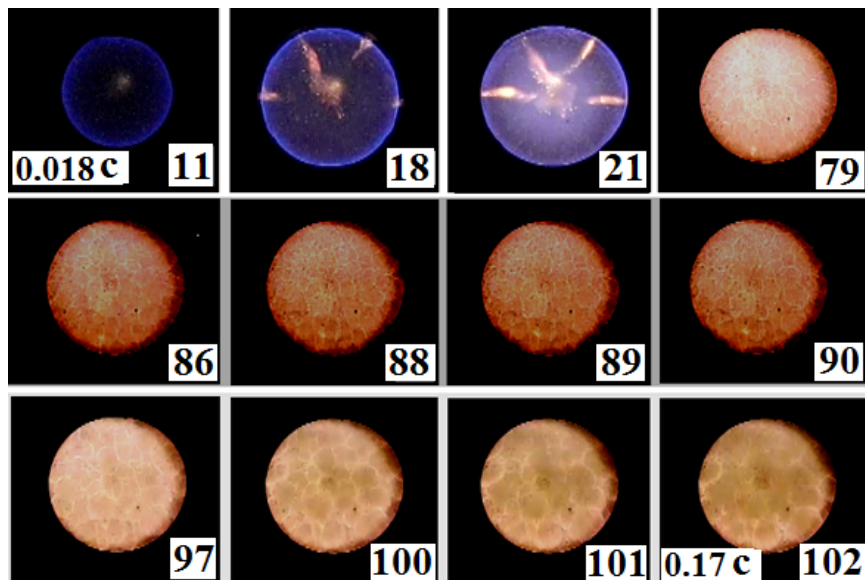


Figure 6. Filming of the process of propagation of a spherical flame front for a mixture of $80\%(\text{C}_5\text{H}_{12} + \text{O}_2)_{\text{stoich.}} + 20\% \text{Ar}$

Indeed, the FF radius grows so rapidly that instability does not develop against this background at the stage of a spherical flame, and the FF is not disturbed [12]. At the stage of propagation along the reactor, a hydrodynamically unstable flat flame arises, as predicted by the theory [2]. This instability, as can be seen in Fig. 6 and 7, is expressed in the formation of cellular structures at the flame front. The formation of cells is characteristic for a certain degree of dilution with an inert additive. In fast-burning (not diluted with an inert gas) mixtures, cells are not recorded. In flames of combustible mixtures diluted with argon, the cellular structures are located motionless in space, while the size of the cells grows slightly (Fig. 6).

With an increase in the degree of dilution of the stoichiometric mixture and the use of carbon dioxide and CCl_4 instead of argon as a diluent, the cellular structures shift in the direction of gravity, the cell size stabilizes. In other words, it can be verified that the size distribution remains practically constant until the end of combustion, while the combustible mixture burns out near the bottom of the reactor (Fig. 7).

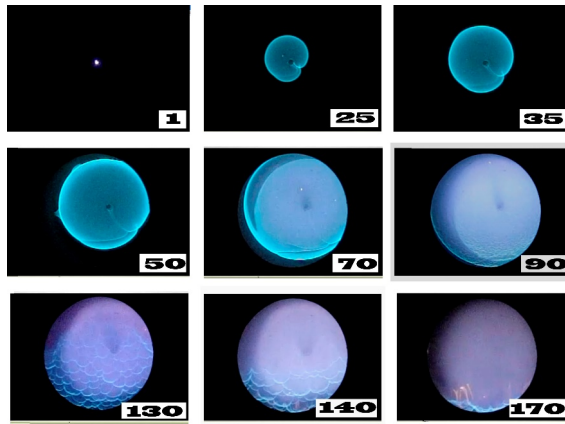


Figure 7. Result of frame-by-frame processing of filming of the process of propagation of a spherical flame front of a stoichiometric mixture of pentane with air + 10% CO₂ + 1% CCl₄

Let us carry out a qualitative examination of the propagation of a flame in a two-dimensional channel using the example of a plane problem in the "side view" projection in order to compare the results of the qualitative calculation with the experimental ones and to establish further directions for modifying the calculation. In this case, both the interaction of the FF with the end wall of the reactor and the transition of the FF of a circular shape to propagation in a flat channel upon initiation by a point source will be considered. As indicated above and as is known from the literature [16], the relationship between the main factors causing the instability of hydrodynamic and acoustic flames can be taken into account when considering the Navier-Stokes equations for a compressible medium in the acoustic approximation (which corresponds to substantially subsonic flames).

Let's make a few important notes. It is well known that theoretical calculations of combustion processes carried out on the basis of kinetic schemes containing hundreds of elementary reactions do not have predictive power. Indeed, the overwhelming majority of rate constants and their temperature coefficients are not accurate enough to make reliable conclusions based on calculations with such errors. Typically, the value of error in the experimental determination of rate constants is from 50% to two orders of magnitude, and this is in the case of experimental determination. On the other hand, the problem of the completeness of the used kinetic mechanism remains unresolved, i.e. whether any important reaction that affects the ignition and combustion parameters has been missed.

Moreover, since there are no uniqueness theorems for the solutions of the Navier-Stokes equations in a compressible reacting medium, the correspondence of the calculated profiles, for example, of intermediate reagents to the experimen-

tal, is not an argument in favor of the agreement between the calculation and experiment. There may be several sets of governing parameters describing the same profiles (until proven otherwise). In this sense, the following consideration of the Navier-Stokes equations in a reacting medium is only of a qualitative nature. It is due to the lack of evidence of the uniqueness of solutions for this type of systems of equations we do not consider a detailed kinetic mechanism, but restrict ourselves to one activated reaction or the simplest chain mechanism (see below).

Thus, a comparison of the recorded picture of the movement of the light emission front and the result of the calculation, carried out without the involvement of a detailed kinetic mechanism in the form available today, is possible only qualitatively according to the trend of change in the speed of the front, namely, the interface between the initial "fresh" and actively reacting medium, as well as the nature of this boundary - the degree of its "smoothness" and disturbances of its structure.

The Navier-Stokes equations for a compressible reacting medium in the low Mach number approximation were proposed in [16-20]. The indices t, x, y, z denote differentiation with respect to t, x, y, z .

$$\begin{aligned}
 \rho T &= P \\
 \rho_t + (\rho u)_x + (\rho v)_y + (\rho w)_z &= 0 \\
 \rho(v_t + u u_x + v u_y + w u_z) + P_x / \gamma M^2 &= 1/Fr + Sc(\nabla^2 u + 1/3 K_x) \\
 \rho(u_t + u v_x + v v_y + w v_z) + P_y / \gamma M^2 &= 1/Fr + Sc(\nabla^2 v + 1/3 K_y) \\
 \rho(w_t + u w_x + v w_y + w w_z) + P_z / \gamma M^2 &= 1/Fr + Sc(\nabla^2 w + 1/3 K_z) \quad (I) \\
 \rho [T_t + u T_x + v T_y + w T_z] - (\gamma - 1) / \gamma P_t - (\gamma - 1) M^2 [P_t + u P_x + v P_y + w P_z] &= \nabla^2 T + \beta_1 W \\
 \rho [C_t + v C_y + u C_x + w C_z] &= \nabla^2 C - \beta W \\
 W &= (1 - C) \exp(\zeta - \zeta/T),
 \end{aligned}$$

where $K = u_x^2 + v_y^2 + w_z^2$ - viscous dissipation term, σ^2 - three-dimensional Laplace operator. $P(x, y, t) = P_0(t) + \gamma M^2 p_2(x, y, t) + O(M^3)$, $P_0(t)$ - static pressure, which is calculated based on conservation laws [17], $p_2(x, y, t)$ - dynamic pressure. Here, (u, v, w) - velocity components in directions (x, y, z) respectively; ρ - density; T - temperature. The chemical reaction is represented by a one-step first-order Arrhenius reaction; P - pressure, C - concentration of the reactant, $1 - C$ - degree of conversion, ζ - dimensionless coefficient, which has the meaning E/R , where E - activation energy, R - gas constant. Dimensionless parameter is Schmidt criterion $Sc = \nu/D$, D - diffusion coefficient, ν - kinematic viscosity, γ - ratio of heat capacities at constant pressure and constant volume; β_1 characterizes the release of heat per unit of concentration C , β - kinetic coefficient proportional to the second Damköhler number [19]. Density, temperature, pressure and concentration are made dimensionless using the initial values $\rho_0 = 0.001 \text{ g/cm}^3$ [5], $T_0 = 1$, $P_0 = \rho_0 T_0$,

$\zeta_5=10.5$, $\gamma=1.4$, $\beta=0.2$, $\beta_l=0.3$, $C_p=0.3$ cal/g.degrees [5] and $C_0=0$, respectively. The Lewis number is assumed to be $Le=1$, which implies the equality $Sc = Pr$, where $Pr = \rho_0 C_p \nu / \lambda$, λ - thermal conductivity and C_p - heat capacity at constant pressure. The length and speed scales are defined as $l_d^2 = Dt_d$, and $U_d = l_d / t_d$ respectively. Then the Reynolds number, taking into account the choice of l_d and U_d has the form $Re = l_d U_d / \nu = 1 / Sc$. The Froude number $Fr = U_d^2 / g l_d$, where g - the gravitational acceleration, was taken equal to 0.07. The Mach number is defined as $M = U_d / c_0$ and is taken equal to 0.025, where c_0 - speed of sound. Obviously, if $M=0$, there are no pressure fluctuations. At $M \rightarrow 0$ the initial value of the average pressure P_0 becomes much higher than the average value of $\rho_0 U_d^2$ for pressure fluctuations around the average pressure P_0 . The velocity field as a function of the pressure gradient is determined by these pressure fluctuations around its mean value. If the standard pressure representation is used, then the usual change of variables $P = P_0 p$ leads to the appearance of the factor $1/M^2$ in the grad p term in the momentum equation [16, 17, 20].

We will consider a two-dimensional problem and exclude the z coordinate:

$$\rho T = P \tag{a}$$

$$\rho_t + (\rho v)_y + (\rho u)_x = 0 \tag{b}$$

$$\rho(u_t + v v_y + u v_x) + P_y / \gamma M^2 = 1 / Fr + Sc(\nabla^2 v + 1/3 K_y) \tag{c}$$

$$\rho(v_t + v u_y + u u_x) + P_x / \gamma M^2 = 1 / Fr + Sc(\nabla^2 u + 1/3 K_x) \tag{d}$$

$$\rho [T_t + v T_y + u T_x] - (\gamma - 1) / \gamma P_t - (\gamma - 1) M^2 [P_t + u P_x + v P_y] = \nabla^2 T + \beta_l W \tag{e} \quad (II)$$

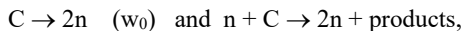
$$\rho [C_t + v C_y + u C_x] = \nabla^2 C - \beta W \tag{f}$$

$$W = (1 - C) \exp(\zeta - \zeta / T) \tag{g}$$

$$P_{tt} - 1 / M^2 \nabla^2 P = q(C_p - 1) \beta_l W_t \tag{h}$$

where $\nabla^2 = ()_{yy} + ()_{xx}$ two-dimensional Laplacian, $K = v_y + u_x$, $P_{tt} = D^2 P / Dt^2$, $D() / Dt$ - substantial derivative. In the calculations, it was assumed that the pressure values satisfy the wave equation (the last equation of system (II)), which, under the assumption of small disturbances introduced by the wave, can be obtained from the equations of continuity and conservation of momentum, taking into account internal energy sources and neglecting terms of order $1 / M^4$ [16, 17, 21, 22].

In a number of calculations, the reaction rate was set not by the Arrhenius equation, but using the simplest chain mechanism:



described by Arrhenius's law. In this case, equations (f) and (g) of system (II) were replaced by the following equations:

$$\rho [C_t + v C_y + u C_x] = \nabla^2 C - \beta n W$$

$$\rho [n_t + v n_y + u n_x] = \nabla^2 n + 2\beta n W$$

$$W = C \exp(\zeta - \zeta/T)$$

The initial condition for the concentration of the initial substance changes to $C_0 = 1, n_0 = 0$.

Since the last equation (h) of system (II), which describes wave processes in a moving inhomogeneous medium with internal heat sources, is obtained using the continuity equation and the equation of conservation of momentum ($q = l d^2 / (U d^4 \rho_0)$) – It is a parameter that arises when the system is reduced equations to dimensionless form and in the subsequent qualitative calculation set equal to one), then system (II) is redefined. In order for the number of equations to correspond to the number of unknowns, the first-order equation (b) was excluded from system (II) during further analysis. The use of equation (h) provided a significant acceleration of the calculations carried out in this section, within the framework of the software package used in this work.

This problem was solved by the finite element method using the software package (FlexPDE 6.08, A Flexible Solution System for Partial Differential equations, 1996-2008 PDE Solutions inc. [23]). The system of equations (II) was solved in an area of the form of a square. On the left boundary, the initiation condition $T = 10$ (initial dimensionless temperature $T = 1$) was set by a step (Fig. 8). At the boundaries of the region, $dC/dx = 0, dC/dy = 0, n=0$ and the convective heat transfer condition $dT/dt = (T - T_0), u=0, v=0, d\rho/dx = 0, d\rho/dy = 0$. The results of a qualitative calculation of the interaction of a flame front in a flat channel with an end wall in order to establish the effect of gravity on the evolution of cellular structures and compare the obtained qualitative results with experiment are shown in Fig. 8. In this figure, the time in seconds is given under each "frame", the top row of the image refers to the absence of gravity. In each "frame" of the bottom row, gravity is directed from top to bottom. The bottom row shows a scale of dimensionless temperatures. In this case, initiation by a section and not point initiation of the opposite end is specified for reducing the calculation time.

After initiation, a stationary combustion wave propagates from left to right that is shown in Fig. 8. When the combustion wave approaches the right end, a cellular structure appears, which at $g = 0$ moves uniformly from left to right. The size of the cells increases slightly over time. In the presence of gravity (the bottom row of images in Fig. 8), it can be seen that FF first approaches the "upper" part of the right boundary of the computational domain and only then to its "lower" part. Accordingly, the cellular structure moves "from top to bottom," in qualitative agreement with the experiment (Fig. 7).

It can also be concluded from Fig. 8 (top row of images) that if the flame velocity is high enough (an increase in Re), then the gravity does not have time to

influence the flame propagation (i.e., formally, $g \approx 0$ takes place), and an immobile cellular structure with a leanly growing cell size should be observed. This is also in qualitative agreement with the experiment (Fig. 6).

When analyzing the combustion kinetics set by the chain mechanism, the calculation results are the same as those shown in Fig. 8 for $\zeta = 7$, i.e. in accordance with [5], the effective activation energy of the chain process is lower than for the molecular reaction described by the Arrhenius law. Thus, the patterns of evolution of the experimentally observed cellular structure obviously depend on the form of the heat release function, which is determined by the kinetic mechanism of the reaction. It is obvious that in order to proceed to the description of the quantitative regularities of the formation of regular structures on the FF, it is necessary to analyze the three-dimensional model. At the same time, the results of two-dimensional modeling are in qualitative agreement with the above-noted interrelation of the main factors responsible for the instability of hydrodynamic and acoustic flames. Since the interpretation of the cellular structure observed in our experiments in the interaction of the FF with the wall requires taking into account both hydrodynamic and acoustic parameters of burning gas.

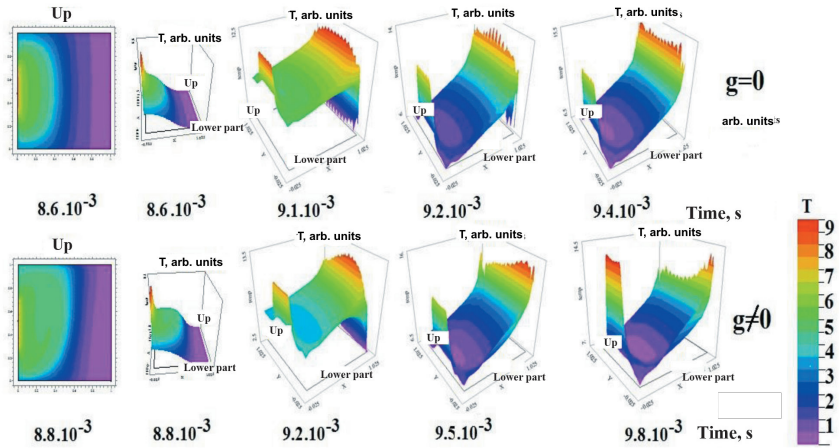


Figure 8. Calculated dependences of the two-dimensional thermal field on time during the propagation of the flame front to the channel wall

The data obtained, in agreement with the information presented in the Introduction, indicate the gas-dynamic nature of the cellular structure of the phase transition observed in our experiments at the end of combustion. Thus, the cellular combustion mode is caused by the gas-dynamic instability inherent in plane flames [2]. It should be noted that the dependence of the FF structure and the role of this structure in the evolution of the flame front in a reactive gaseous medium

on the initial conditions, in particular on the size of the reaction volume, have not yet been sufficiently investigated and require further study under conditions of large volumes.

We point out that the above numerical simulation only allowed to establish the hydrodynamic nature of the flame instability. However, it does not allow us to reveal the features of combustion in each individual cell, in particular, due to the conventionality of the reaction kinetics considered in the simulation.

This issue was solved experimentally using 4D spectroscopy, which allows recording optical radiation spectra from a given point in space. It allowed to obtain a spectrum emitted both from the boundary between the cells and from the inner region of the flame cell under our conditions. Hyperspectral cubes of the investigated combustible mixtures: 40% hydrogen + air + 1% CCl_4 , stoichiometric mixture of pentane with air + 10% CO_2 , stoichiometric mixture of pentane with air + 10% CO_2 + 1% CCl_4 are shown in Fig. 9a-c. In Fig. 9a-c, the x-axis corresponds to the red strip in Fig. 1, and the y-axis corresponds to the dependence of the combustion process on time. Each line y corresponds to one frame of information accumulation on the photodetector matrix of the hyperspectrometer (300 frames/s).

The optical combustion spectra of a mixture 40% H_2 + air + 1% CCl_4 , recorded along a vertical strip along the diameter of the optical window (strip 3, Fig. 1), are shown in Fig. 10. It should be noted that the hydrogen flame at low pressures is practically invisible, since its radiation is mainly due to the radiation of hydroxyl radicals $\text{OH } A^2\Sigma - X^2\Pi$ in the ultraviolet region at 306 nm [24]. Attention is drawn to the features of the flame spectrum in the visible region, namely, the system of radiative bands in the region of 570 - 650 nm. They “visualize” the hydrogen flame at elevated pressures along with the lines of sodium (581 nm) and potassium (755 nm) atoms inherent in all hot flames [24] and in this case emitted from the region filled with combustion products.

It can be seen from Fig. 10 that at the selected time only one FF is recorded along the x axis, located between coordinates 234 and 140, while the intensities of all spectral lines from the spectrum with coordinate 234 to the spectrum with coordinate 1 change symbatically. There is no situation when the intensity of the bands in one region of the spectrum in space increases, and in the other region of the spectrum decreases. This is due to the fact that the observed spectral lines belong only to the reaction products or appear in the zone of the reaction products (Na, K). They indicates the stability of the hydrogen combustion flame front (the presence of only one flame front), which can also be seen from the high-speed filming frames given in Fig. 4.

Bands in the region of 600 nm were also observed in a hydrogen flame in [25]. Below is Table 4 from [25], in which the assignment of the bands in Fig. 12 to water vapor, which is a product of the hydrogen oxidation reaction is made.

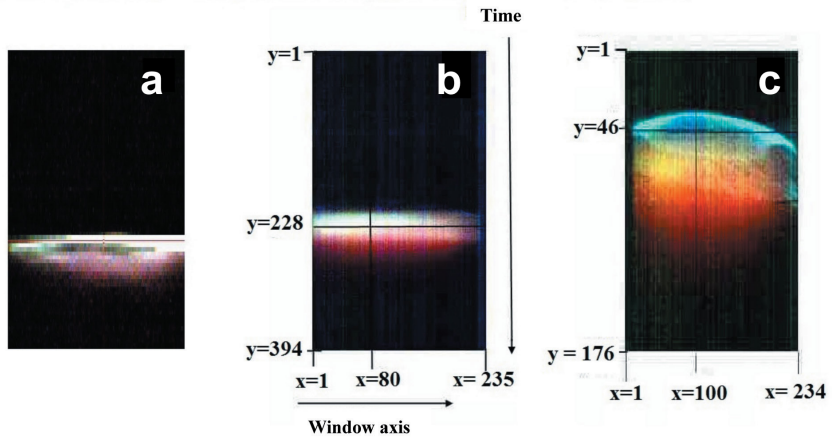


Figure 9. Hyperspectral cubes:

a) - combustion of 40% hydrogen in air, b) - combustion of a stoichiometric mixture of n-pentane with air and 10% CO₂, c) - combustion of a stoichiometric mixture of n-pentane with air, 10% CO₂ and 1% CCl₄

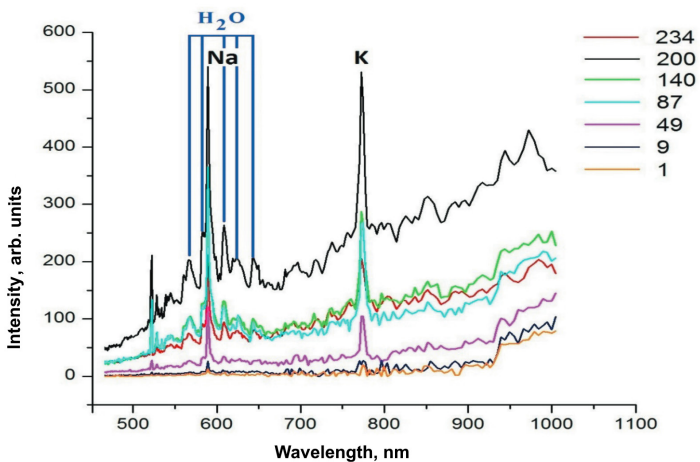


Figure 10. Combustion spectrum of a mixture of 40% hydrogen + air + 1% CCl₄, pressure of 1 atm along the red strip $y = 15$ (Fig. 1a)

Table 4.

Comparison of the radiative bands of a hydrogen flame with bands of water

I			II			III	
Quantum by R. Mecke		Quantum numbers	Radiant flame band		Difference	Water vapor absorption band	
No.	ν	$V\sigma, V\pi, V\delta$	No.	ν, cm^{-1}	$\Delta\nu, \text{cm}^{-1}$	No.	ν, cm^{-1}
1	17495.44	3, 2, 0	2	17492	+3		–
2	16898.44	1, 4, 0	7	16878	+21	2	16903
3	16821.62	1, 3, 2	8	16807	+15	3	16821
4	15832.47	3, 1, 1	15	15815	+17		–
5	15347.90	1, 3, 1	20	15340	+8	4	15340

The combustion spectrum of a stoichiometric mixture of pentane with air + 10% CO₂ is shown in Fig. 11. This spectrum contains intense lines of atoms of alkali metals Na, K and bands of water vapor [26, 27]. All these particles appear in the zone of the reaction products.

The absence of emission bands of intermediate products of the oxidation of hydrocarbons (C₂, CH) is due to the fact that the intensity of the “hot” lines of atoms is high in comparison with the intensity of the emission bands of intermediate particles C₂ and CH. A decrease in the reaction rate by introducing an active chemical additive (CCl₄ in this work) should allow registration of the emission of C₂ and CH particles, which will be demonstrated below.

When analyzing the hyperspectral cube for the combustion spectrum of this combustible mixture (Fig. 9b), it was also found that only one FF is recorded at the selected time. The intensities of all spectral lines (Fig. 11) change in the same symbatic manner as in the case of a flame combustion of hydrogen, since all of them, as indicated above, belong to the reaction products.

The result obtained indicates the stability of the flame front of a stoichiometric mixture of pentane with air + 10% CO₂, which can also be seen from the high-speed filming frames shown in Fig. 5.

It was shown above that the combustion of stoichiometric mixtures of pentane with air upon dilution with argon and CO₂ becomes unstable and becomes cellular in the transition to combustion in a cylindrical tube.

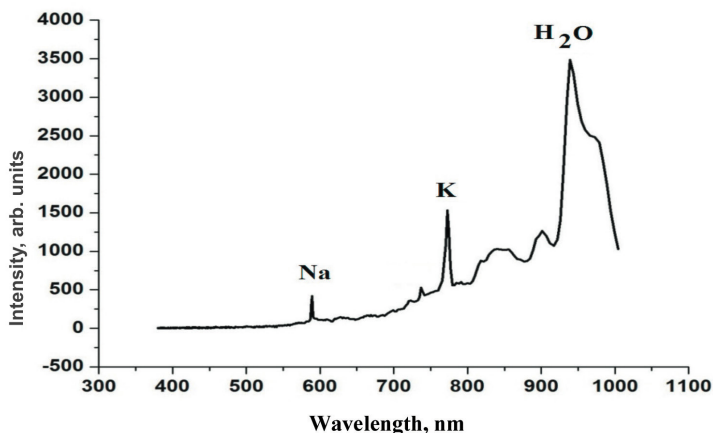


Figure 11. Combustion spectrum of a mixture of pentane with air + 10% CO₂, pressure 1 atm (point $x = 105$, $y = 228$)

Let us consider the experimental results on the study of this cellular flame, caused, as established above, by gas-dynamic instability, by 4D spectroscopy.

A typical frame characterizing the cellular combustion of a stoichiometric mixture of pentane with air with additives of 10% CO₂ and 1% CCl₄ at a total pressure of 1 atm is shown in Fig. 12a. A hyperspectral cube for this image along the vertical axis in the blue region C is demonstrated in Fig. 12b. In Fig. 12c a fragment of this cube is shown, on which the point of spectrum analysis is indicated. In Fig. 12b and 12c clearly visible bands are seen, associated with the boundaries of the cells, formed as a result of the movement in time of these boundaries.

In Fig. 13, the spectrum of the flame recorded at the point indicated in Fig. 12 on the border of one of the cells, is demonstrated. Since the mixture contains the inhibiting additive CCl₄, the combustion intensity is lower than in the absence of the additive. The release of heat is less, therefore, “hot” lines of Na and K atoms are not observed in the emission spectrum.

This spectrum is consistent with the literature data [5] and contains CH (A¹ Δ-X² Π) bands in the 431 nm region, C₂ (A³Pg -X³Pu) (1-0, 0-0, 0-1 transitions) in the 470 - 570 nm [28] and emission bands of water vapor (for example, (1, 2, 0), (3, 0, 0) [27]).

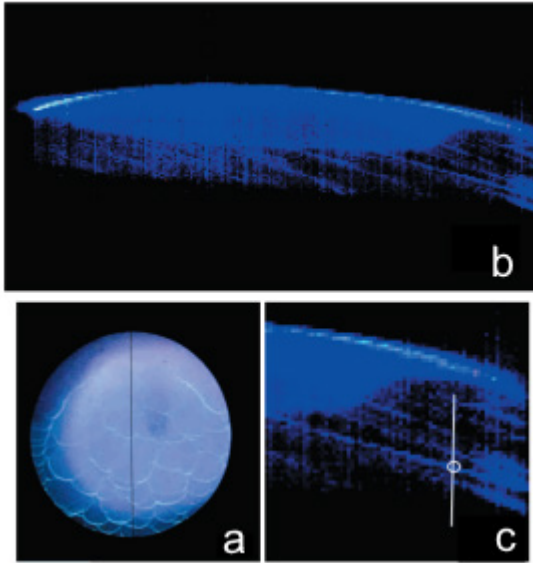


Figure 12.

- a) Video frame of cellular combustion of a stoichiometric mixture of pentane with air + 10% CO₂ + 1% CCl₄ pressure 1 atm,
b) Hyperspectral image (hypercube) in pseudo color B c) highlighted fragment of Fig. 12b

It should be noted that the CH and C₂ bands refer to the contribution of the zone of intense chemical transformation (FF zone) [5] to the total spectrum, and the emission bands of water vapor to the emission region of the combustion reaction products. This means that from the ratio of the intensities of the C₂ and H₂O bands in the spectrum, it is possible to make a qualitative conclusion about which combustion zone the spectrum characterizes i.e. the zone of the immediate flame front or the zone of reaction products. Namely, if the relative intensity of the C₂ bands significantly exceeds the relative intensity of the water bands in the flame, then the radiation spectrum corresponds to the combustion zone. If the ratio of intensities is the opposite, then the spectrum refers to the reaction products. Drawing on the coordinate of the emission spectra of a stoichiometric mixture of pentane with air, diluted with 10% CO₂ is shown in Fig. 14 with the presence of 1% CCl₄ along the window axis (along the vertical line in Fig. 12c) from top to bottom.

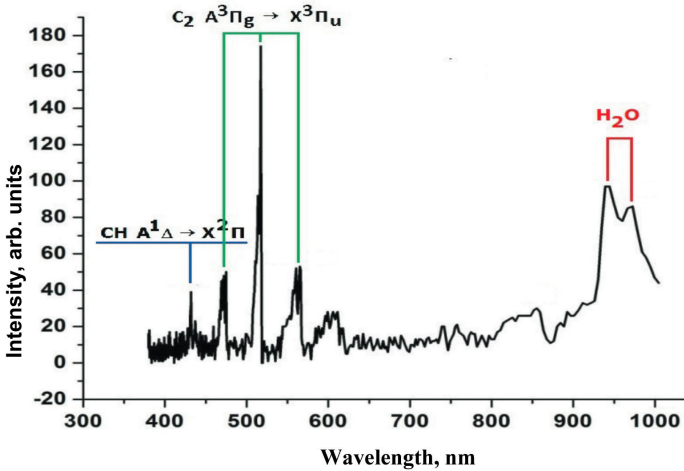


Figure 13. The spectrum of combustion of the mixture of pentane with air + 10% CO_2 + 1% CCl_4 pressure 1 atm (point $x = 15$, $y = 46$)

As is seen in Fig. 14 along the window axis the intensities of the spectral bands do not change symbatically. While the relative intensity of the C_2 bands has a maximum at $x = 20$ and $x = 180$ (where x is the coordinate shown in Fig. 9), the intensity of the H_2O bands at those the same values of x has a minimum.

This means, first, that combustion in space is heterogeneous, otherwise the intensities of the spectral lines would change smoothly in the direction of decreasing or increasing. In other words, using 4D spectroscopy, it is possible to register combustion cells, as was done by high-speed filming (Figs. 7, 12a). Second, the fact that the intensity of the C_2 bands has a maximum at the same values ($x = 20$, $x = 180$ Fig. 14), at which the intensity of the H_2O bands is minimal. It means that at these values of x , radiation occurs mainly from the flame front zone. At values of x at which the ratio of the intensities of the C_2 and H_2O bands is opposite, the radiation comes from the zone of the reaction products.

Consequently, it was possible to state that each combustion cell observed by using the 4D spectroscopy method in Fig. 12a, is essentially a separate "chemical reactor", in each of which the process of complete chemical conversion is carried out.

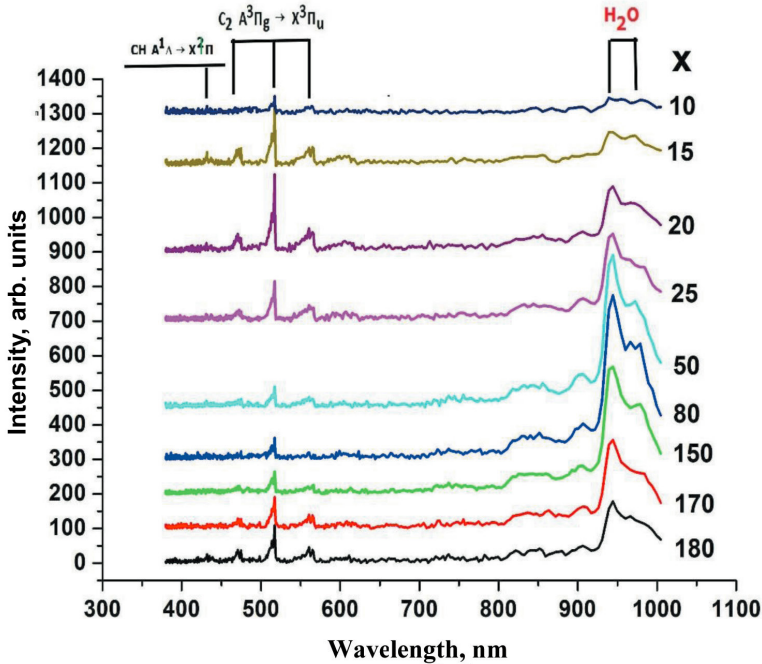


Figure 14. Combustion spectra of the mixture of pentane with air + 10% CO₂ + 1% CCl₄ pressure 1 atm along the axis of the window (along the vertical line in Fig. 12c) $y = 46$ ($t = 9$ ms)

Let us recall that it was experimentally shown in [10] for the first time that in the presence of instabilities of a thermodiffusion nature (lean mixtures of hydrogen with oxygen) under zero gravity, there is a mode of formation of separate isolated stationary combustion cells, i.e. separate "chemical reactors" in a combustible environment. In this work, the features of combustion in flame cells caused by hydrodynamic instability are experimentally established for the first time by using the methods of 4D optical spectroscopy and color high-speed filming.

In addition, as a result of direct experimental test of Landau hypothesis of the hydrodynamic instability of a plane flame front [11], the relationship was observed between the main factors responsible for the instability of hydrodynamic and acoustic flames [9]. This means that in the cell of the combustion front, caused by an instability of any nature (thermodiffusion, hydrodynamic, thermoacoustic), a complete cycle of transformations is carried out, which is characteristic of a given combustion process.

Conclusions for Chapter 4

It is shown by the example of combustion of stoichiometric mixtures of n-pentane (C_5H_{12}) with air, diluted with carbon dioxide (CO_2) and argon (Ar), at total atmospheric pressure that when the FF propagation goes from spherical to propagation in a tube, the phenomena caused by instability of the flat flame appear in the reactor. It is shown that, upon deceleration of the FF near the end wall of the reactor, a smooth FF acquires a cellular structure. It is demonstrated that qualitative modeling of the results is possible when analyzing the Navier-Stokes equations for a compressible medium in the approximation of a small Mach number. Using the methods of 4D optical spectroscopy and color high-speed filming, the features of combustion in flame cells caused by hydrodynamic instability have been experimentally established for the first time. It is shown that any combustion cell is essentially a separate “chemical reactor”, in each of which the process of complete chemical transformation is carried out. The results obtained on the spectral study and visualization of the propagation of fronts of unstable flames are important in solving the issues of explosion safety for volumes of complex geometry.

References for Chapter 4

1. *Nonsteady flame propagation* (ed. by George Markstein). Perg. Press. Oxford. London. 1964. 370 p.
2. Landau L. *On the theory of slow combustion*. *Acta Phys.-Chim. URSS*. 1944. Vol. 19. pp. 77-85.
3. Williams F. A., Grcar J. F. *A hypothetical burning-velocity formula for very lean hydrogen-air mixtures*. *Proc. of the Combustion Institute*. 2009. Vol. 32. №1. pp. 1351-1360.
4. Zeldovich Ya. B. *Selected Works. Vol. 1: Chemical Physics and Hydrodynamics* (Princeton Legacy Library, 140). 1992. 490 p.
5. Lewis B., Von Elbe G. *Combustion, Flames and Explosions of Gases*. 3rd Edition. New York. London: Acad. Press. 1987. 566 p.
6. Sivashinsky G. I. *Nonlinear analysis of hydrodynamic instability in laminar flames-I. Derivation of basic equations*. *Acta Astronaut*. 1977. Vol. 4. No. 11-12. pp. 1177-1206.
7. Clavin P., Williams F. A. *Effects of molecular diffusion and of thermal expansion on the structure and dynamics of premixed flames in turbulent flows of large scale and low intensity*. *J. Fluid Mech*. 1982. Vol. 116. pp. 251-282.
8. Pelcé P., Clavin P. *Influence of hydrodynamics and diffusion upon the stability limits of laminar premixed flame*. *J. Fluid Mech*. 1982. Vol. 124. pp. 219-237.

9. van Kampen J. F. *Acoustic pressure oscillations induced by confined turbulent premixed natural gas flames*. PhD thesis. University of Twente. Enschede. The Netherlands, March 2006. ISBN 90-365-2277-3. Printed by Febodruk BV. Enschede. The Netherlands. 274 p.

10. Ronney P. D. *Premixed-Gas Flames in: Microgravity Combustion: Fires in Free Fall* (H. Ross, Ed.). Academic Press. London, U. K. 2001. pp. 35-82.

11. Clanet C., Searby G. *First experimental study of the Darrieus- Landau instability*. *Phys. Rev. Lett.* 1998. Vol. 27. pp. 3867-3870.

12. Zeldovich Ya. B., Barenblatt G. I., Makhviladze G. M., Librovich V. B., Makhviladze D. M. *The Mathematical Theory of Combustion and Explosion*. Consultants Bureau. New York. 1985. DOI: 10.1007/978-1-4613-2349-5

13. Kalinin A. P., Orlov A. G., Rodionov A. I., Troshin K. Ya. *Demonstratsiya vozmozhnosti izucheniya processov goreniya ivzryva s pomoshch'yu distantsionnogo giperspektral'nogo zondirovaniya (Demonstration of the possibilities to study combustion and explosion processes on the base of hyperspectral remote sensing)*. *Physical-Chemical Kinetics in Gas Dynamics*. 2009. Vol. 8. <http://chemphys.edu.ru/issues/2009-8/articles/202/> (in Russian)

14. Vinogradov A. N., Egorov V. V., Kalinin A. P., Melnikova E. M., Rodionov A. I., Rodionov I. D. *Lineyka giperspektral'nykh sensorov opticheskogo diapazona (Line of hyperspectral sensors of the optical range)*. Preprint of Space Research Institute of RAS. Pr-2176. 2015. 16 p. (in Russian)

15. Egorov V. V., Kalinin A. P., Rodionov I. D., Rodionova I. P., Orlov A. G. *Giperspektrometr – kak element sistemy intellektual'nogo tekhnicheskogo zreniya (Hyperspectrometer - as an element of an intelligent technical vision system)*. *Sensors & systems*. 2007. No. 8. pp. 33-35. (in Russian)

16. Alasard T. *Low Mach number limit of the full Navier-Stokes equations*, *Archive for Rational Mechanics and Analysis*. 2006. Vol. 180. No. 1. pp. 73-97.

17. Nicoud F. *Conservative High-Order Finite-Difference Schemes for Low-Mach Number Flows*. *Journal of Computational Physics*. 2000. Vol. 158. No. 1. pp. 71-96.

18. Williams, F. A. *Combustion Theory*. 2nd Ed. The Benjamin/Cummings Pub. Co., Menlo Park, Cal. 1985. 450 p.

19. Akkerman V., Bychkov V., Petchenko A., Eriksson L.-E. *Flame oscillations in tubes with nonslip at the walls*. *Combustion and Flame*. 2006. Vol. 145. No. 4. pp. 675- 687. DOI:10.1016/j.combustflame.2006.01.013

20. Majda A. *Compressible fluid flow and systems of conservation laws in several space variables*. *Applied Mathematical Sciences*. Springer-Verlag, New York. 1984. Vol. 53. 172 p.

21. Abugov D. I., Bobylev V. M. *Teoriya i raschet raketnykh dvigateley tverdogo topliva (Theory and calculation of solid propellant rocket engines)*. M: Mashinostroyeniye. 1987. 271 p. (in Russian)

22. Clavin P. *Premixed combustion and gasdynamics. Ann. Rev. Fluid Mech.* 1994. Vol. 26. pp. 321-352.

23. Backstrom G. *Simple Fields of Physics by Finite Element Analysis (Paperback).* GB Publishing. 2005. 324 p.

24. Pierse R., Gaydon A. *The identification of molecular spectra.* N.-Y., London, Acad. Press. 1941. 240 p.

25. Icitaga T. *Emission spectrum of the oxy-hydrogen flame and its reaction mechanism. (1) Formation of the Activated Water Molecule in Higher Vibrational States. The Review of Physical Chemistry of Japan.* 1939. Vol. 13f. No. 2. pp. 96- 107.

26. Rothman L. S, Gordon L. E., Bakikov Y. et al. *The HITRAN 2012 molecular spectroscopic database. Journal of Quantitative Spectroscopy and Radiative Transfer.* 2013. 130. pp. 4–50.

27. Coheur P.-F., Bernath P. F., Carleer M., Colin R., Polyansky O. L., Zobov N. F., Shirin S. V., Barber R. J., Tennyson J. *A 3000 K laboratory emission spectrum of water. The Journal of Chemical Physics.* 2005. 122(7): 074307. DOI:10.1063/1.1847571

28. Herzberg G. *Molecular Spectra and Molecular Structure. Vol. 1. Spectra of Diatomic Molecules.* 2nd ed. Van Nostrand. New York. 1950.

CHAPTER 5. The use of high-speed optical multidimensional technique to determine the characteristics of ignition and combustion of 40% H₂ - air mix in the presence of platinum metal

A cellular mode of combustion of a 40% mixture of hydrogen with air in the presence of platinum wire and foil in the range of 270-350 °C at atmospheric pressure was found. Combustion cells caused by catalytic instability have been experimentally detected for the first time by using the methods of routine and 4D optical spectroscopy, which allows registering the intensity of the optical spectrum simultaneously depending on the wavelength. It was found that the cellular mode is determined by the catalytic combustion of hydrogen on Pt containing particles formed during the decomposition of unstable platinum oxide in the gas phase. It is shown that the temperature dependence of the delays of hydrogen ignition on platinum wire and foil in both stationary and rotating gases corresponds to an activation energy of 19 ± 3 kcal/mol, which is close to the activation energy of branching of the reaction chains of hydrogen oxidation.

Keywords: *hydrogen oxidation, platinum wire, foil, ignition delay, catalytic instability, platinum oxide*

The development of the technology of catalytically stabilized (CS) combustion requires the development of catalysts with increased activity (the temperature of reaching 50% conversion should be less than 450 °C) and thermal stability. This requires an understanding of the nature of catalytic surface processes, knowledge of the detailed low-temperature homogeneous kinetic mechanism and its relationship with the mechanism of heterogeneous chemical transformations. The homogeneous ignition in a catalytic reactor threatens the integrity of the catalyst and the reactor (and can cause their destruction), therefore the possibility of preventing such an event is of primary interest for the design of the CS reactor. Ignition in the gas phase is determined by the interrelation of heterogeneous and homogeneous factors (catalytic fuel consumption, adsorption / desorption reactions involving radicals). Therefore, reliable control of homogeneous ignition requires knowledge of the combustion mechanism in the presence of a catalyst. Turbines, in which natural gas is the main fuel, but natural gas combustion is stimulated by hydrogen in the presence of a CS catalyst are of particular interest [1]. The addition of small amounts of H₂ to natural gas increases the efficiency of the catalyst, stabilizes combustion and prevents flame pulsation. Therefore, knowledge of the features of catalytic combustion of hydrogen is an important step for understanding the stimulating effect of hydrogen in the combustion of hydrocarbon fuels [1-6].

In [3], relatively long ignition delays were found in a 40% H₂ - air mixture over a Pt foil at a total pressure of 1 atm. It was found that the ignition of H₂-air mixtures at atmospheric pressure begins with the appearance of a primary combustion

center at the most chemically active surface area, which initiates the propagation of the flame in the reactor. In addition, as shown in [7], the introduction of a platinum wire into the reactor eliminates the phenomenon of a negative temperature coefficient (the nature of which is still unclear) during combustion of a stoichiometric mixture of n-pentane with air, while platinum wire has no effect on the delay time of the thermal ignition of the mixture at lower temperatures.

It follows from the above that in the understanding of combustion processes over catalytic surfaces at the present time there are quite a lot of “white spots”.

This Chapter is devoted to the detection and determining of the reasons for the instability of the spatial propagation of a mixture of 40% H₂ - air in the presence of platinum foil or wire using high-speed color filming, routine optical and 4D spectroscopy. It discusses also the establishment of the temperature dependence of the ignition delay times of this mixture in a heated reactor at 1 atm. in a static bypass device.

Experimental

Two installations were used for the experiments. In the first setup (setup 1), hyperspectrometers and a high-speed color camera were used to register the light emission. The presence of a hyperspectrometer made it possible to carry out 4D measurements (recall that 1-time, 2-wavelength, 3-spectrum intensity at a given wavelength, 4-coordinate of the emitting fragment of the light source are recorded). This setup was used to carry out experiments to analyze the optical spectra of cellular combustion of hydrogen over a platinum surface.

An STE-1 spectrometer with crossed dispersion was used in the second setup (setup 2) for the traditional registration of radiation, followed by recording the spectrum with a SONY DCR-SR200E video camera, sensitive in the wavelength range of 420–900 nm. It was processed then using the Hesperus 3.0 program. This setup was used to carry out experiments to find out the nature of the 552 nm emission band, which is often recorded in combustion processes.

Installation 1 (Figs. 1, 2) [8-11] consisted of a heated reactor 1, an electromagnetic valve 2, a buffer storage capacity 3, a cylinder with a gas mixture 4, a hyperspectrometer 5, a digital video camera 6, a rotating mirror 7, internal asbestos insulation 8, heater 9, external asbestos insulation 10, optical window 11, pressure sensor 12, ADC converter and computer for receiving and accumulating data 13, millivoltmeter for taking readings of thermocouple 14, aluminum ring to prevent gas circulation 15, spark ignition circuit 16. The strip in red along which the 4D spectral survey is shown in Fig. 2b. The width of this strip is about 1 mm. The blue circle marks the node for tangential gas injection into the reactor. The heated reactor 25 cm long and 12 cm in diameter was made of stainless steel and equipped with a tangential gas inlet (marked with a blue circle in Fig. 2a, b), collapsible covers, and an optical quartz window. An aluminum ring with an outer

diameter of 11.2 cm and an inner diameter of 11 cm was introduced into the reactor perpendicular to the gas flow in experiments where it was required to avoid gas circulation due to the presence of a tangential inlet (Fig. 2).

The temperature measurement accuracy was 0.3 K. An electromagnetic valve was used to open and close the gas pipelines. The reactor evacuated and heated to the required temperature was filled through the valve with a gas mixture from the high-pressure buffer storage capacity to the required pressure. Due to the sharp pressure drop in the buffer storage capacity and the reactor, a gas vortex arises after the solenoid valve is triggered in the reactor, leading to a reduction in the time required to establish a uniform temperature distribution [8]. As already mentioned, to prevent gas circulation, an aluminum ring was introduced into the reactor perpendicular to the gas flow.

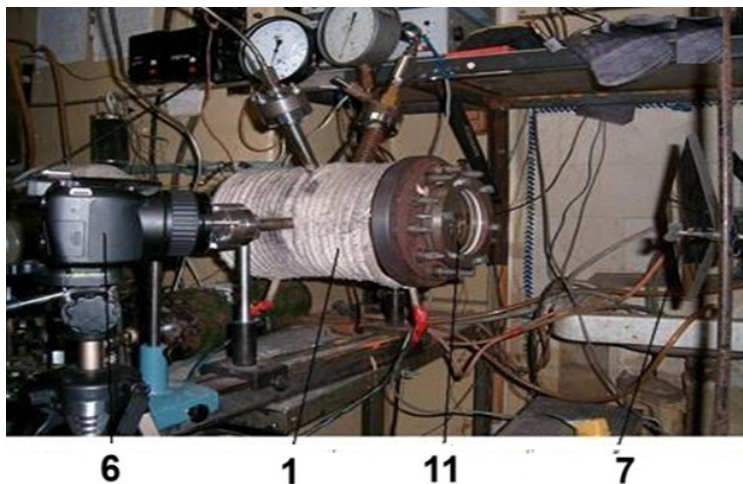


Figure 1. Installation 1, photograph of the experimental installation

It should be noted that direct measurements of the dynamics of temperature changes in the center of the reactor using thin thermocouples were performed under similar conditions in [8]. In this work, it was experimentally shown that the heating time of the gas mixture did not exceed 0.3 s. The formula, which takes into account only the convective heating of the gas mixture, gives a heating time of the order of several tens of seconds [9].

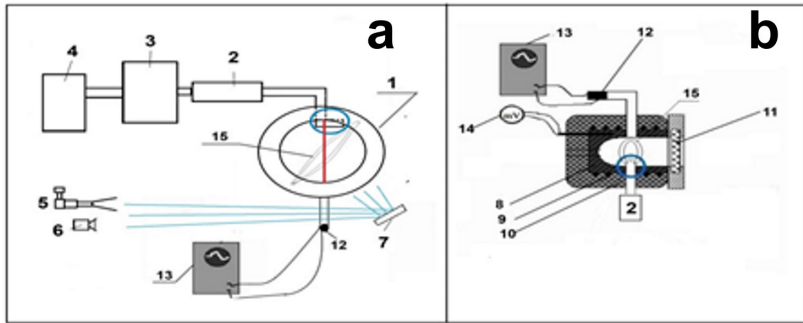


Figure 2. Installation 1,

a) - diagram of the experimental installation; b) - diagram of the reactor

In the present work, the pressure during admission and combustion was recorded using a "Karat-DI" tensoresistive sensor, the signal from which was fed through an ADC to a computer. At the moment of opening the solenoid valve, a light-emitting diode was switched on. Its radiation was recorded by a movie camera. This moment was taken as the origin of the ignition delay period, which made it possible, independently of pressure measurements, to determine its duration from a sequence of frames for each individual ignition. The flame velocities were determined from the change in the visible radius of the spherical flame, from which the visible velocity was calculated. The magnitude of the degree of expansion of the combustion products ε_T was determined, as in § 1 of Chapter 3, by the value of the maximum pressure developed during the combustion of the mixture P_b [6]:

$$P_b / P_0 = 1 + \gamma(\varepsilon_T - 1)$$

The magnitude of the normal propagation velocity U_n was determined from the relation $U_n = V_v / \varepsilon_T$ [6].

A Pt foil 12×6 cm² in size, with thickness 0.3 cm or a Pt wire 15 cm long, and 0.3 cm thick was placed in the reactor of setup 1. Before each experiment, the reactor was evacuated to 10^{-1} mm Hg. The pressure in the reactor was recorded with an exemplary vacuum gauge, and in the buffer storage capacity with an exemplary pressure gauge. Gases (hydrogen, oxygen, methane) were reagent grade and Pt purity was 99.99%.

The combustion process was recorded with an STE-1 spectrometer equipped with a SONY DCR_SR200E color video camera, or with a 4D spectrometer (hyperspectrometer) through an optical window in one of the removable covers (Fig. 1). Experiments on high-speed filming were carried out with gas mixtures of 40% H₂ + 60% air in the range 270 - 350 °C without gas circulation. In this work, both video recording of combustion was carried out with a color high-speed camera

Casio Exilim F1 Pro (frame rate - 60 - 1200 s⁻¹) through an optical quartz window (the resulting video file was recorded in the computer memory and then processed frame-by-frame) and registration with a hyperspectrometer combustion process (Fig. 2a). Then the obtained data were compared. The measurements were performed using VID-IK3 hyperspectrometers [14, 15] and its modified version (the photodetector array was rotated in it, and due to this, it became possible to control the angle of view and, accordingly, the frame rate). The appearance of both devices mounted on a rotary device is shown in Fig. 3, and the construction (the same for both devices) is presented in Chapter 2.

The optical layout of the hyperspectrometer and the results obtained are discussed in Chapter 2. The VID-IK3 hyperspectrometer has a better spectral resolution, and the modified VID-IK3 hyperspectrometer has a better spatial and temporal resolution. The use of two devices at once made it possible to reveal new features of the hydrogen combustion process over the platinum surface.

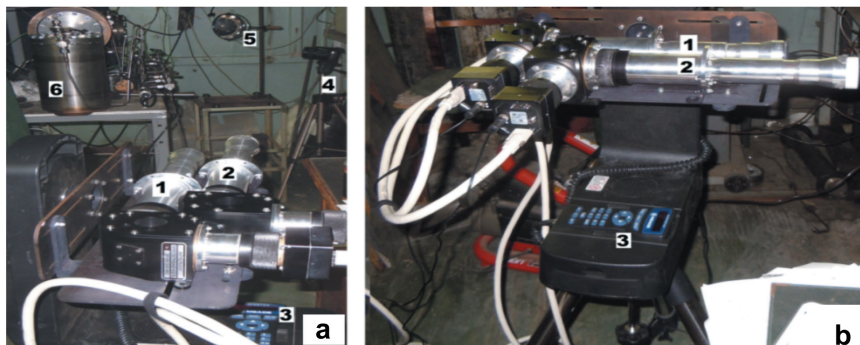


Figure 3. Location of hyperspectrometers for studying flames:

- a) - VID-IK3 hyperspectrometer, 2 - VID-IK3 hyperspectrometer (modified), 3 - rotary device, 4 - Casio Exilim F1 Pro video camera on a tripod, 5 - rotary mirror with an image of the optical window of the reactor, 6 - bypass volume; b) - a block of hyperspectrometers on a rotating device

For comparison of hyperspectrometers, we present RGB hyperspectral images recorded by these devices during the combustion of a mixture of 40% H₂ - air (T₀ = 320 °C, P₀ = 1 atm, initiated by a Pt wire (Fig. 4).

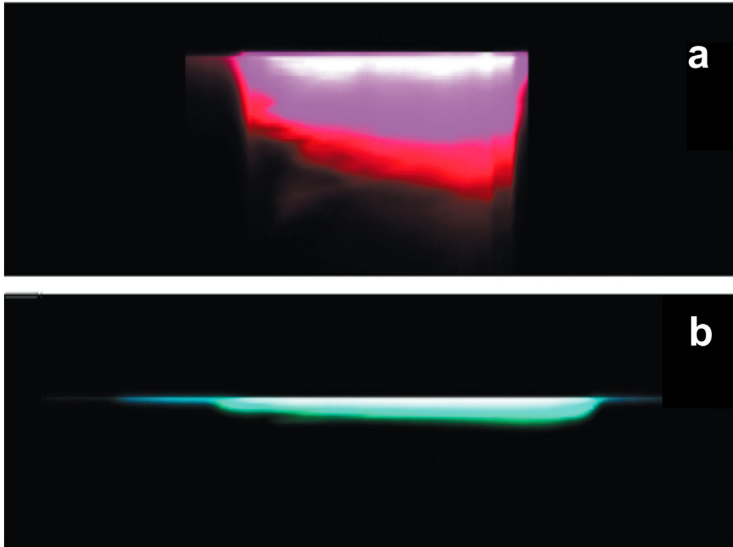


Figure 4. Comparison of RGB hyperspectral images obtained by different hyperspectrometers:

a) - modified VID-IK3; b) - VID-IK3 hyperspectrometer

To demonstrate the capabilities of the VID-IK3 hyperspectrometer, we present the dependences of the intensity of the combustion spectra of a 40% H_2 - air mixture initiated by a Pt wire on the wavelength for different points (Fig. 5) on the position on the registration strip (red strip in Fig. 2a) and on time (Fig. 6).

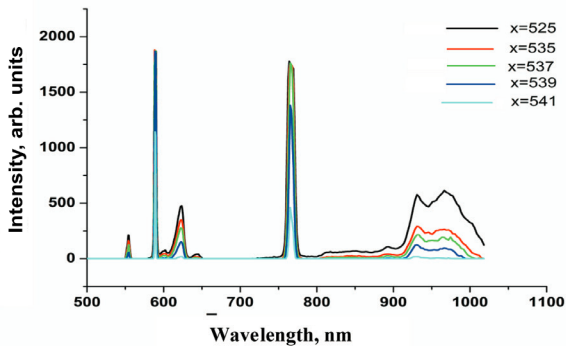


Figure 5. Dependence of the emission spectra of combustion of a 40% H_2 - air mixture, initiated by a Pt wire, on the position on the registration strip. The initial temperature is $T_0 = 320$ °C, $P_0 = 1$ atm

As indicated above, since the time dependence for the combustion processes under study is quite smooth, and the spectral resolution of the VID-IK3 hyperspectrometer is two times better than that of the modified VID-IK3 hyperspectrometer. Then experiments on the study of the combustion of a mixture of 40% H₂ - air, 320 °C, 1 atm initiated by Pt was measured with a VID-IK3 hyperspectrometer. To establish some spatial features on the hypercube, a modified VID-IK3 hyperspectrometer was used.

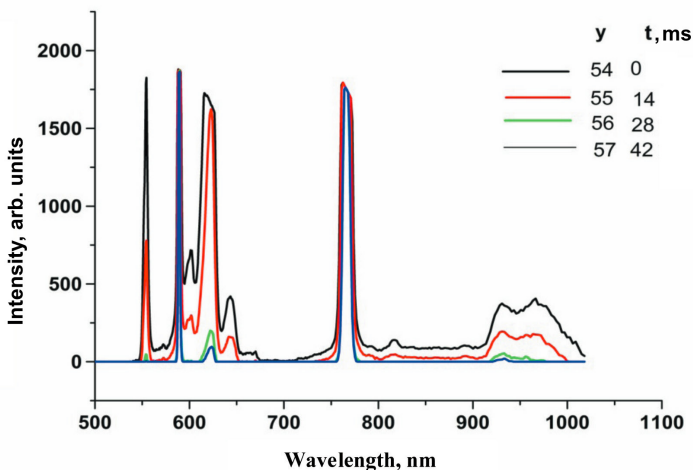


Figure 6. Time dependence of the combustion spectra of a 40% H₂ - air mixture initiated by a Pt wire. $T_0 = 320$ °C, $P_0 = 1$ atm

To diagnose dusty structures, particles emitted by a platinum wire when it was heated in atmospheric air were illuminated with a flat laser beam (“laser knife”), the shifting of which was no more than 200 μm.

For visualization of solid particles, a semiconductor laser $\lambda = 532$ nm was used. The diagram and photographs of setup 2 are shown in Fig. 7. Here: 1 - stainless steel reactor 15 cm long and 13 cm in diameter, equipped with an optical window 8, 2 - rotary mirror, 3 - collimator with holder, 4 - spectrometer STE-1 with crossed dispersion, 5 - spectrometer entrance slit, 6 - SONY DCR_SR200E video camera, 7 - spectrometer output window.

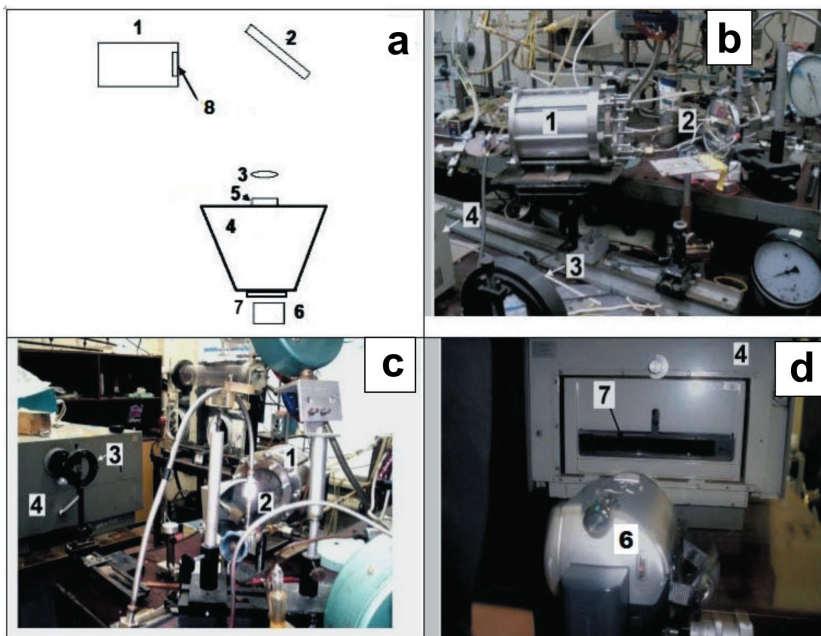


Figure 7. Installation for registration of radiation spectra by optical spectroscopy.

a) - block diagram of the installation; c-d) - photographs of the installation units

Results and discussion

Installation 1 was used to study the spatial development of the ignition of mixtures of 40% H_2 - air at a pressure of 1 atm. It should be noted that the ignition temperature of H_2 - air mixtures at 1 atm in a reactor containing Pt foil [3] is $\sim 170^\circ C$ lower than in a stainless steel reactor. It should be noted that the transition through the critical ignition condition is accompanied by a significant increase in the ignition delay period τ only over the catalytic Pt surface. When ignited over stainless steel, τ does not exceed 0.5 s and changes abruptly in a very narrow temperature range of ~ 1 degree. The retention periods in a 40% hydrogen-air mixture can reach tens of seconds both at temperatures less than $260^\circ C$ and above the “fresh” surface of the platinum foil. It is believed that the state of the “fresh” surface is realized in each initial (first) experiment, in which Pt is not pretreated with active centers of ignition.

A sequence of video images of the development of the ignition of the mixture of 40% hydrogen with air for various initiation conditions is shown in Fig. 8. As seen from Fig. 8a, a smooth homogeneous flame is observed during ignition

initiated by a spark discharge at room temperature of the walls of the reactor, in the case of a stainless steel surface. As shown in Fig. 8b, if the Pt foil is placed in a stainless steel reactor, the flame front is also almost uniform. However, in the presence of a Pt wire (Fig. 8c), a cellular flame structure is observed. Before and after ignition, the Pt wire is heated due to catalytic reactions on the Pt surface. The addition of 15% CO₂ to the combustible mixture ensures complete suppression of the cellular combustion mode (Fig. 8d), while the 15% addition of helium practically does not affect the cellular combustion mode (Fig. 8e).

The results of a qualitative assessment of the flame velocities from the change in the visible radius of a spherical flame according to the equation given in the Experimental are shown in Fig. 9. It can be seen from Fig. 9 that with spark initiation in a mixture diluted with carbon dioxide, a constant flame velocity is achieved after a certain time interval corresponding to the formation of a stable flame front (FF) [16, 17]. However, in the presence of a platinum catalyst, as can be seen from Fig. 9, a constant flame velocity (within the experimental error) is achieved almost immediately. In other words, the catalytic action of platinum leads to a sharp reduction in the time of formation of a stable FF. In addition, it can be seen from this figure that the normal flame velocity in the presence of a catalytic surface is noticeably higher (≈ 2.6 m/s) than under conditions excluding the action of the catalyst (upon initiation by a spark discharge, ≈ 1.9 m/s, in the presence of 15% CO₂, ≈ 1.8 m/s). The obtained values of normal velocities (without catalyst) agree within the error with the literature data [17]. On the other hand, it is known that the velocity of a laminar flame does not depend on the energy of the initiation source if the initiation energy is low (the so-called lean initiation [6]). Thus, the obtained experimental result requires an explanation.

Let us turn to the facts known from the literature. In [2] some experimental facts related to the reaction between platinum (the most effective catalyst for the combustion of hydrogen and hydrocarbons) and oxygen at temperatures up to the melting point of platinum are considered. In [2], it was found that a thin film of thermally unstable solid platinum oxide (more likely, platinum dioxide PtO₂, or PtO [3]) is formed in air or oxygen at room temperature [4] on the surfaces of a Pt wire or thin foil and it thickens with an increase in temperature to about 500 °C. However, when this temperature is exceeded, it disproportionates with the formation of metal [5]. Therefore, the weight loss of platinum in an oxidizing environment at elevated temperatures (470-540 °C) is explained by the formation of volatile platinum oxides, followed by the deposition of platinum on colder surfaces as a result of the decomposition of oxides. This is shown in the illustration (Fig. 1) given in [2]. It shows a platinum-containing layer on a lining brick of a CS reactor, recovered after long-term operation. It can be seen from the illustration that a black oxide film is deposited at cooler edges, and crystalline platinum is deposited at a hotter surface.

This means that molecules or clusters of both platinum oxides and platinum

metal exist in the gas phase at temperatures above 500 °C. Therefore, Pt-containing particles diffusing into a medium containing a combustible gas (for example, into a hydrogen-air mixture), for example, during the heating of a Pt wire, are catalytic centers, on which hydrogen can be ignited directly during the propagation of the flame front.

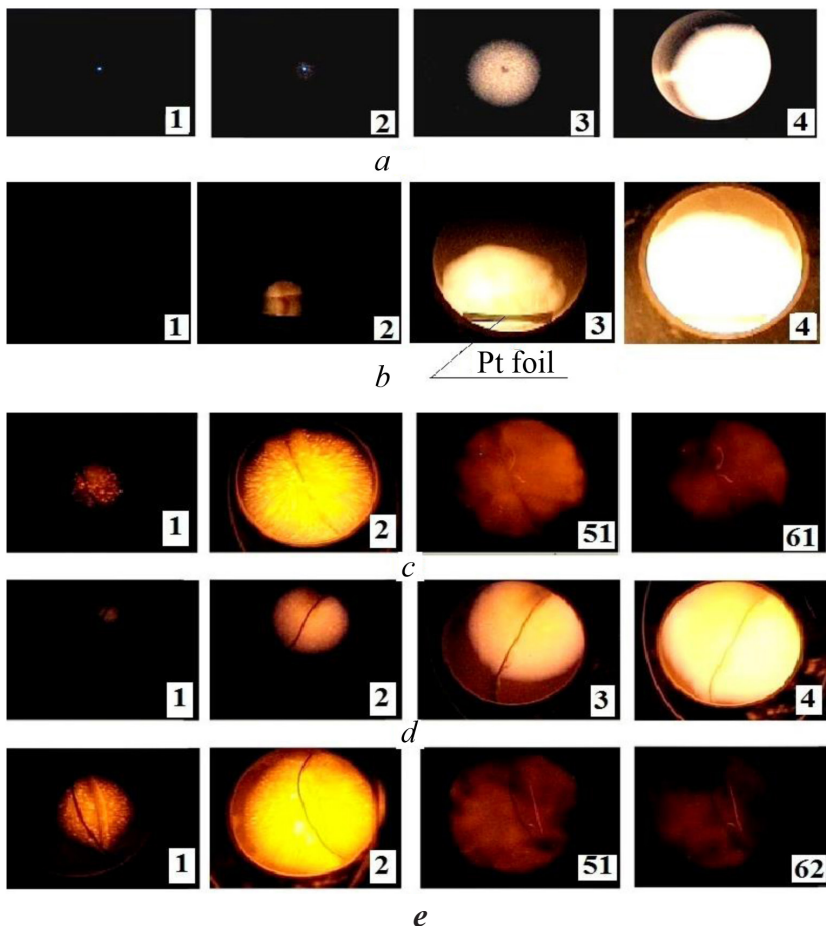


Figure 8. Sequences of video images of the spatial development of the combustion process. The numbers on the frame correspond to the sequential number of the video image:

- a) - ignition of the mixture of 40% H₂ + 60% air at wall temperature of 200 °C, initiated by a spark; 600 frames/s; P = 1 atm; there is no platinum in the reactor;
- b) - ignition of the mixture of 40% H₂ + 60% air at wall temperature of 247 °C; Pt foil is placed in the reactor.

c) - ignition of the mixture of 40% H_2 + 60% air at wall temperature of 316 °C; The Pt wire is placed in the reactor. It can be clearly seen in frames 1, 61. It is also seen from these frames that the Pt wire is heated before and after the explosion due to catalytic reactions on the Pt surface;

d) - ignition of the mixture of 85% (40% H_2 + 60% air) + 15% CO_2 at wall temperature of 320 °C in the presence of a Pt wire;

e) - ignition of the mixture of 85% (40% H_2 + 60% air) + 15% He at wall temperature of 309 °C in the presence of Pt wire.

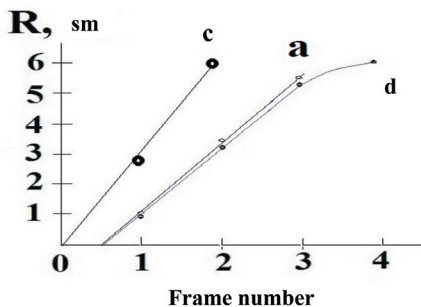


Figure 9. The dynamics of an increase in the radius R of the front of the laminar flame, calculated from an increase in the visible radius of the flame front from the data in Fig. 8: experiments a; b; c; $P_0 = 1 \text{ atm}$, 600 frames/s

Consequently, one can expect the appearance of an unstable FF caused by catalytic centers distributed in the gas phase during the combustion of hydrogen initiated by a Pt wire. This instability should be observed under the conditions, under which there is no thermal diffusion instability (the composition of the combustible mixture is close to stoichiometric [6]). Let us recall that the thermal diffusion instability is observed in flames in which the rates of heat transfer and diffusion are different, i.e. $Le \neq 1$ (Lewis number $Le = D/\alpha$, where D is the diffusion coefficient of the component that determines the combustion process, α is the thermal diffusivity). Such instability leads, for example, to the cellular nature of the propagation of flames in lean hydrogen-air and hydrogen-oxygen mixtures. In this work, a cellular regime is discovered and investigated, which is not associated with thermal diffusion instability.

The experimental data presented are in agreement with the experimental fact [2, 4, 5], indicating that the oxide layer on a bulk Pt sample with a lower surface-to-volume ratio is thinner than on a Pt wire, for which the surface-to-volume ratio, obviously, is larger. Therefore, the number of Pt particles in the volume during heating of a massive sample is not high enough to affect the structure of the flame front.

We investigated the behavior of a heated platinum wire in an oxidizing atmosphere (air) under various conditions (Fig. 10) for a clearer illustration of the above

in the next series of experiments. The results of visualizing the process of heating a Pt wire with a current of 2 A is demonstrated in Fig. 10a. For this purpose, the wire was illuminated with a vertical flat “laser knife” (see Experimental). It can be seen from Fig. 10a that ultradispersed particles evaporate from a platinum wire when heated, which are platinum oxide, according to the literature data [2-5].

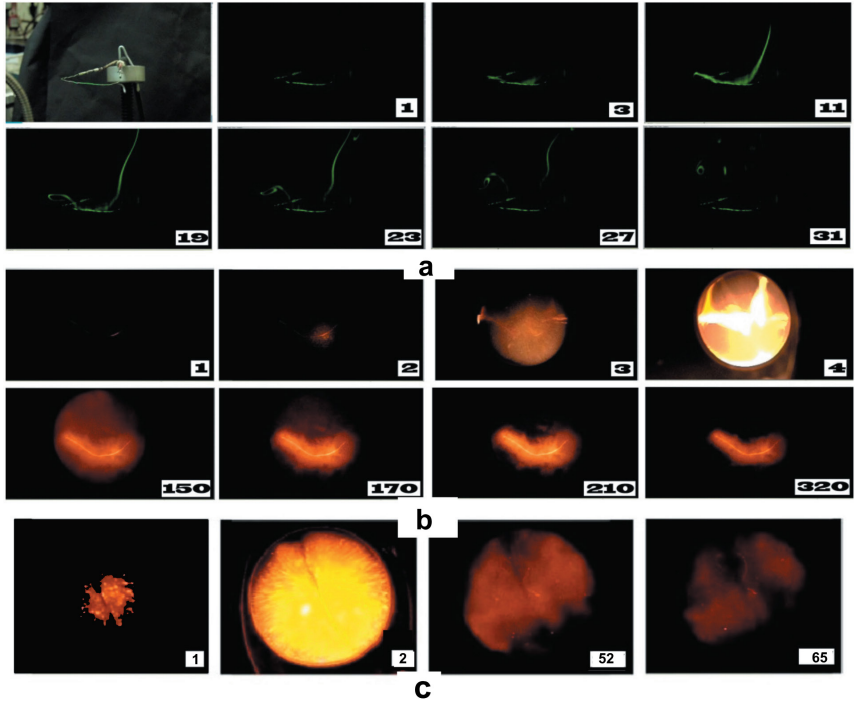


Figure 10. Behavior of heated platinum wire under various conditions:

- a) - heating the Pt wire (current 2 A). The wire is illuminated with a vertical flat “laser knife”. 60 frames/s;
- b) - ignition of the mixture of 40% H₂ + 60% air initiated by heated Pt wire at wall temperature of 200 °C;
- c) - ignition of the mixture of 40% H₂ + 60% air at wall temperature of 316 °C in the presence of a Pt wire.

It is obvious that in the experiment on the initiation of the ignition of hydrogen with Pt wire in a heated reactor during a delay period of 3 ÷ 70 s under our conditions, ultradispersed platinum oxide can spread up to ignition throughout the entire volume of the reactor because the registration of the evaporation of platinum oxide from the wire is carried out at a rate of 60 frames per second.

In a “cold” reactor (Fig. 10b), i.e. when the ignition of a 40% H₂ + 60% air

mixture is initiated by heating a Pt wire at wall temperature of 200 °C, platinum oxide does not have time to spread evenly throughout the reactor before ignition, since the delay time of thermal ignition is already hundredths of a second. In this regard, under these conditions, the cellular combustion mode is practically not manifested, to the same extent as in a heated reactor (compare Fig. 10b and Fig. 10c).

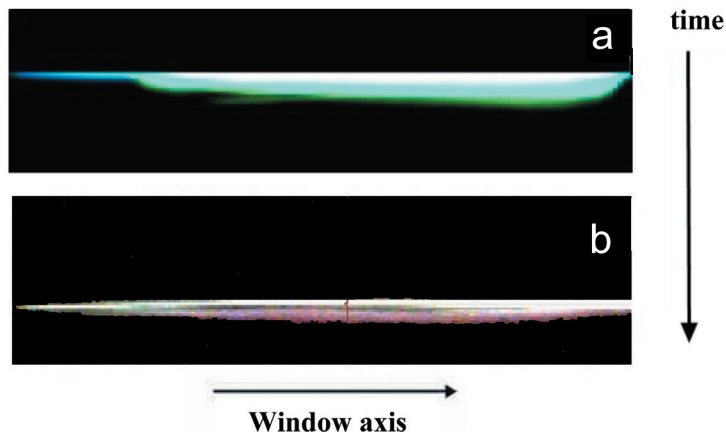


Figure 11. RGB hyperspectral images:

- a) - combustion of 40% hydrogen in air, initiated by a platinum wire,
- b) - combustion of 40% hydrogen in air, initiated by a spark discharge

The issue of the mechanism of the participation of ultradispersed Pt particles in combustion, as well as the determination of the features of hydrogen combustion in the presence of platinum, was solved experimentally using 4D spectroscopy. Thanks to this method, it is possible to record optical spectra of radiation from a given point in space at facility 1, as well as routine optical spectroscopy at facility 2. RGB of hyperspectral images of the investigated combustible mixtures: 40% hydrogen + air upon initiation by a spark discharge [15], 40% hydrogen + air upon initiation with a platinum wire are shown in Fig. 11a, b.

In Fig. 11a, b, the window axis (x-axis) corresponds to the red strip in Fig. 2a, and the y-axis corresponds to the dependence of the combustion process on time. Each strip along the y-axis in Fig. 11 corresponds to one frame of information accumulation on the photodetector matrix of the hyperspectrometer (300 frames/s).

A comparison of the optical emission spectra of a hydrogen flame initiated by a platinum wire and recorded along a vertical strip along the diameter of the optical window (red strip, Fig. 2a), and a spark discharge is demonstrated in Fig. 12a. Let us preliminarily point out that the hydrogen flame at low pressures is practically invisible. The reason to this is that its radiation is mainly due to the radiation of

hydroxyl radicals $\text{OH } A^2\Sigma-X^2\Pi$ in the ultraviolet region at 306 nm [18]. Attention is drawn to the features of the flame spectrum (Fig. 12a, b) in the visible region, namely the system of emission bands in the range of 570 - 650 nm, which makes the hydrogen flame visible at elevated pressures, along with the lines of sodium atoms (581 nm) and potassium (755 nm), inherent in all hot flames [18] and in this case emitted from the region filled with combustion products. In [15], we showed that the bands in the region of 600 nm in a hydrogen flame, according to the data of [19], relate to the radiation of water vapor. In Table 4 from [19], cited in [15], the assignment of the bands in Fig. 12a (black curve, see also Fig. 4d) to water vapor, which is a product of the hydrogen oxidation reaction is given. Thus, the observed spectral lines belong only to the reaction products.

It can be seen in Fig. 12b and 12c, which show the combustion spectra of the mixture of 40% H_2 - air, ($T_0 = 320^\circ\text{C}$, $P_0 = 1$ atm) in the range of 550 - 650 nm, recorded after initiation with platinum wire, deployed along the vertical x axis of the reactor, and the dependence of the maximum values of the spectrum intensity for a wavelength of 622 nm from the x coordinate along the vertical axis of the reactor, that at the selected time two maxima are recorded at $x = 488$ and $x = 503$ along the x axis, located between the spatial coordinates with relative values of 485 and 510. This means that combustion in space is inhomogeneous, otherwise the intensities of the spectral lines would change smoothly in the direction of decreasing or increasing coordinates. In other words, 4D spectroscopy makes it possible to register combustion cells, as was done above by high-speed filming (Fig. 8c, f; Fig. 10c).

The experimenter may be questioned whether the observed maxima in Fig. 12c are concerned with various noises, namely read noise, dark noise, quantization error or shot effect.

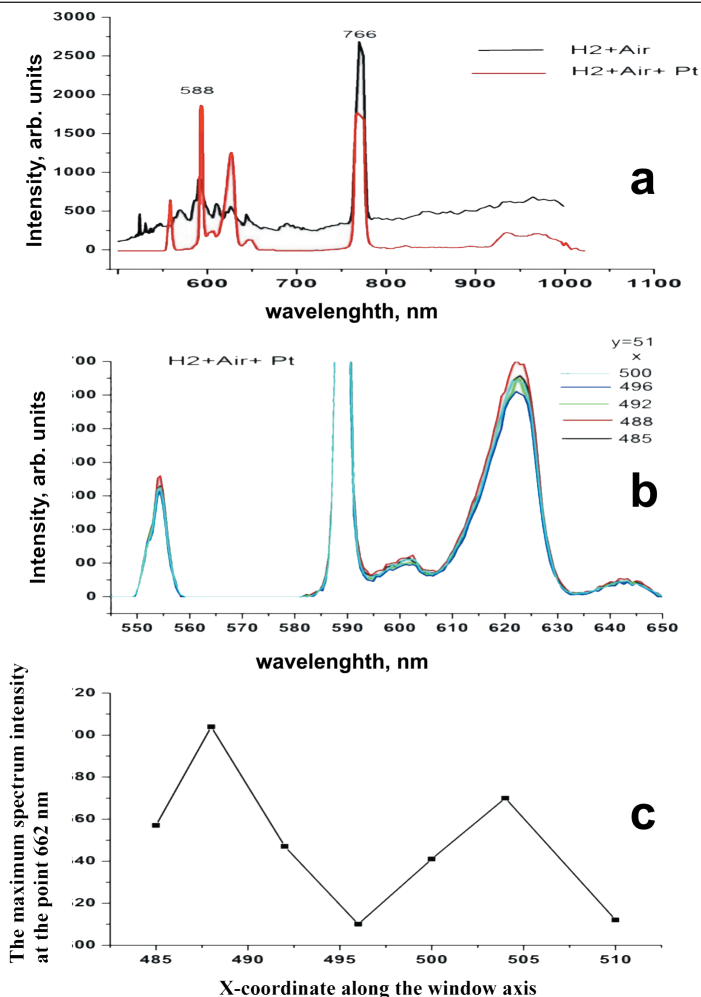


Figure 12.

a) - comparison of the spectra of hydrogen combustion initiated by a spark discharge. 40% H_2 - air, 20 °C, 1 atm (black curve) and initiated by a platinum wire. 40% H_2 - air, 320 °C, 1 atm (red curve)

b) - combustion spectra of a mixture of 40% H_2 - air, 320 °C, 1 atm in the range 550 - 650 nm, recorded after initiation with a platinum wire, deployed at the moment corresponding to frame 2 in Fig. 5c, along the vertical x-axis of the reactor (red strip in Fig. 2a).

c) - dependence of the maximum value of the spectrum intensity for a wavelength of 662 nm on the x coordinate along the vertical axis of the reactor.

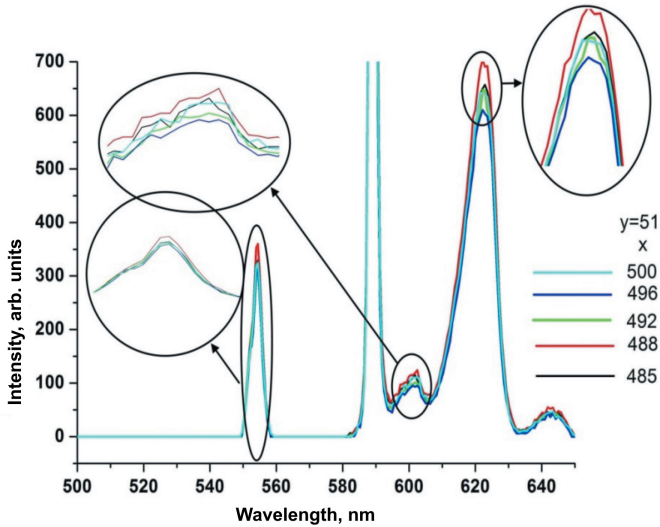


Figure 13. Dependences of the light emission intensity of the combustion of a mixture of 40% H_2 - 60% air in the range 550 - 650 nm, recorded after initiation with a platinum wire, $T_0 = 320$ °C, $P_0 = 1$ atm

Among these problems, the most important is the shot effect, since in our case it exceeds the other noises in intensity by orders of magnitude. However, special experiments have shown that the shot effect does not significantly affect the features of the behavior of the spectra shown in Fig. 12c. Primary data are shown in Fig. 13.

The foregoing is confirmed by the fact that the luminescence inhomogeneities caused by the catalytic instability of the phase transition are recorded not only by the high-speed filming method (Fig. 8c), but also by a hyperspectrometer (the same experiment, Fig. 14) directly on the hypercube. Indeed, it can be seen from Fig. 14 that when measured with a modified VID-IK3 hyperspectrometer on a combustion hypercube of a 40% H_2 - air mixture ($T_0 = 320$ °C, $P_0 = 1$ atm), bright spots (hot spots) are recorded corresponding to the combustion cells observed in Figs. 8c, 8d and 10c.

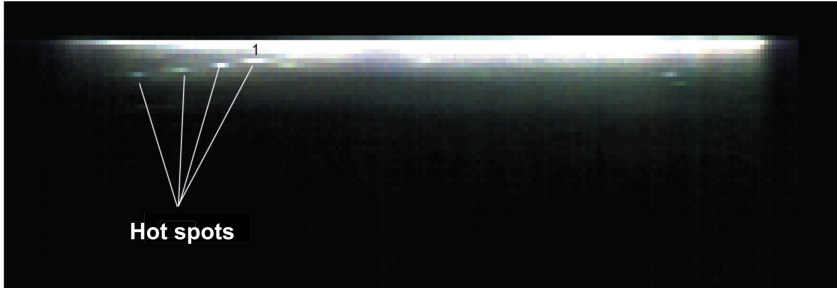


Figure 14. RGB hyperspectral image of the combustion of a mixture of 40% H_2 - air, initiated by a platinum wire, obtained using a modified VID-IK3 hyperspectrometer, $T_0 = 320$ °C, $P_0 = 1$ atm, spectral interval 550 - 650 nm

The main feature of these “hot spots” is that the emission spectra of combustion along and across these points, depending on both the y coordinate and x (time), behave not symmetrically and have a maximum inside this point.

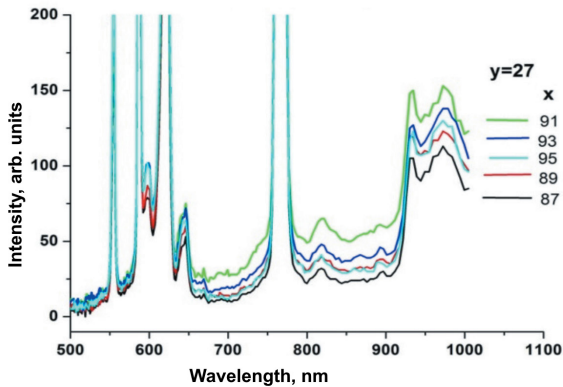


Figure 15. Dependence of the intensity of combustion emission spectra for different values of x (along the red strip in Fig. 2a) for point 1 (Fig. 14)

The spectra along one of these points (point 1 in Fig. 14) for different values of x (along the red strip in Fig. 2a) are shown in Fig. 15. The dependence of the position of the spectrum maximum for a wavelength of 972 nm on the x coordinate for point 1 (Fig. 14) is demonstrated in Fig. 16.

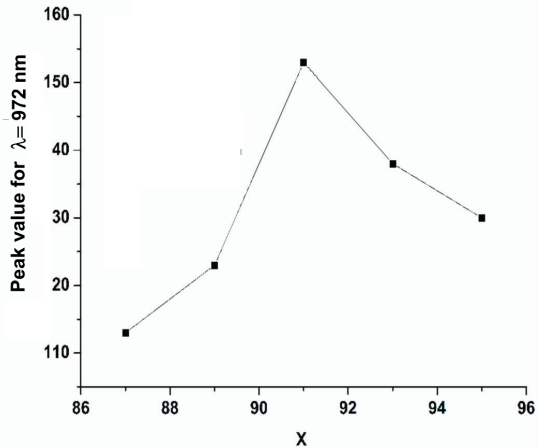


Figure 16. Dependence of the position of the spectrum maximum for a wavelength of 972 nm on the x coordinate for point 1 (Fig. 14)

The spectra across point 1 for different values of y (time) are indicated in Fig. 17.

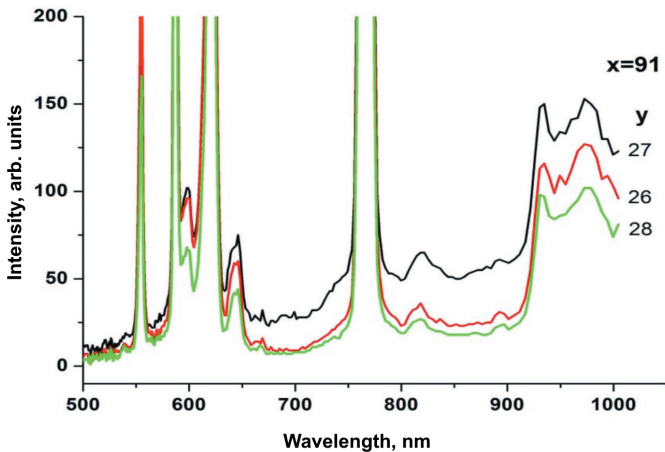


Figure 17. Dependence of the emission spectra of combustion on y (time) for point 1 (Fig. 14)

The dependence of the intensity maximum for the 972 nm line (Fig. 18) of point 1 (Fig. 14) on y (time) is shown in Fig. 18 .

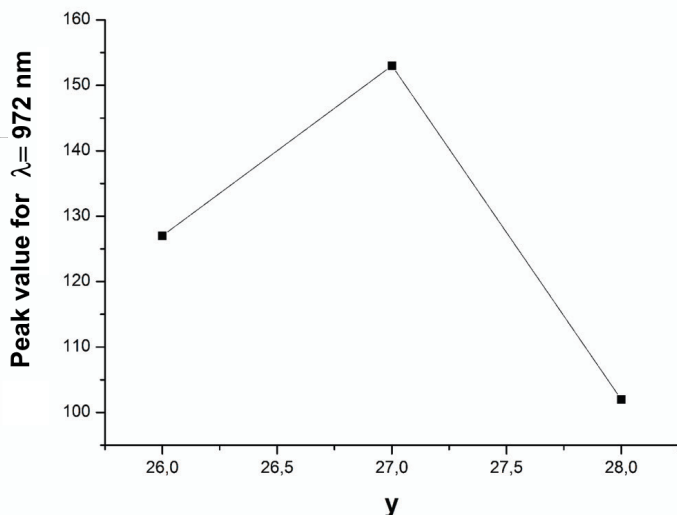


Figure 18. *Dependence of the maximum intensity for the line 972 nm (Fig. 16) point 1 (Fig. 14) on y (time)*

As is seen from Fig. 16 and 18, the spectral intensities for these points do not behave symbolically. It is interesting to note that these points are displaced along the x-axis depending on the recording time, that is, as cells that change their position in the video frames in Figs. 8c, 8d, 10c. An important conclusion also follows from the data obtained that the emission spectrum of the cells is close to the emission spectrum of a gray body (intensity maxima in space are observed simultaneously in different parts of the investigated spectral interval), that is, the emission of points (cells) really corresponds to the emission of incandescent catalyst particles.

Let us focus on the features of the emission spectrum of hydrogen combustion in a heated reactor in the presence of a platinum wire. It can be seen from Fig. 12a (compare also with Figs. 4d and 12b) that in this case an additional band at 552 nm appears in the emission spectrum of the hydrogen flame. According to the literature, the nature of the appearance of radiation at this wavelength has not yet been established. The indicated band in the emission spectrum (Fig. 13a) is observed during intense combustion of rich mixtures of industrial hydrocarbons, i.e. in the presence of soot particles [20], as well as in the combustion of methane in the presence of heated coal dust. Obviously, in both of these cases, neither hydrogen nor platinum is involved in the combustion process. Therefore, for this study, to find out whether the radiation source at a wavelength of 552 nm is associated with the evaporation of platinum oxide from a heated platinum surface was of fundamental importance.

For this purpose, a cylindrical furnace 6 cm in diameter and 3 cm long was placed in reactor 1. A compressed coal tablet (anthracite, trade mark GOST 25543-88b, particles with an average diameter of 55 μm) was placed in its internal hole, heated for 3 minutes to 400 $^{\circ}\text{C}$ and a stoichiometric mixture of natural gas with oxygen up to 150 mm Hg and admitted a stoichiometric in installation 2 (Fig. 2). Ignition was initiated by a spark discharge. The emission spectrum recorded using optical spectroscopy is shown in Fig. 19a. As seen from Fig. 19a, the 552 nm band is clearly observed in this spectrum. However, as indicated above, to observe this band, a hydrocarbon is needed as a combustible, as well as a heated coal powder. In the next experiment, the conditions remained the same, only methane was replaced by hydrogen. At the same time, the 552 nm band remained in the spectrum. In the absence of carbon dust in a clean (washed with ethanol) reactor, this band was no longer observed (cf. Figs. 4d and 12b) both upon initiation of ignition by a spark discharge or by a heated platinum wire. Thus, the method of initiating the ignition is not associated with the occurrence of this emission band.

This led us to the conclusion that experiments at room temperature and in a heated reactor differ methodically by the presence of an aluminum ring to prevent gas circulation in the heated reactor (see Experimental).

Therefore, a thin aluminum foil was introduced into the “cold” reactor, which was used to cover the inner walls of the reactor. The initiation was carried out with a heated platinum wire. The result of the experiment is shown in Fig. 19b, and the result of its digital processing using the Hesperus 3.0 program is shown in Fig. 19c. It can be seen from Fig. 19b that when a mixture of 40% H_2 - air is ignited, it is possible to observe a band at 552 nm. It should be noted that the appearance of copper lines (515, 521, 529, 532 nm [21]) is because the platinum wire was attached to copper electrodes, which were heated at the attachment points.

Thus, the occurrence of emission at a wavelength of 552 nm is most likely due to the radiation of metal impurities contained in aluminum. Excitation of metal atoms is carried out during the recombination of atoms and radicals arising during combustion on the hot surface of aluminum (the flame temperature of a mixture of 40% H_2 - air is ~ 2200 $^{\circ}\text{C}$ [22]) with the release of a significant amount of energy. For example, it is known that a platinum wire placed at a distance of 7 cm from the RF discharge can even melt due to the energy released during the recombination of oxygen atoms on the surface ($2\text{O} \rightarrow \text{O}_2 + 116.4$ kcal/mol) [23].

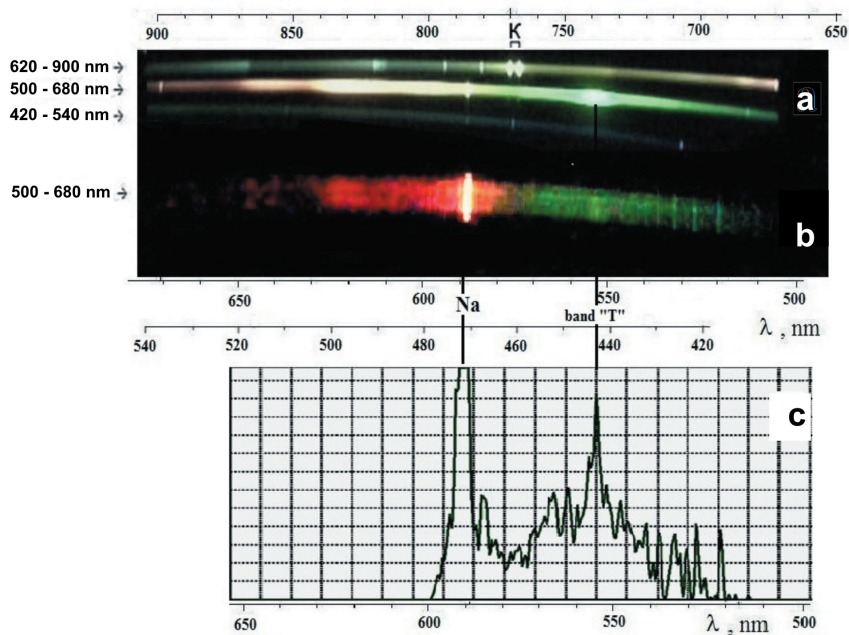


Figure 19.

a) - optical spectrum of radiation during combustion of a stoichiometric mixture of methane in oxygen in the presence of carbon dust heated to 400 °C. P = 150 mm Hg;

b) - optical spectrum of hydrogen combustion in air upon initiation by a heated platinum wire in the presence of a thin (0.1 mm) aluminum foil covering the reactor walls. P = 1 atm, initial temperature 20 °C.

c) - spectrum b after processing using the Hesperus 3.0 software package.

This energy corresponds to ultraviolet radiation at a wavelength of about 270 nm. Sources of radiation at a wavelength of 552 nm can be impurities of atoms of alkaline earth metals in industrial aluminum, which contains Fe, Cu, Mn, Mg, Cr, Ni [24] and trace amounts of alkali and alkaline earth metals, in particular, Ca [25]. As shown in [26], excited CaOH and CuOH (calcium monohydroxide, copper monohydroxide) molecules can provide radiation at 552 nm. Since carbon powders contain a large amount of inorganic impurities, including metals and their salts [27], the 552 nm band during coal combustion is obviously of the same origin.

This result also means that the introduction of platinum into the hydrogen oxidation flame does not lead to changes in the visible emission spectrum of this flame as compared to initiation by an electric discharge. Thus, the processes of evaporation and decomposition of Pt oxide, which has catalytic properties, like

platinum itself, determine the role of platinum. Directly related to these processes is the cellular mode discovered in this work for the Pt-initiated combustion of a mixture of 40% H₂ with air - a composition close to stoichiometric one. Thus, in accordance with the above, during the ignition delay period in the gas phase, the molecules or clusters of Pt and platinum oxide are formed at the temperature of the platinum wire in the combustible gas above 500 °C. Pt-containing ultrafine particles diffusing into the reaction volume act as catalytic centers, on which hydrogen is oxidized, which leads to strong heating of these particles. These incandescent particles are perceived as flame cells on video filming and when recording by the 4D spectroscopy method. In fact, they are such cells, in the area of which combustion occurs most intensely. We point out that the rate of diffusion of catalytic particles in the gas should determine the possibility of implementing cellular combustion. This is indeed the case. For example, the diffusion rate of catalytic particles decreases in the presence of 15% CO₂. These particles “do not keep up” behind the propagating combustion front (Fig. 8d), and the cellular combustion mode is not recorded. On the other hand, the addition of 15% light He (Fig. 8e) does not lead to the disappearance of the cellular combustion regime.

Let us turn to the analysis of the temperature dependences of the ignition delay times during the combustion of hydrogen in the presence of a platinum surface in a heated reactor. The ignition delay time τ is one of the most important macrokinetic characteristics of thermal ignition, which can be measured in relatively simple ways.

In this case, an important experimental fact is that, according to [26, 28], in a shock tube and in a rapid compression machine, thermal ignition has a cellular nature. We have also recently shown [3, 7] that the ignition of mixtures of hydrogen and n-pentane with air in a bypass plant at a total pressure of 0.6 - 2 atm begins with the appearance of a primary ignition center on the most chemically active area of the surface (see paragraph 4 of Chapter 3). Thus, thermal ignition includes the stages of warm-up, local ignition and flame propagation. This means that cellular ignition is the rule, not the exception, i.e. “self-ignition” as a process that occurs simultaneously in the entire volume of the reactor, apparently, is not provided in principle.

The temperature dependence of the ignition delay times for a mixture of 40% H₂ and air in the reactor in the presence and in the absence of a gas flow (Fig. 19) above the catalytic surface (Pt foil or Pt wire) in Arrhenius coordinates is shown in Fig. 20. As seen from Fig. 20, the effective activation energy E is practically the same for both the Pt foil and the Pt wire, both in the presence and in the absence of a gas flow. The experimental value of E is 19 ± 3 kcal/mol and is close to the that of the hydrogen combustion branching reaction $H + O_2 \rightarrow OH + O$ (16.7 kcal/mol [22, 29]). This means that the ignition delay in the initiation of hydrogen combustion by the platinum surface is determined by the slowest stage of the kinetic mechanism, namely, the branching reaction, the slowest stage in the sequence

of reactions leading to flame propagation. Indeed, the value of the delay period for the initial stage of the combustion process is $\tau \approx 1/\phi$, where ϕ is the so-called branching factor, which includes the value of the rate constant of the activated branching reaction in the case of a hydrogen oxidation reaction.

As is known [22], the coordinate of the point of intersection of straight lines with the ordinate axis in Fig. 20 is approximately inversely proportional to the frequency of active collisions. Since the surface area of the Pt wire is less than that of the Pt foil, the frequency of collisions with the surface is lower for the Pt wire. In addition, the collision frequency for a Pt foil in a stationary gas is less than for the same foil in a circulating gas. This is illustrated in Fig. 20.

Conclusions for Chapter 5

A cellular mode of combustion of a 40% hydrogen - air mixture in the presence of platinum wire and foil in the range of 270-350 °C at atmospheric pressure was discovered. Combustion cells caused by catalytic instability have been experimentally detected for the first time using the 4D optical spectroscopy method, which allows recording the intensity of the optical spectrum simultaneously depending on the wavelength, time and coordinate.

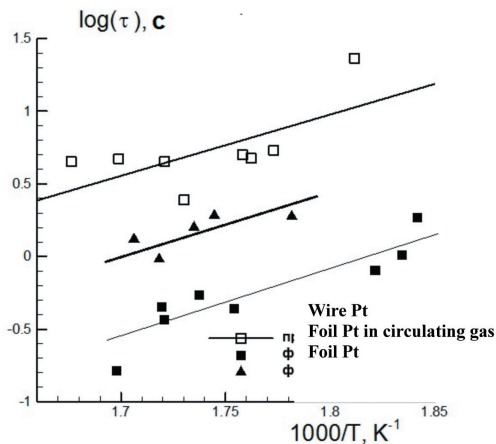


Figure 20. Temperature dependence of the delay times of thermal ignition for a mixture of 40% H_2 with air in the reactor of the bypass installation in the presence and in the absence of a gas flow at a pressure of 1 atm. Black triangles - ignition initiated by platinum foil, gas at rest; black squares - platinum foil initiated ignition, circulating gas; empty squares - ignition initiated by platinum wire, the gas is at rest

It was found that the cellular mode is determined by the catalytic combustion of hydrogen on Pt - containing particles formed during the decomposition of unstable platinum oxide in the gas phase. During the ignition delay period at the temperature of the platinum wire in the combustible gas above 500 °C, molecules or clusters of Pt oxide and platinum are formed in the gas phase. Pt-containing ultrafine particles diffusing into the reaction volume act as catalytic centers, on which hydrogen is oxidized, which leads to strong heating of these particles. These incandescent particles are perceived as flame cells on video filming and, in fact, are such cells, in the area of which combustion is most intense. It is shown that the temperature dependence of the hydrogen ignition delays on a platinum wire and foil in both stationary and rotating gases corresponds to an activation energy of 19 ± 3 kcal/mol, which is close to the activation energy of branching of hydrogen oxidation reaction chains. The impurity origin of the 552 nm emitting band, which is often recorded during combustion of gas and dust-gas mixtures, has been established.

The results obtained are of immediate importance for the development of Catalytic Stabilization (CS) technology and the development of catalysts with increased activity. The results are also important for verification of theoretical concepts of the propagation of dust and gas flames.

References for Chapter 5

1. Appel C., Mantzaras J., Schaeren R., Bombach R., Inauen A. *Catalytic combustion of hydrogen – air mixtures over platinum: Validation of hetero-homogeneous reaction schemes*. 2004. *Clean Air*. Vol. 5. No. 1. pp. 21–44. DOI: 10.1615/InterJEnerCleanEnv.v5.i1.20
2. Chaston J. C. *Reaction of Oxygen with the Platinum Metals. The oxidation of platinum*. *Platinum Metals Rev.* 1964. Vol. 8. No. 2. pp. 50-54.
3. Rubtsov N. M., Seplyarskii B. S., Troshin K. Ya, Chernysh V.I., Tsvetkov G. I. *Investigation into spontaneous ignition of hydrogen–air mixtures in a heated reactor at atmospheric pressure by high-speed cinematography*. *Mendeleev Communications*. 2012. Vol. 22. No. 4. pp. 222-224. DOI: 10.1016/j.mencom.2012.07.001
4. Perry D. L. Phillips S. *Handbook of Inorganic Compounds*. CRC Press. 1995. pp. 296–298.
5. *Chemistry Foundations and Applications*. 3. (ed. Lagowski J. J.). Thomson Gale. 2004. pp. 267–268.
6. Zeldovich Ya. B., Barenblatt G. I., Makhviladze G.M., Librovich V. B. *The Mathematical Theory of Combustion and Explosion*. Consultants Bureau. New York. 1985.

7. Borisov A. A., Rubtsov N. M., Skachkov G. I., Troshin K. Ya. *Gas Phase Spontaneous Ignition of Hydrocarbons. Russian Journal of Physical Chemistry B*. 2012. Vol. 6. No. 4. pp. 517-522. DOI: 10.1134/S1990793112080040

9. Rubtsov N. M., Septyarskii B. S., Troshin K. Ya., Tsvetkov G. I., Chernysh V. I. *High-speed color cinematography of the spontaneous ignition of propane-air and n-pentane-air mixtures. Mendeleev Communications*. 2011. Vol. 21. No. 1. pp. 31-33. DOI: 10.1016/j.mencom.2011.01.013

10. Khalil A., Gupta A. K. *Dual Injection Distributed Combustion for Gas Turbine Application. J. Energy Resources and Technology*. 2014. Vol. 136. No 1. 011601. <https://doi.org/10.1115/1.4025020>

11. Khalil A., Gupta A. K., Bryden K. M., Lee S. C. *Mixture preparation effects on distributed Combustion for Gas Turbine application, J. Energy Resources and Technology*. 2012, Vol. 134. No. 3. 032201. <https://doi.org/10.1115/1.4006481>

13. Kalinin A. P., Orlov A. G., Rodionov A. I., Troshin K. Ya. *Demonstraciya vozmozhnosti izucheniya processov goreniya ivzryvas pomoshch'yudistancionnogo giperspektral'nogo zondirovaniya (Demonstration of the possibilities to study combustion and explosion processes on the base of hyperspectral remote sensing). Physical-Chemical Kinetics in Gas Dynamics*. 2009. Vol. 8. <http://chemphys.edu.ru/issues/2009-8/articles/202/> (in Russian)

14. Vinogradov A. N., Egorov V. V., Kalinin A. P., Melnikova E. M., Rodionov A. I., Rodionov I. D. *Lineyka giperspektral'nykh sensorov opticheskogo diapazona (Line of hyperspectral sensors of the optical range). Preprint of Space Research Institute of RAS. Pr-2176*. 2015. 16 p. (in Russian)

15. Rubtsov N. M., Vinogradov A. N., Kalinin A. P., Rodionov A. I., Troshin K. Ya., Tsvetkov G. I. *Ustanovleniye zakonmernostey rasprostraneniya neustoychivogo fronta plameni metodami opticheskoy 3D spektroskopii i tsvetnoy skorostnoy kinos'yomki (Establishing the Regularities of the Propagation of an Unstable Flame Front by the Methods of Optical 3D Spectroscopy and Color High-Speed Filming). Ishlinsky Institute for Problems in Mechanics RAS. Preprint No. 1097*. (in Russian)

16. Rubtsov N. M. *The Modes of Gaseous Combustion. Springer International Publishing*. 296 p. DOI: 10.1007/978-3-319-25933-8

17. Rubtsov N. M., Septyarsky B. S., Troshin K. Ya., Chernysh V.I., Tsvetkov G. I. *Initiation and propagation of laminar spherical flames at atmospheric pressure. Mendeleev Communications*. 2011. Vol. 21. No. 4. pp. 218-220. DOI: 10.1016/j.mencom.2011.07.016

18. Pierse R., Gaydon A. *The identification of molecular spectra*. 1941. N.- Y., London, Acad. Press. 240 p.

19. Icitaga T. *Emission spectrum of the oxy-hydrogen flame and its reaction mechanism. (1) Formation of the Activated Water Molecule in Higher Vibrational States. The Review of Physical Chemistry of Japan*. 1939. Vol. 13f. No. 2. p. 96-107.

20. Stamatoglou P. *Spectral Analysis of Flame Emission for Optimization of Combustion Devices on Marine Vessels. Master of Science Thesis. Department of Physics, Lund University, Kockumation Group, Malmö(Sweden), May 2014.*

21. NIST Atomic Spectra Database. http://physics.nist.gov/PhysRefData/ASD/lines_form.html

22. Lewis B., Von Elbe G. *Combustion, Explosions and Flame in Gases.* New York, London.: Acad. Press. 1987. 566 p.

23. Maltsev V. M., Maltsev M. I., Kashporov L. Y. *Osnovnyye kharakteristiki goreniya (Basic combustion characteristics).* M: Chemistry. 1977. 320 p. (in Russian)

24. Thomas H. L. *Trace Elements in Al-Si Foundry Alloys. PhD thesis. Trondheim, Norwegian University of Science and Technology. September 2013. 156 p.*

25. Arzamasov B. N., Brostrem V. A., Bushe N. A. et al. *Konstruksionnyye materialy: Spravochnik (Structural materials: Reference book).* M.: Mashinostroyeniye. 1990. 688 p. (in Russian)

26. Meyerriecks W., Kosanke K. L. *Color Values and Spectra of the Principal Emitters in Colored Flames. Journal of Pyrotechnics. 2003. No. 18. pp. 720 - 731.*

26. Saytzev S. G., Soloukhin R. I. *Proceedings of the 8th symposium (International) on combustion. California Institute of Technology Pasadena, California, (The Combust. Inst., Pittsburgh, PA). 1962. p. 2771.*

27. Eckhoff R. K. *Dust Explosions in the Process Industries. 3rd edn. Gulf Professional Publishing/Elsevier, Boston. 2003. 720 p.*

28. Livengood J. C., Leary W. A. *Autoignition by rapid compression. Industrial & Engineering Chemistry. 1951. Vol. 43. No. 12. pp. 2797-2805.*

29. Germann T. C., Miller W. H. *Quantum mechanical pressure dependent reaction and recombination rates for $\text{OH} + \text{O} \rightarrow \text{O}_2 + \text{H}$. J. Phys. Chem. A. 1997. Vol. 101. pp. 6358-6367.*

30. Frank-Kamenetsky D. A. *Diffuziya i teploperedacha v khimicheskoy kinetike (Diffusion and heat transfer in chemical kinetics).* Moskva : Nauka. 1967. 491 p. (in Russian)

CHAPTER 6. Determining of the gas-dynamic and kinetic features of the penetration of methane-oxygen flames through obstacles by using 4D spectroscopy and high-speed filming

It has been shown experimentally that in the case of flame penetration through an obstacle, gas-dynamic factors, for example, flame-generated turbulence, can determine the kinetics of the process, including the transition of low-temperature combustion of a hydrocarbon to a high-temperature regime.

It has been established that the flame front after a single obstacle does not arise in the immediate vicinity of the obstacle. The first ignition source can be observed relatively far from the obstacle surface. It is experimentally shown that the flame does not penetrate from the side of the funnel (confuser) below the limit of penetration of the flame of a diluted mixture of methane with oxygen through a flat obstacle with one hole for an obstacle in the form of a funnel. However, it penetrates from the side of the funnel nose (diffuser). Within the framework of an approximate consideration using the Navier-Stokes equations in a compressible reacting medium, the features of flame propagation through a conical obstacle with additional holes on the converging generatrix are qualitatively described. In other words, the flame does not penetrate through the central hole of the converging tube, but only penetrates through the central hole of the diffuser, even if there are holes in the generatrix of the cone. The performed modeling in small volumes suggests that the most effective two-way flame-arrester in the pipe can be a system of two confusers, the funnels of which are located on the pipe axis along the gas flow and against it. An emergency can occur before and after the obstacle. The features of the penetration of the flame front through rectangular holes in comparison with round holes were experimentally investigated using color filming and visualization of a gas flow. It is shown that the length of the “flame jump” after the hole in the obstacle is mainly determined by the time of occurrence of the laminar-turbulent transition, and not by the ignition delay period. It was found that C_2 radicals in detectable quantities and the main heat release in the process are observed after the flame passes the first obstacle by using 4D spectroscopy combined with high-speed color filming, i.e. after turbulization of the gas flow. The obtained result means that the used experimental technique makes it possible to separate in time and space “cold” and “hot” flames in a single experiment.

Keywords: flame front, obstacle, hole, flame jump, laminar, turbulent, transition, diffuser, confuser

Flame propagation in pipes and channels is important for establishing criteria for safe gas pumping through pipes, ensuring explosion safety in the electric power industry, mining and petrochemical industries, and also for ensuring the

completeness of gas conversion in internal combustion engines [1]. The interaction between the flame and obstacles caused by the presence of equipment parts in the reaction volumes can lead to local acceleration of the flame front (FF) [2]. The influence of obstacles on the course of explosive processes, the shape of the flame in pipes and channels were studied in laboratory conditions [3, 4-6]. The authors of [5, 6] pointed out the important role of acoustic waves generated by a flame and formed waves of finite amplitude on the shape of the FF.

In [6, 7], it was found that the simultaneous occurrence of intense chemical transformation, heat transfer and mass transfer during turbulent mixing caused by obstacles, in combination with momentum exchange processes, can significantly accelerate a flame, cause an explosion, a transition to a supersonic combustion mode and lead to damage to a building or highway. This influence of obstacles on flame acceleration was studied, for example, in [8-10].

The purpose of this Chapter was to establish the gas-dynamic and kinetic features of the penetration of methane-oxygen flames through obstacles of various geometries using 4D spectroscopy and high-speed filming.

§ 1. Gas-dynamic and kinetic features of the penetration of methane-oxygen flame through single holes and fine-meshed obstacles

As suggested in [9, 10], when studying obstacles with small holes, flame acceleration can be explained not only by an increase in the degree of turbulence of the gas flow expanding when passing through the obstacle, but also by the accumulation of free radicals behind the obstacle. Mixing these radicals with unreacted gas should increase the flammability of the mixture.

It is shown in [11, 12] that spark-initiated flames of lean hydrogen-air mixtures at 1 atm penetrate through mesh aluminum spherical obstacles with a cell size of 0.04–0.1 mm². The flame of a mixture of 15% H₂ in the air after the obstacle is accelerated. Acoustic vibrations are observed in the reactor i.e. local pulsations of gas density. In this case, the smaller the diameter of the grid sphere is, the earlier the acoustic vibrations occur. On the other hand, the FF of a stoichiometric mixture of natural gas (NG) with air is not accelerated after an obstacle. In the works, it was concluded that the active centers of combustion of methane and hydrogen, which determine the propagation of the flame, have a different chemical nature. In other words, the contribution of the termination of active radicals on the surface of the obstacle is decisive in the case of NG-air mixtures. This result, along with those presented in [9, 10], indicates the important role of active intermediate combustion products during the penetration of a flame through an obstacle.

This section presents experimental results on flame propagation in a cylindrical channel with obstacles. The aim was to reveal the features of the FF penetration through the simplest single obstacles with one round hole and fine-mesh obstacles, and also to evaluate the effectiveness of such obstacles for suppressing

the combustion of methane.

The peculiarities of the penetration of the FF through a single obstacle are considered in the first part of the section. An experimental evaluation of the effectiveness of fine mesh barriers for suppressing methane combustion is described in the second part.

The experiments were carried out with stoichiometric mixtures of methane with oxygen diluted with CO₂ and Kr at initial pressures of 100-200 Torr and a temperature of 298 K in an evacuated horizontal cylindrical quartz reactor 70 cm long and 14 cm in diameter. The reactor was fixed with two stainless steel locks at the ends (Fig. 1) and was equipped with vacuum inlets for gas admitting and pumping out and a safety door that opened outward when the total pressure in the reactor exceeded 1 atm.

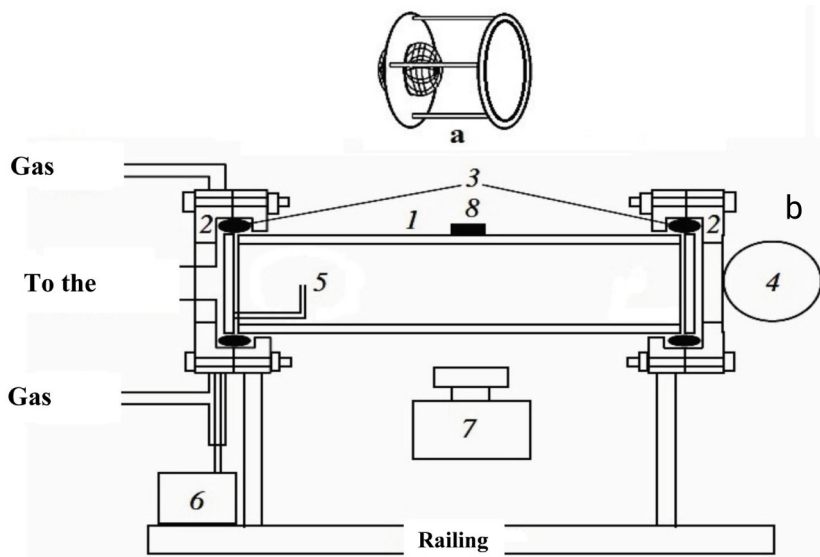


Figure 1. *Experimental setup*

a) - mesh sphere 4 cm in diameter b (wire diameter 0.1 mm, cell size 0.15 mm²) inserted into a flat obstacle 14 cm in diameter.

b) - (1) quartz reactor, (2) stainless steel gateways, (3) silicone gasket, (4) safety door, (5) spark ignition electrodes, (6) power supply, (7) high-speed movie camera, (8) microphone.

Two spark ignition electrodes were located at one of the ends of the reactor. The spherical obstacle consisted of two stainless steel mesh hemispheres attached to a ring. Mesh spheres with a diameter of 8 cm (wire thickness 0.3 mm, cell size

0.3 mm²), 10 cm diameter (wire thickness 0.35 mm, cell size 0.5 mm²), and 13 cm diameter (wire thickness 0.5 mm, cell size 1 mm²) were used. We also used flat stainless steel mesh obstacles with a diameter of 14 cm, equal to the reactor diameter (wire thickness 0.3 mm, cell size 0.5 mm²; or with a wire thickness of 0.5 mm and cell size 0.1 mm²). In addition, mesh spheres with a diameter of 4 cm (wire thickness $d = 0.1$ mm, cell size 0.15 mm²) and 5 cm (wire thickness 0.15 mm, cell size 0.15 mm²) were used, inserted into a flat obstacle with a diameter of 14 cm and overlapping the cross section of the reactor. (Fig. 1a). The results obtained with fine-mesh obstacles were compared with experimental data on the penetration of a flame through flat obstacles with single central holes 2.5 cm and 4 cm in diameter. The investigated combustible mixture (15.4% CH₄ + 30.8% O₂ + 46% CO₂ + 7.8% Kr) was preliminarily prepared. CO₂ was added to reduce the FF velocity and improve the quality of the filming. Kr was added to reduce the gas ionization threshold. The reactor was filled with a combustible mixture to the required pressure. Then, ignition was initiated with a spark (energy 1.5 J). High-speed shooting of the dynamics of the ignition and propagation of the FF was carried out from the side of the reactor (Fig. 1) using a color high-speed digital camera Casio Exilim F1 Pro (frame speed 600 s⁻¹) [13]. The video file was saved in the computer memory, then frame-by-frame processing was carried out. [14]. The change in pressure during combustion was recorded using a piezoelectric sensor synchronized with a spark discharge. Acoustic vibrations were recorded with a Ritmix microphone (frequency range up to 40 kHz). The audio recording was turned on at an arbitrary moment before the ignition was initiated. During the experiment, the level of extraneous noise was minimized. The audio file was analyzed using the Spectra Plus 5.0 software package. The gases used were of "chemically pure" grade.

A typical picture of flame propagation in a combustible mixture through a single obstacle is shown in Fig. 2.

The footage of flame propagation through various obstacles recorded by a high-speed video camera is shown in Fig. 2: a - hole diameter 4 cm; b - mesh sphere with a diameter of 4 cm; c - mesh sphere 4 cm in diameter inserted into a flat obstacle 14 cm in diameter (Fig. 1a). Let us pay attention to the following experimental features of the process. FF after the obstacle does not arise in the immediate vicinity of the obstacle. The first ignition site can be observed relatively far from the surface of the obstacle. As follows from Fig. 2, the smaller the hole diameter is, the farther from the obstacle the flame front appears (the difference is indicated by the arrows in the figure).

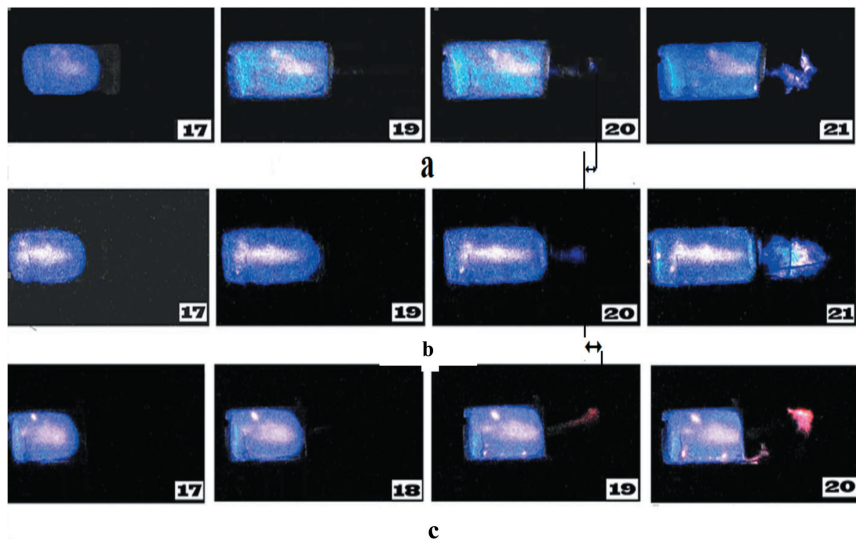


Figure 2.

a) - high-speed shooting of the FF propagation through a round hole 2.5 cm in diameter in a flat obstacle 14 cm in diameter,

b) - high-speed shooting of FF propagation through a round hole 4 cm in diameter in a flat obstacle 14 cm in diameter,

c) - high-speed shooting of the FF propagation through a mesh sphere with a diameter of 4 cm (wire diameter 0.1 mm, cell size 0.15 mm²) inserted into a flat obstacle with a diameter of 14 cm, Fig. 1a), combustion of a mixture of 15.4% CH₄ + 30.8% O₂ + 46% CO₂ + 7.8% Kr at an initial pressure of 170 Torr. The frame number is counted from the moment of ignition initiation. The arrows indicate the distances of the flame front after the obstacle.

As is seen from Fig. 2c, the FF occurs at the greatest distance from the obstacle when an obstacle in the form of a mesh sphere is used, while a "jump" of the flame through a single obstacle can be observed at initial pressures less than atmospheric. In addition, the flame "skips" in a diluted mixture much farther than in a stoichiometric mixture at 1 atm [9]. The determination of the dependence of the magnitude of the "jump" of the flame on the geometrical arrangement of a complex obstacle will be carried out below in §3.

It should be noted that the accumulation of free radicals behind the obstacle was observed experimentally [9]. Mixing these radicals with an unreacted combustible mixture increases the flammability of the mixture. This means that the analysis should take into account the main features of the kinetic mechanism of combustion.

In the course of the preliminary analysis, a qualitative two-dimensional numerical simulation of the passage of a flame through an obstacle was carried out using the Navier-Stokes equations with a chemical reaction in the approximation of a small Mach number (acoustic approximation). We considered the simplest single flat obstacle with a central hole. Let us recall that any comparison of the experimentally recorded motion of the FF with the result of numerical simulation can be considered reliable only in a qualitative aspect because there are no uniqueness theorems for the Navier-Stokes equations in a compressible reacting medium. Therefore, the agreement between the calculated and experimental values is not an argument in favor of the chosen kinetic reaction mechanism, since there may be other sets of control parameters describing the same experimental profiles (the uniqueness of the solution has not been proven). It is possible to analyze reliably only the qualitative change in the speed of movement of the boundary of the front of a chemical reaction, as well as the shape of this boundary, the degree of its disturbance. Consideration of the detailed kinetic mechanism of combustion introduces additional uncertainty in the simulation results. The overwhelming majority of kinetic parameters are not known with sufficient accuracy. The question of the completeness of the kinetic mechanism is always open, so that adequate conclusions can be drawn based on numerical simulations. Thus, it is desirable to estimate qualitative calculations that allow tracing the trends in the development of processes in the conditions of the experiments being performed.

A qualitative consideration of the transition of flame propagation from spherical to cylindrical mode was carried out using the example of a two-dimensional plane problem in the side view projection in order to compare the results of the qualitative calculation with experimental ones and to establish further directions for modifying the calculation. As is known from the literature [15], the relationship between the main factors causing the instability of hydrodynamic and acoustic flames can be taken into account when considering the Navier-Stokes equations for a compressible medium in the acoustic approximation (which corresponds to substantially subsonic flames). The system of dimensionless Navier-Stokes equations in the approximation of a small Mach number [see. 13, 16-21], which describes the propagation of a flame in a two-dimensional channel, showed qualitative agreement with experiments [13] and is discussed in detail in Chapter 4. The initial values and dimensionless parameters were chosen the same as in [13].

In a number of calculations, the reaction rate was specified not by the Arrhenius equation, but using the simplest chain mechanism



where C is the dimensionless concentration of the initial substance, n is the dimensionless concentration of the active intermediate, w_0 and W are the rates of initiation and branching of reaction chains, respectively. In further calculations, the initiation reaction rate w_0 for the flame propagation process is assumed to be

small according to [22].

The Arrhenius law describes the temperature dependence of the reaction rate $n + C \rightarrow 3n + \text{products}$. In this case, equations (f) and (g) of system (1), (see Chapter 4) were replaced by the following equations:

$$\rho [C_t + vC_y + uC_x] = \nabla^2 C - \beta n W,$$

$$\rho [n_t + vn_y + un_x] = \nabla^2 n + 2\beta n W,$$

$$W = C \exp\left(\zeta - \frac{\zeta}{T}\right)$$

The initial condition for the concentration of the starting substance is changed to $C_0=1$.

The initiation condition is $T = 10$ at the right boundary of the channel (the initial dimensionless temperature is $T = 1$). The channel contains a single vertical obstruction with a centrally located hole or a spherical mesh obstruction. There are also boundary conditions (including obstruction) $C_x = 0, C_y = 0, n = 0, u = 0, v = 0, \rho_x = 0, \rho_y = 0$, as well as convective heat transfer $T_t = T - T_0$.

The calculation results are shown in Fig. 3. As can be seen in Fig. 3, the analysis of the Navier-Stokes equations in the approximation of a small Mach number makes it possible to qualitatively describe the experimental features of the penetration of the FF through a single obstacle (see Fig. 2) namely, the appearance of a flame front not in the immediate vicinity of the obstacle, but at some distance behind him. Thus, it is sufficient to analyze the simplest model of a single plane obstacle with a hole using the first-order Arrhenius reaction to describe this important experimental regularity. As also follows from Fig. 3, taking into account the chain transformation mechanism makes it possible to describe the movement of the reaction zone back to the obstacle after the flame breakthrough (Fig. 3c, frame d) in comparison with the representation of the reaction by a simple Arrhenius dependence.

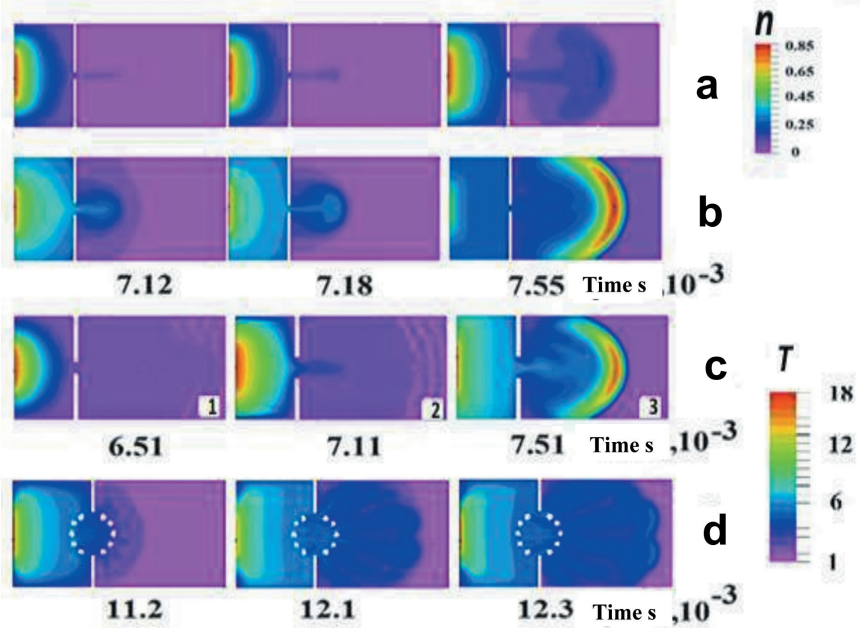


Figure 3. Simulation results of flame propagation through a hole (a-c) and an z -spherical mesh obstacle. The time is counted from the moment of initiation

a) - Change in the dimensionless concentration n when the flame propagates through the hole. First-order Arrhenius reaction. The scale of the change in the degree of conversion of the reaction n is shown on the right;

b) - Change in dimensionless temperature T when the flame propagates through the hole. First-order Arrhenius reaction. On the right is the scale of the change in the reaction temperature T ;

c) - Dimensionless concentration of the active intermediate product (n) for two moments of time (frame numbers 1 and 2) and dimensionless temperature (frame number 3), when a chemical reaction is represented by a simple chain mechanism. The scales for n and T are shown on the right.

d) - Change in dimensionless temperature during flame propagation through the mesh sphere. First-order Arrhenius reaction. The scale of the change in the dimensionless reaction temperature T is shown on the right.

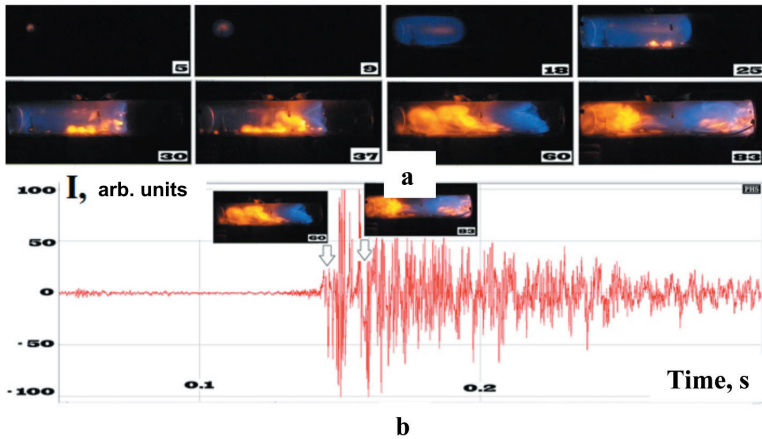
Thus, there is a qualitative difference in the results of calculations using the simplest chain mechanism as compared to modeling taking into account only one reaction obeying the Arrhenius law (Fig. 3a, b). Consequently, although the appearance of a flame "jump" is mainly determined by the gas-dynamic features of the penetration of a combustible gas through an obstacle, the kinetic mechanism of combustion also noticeably affects the process.

The laws governing the penetration of the flame front through the spherical mesh also qualitatively (note that the mesh was modeled very illustratively, as well as the reaction mechanism) coincide with the experiment. When using an obstacle in the form of a mesh sphere in qualitative agreement with Fig. 2c FF occurs at the greatest distance from the obstacle. This means, however, that we managed to take into account the main features of the penetration of the flame through the obstacle. These features, as can be seen from the simulation, are mainly determined by the gas dynamics of the combustion process.

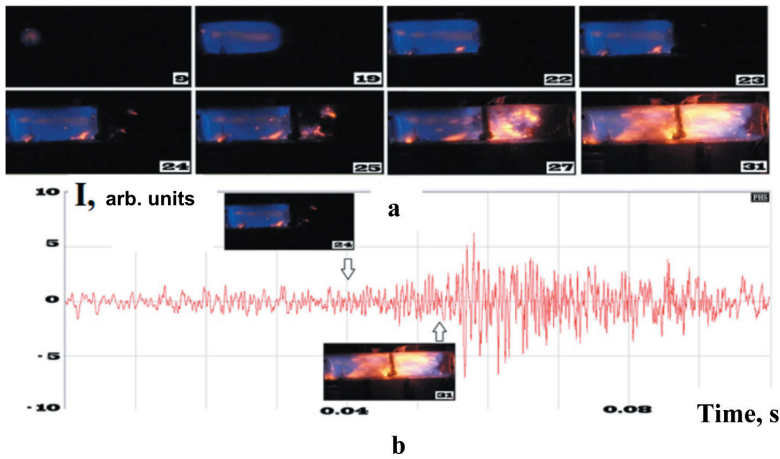
The next part of the paragraph is devoted to assessing the effectiveness of obstacles to suppress flame propagation during methane combustion. Video footage of the FF propagation in a gas mixture is indicated in Fig. 4 (I): a - in the absence of obstacles; b - dependence of the amplitude of acoustic vibrations on time. A video footage of the FF propagation in a gas mixture is shown in Fig. 4 (II): a - in the presence of three mesh obstacles (8, 10, 13 cm in diameter) nested into each other, b - the dependence of the amplitude of acoustic vibrations on time. As can be seen from the above figures, the introduction of obstacles in the form of nested mesh spheres leads to a noticeable suppression of the flame after the obstacle, which is indicated by a change in the maximum level of the acoustic signal, which in the presence of obstacles is approximately 20 times less than in an empty reactor. It was of interest to determine the dependence of the maximum intensity of the acoustic signal during the propagation of the combustion wave on the number of obstacles. We point out that the influence of obstacles is expressed in a dual way. On the one hand, the interaction of the FF with an obstacle can cause the development of flame instability, contributing to the acceleration of the FF. On the other hand, the contact of the FF with the surface of the obstacle can lead to an increase in the contribution of heterogeneous reactions, especially the termination of reaction chains [12], as well as to an increase in heat losses. The dependence of the maximum intensity of the acoustic signal on the number of obstacles is shown in Fig. 4 (III). Let's pay attention to the following experimental features. The experiment has shown the acceleration of the flame in the presence of a single obstacle in comparison with combustion without an obstacle. In these cases, the reactor safety door opened outward, i.e. the pressure in the reactor exceeded 1 atm (the established limit) (according to the readings of the pressure sensor, 1.5 atm was recorded), it did not matter whether the obstacle was flat or spherical. As seen in Fig. 4, two or more obstacles (both nested spherical and flat) greatly suppress flame propagation. We point out that in these cases the reactor safety door did not open, i.e. the pressure in the reactor did not exceed 1 atm (<500 Torr according to the readings of the pressure sensor). Thus, Fig. 4 illustrates the existence of two modes: flame acceleration after an obstacle and its suppression after an obstacle. In this case, one obstacle in the conditions of our experiment leads to the acceleration of the flame, and a larger number of obstacles leads to the suppression of the flame. In this case, the suppression of the flame is due to both chain termination

and heat losses on the surface of the obstacle. Let us generalize the results obtained in this section.

It is shown that the specific features of the penetration of a flame of a methane-oxygen mixture diluted with an inert gas through single holes and spherical obstacles are mainly determined by gas-dynamic factors. In this case, the kinetic mechanism of combustion also affects the process of flame penetration through the obstacle.



I



II

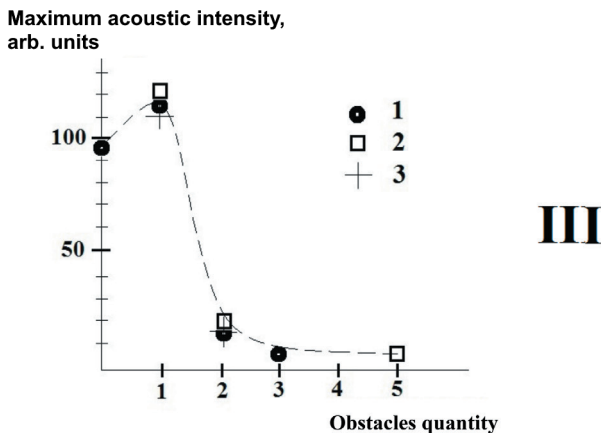


Figure 4. Dependence of the efficiency of flame suppression on the number of obstacles. A mixture of 15.4% PG + 30.8% O₂ + 46% CO₂ + 7.8% Kr at an initial pressure of 170 Torr. The frame number is counted from the frame with the moment of ignition initiation

I - a - high-speed shooting of FF propagation in a gas mixture in a quartz reactor without obstacles, spark discharge (1.5 J), shooting speed 600 frames/s;

b - dependence of the amplitude of acoustic vibrations on time. Several frames from (a) are shown to compare the times for high-speed video filming and acoustic oscillogram;

II - a - high-speed shooting of FF propagation in a gas mixture in a quartz reactor in the presence of three nested mesh obstacles (8, 10, 13 cm in diameter), spark discharge (1.5 J), shooting speed 600 frames/s;

b - time dependence of the acoustic vibration amplitude. Also some frames from a are shown.

III - dependence of the maximum intensity of acoustic vibrations on the number of obstacles. 15.4% CH₄ + 30.8% O₂ + 46% CO₂ + 7.8% Kr at an initial pressure of 170 Torr:

1 - spherical mesh nested obstacles,

2 - flat mesh obstacles with a diameter of 14 cm (wire diameter 0.5 mm and cell size 0.1 mm²);

It has been established that the flame front after a single obstacle does not arise in the immediate vicinity of the obstacle. The first ignition site can be observed relatively far from the obstacle surface. It is shown that the use of a mesh sphere as an obstacle leads to an increase in the length of the flame "jump" behind the obstacle in comparison with a round hole. It is shown that two or more obstacles, both spherical and flat, under experimental conditions noticeably suppress the propagation of the flame.

The results obtained in visualizing the development of flame front instability are important for solving the problems of explosion safety for volumes with complex geometrical arrangement.

§ 2. Peculiarities of penetration of flames of dilute mixtures of methane with oxygen through a single hole in a flat obstacle, diffuser, confuser and combined obstacles

In the event of a hypothetical industrial accident, a significant amount of highly flammable gas could be released. After mixing with atmospheric air, the resulting explosive mixture, if ignited, can endanger the integrity of the room, in which the accident occurred. Due to the complexity of both the physical and chemical processes of combustion and the geometrical arrangement of the reactor, the features of the propagation of the flame and the load on separate fragments of the reactor of complex geometry cannot be calculated with sufficient accuracy by now. It should be noted that the complete system of Navier-Stokes equations for a compressible reacting medium can be simplified and solved for non-isothermal flows only if the approximation of a small Mach number (acoustic approximation) is used. In order to describe slow processes of turbulent combustion, the Navier-Stokes equations are a good basis for modeling in a reacting medium in the approximation of a small Mach number [14-16, 18]. When the laminar flame moves into the area of unburnt premixed combustible gases, the combustion wave propagates due to the appearance of a heating zone (thermal conductivity) and diffusion of active combustion centers into the unreacted mixture. The structure of the flame determines how much energy is transferred to the unreacted gas. In accordance with how the gradients of temperature and concentrations of active centers change, the flame can either accelerate or go out. The gas-dynamic characteristics of the flow also affect the structure of the flame.

This section describes the features of flame propagation through a flat obstacle and a conical funnel with a round hole. To know the diameter of the hole through which the flame front does not penetrate under these conditions is of practical interest for solving the problems of explosion safety [9].

In the publication, the penetration of a flame through an obstacle with a single circular hole (which is characterized by a blocking ratio $BR = 1 - (d/D)^2$, where d and D denote the hole diameter and the internal diameter of the reactor, respectively) is discussed, for example, in [27-30]. In [30], it was proposed to use the Karlovitz number K to estimate the probability of the penetration of an isotropic turbulent flame through a single hole: $K \approx (v_{jet}^2 / d_{jet})^{1/2} u_l^2$, where v - kinematic viscosity of the gas mixture, u_l - velocity of the laminar flame, u_{jet} - local flow rate directly behind the obstacle, d_{jet} - diameter of the hole. It was postulated that flame extinguishing occurs at a critical value K . According to [29], flame extinguishing takes place when the product $K * Le > 1.5$, where Le - Lewis number. However,

the determination of the quantity is associated with significant difficulties, which, along with attempts at determination K are described in [7]. This semi-empirical approach takes into account the role of the kinetic mechanism of combustion when the flame penetrates through the hole only in the magnitude of the laminar flame velocity u_l .

This section describes an experimental study of flame penetration through a single hole in a flat obstacle and a conical funnel for diluted methane-oxygen mixtures with inert additives. The ways of developing numerical models of combustion are also discussed, which can be used to calculate the process of flame propagation through obstacles of various geometrical shape. The experimental results can be used to improve numerical models of flame propagation.

The experiments were carried out with stoichiometric mixtures of methane with oxygen diluted with CO_2 and Kr at initial pressures of 100-200 mm Hg and an initial temperature of 298 K. The setup shown in Fig. 1, namely, a horizontally disposed cylindrical quartz reactor 70 cm long and 14 cm in diameter (reactor 1), into which either a funnel or flat obstacles with holes or their combination were inserted. Evacuated steel cylindrical reactor (reactor 2), 12 cm in diameter and 25 cm long with an optical quartz window at the end was used (as described in [13] and in Chapter 3 [31, 32]). Two electrodes for initiating the flame with a spark discharge were located at the end of reactor 1 and in the center of reactor 2. Reactor 1 was vacuum-sealed in two stainless steel sluices equipped with inlets for gas admission and evacuation. One of the locks was equipped with a safety door that opened outward when the total pressure in the reactor exceeded 1 atm. Flat plastic obstacles $D = 14$ cm with round holes, $BR = 0.993$, $BR = 0.968$ and $BR = 0.918$ were placed in the reactor. A plastic conical funnel with a diameter of 14 cm was also used as a barrier (the nose of the funnel was 1 cm long and 1 cm in diameter ($BR = 0.995$)).

In a number of experiments, complex obstacles were used. They consisted of a confuser ($BR = 0.99$) and a flat obstacle 14 cm in diameter with a 4 cm hole covered with a net (obstacle A), or a mesh sphere 4 cm in diameter (obstacle B) (wire diameter 0.1 mm, mesh size 0.15 mm^2) inserted into a flat obstacle with a diameter of 14 cm, placed directly behind the confuser.

Complex obstacles consisting of a flat obstacle with a diameter of 14 cm with a single hole 25 mm in diameter and a second flat obstacle with a single hole 25 mm in diameter (obstacle C, Fig. 5, 1), a second flat obstacle with a single hole 25 mm in diameter, closed with a flat mesh (obstacle D, Fig. 5, 2) and a second flat obstacle with a single hole 40 mm in diameter, into which a mesh sphere was inserted (obstacle E, Fig. 5, 3) were also used. The second obstacle was located at a distance of the magnitude of the "flame jump" after a flat obstacle with a single hole 25 mm in diameter. This distance, measured empirically, was 12 cm.



Figure 5. Complex obstacles, consisting of a flat obstacle with a diameter of 14 cm with a single hole 25 mm in diameter and a second flat obstacle with a single hole of 25 mm in diameter (1), a second flat obstacle with a single hole 25 mm in diameter, covered with a flat mesh (2) and a second a flat obstacle with a single hole 40 mm in diameter, into which a mesh sphere was inserted (3)

The obstacles were located in such a way that the combustion wave could move them, but could penetrate the obstacle only through the central hole. The combustible mixture (15.4% CH_4 + 30.8% O_2 + 46% CO_2 + 7.8% Kr) was previously prepared. CO_2 was added to reduce the velocity of the flame front and thus improve the quality of the filming. Kr was added to reduce the breakdown energy of the gas mixture discharge. The reactor was filled with a combustible mixture to the required pressure. Then, a spark discharge was carried out (the discharge energy was 1.5 J). Filming of the dynamics of ignition and propagation of the combustion dynamics was carried out from the side of the reactor 1 and from the end of the reactor 2 through an optical window using a color high-speed digital camera Casio Exilim F1 Pro (frame rate 600 s^{-1}) [31]. The video file was saved in the computer memory and then its frame-by-frame processing was carried out [32]. The change in pressure during combustion was recorded by a piezoelectric sensor synchronized with a spark discharge. We used gases of chemically pure grade. The typical results of experiments on high-speed shooting of the flame front propagation in a mixture of 15.4% CH_4 + 30.8% O_2 + 46% CO_2 + 7.8% Kr at an initial pressure of 170 mm Hg through round holes a) = 0.993, b) = 0.968 and c) = 0.918 in a flat obstacle with a diameter of 14 cm was demonstrated in Fig. 6.

After ignition, a laminar flame propagation is observed. When the flame reaches the hole, the flame is extinguished at $\text{BR} = 0.993$ i.e. the disappearance of the flame behind the hole, and at lower values $\text{BR} = 0.968$ and $\text{BR} = 0.918$, the flame front penetrates through the hole. This indicates the existence of a critical hole diameter for flame penetration, in accordance with [7]. Since it was not possible to verify the criterion $\text{K}^* \text{Le} > 1.5$ (see above) due to the difficulty of experimental determination [7] under our conditions, then an attempt was made to identify the control parameters that determine the critical condition for flame attenuation when passing through the hole.

In the next series of experiments (see Fig. 7a, b), high-speed filming of the propagation of the flame front in a mixture of 15.4% CH₄ + 30.8% O₂ + 46% CO₂ + 7.8% Kr at an initial pressure of 170 Torr was carried out through a conical funnel 14 cm in diameter described in the Experimental. Here a - from the side of the funnel spout (diffuser); b - from the side of the funnel socket (confuser).

As can be seen from Fig. 7, under our conditions, the flame front penetrates through the funnel from the side of its nose (diffuser), but if the flame front approaches from the side of the funnel inlet (confuser), then the flame is extinguished.

It is noteworthy that in the case of a funnel as an obstacle, the use of BR to characterize an obstacle becomes ambiguous, since at BR = 0.995 (which is much lower than the penetration limit (see Fig. 2) for a flat obstacle), the flame does not really penetrate from the funnel mouth (confuser). However, it easily penetrates from the side of the funnel spout (diffuser).

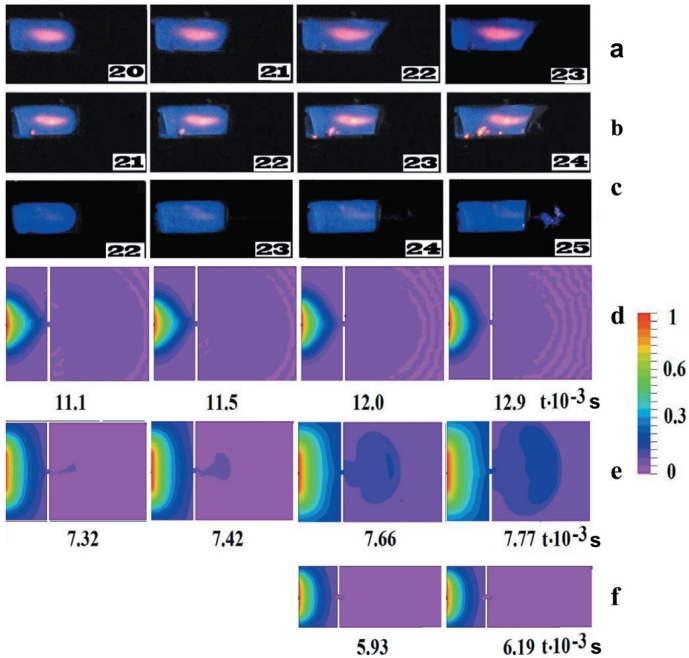


Figure 6. Results of high-speed survey of flame propagation through a round hole a) - BR = 0.993, b) BR = 0.968 and c) BR = 0.918. 15.4% CH₄ + 30.8% O₂ + 46% CO₂ + 7.8% Kr at an initial pressure of 170 Torr and a capture rate of 600 frames/s. The number in each frame corresponds to the frame number after ignition is initiated

Results of numerical calculation of the process of flame propagation through the hole.

- d) - change in the degree of transformation for a simple chain mechanism;
- e) - change in the degree of conversion of the reaction for a first-order reaction;
- f) - change in the degree of conversion of the reaction for a first-order reaction for a narrower channel.

The scale of the degree of conversion of the reaction is shown on the right.

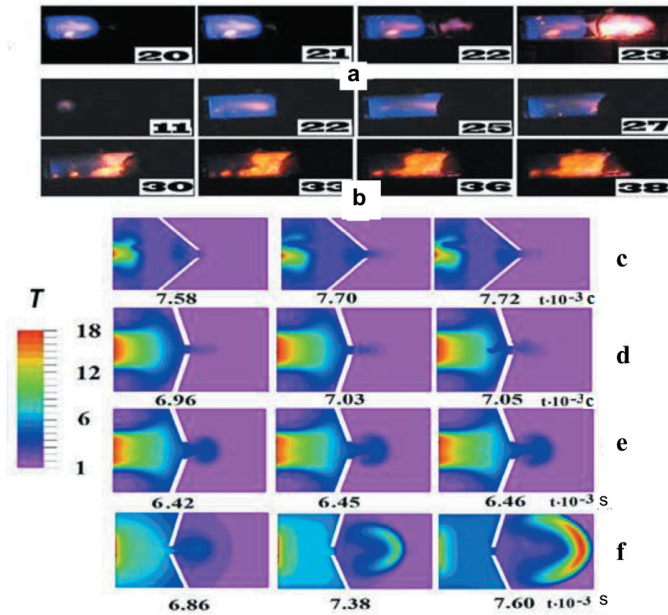


Figure 7. The results of high-speed shooting of flame propagation through a funnel 14 cm in diameter with an opening angle of 90° :

- a) - diffuser,
- b) - confuser. A mixture of 15.4% $\text{CH}_4 + 30.8\% \text{O}_2 + 46\% \text{CO}_2 + 7.8\% \text{Kr}$ at an initial pressure of 170 Torr, a shooting speed of 600 frames/s. The number in each frame corresponds to the frame number after ignition is initiated.

Results of numerical calculation of the process of flame propagation through the funnel.

- c) - change in the dimensionless flame temperature from the side of the funnel funnel for the first order reaction, funnel opening angle 90° ;
- d) - change in the dimensionless flame temperature from the side of the funnel funnel for a first-order reaction, funnel opening angle 150° ;
- e) - change in the dimensionless flame temperature from the side of the funnel funnel for a first-order reaction, funnel opening angle 150° , larger opening;
- f) - change in the dimensionless flame temperature on the side of the funnel bell for a first-order reaction, funnel opening angle 150° , smaller opening;

The scale of the dimensionless temperature change is shown on the left.

It was of interest to reveal the features of flame propagation through a confuser and a diffuser with additional holes on the generatrix of the cone. A plastic funnel $d = 14$ cm with a central hole and two holes (each 17 mm in diameter) on the generatrix of the cone (the opening angles of the cones were 45° , 55° and 83° (Fig. 8)) was oriented as a diffuser or as a confuser and placed in the center reactor. The obstacle was fixed in the reactor with a polyurethane foam ring.

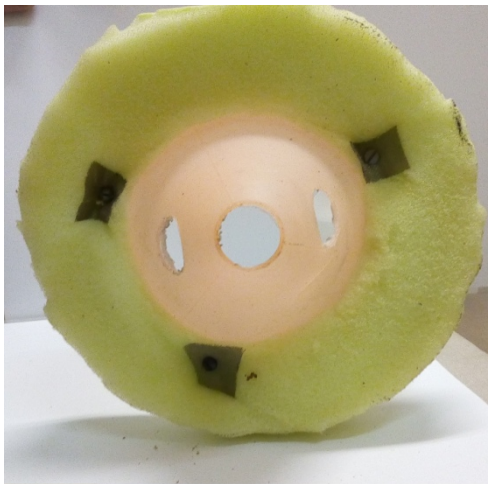


Figure 8. Conical obstacle with three holes (opening angle 83°)

Acoustic vibrations were recorded by using a Ritmix microphone (up to 40 kHz). The audio file was analyzed by using the Spectra Plus 5.0 software package. Typical sequences of video frames of high-speed shooting of the flame front propagation in a combustible mixture at an initial pressure of 165 Torr through a conical obstacle oriented as a confuser a), c), d) and as a diffuser b), e), f) are shown in Fig. 9 for the angles of disclosure of the cone 55° and 83° . As can be seen from Fig. 9, in our conditions the flame always penetrates only through the central opening of the diffuser. If we talk about a confuser, the flame penetrates only through its side holes at a cone opening angle of 55° (Fig. 9a, frames 21, 22, Fig. 9c, frame 19). The penetration of the flame through the confuser is accompanied with a sharp and loud sound, while the safety door opens. We point out that the propagation of the flame through the diffuser is not accompanied by a sharp sound effect, the safety door does not open. The above-said dependences of the acoustic amplitude on time when the flame penetrates through an obstacle in the form of a confuser Fig. 10a and a diffuser (Fig. 10b) is illustrated in Fig. 10. Several video frames from Fig. 9a and Fig. 9b are shown in Fig. 10. The center of

each video frame corresponds to the current time. From the results obtained above, it can be concluded that a full-scale experiment with a confuser with an opening angle of less than 83° on a large scale at atmospheric pressure is dangerous for the integrity of the installation and for the life of personnel, i.e. its implementation is impractical.

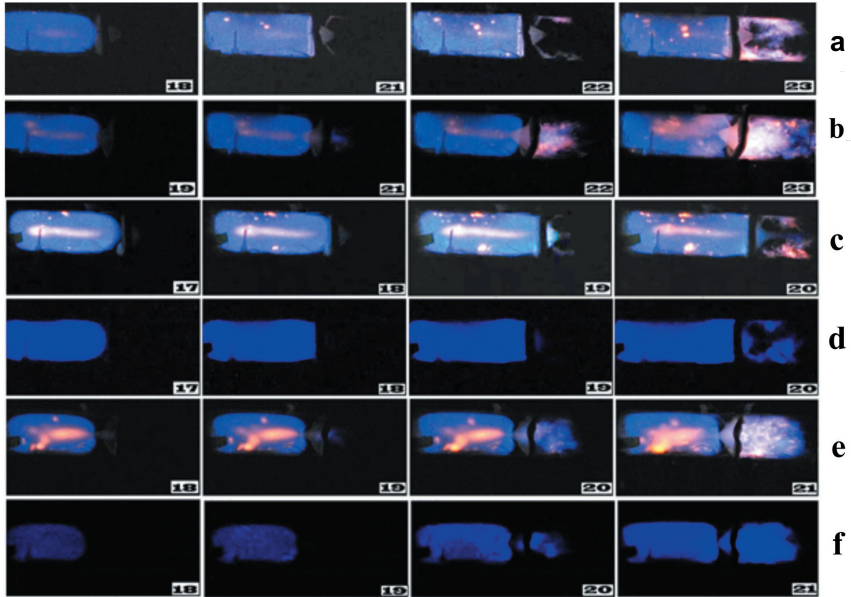


Figure 9. Video footage of high-speed filming of the flame front propagation through a conical obstacle with a central hole and two holes on the generatrix of the cone;

a) - confuser (opening angle of the cone 55°), b) - diffuser (opening angle of the cone 55°),

c) - confuser (opening angle of the cone 83°), d) - confuser (opening angle of the cone 83°), an interference filter of 430 nm is placed in front of the video camera;

e) - diffuser (opening angle of the cone 83°), f) - diffuser (opening angle of the cone 83°), an interference filter of 430 nm is placed in front of the video camera.

The initial pressure is 165 Torr. The number on the frame corresponds to the sequence number of the video frame after the moment of initiation.

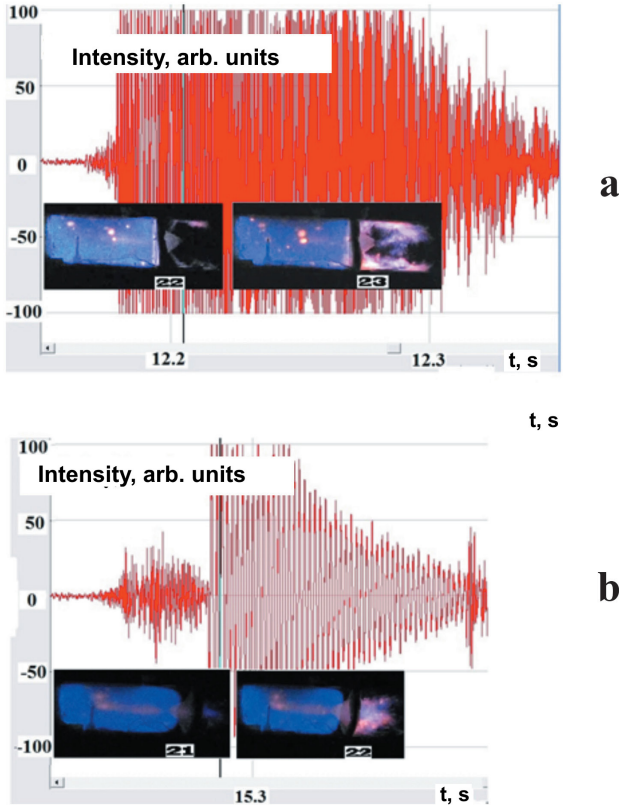


Figure 10. Dependences of the amplitudes of acoustic vibrations on time during the propagation of a flame in a gas mixture at an initial pressure of 165 Torr

a) - confuser, several frames from Fig. 2a, the center of each frame corresponds to the current time.

b) - diffuser, several frames from Fig. 2b, the center of each frame corresponds to the current time.

The flame begins to penetrate through the central opening of the diffuser (Fig. 9c, frames 19, 20) with an increase in the opening angle. It should be noted that the diameters of the holes in the conical obstacle are much less than the minimum diameter of flame penetration through a flat obstacle with a single central hole (20 mm [13]). Therefore, the value of the minimum size of a single hole should not be used when assessing the fire safety of a room with several openings. It is because the diameter of the hole sufficient for flame penetration decreases with an increase in the number of holes.

It should be noted also that in the case of a flat obstacle with three holes (the opening angle is obviously 180°), the flame penetrates through each of these three holes. In our case, reflected acoustic waves appear in the conical cavity, which is accompanied by the appearance of stagnant zones and the interaction of these waves with the initial combustion front, which generated these waves. The maximum pressure in this case is recorded at some distance from the top of the cone.

We also point out that the flame does not penetrate through the central opening, regardless of the existence of additional holes on the generatrix of the cone with a decrease in the opening angle in a confuser with a central hole (opening angle less than 45°).

For obstacles of this type, numerical modeling was also carried out using the Navier-Stokes equations for a compressible reacting medium in the approximation of a small Mach number. The initiation condition and boundary conditions were taken the same as in the analysis of the above problem of flame penetration through a cone with a central hole. The chemical reaction was represented by a single first-order Arrhenius reaction. The qualitative results of numerical simulation of the process of flame penetration through a conical obstacle in the form of a confuser and a diffuser are shown in Fig. 11. As can be seen, the results of the calculations are in qualitative agreement with the experiments shown in Fig. 9, i.e. the flame penetrates through the diffuser (Fig. 11c). The flame does not penetrate through the central opening of the confuser with an opening angle of 100° (Fig. 11a). At a larger aperture angle (150° , Fig. 11b), the flame penetrates through all three holes in the confuser in qualitative agreement with experiment (Fig. 9). It should be noted that in the case of a flat obstacle with three holes (one of them is central, the opening angle is 180°), the flame penetrates through each of these three holes.

Obviously, qualitative consideration (for example, a single reaction instead of a complete chemical mechanism, two-dimensional modeling, etc.) does not allow one to obtain an exact value of the opening angle, at which the flame begins to penetrate through the central opening of the confuser.

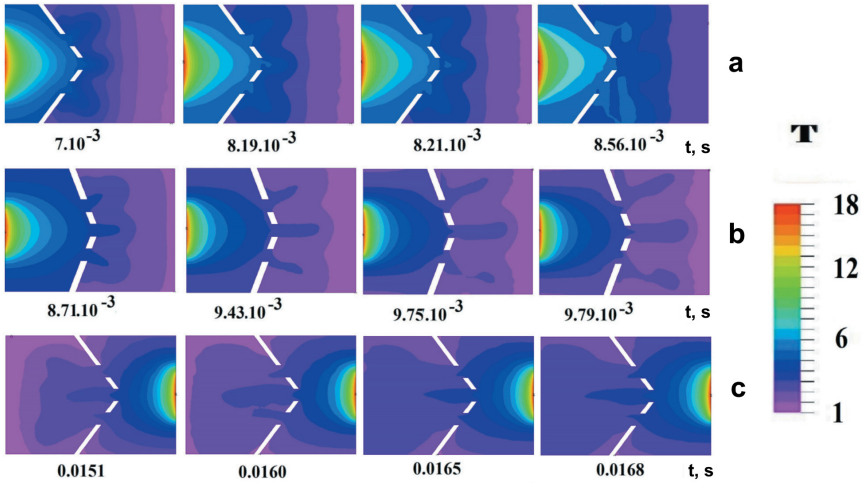


Figure 11. Results of numerical calculation of the process of flame penetration through a conical obstacle

- a) - change in dimensionless temperature when the flame penetrates through the confuser, opening angle 100° ;
- b) - change in dimensionless temperature during flame propagation through the confuser, opening angle 150° ;
- c) - change in dimensionless temperature during flame propagation through the diffuser, opening angle 100° .

The dimensionless temperature scale is shown on the right.

In addition, such a qualitative difference from the process of flame penetration through a flat obstacle with a central hole indicates a significant role of the interaction of acoustic vibrations of a reactor containing a conical cavity with a propagating combustion front [13] even in the case of a subsonic flame. The simulation carried out in small volumes allows us to assume that in the event of an emergency situation, the flame will not penetrate through the open valve located in the center of the confuser located in the pipe. In this case, the most effective double-sided flame arrester in the pipe can be a system of two confusers, the funnels of which are located on the pipe axis along the gas flow and against it. It is because an emergency can occur before and after the obstacle. A hole or valve can be located in the middle.

The sequences of frames of high-speed shooting of the FF propagation in the combustible mixture at an initial pressure of 180 Torr through complex obstacles A and B are shown in Figs. 12a and 13a, respectively.

As seen from Figs. 12a and 13a, the first ignition site is observed at a noticeable distance from the surface of the obstacle, especially in the case of obstacle

B. Also from Figs. 12a and 13a, it follows that the magnitude of the “flame jump” (the distance of the appearance of the flame behind the obstacle) is much greater in the presence of a mesh sphere compared to an obstacle containing a flat mesh. It should be noted that in agreement with the results presented in Fig. 7b (diffuser), the flame under our conditions does not pass through a complex obstacle containing a diffuser instead of a confuser.

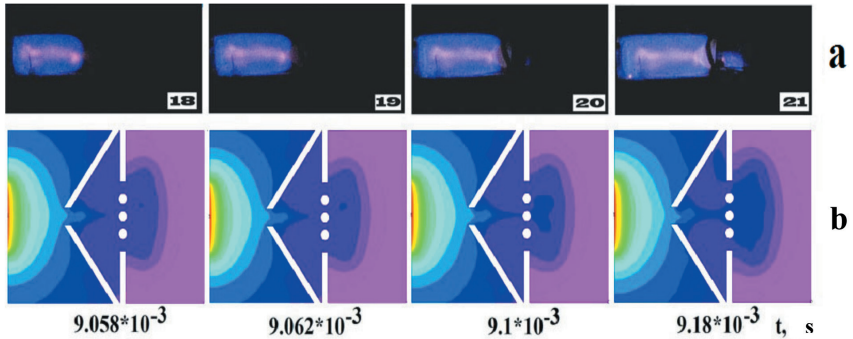


Figure 12.

a) - High-speed imaging of FF propagation through a complex obstacle consisting of a confuser 14 cm in diameter and a flat mesh with a hole 4 cm in diameter with a mixture of 15.4% PG + 30.8% O₂ + 46% CO₂ + 7.8% Kr at an initial pressure of 180 Torr. The number on the frame corresponds to the sequence number of the frame after the moment of ignition initiation.

b) - Numerical modeling of the process of flame propagation through a complex obstacle.

As is seen from Fig. 14, ignition after these combined obstacles occurs in our conditions already in the immediate vicinity of the second obstacle, the first ignition source is observed directly at the surface of the second obstacle for all three combinations. This means that the magnitude of the “flame jump” is mainly determined by the nature of the combination of obstacles, i.e. gas dynamic factors.

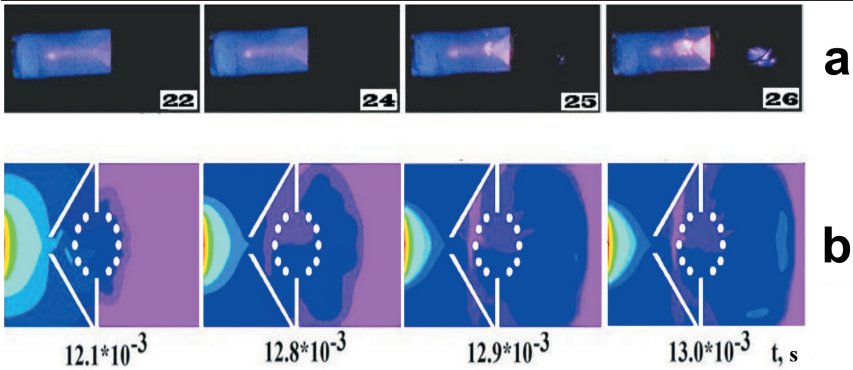


Figure 13.

a) - High-speed imaging of the process of FF propagation through a complex obstacle consisting of a confuser 14 cm in diameter and a mesh sphere of 4 cm in diameter 15.4% PG mixture + 30.8% O₂ + 46% CO₂ + 7.8% Kr at an initial pressure of 180 Torr. The number on the frame corresponds to the sequence number of the frame after the moment of initiation.

b) - The results of calculating the process of flame propagation through a complex obstacle.

The sequences of frames of high-speed shooting of the FF propagation in a combustible mixture at an initial pressure of 180 Torr through complex obstacles C, D, and E are shown in Fig. 14. Numerical simulations using dimensionless Navier-Stokes equations for a reacting compressible medium in the low Mach number approximation (see Chapter 4, system (I)) describing flame propagation in a two-dimensional channel showed qualitative agreement with experiments. In this work, the initial values and dimensionless parameters were chosen the same as in Chapter 4.

The problem was solved by the finite element method using the FlexPDE 6.08 software package, 1996-2008 PDE Solutions Inc. [15]. The initial condition was $T = 10$ at the right boundary of the channel; there was a vertically located obstacle in the channel with a hole in the center. The boundary conditions (including the hole) were $C_x = 0, C_y = 0, n = 0, u = 0, v = 0, \rho_x = 0, \rho_y = 0$, as well as convective heat transfer on the wall $T_i = T - T_0$.

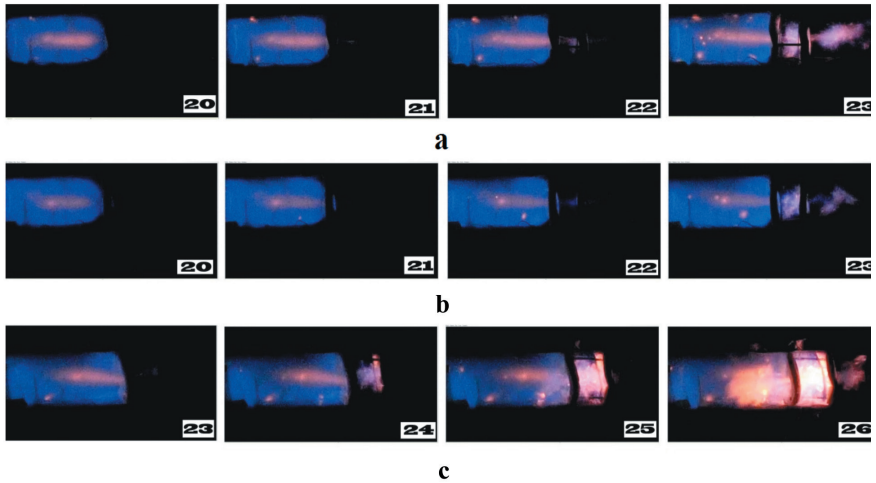


Figure 14. High-speed survey of FF propagation through combined obstacles, consisting of:

a) - a flat obstacle with a diameter of 14 cm with a single hole 25 mm in diameter and a second flat obstacle with a single hole with a diameter of 25 mm (obstacle C)

b) - a flat obstacle with a diameter of 14 cm with a single hole 25 mm in diameter and a second flat obstacle with a single hole with a diameter of 25 mm, covered with a flat mesh (obstacle D);

c) - a flat obstacle with a diameter of 14 cm with a single hole 25 mm in diameter and a second flat obstacle with a single hole with a diameter of 40 mm, into which a mesh sphere was inserted (obstacle E);

A mixture of 15.4% PG + 30.8% O₂ + 46% CO₂ + 7.8% Kr at an initial pressure of 180 Torr. The number on the frame corresponds to the sequence number of the frame after the moment of initiation.

The results of calculations carried out near the limit of flame penetration through the obstacle are shown in Fig. 6d, e, f. As can be seen from the figure, the calculation results are in qualitative agreement with the experimental data presented in Fig. 6a, b. The performed calculation also makes it possible to qualitatively reveal both the role of active combustion centers (Fig. 6d) and heat losses (Fig. 6f) when the flame penetrates through the obstacle. Under the conditions of penetration of the flame front through the hole (Fig. 6e) for a single first-order reaction obeying the Arrhenius law, taking into account either heat losses (the channel width in Fig. 6f is equal to 0.6 of the channel width in Fig. 6e) or the simplest chain mechanism (instead of one reaction) leads to a limit for the penetration of the flame through the hole. In this latter case, the losses are provided by taking into

account the termination of the active centers of the circuits ($n_{wall} = 0$). It should be noted that in Fig. 6d, e, f all other parameters in the calculation are the same.

The results of numerical simulation of flame penetration through a conical funnel are shown in Fig. 7c-e. As can be seen from the figure, the simulation results are in qualitative agreement with the experimental results shown in Fig. 7a, b. Indeed, in accordance with the experiment, the flame penetrates through the funnel from the side of its nose (Fig. 7a, f), and when the flame propagates from the side of the funnel funnel, no flame penetration is observed (Fig. 7b, c, d), the flame is extinguished. This qualitative difference from the process of flame penetration through a flat obstacle with a central hole indicates a noticeable role of the interaction of acoustic vibrations in a reactor containing an obstacle with a propagating combustion front. Thus, a numerical experiment shows that with a wider opening of the funnel, the flame does not penetrate through the obstacle on the side of the funnel mouth. In other words, there is a critical hole diameter.

The peculiarities of FF penetration through complex obstacles also qualitatively coincide with experiment. In qualitative agreement with Figs. 8a, 9a, in the presence of a mesh sphere as an obstacle, the length of the "flame jump" is much larger than with a flat mesh (Figs. 8b, 9b). Therefore, (even taking into account the qualitative nature of the calculations and the very formal modeling of the mesh sphere), we were able to illustrate the main features of the FF propagation through complex obstacles. The same applies to the peculiarities of flame penetration through the combined obstacles C, D and E (Figs. 12-15).

At the end of the section, let us stop on the possibilities of analysis based on the Navier-Stokes equations in the acoustic approximation. Fig. 11,IIb of Chapter 3 experimentally demonstrates the appearance of streams of hot glowing gas from a volume bounded by a spherical mesh obstacle that appears after the flame reaches the walls of the reactor. It was of interest to determine whether it is possible to interpret this phenomenon using the acoustic approximation of the Navier-Stokes equations (Chapter 4, system of equations (II)). The problem was solved by the finite element method using the FlexPDE 6.08 software package, 1996-2008 PDE Solutions Inc. [15].

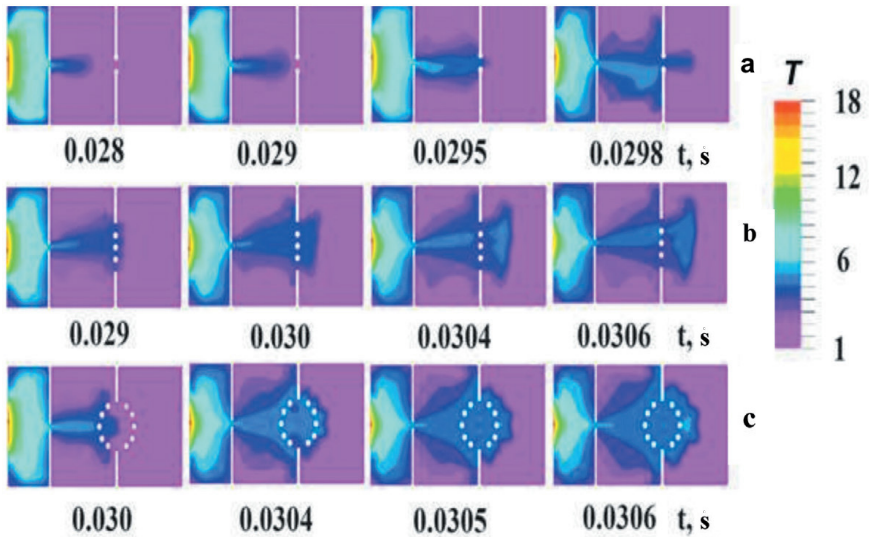


Figure 15. Results of numerical modeling of the flame propagation process through a complex obstacle:

a) - obstacle C; b) - obstacle D; c) - obstacle E.

The dimensionless temperature scale T is shown on the right.

The initial condition was $T = 10$ on the left channel segment at $y = 0.5$. There was a mesh obstacle in the channel (Fig. 16). The boundary conditions (including the hole) were $C_\xi = 0$, $u = 0$, $v = 0$, $p_\xi = 0$, $n_\xi = 0$ on the reactor wall and $n = 0$ on the grid surface, where ξ - dimensionless coordinate (x, y), as well as the condition for convective heat transfer $T_t = T - T_0$. The chemical reaction was represented by the simplest chain mechanism (Chapter 4, system of equations (II)).

From the calculation results presented in Fig. 16, it can be seen that density fluctuations are actually observed in the area of the mesh obstacle. The physical interpretation of this phenomenon requires further research.

Modeling based on the Navier-Stokes equations for a compressible reacting medium also allows analyzing the influence of scale on the course of the process and establish the possibility of manifestation of scale effects, which were discussed in paragraph 2 of Chapter 3.

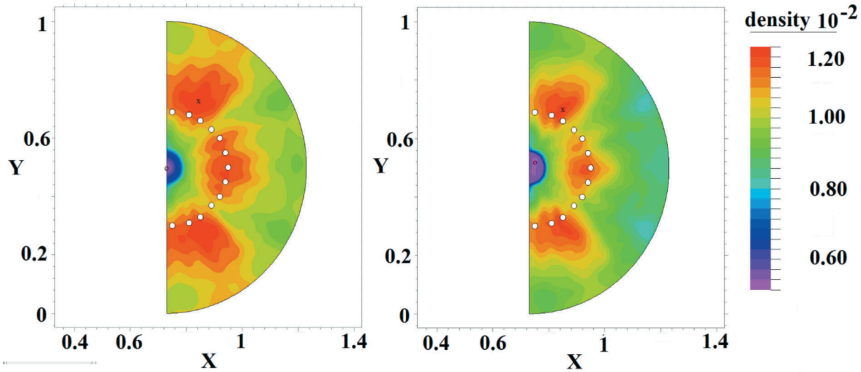


Figure 16. The emergence of gas flows in the area of a circular mesh obstacle after initiated ignition at successive times in 0.05 s (from left to right). Calculation based on the Navier-Stokes equations for a compressible reacting medium in the acoustic approximation

In this section, experimental data are presented that can be an argument in favor of the existence of a scale effect when hydrodynamic instability occurs. Let us first note that combustion processes in large volumes have attracted great interest in recent decades. Tests in large volumes are performed to characterize the explosion and detonation characteristics of hydrogen-air and hydrogen-oxygen mixtures. Most of the existing experiments use shock tubes for these types of explosions. A small part of these works is devoted to experiments in spherical geometry [33-36]. At the same time, one can conclude from the existing publications that modeling, and, accordingly, understanding, ignition and combustion in large volumes in the presence of mesh obstacles are still at an early stage. In particular, this is due to the lack of experimental data because of the cost and danger of creating large-scale experimental stands.

The problem was solved by the finite element method [15]. The initial condition was $T = 10$ on a circle enclosed in a circular mesh obstacle (Fig. 17). The boundary conditions were $C_{\xi} = 0, u = 0, v = 0, p_{\xi} = 0, n_{\xi} = 0$ at the reactor wall and $n = 0$ at the grid surface for Fig. 17, where ξ - dimensionless coordinate (x, y) , as well as the condition for convective heat transfer $T_i = T - T_0$. The chemical reaction was represented by a single Arrhenius reaction (Chapter 4, system of equations (II)).

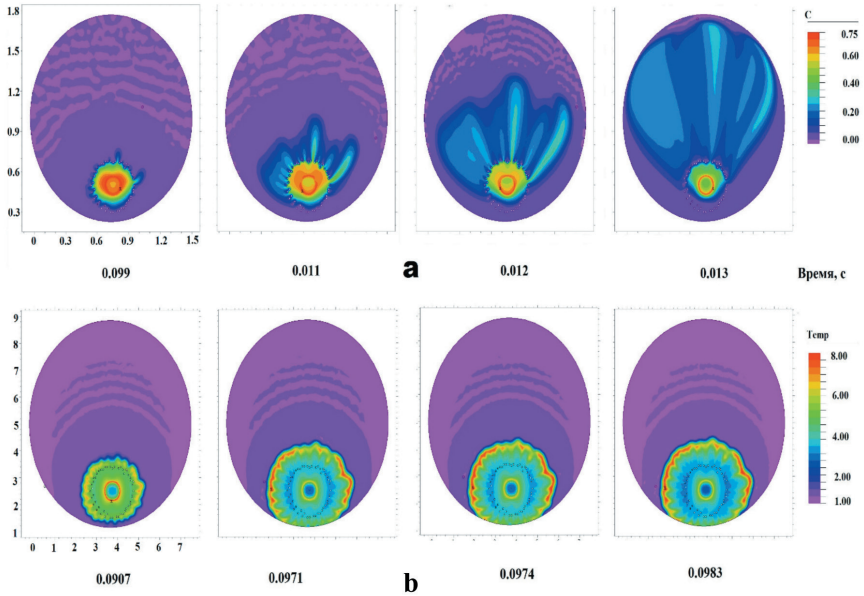


Figure 17. Calculation of flame penetration through the mesh obstacle, model scale

a) is 5 times smaller than model b). Figure a) shows the propagation of the front with respect to the concentration of the initial substance

The dependences of the path X , which the flame front passes (estimated by the largest value of the y coordinate at the temperature front) after the mesh obstacle, on time are illustrated in Fig. 18.

It is seen from Fig. 18 (dependences 1 and 3) that under the condition $n_{\xi} = 0$ on the surface of the mesh (dependence 3), that is, the mesh is chemically inert, the flame begins to propagate outside the mesh earlier than under the condition $n = 0$ on the surface of the mesh, that is, when the mesh is chemically active. In other words, it provides effective destruction of active intermediate combustion products (dependence 1). The result obtained is in qualitative agreement with the experimental dependences shown in Figs. 11 IIb and 13b Chapters 4.

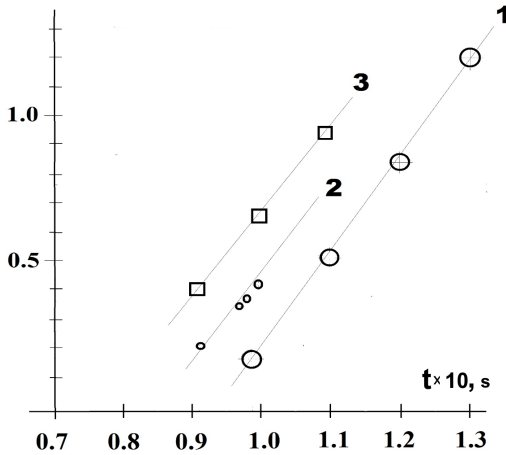


Figure 18. Dependences of the path X , which the flame front passes (estimated by the largest value of the y coordinate at the temperature front) after the mesh obstacle, on time. 1 - Fig. 16

a); 2 - Fig. 16b), all X values are divided by a scale factor of 5; 3 - Fig. 16a), but $n_{\xi} = 0$ on the mesh surface

It also follows from Fig. 18 that the propagation velocities of the combustion front, taking into account the scale factor, are practically the same. This means that within the framework of the acoustic approximation of the Navier-Stokes equations for a compressible reacting medium with one reaction in the form of Arrhenius, one should not expect the manifestation of scale effects.

Let us pay attention to the fact that in order to describe the quantitative regularities of the penetration of the flame front through a single hole, it is necessary to analyze the three-dimensional model. At the same time, the results of two-dimensional modeling are in qualitative agreement with the experimentally observed regularities.

We briefly summarize the results obtained in this section.

It has been shown experimentally that below the limit of penetration of the flame of a dilute methane-oxygen mixture through a flat obstacle with a single hole, the flame does not penetrate through the confuser, but penetrates through the diffuser. Such a qualitative difference from the process of flame penetration through a plane obstacle with a central hole according to numerical modeling using the dimensionless Navier-Stokes equations for a reacting compressible medium in the low Mach number approximation indicates a noticeable role of the interaction of acoustic vibrations in the reactor containing an obstacle with a propagating combustion front.

In addition, the simulation performed in small volumes suggests that in the event of an emergency, the flame will not penetrate through the open valve located in the center of the confuser located in the pipe. In this case, the most effective double-sided flame-arrester in the pipe can be a system of two confusers, the funnels of which are located on the pipe axis along the gas flow and against it. It is because an emergency can occur before and after the obstacle. A hole or valve can be located in the middle.

It should be noted that the results obtained when visualizing the penetration of a flame through obstacles of various shapes are important for solving explosion safety problems in volumes with complex geometrical arrangements.

§ 3. Factors determining a length of a flame jump after penetration through a small hole

One of the oldest unsolved problems in fluid mechanics is the theoretical description of the occurrence and growth of disturbances in laminar flow, which lead to turbulent flow. This extremely complex process is not fully understood at this time. Despite many systematic experimental and theoretical studies, the reason for the violation of the laminarity of the gas flow, the appearance of turbulence, for example, in the presence of obstacles in round pipes, remains unclear [37, 38].

In the event of ignition after an emergency in the gas infrastructure in an industrial or civil facility, pressure buildup due to flame acceleration because of the flame front turbulence can endanger the integrity of the building and the life of personnel [2, 8, 28, 39].

Although the main features of flame acceleration have been investigated by various authors [6, 7, 9, 40], the array of reliable experimental data obtained by high-resolution measurement methods that determine such process variables as density, temperature, velocity, and concentration of active particles is still relatively small. In particular, this is because the required resolution in time and space cannot be easily achieved. Only at the present time the use of inertialess optical methods has become widespread for the study of fast transient processes [2].

It should be noted that in [9, 40], the study of combustion of lean mixtures of hydrogen with air was carried out in a cylindrical tube separated by an obstacle with a small hole in the center. The studies have shown that the attenuation of a hydrogen flame when propagating through a small hole can occur at concentrations much higher than the concentration limit of flammability of the mixture. In addition, it was experimentally shown [14] that an acoustic resonator (Helmholtz resonator) connected to a cylindrical reactor can provide significant flame acceleration upon initiated ignition of a lean (15%) mixture of hydrogen and oxygen near the detonation limit. These data are important both for solving explosion safety problems and for developing calculation methods for simulating and establishing the causes of the accidents described above.

It was shown above that the ignition of a diluted stoichiometric methane-oxygen mixture (total pressure up to 200 Torr) after a single obstacle with a small round hole is observed at some distance after the obstacle, and not immediately after it. The mesh sphere as an obstacle leads to an increase in the magnitude of the "jump" of the flame through the obstacle in comparison with the round hole. The symmetry of the described obstacles made it possible to use 2D modeling for high-quality calculations, however, modeling the penetration of flame through rectangular holes involves 3D analysis. For this purpose, it is necessary to obtain reliable experimental data on the penetration of the flame front (FF) through a narrow rectangular opening.

It was shown in [12, 41] that the active centers of combustion of methane and hydrogen, which determine the propagation of the flame, have a different chemical nature. In other words, the rate of termination of active intermediate combustion centers on the surface of the obstacle makes a significant contribution to the penetration of the FF through the obstacle in the case of the mixtures of natural gas with air, but it is insignificant in the propagation of a hydrogen flame.

The results of experiments on flame propagation through obstacles with spherical and rectangular holes placed in a cylindrical channel are shown below. The purpose of this section was to establish the peculiarities of FF penetration through rectangular versus round holes using high-speed color flame filming and gas flow visualization when a fine inert powder is illuminated in the flow with a flat laser beam. In this section, the phenomenon of acceleration of an initially slow flame of stoichiometric methane-air mixtures diluted with inert additives by single obstacles of various geometric shapes is investigated.

The flame propagation in stoichiometric mixtures of methane with oxygen, diluted with CO_2 and Kr at initial pressures in the range of 100-200 Torr and a temperature of 298 K was investigated in an evacuated horizontally located cylindrical quartz reactor 70 cm long and 14 cm in diameter. The reactor was fixed in two stainless steel locks equipped with holes for gas evacuation and a safety lock that opened outward when the total pressure in the reactor exceeded 1 atm [13]. A pair of spark discharge electrodes were located at the left end of the reactor (Fig. 19).

Thin obstacles 14 cm in diameter with rectangular holes (7 and 10 mm wide and 65 mm long) and and spherical ones 20 and 25 mm in diameter were placed vertically in the center of the reactor. In some experiments, a rectangular hole 10 mm wide and 65 mm long was covered with an iron mesh with cells 0.5 mm in size (wire diameter 0.25 mm). The possibility of registering the gas flow was provided by illumination of ultrafine MgCO_3 particles carried away from the shelf (14) with a flat laser beam as the flame propagated from left to right (Fig. 19). The combustible mixture (15.4% CH_4 + 30.8% O_2 + 46% CO_2 + 7.8% Kr) was preliminarily prepared. CO_2 was added to reduce the FF velocity and thereby improve the quality of the filming. Kr was added to reduce the discharge threshold. The reactor was filled with a combustible mixture to the required pressure. Then, the flame was

initiated by a spark discharge ($J = 1.5 \text{ J}$). The dynamics of ignition and FF propagation was recorded from the side of the reactor (Fig. 19) with a Casio Exilim F1 Pro color high-speed digital video camera (frame rate 600 s^{-1}) [13, 14]. The video file was saved in the computer memory, and then it was digitally processed [32]. In the experiments, reagents of the chemically pure grade were used.

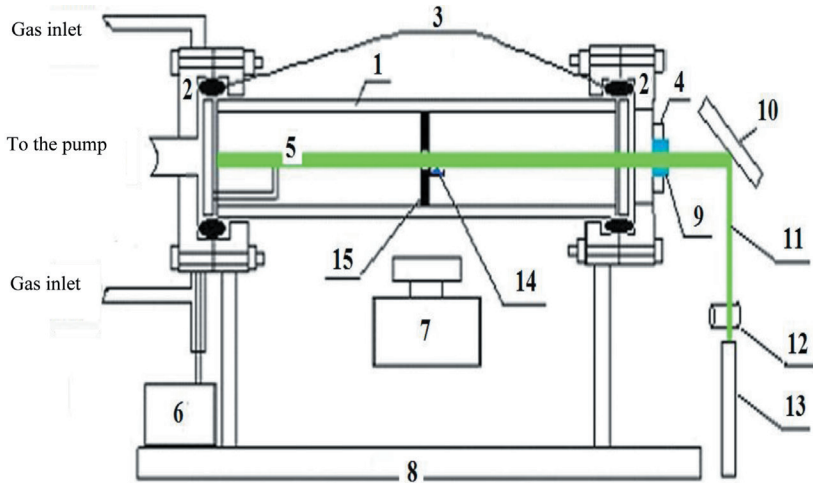


Figure 19. Experimental setup. (1) quartz reactor 14 cm in diameter and 70 cm long, (2) stainless steel airlock, (3) Viton gasket, (4) stainless steel door, (5) spark ignition electrodes, (6) power supply, (7) high-speed video camera, (8) rail, (9) optical window, (10) swing mirror, (11) flat laser beam, (12) short-focus-lens, (13) semiconductor laser (534 nm), (14) reservoir with ultrafine powder MgCO_3 , (15) an obstacle with a hole. The pressure sensor is located on the door (4)

The sequences of video frames of the penetration of the combustible mixture flame through round and rectangular holes are shown in Fig. 20.

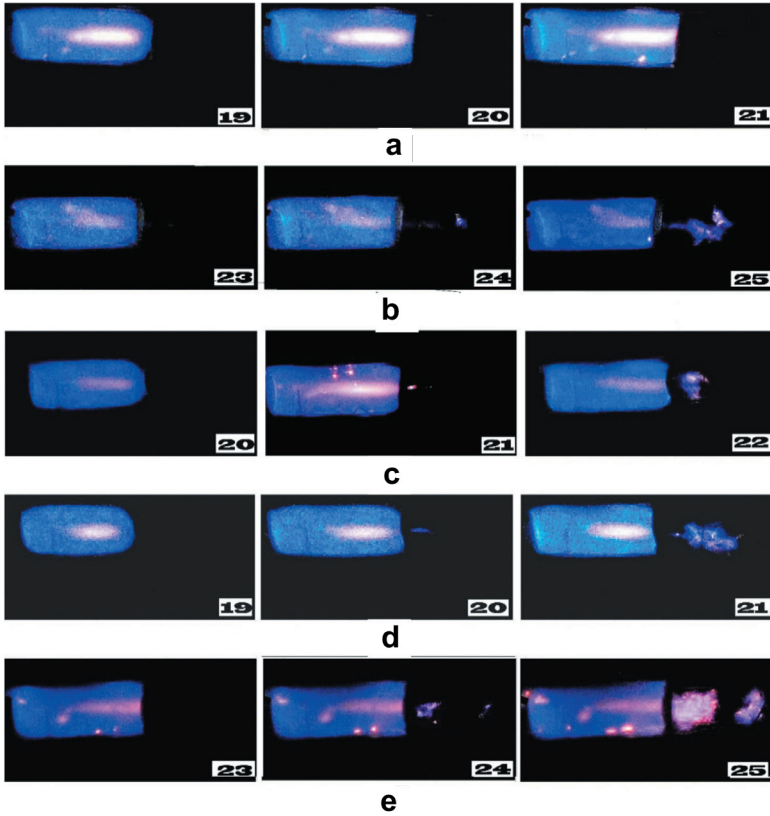


Figure 20.

a) - high-speed filming of FF propagation through a rectangular hole 7 mm wide and 65 mm long,

b) - high-speed shooting of the FF propagation through a round hole 25 mm in diameter,

c) - high-speed shooting of FF propagation through a rectangular hole 10 mm wide and 65 mm long (the slit is located vertically),

d) - high-speed shooting of FF propagation through a rectangular hole 10 mm wide and 65 mm long (the slit is located horizontally)

e) - high-speed shooting of the FF propagation through a rectangular hole 10 mm wide and 65 mm long, covered with a mesh (the slit is placed vertically),

The initial pressure is 170 Torr. The number on the frame corresponds to the sequence number of the frame after spark ignition. (frame rate 600 s^{-1}).

A video sequences of flame propagation through a 7 mm wide rectangular hole is shown in Fig. 20a. As can be seen from the figure, the FF does not penetrate

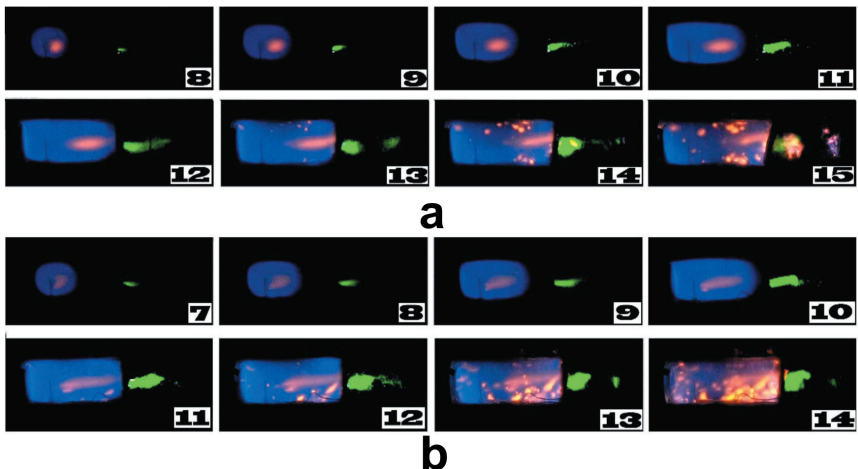
through the obstacle, which indicates the existence of a limit for flame penetration along the width of the slit, since the FF penetrates through a slit 10 mm wide (Fig. 20c). Ignition after the penetration of the FF through the obstacle does not occur immediately after the obstacle. The first ignition site is observed in the immediate vicinity of the obstacle surface, in contrast to the penetration of the FF through a round hole (Fig. 20b), see also [13], when a noticeable “flame jump” is observed after the obstacle (“flame jump” is the distance, at which there is a flame front behind the obstacle, see the previous paragraph). As can be seen from Fig. 20e (frames 24, 25), in the presence of a mesh on a rectangular obstacle 10 mm wide and 65 mm long, a second “flame jump” is observed.

It should be noted that the accumulation of free radicals behind the obstacle is observed experimentally [7-9]. Mixing these radicals with unreacted gas obviously increases the explosiveness of the mixture. This indicates the need to take into account the main features of the combustion chain mechanism in 3D numerical modeling, as was done during the analysis of the two-dimensional problem in [13].

The results of registration of the gas flow by illuminating the $MgCO_3$ particles blown out by the gas flow from reservoir 14 (Fig. 19) with a flat laser beam after round and rectangular holes are shown in Fig. 21.

As seen from Fig. 21a, b, d, the flux density after the obstacle has two maxima: the first maximum is near the obstacle, the second maximum is observed noticeably farther from the obstacle surface. It can be seen that the distance of the appearance of the second density maximum correlates with the distance of the appearance of the “flame jump” through the corresponding obstacle.

The results of filming a gas flow through a rectangular hole 10 mm wide and 65 mm long and through the same hole, but closed with a metal mesh, are shown in Fig. 21c and Fig. 21d respectively.



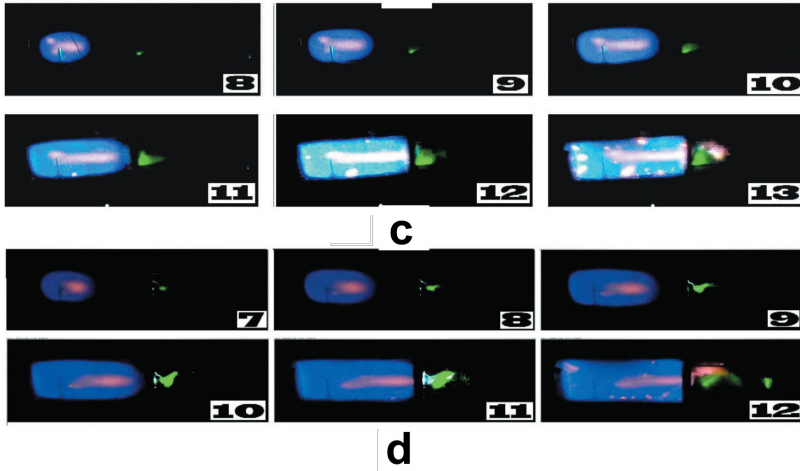


Figure 21. *High-speed filming with gas flow visualization:*

- a) - the propagation of the FF through a round hole 25 mm in diameter;
- b) - propagation of FF through a rectangular hole 10 mm wide and 65 mm long (the slit is located vertically);
- c) - FF propagation through a rectangular hole 10 mm wide and 65 mm long (the slit is located horizontally);
- d) - FF propagation through a rectangular hole 10 mm wide and 65 mm long, closed by a mesh (the slit is placed horizontally).

The initial pressure is 170 Torr. The number on the frame corresponds to the sequence number of the frame after spark ignition (frame speed - 300 s⁻¹).

As in the case of FF penetration through a round hole, the flux density after the obstacle shows two maxima. The first maximum is near the obstacle, the second maximum is observed noticeably farther from the obstacle surface (Fig. 21c frame 12, Fig. 21d frames 11, 12).

As can be seen, in the presence of a mesh, the second “flame jump” is observed at a greater distance. Consequently, a correlation between the position of the second density maximum and the magnitude of the “flame jump” also exists, i.e. in the presence of a mesh, the flame occurs at a greater distance both after the round and after the rectangular holes compared to the value of the "flame jump" through the hole without the mesh.

To identify the main factors affecting the length of the "flame jump" when the FF penetrates through small holes, let us compare the features of the FF penetration through round and rectangular holes. It can be seen from Fig. 21 that long before the FF contact with the obstacle, small particles illuminated by the laser beam already begin to move (Fig. 21a, frame 8, Fig. 21b, frame 7, Fig. 21c, frame 8, Fig. 21d, frame 7). In other words, an initially undisturbed submerged jet is formed in

the gas behind the obstacle (Fig. 21c, frames 8-10, Fig. 21d, frames 7-9).

After the contact of the FF with the obstacle, the primary ignition sites (local volumes containing gas heated to the combustion temperature and active combustion centers [7-9]) arise in this submerged jet.

It can be assumed that the primary ignition centers move in the submerged jet during the ignition delay period (induction period), and then ignition occurs. However, the above mentioned does not agree with [9], where it is stated that when the flame front passes through the hole, a high degree of flow turbulence leads to the suppression of the flame behind the hole in the region before combustion occurs.

Let us estimate approximately the time t of motion of the primary source in a submerged jet in the approximation of an incompressible medium [42]. For the axial component of the velocity v_L in a parallel flow $v_L/v_0 = 1.2/\sqrt{(0.1x/L - 0.41)}$ in an axisymmetric flow $vR/v_0 = 0.96/(0.07x/R - 0.29)$. Here v_0 - is the flame velocity at the moment of contact between the FF and the obstacle, x is the coordinate, L is the width of the rectangular slot, R is the radius of the round hole, and the numerical values are empirical parameters from [42]. Then $t_L = \int_{0.41}^x dx/(v_L/v_0)$

and, accordingly, the ratio t_R/t_L [42] for the same values of the upper limit of integration $x = 10$ is ~ 4 ; for $x = 3$, this ratio is ~ 2 . This means that in the case of a parallel flow, the primary site moves by a distance x during a time that is much less than in the case of an axisymmetric flow. Therefore, during the ignition delay period, the primary site will move farther from the obstacle than in the case of an axisymmetric flow. On the other hand, the experiment shows (cf. Figs. 20b and 20d) that ignition occurs earlier in the case of the penetration of the FF through a rectangular hole rather than a round one. This means that if the “flame jump” were determined by the ignition delay period, then the length of the “flame jump” would be shorter for a round hole, which contradicts the experiment.

Another explanation could be as follows. Lemanov et al. in [43] determined the coordinate of the laminar-turbulent transition in a submerged jet for various values of the Reynolds number by means of visualization and anemometric measurements. They showed that the length of the laminar section in a plane flow is much shorter (by a factor of 2–5) than in an axisymmetric one. This suggests that the magnitude of the “flame jump” in the submerged jet formed after the hole is determined by the time of occurrence of the transition from laminar to turbulent flow, and not by the delay time of the ignition of the combustible mixture.

The relatively lean influence of the rate of combustion reaction on the magnitude of the flame jump is another reason in favor of the above explanation. The comparative contribution of gas-dynamic and chemical factors to the magnitude of the flame jump was approximately estimated using numerical modeling based on the analysis of the Navier-Stokes equations for a compressible reacting medium in the approximation of a small Mach number. These equations were proposed

in [15-19] and they describe the propagation of a flame in a two-dimensional channel. The solution of these equations showed qualitative agreement between the calculations and experiments [13, 26]. The penetration of flame through an axisymmetric obstacle in three channels of different widths was analyzed. The system of Navier-Stokes equations in a compressible reacting medium in the acoustic approximation was solved by the finite element method using a package (FlexPDE 6.08, 1996-2008 Inc. [24]). The simplest chain mechanism was used [16, 23, see also Chapter 4].

The results of numerical simulation of flame penetration through the hole are shown in Fig. 22. The boundary conditions (including the hole) were $C_\xi = 0, u = 0, v = 0, p_\xi = 0, n_\xi = 0$ (Fig. 22 I) $n = 0$ (Fig. 22 II), and the condition of convective heat transfer $T_l = T - T_0$ where ξ - dimensionless coordinate (x, y). The ignition initiation condition was $T = 10$ at the right border of the channel; there was a vertically located obstacle in the channel with an axisymmetric hole.

As can be seen from the calculations, the results of calculations for $n_\xi = 0$ (the calculation is shown in Fig. 22 I) and $n = 0$ (the calculation is shown in Fig. 22 II) show that the smaller the channel width, the shorter the “flame jump” is.

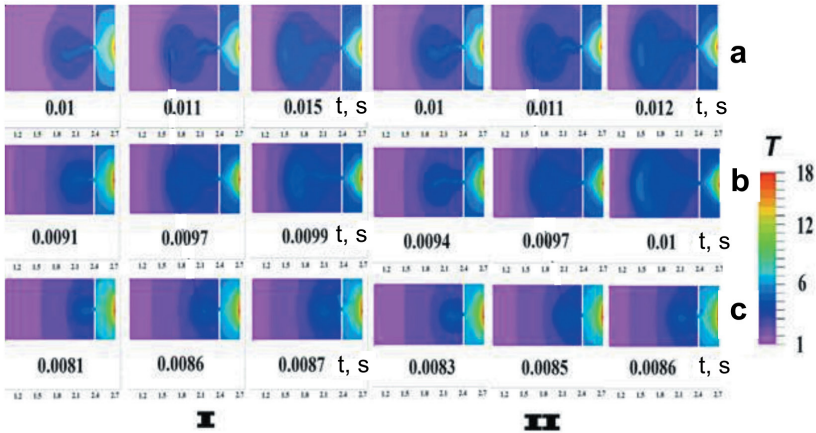


Figure 22. Results of calculating the process of flame propagation through the hole, a, b, c - different values of the channel width (1, 0.8, 0.6 in dimensionless units, respectively)

I - the change in the dimensionless temperature of flame propagation through the hole for $n_\xi = 0$;

II - change in the dimensionless temperature of flame propagation through the hole for $n = 0$;

The dimensionless temperature scale T is shown on the right.

In addition, in the case (Fig. 22 II), the termination of active combustion centers occurs at each collision of an intermediate particle with a wall (the so-called diffusion region of chain termination [22]); the rate of termination of active centers is higher than for the $n_{\xi} = 0$ (the so-called kinetic region of chain termination [22], Fig. 22 I). Therefore, the value of the ignition delay period for $n = 0$ should be greater than for $n_{\xi} = 0$ [22], and the value of the "flame jump" should be correspondingly larger for $n = 0$. This contradicts the calculations. On the other hand, experimental data [44] demonstrate an increase in the time of occurrence of a laminar-turbulent transition in pipes with an increase in the pipe diameter. As follows from Fig. 22, the results of the numerical experiment agree precisely with the experimental data [44], which also testifies in favor of the main contribution of gas-dynamic factors to the magnitude of the "flame jump".

§ 4. Spectral features of emission of methane-oxygen flames under conditions of penetration through obstacles. The possibilities of the 4D spectroscopy method

It can be seen that after ignition is initiated by a spark discharge at the left end of the pipe from the above sequences of video frames (see Fig. 7a, frame 23, as well as the results of works [12, 45-47]), the "blue" FF propagates from left to right and reaches the obstacle. Then a secondary "yellow" FF occurs. This means that the degree of conversion in the blue FF and active intermediate products of methane combustion after the flame passes through the obstacle initiate the propagation of the "yellow" FF.

The results obtained correlate with the results of [47], where it was shown that the FF in a hydrocarbon-air mixture in a heated cylindrical reactor is always of yellow color ("hot" flame, Fig. 1b [47]), although the flame at the initial room temperature in the same mixture and in the same blue reactor is of blue color ("cold" flame, Fig. 1a, b [47]). It should be noted that the color of the flame is due to the emission of CH (431 nm) and, possibly, CH₂O (470 nm) radicals. The yellow color of the hot flame is caused by the emission of excited Na atoms or a lack of an oxidizing agent, i.e. the formation of soot [12]. A block of reactions of hydrocarbon oxidation to CO is considered [22] to be realized in a "blue", "cold" flame, and in a "yellow", "hot" flame, the next block of reactions of CO oxidation to CO₂ is realized.

This means that it is possible to separate these two macrokinetic processes in space in experiments on the penetration of flames through obstacles.

The complex obstacles described in Section 2 consisted of a flat obstacle with a diameter of 14 cm (reactor diameter) with a single hole 25 mm in diameter and a second flat obstacle with a diameter of 14 cm with a single hole 25 mm in diameter (obstacle C §2 of this Chapter) or a second flat obstacle with a diameter of 14 cm with a single hole with a diameter of 25 mm, covered with a flat mesh (obstacle D §2 of this Chapter). The second obstacle was located at a distance of the magnitude

of the “flame jump” after a flat obstacle 14 cm in diameter with a single hole 25 mm in diameter. According to experimental data, this distance was 12 cm.

In the experiments described in this section, along with high-speed filming, the combustion process was recorded by the 4D spectroscopy method (1-time, 2-wavelength, 3-spectrum intensity at a given wavelength, 4-coordinate of the emitting fragment of the light source) through the side surface of the quartz reactor (Fig. 23).

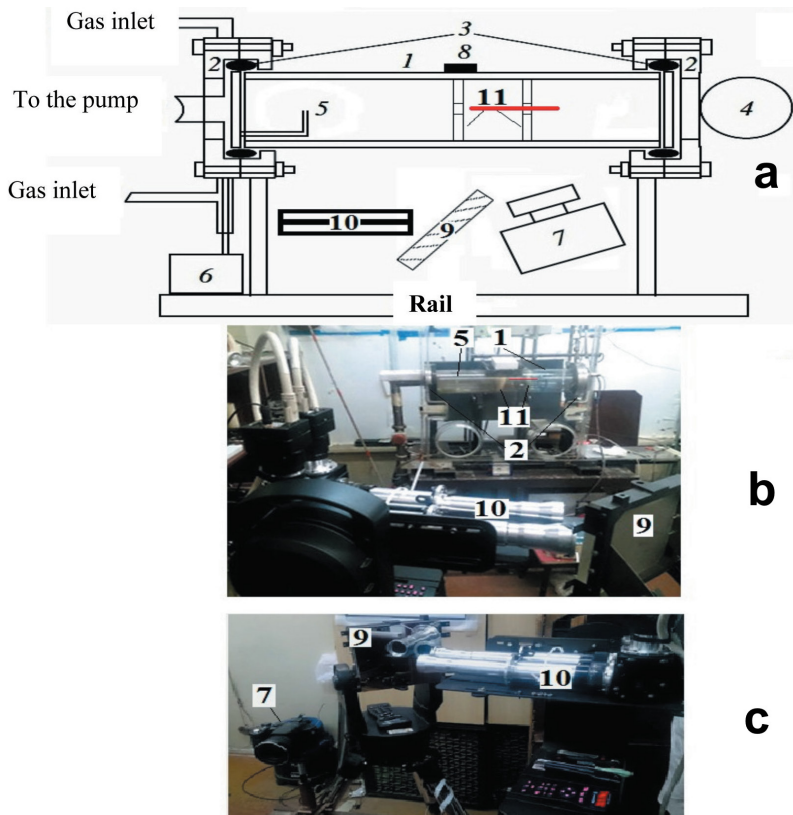


Figure 23. Using hyperspectrometers to study flames:

a) - (1) quartz reactor, (2) stainless steel airlocks, (3) silicone gasket, (4) safety door, (5) spark ignition electrodes, (6) power supply, (7)) high-speed movie camera, (8) microphone, (9) - rotating mirror, (10) - hyperspectrometers unit, (11) - obstacles,

b) and c) - photographs of the setup. In Fig. 23a) and b) the strip along which the 4D spectral survey was carried out is marked in red. The width of this strip is about 1 mm

In the experiments described in this section, video recording of the combustion was also carried out with a single color high-speed video camera Casio Exilim F1 Pro (frame rate - 60 - 1200 s⁻¹) simultaneously with registration with hyperspectrometers, or simultaneously with two Casio Exilim F1 Pro cameras from the side of the reactor, as described above. (The resulting video files were recorded in the computer memory and then frame-by-frame processing was carried out) (Fig. 24).

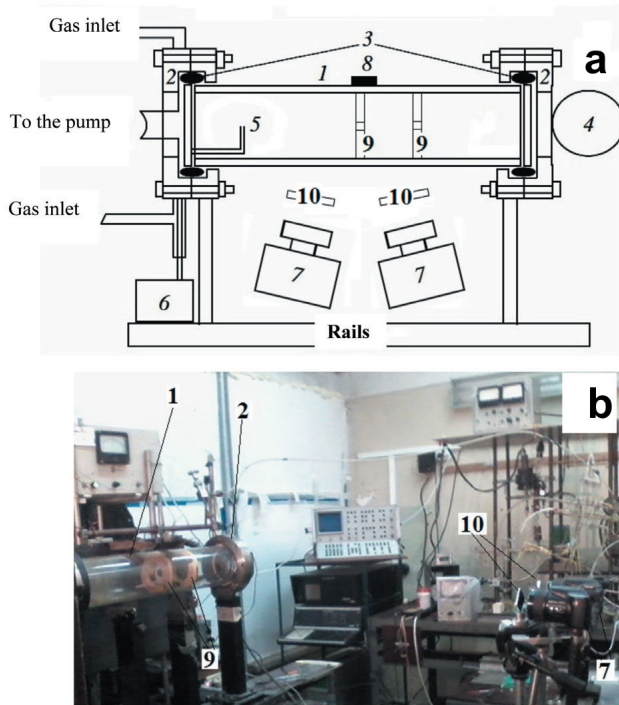


Figure 24. *Experimental setup*

- a) - (1) quartz reactor, (2) stainless steel gateways, (3) silicone gasket, (4) safety door, (5) spark ignition electrodes, (6) power supply, (7) high-speed movie camera, (8) microphone, (9) - obstacle, (10) - interference filter,
 b) - photograph of the experimental setup.

The design and use of the VID-IK3 hyperspectrometer (*push broom* type) [45, 46] and its modified version are described in detail in Chapter 2 and Chapter 4. The characteristics of the hyperspectrometers are given in Table 1 of Chapter 2. The appearance of both instruments installed on the rotating device, is shown in Fig. 23, and the construction (the same for both units) is shown in Chapter 2.

The spectrum (a) and the time-base sweep of the spectrum of the methane-oxygen flame (b) is shown in Fig. 25a, b. Bands in the region of 600 nm were observed in a hydrogen flame in [48]. Table 4 of Chapter 4 from [48] shows the assignment of the bands in Fig. 25 to water vapor, which is a product of the oxidation reaction of hydrogen and hydrocarbons.

The spectrum shown in Fig. 25, agrees with the literature data [22] and contains CH ($A^1\Delta-X^2\Pi$) bands in the 431 nm region, C_2 ($A^3P_g-X^3P_u$) (1-0, 0-0, 0-1 transitions) in the 470 - 570 nm region [48] and emission bands of water vapor (for example, (1, 2, 0), (3, 0, 0) [49]). It should be noted that the CH and C_2 bands refer to the contribution of the zone of intense chemical transformation (FF zone) [22] to the total spectrum, and the emission bands of water vapor - to the emission region of combustion reaction products.

Thus, the features of the flame spectrum in the visible region, namely the system of radiative bands of water in the region of 570 - 650 nm, along with the doublets of sodium (581 nm) and potassium (755 nm) atoms inherent in all hot flames [22], are related in this case to radiation from an area filled with combustion products.

It can be seen from Fig. 25b that the intensities of all spectral lines from the spectrum with the $x = 234$ coordinate to the spectrum with the $x = 1$ coordinate change symbatically. There is no situation when the intensity of the bands in one region of the spectrum increases in space and decreases in the other region of the spectrum. This is because the observed spectral lines belong only to the reaction products or appear in the zone of the reaction products (Na, K). Thus, it was observed by 4D spectroscopy that after the obstacle (see Fig. 23) a high-temperature mechanism of methane combustion is realized, accompanied by the excitation of atomic lines of alkali metals.

The establishment of the regularities of the formation of intermediate particles in the low-temperature region of combustion (before the obstacle) was also carried out using two high-speed movie cameras Casio Exilim F1 Pro, equipped with interference filters (Fig. 23a, b). This made it possible not only to increase significantly the sensitivity of the measuring equipment, but also to reveal the spatial features of the formation of intermediate combustion particles.

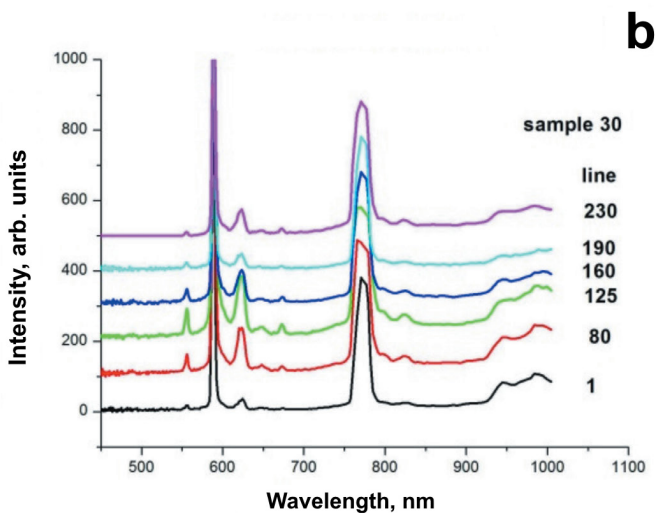
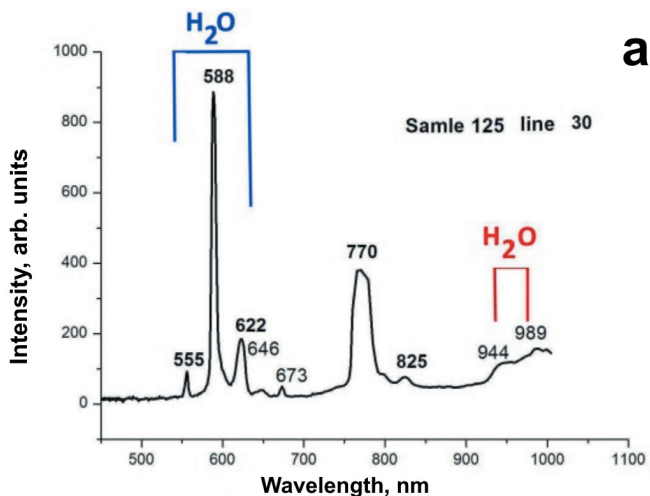


Figure 25. Emission spectra of the flame of a mixture of 15.4% NG + 30.8% O₂ + 46% CO₂ + 7.8% Kr after the first obstacle at an initial pressure of 180 Torr
 a) - x = 125, y = 30;
 b) - x = 30, y = 80, 125, 160, 190, 230. The registration rate is 300 spectra/s.

We used simultaneously two interference filters 435 nm CH (A¹ Δ-X² Π) (transmission at a maximum of 40%, ± 16 nm) and 520 nm C₂ (A³P_g-X³P_u) (transition 0-0) (transmission at a maximum of 40%, ± 15 nm) to establish the features

of the appearance in time and space of active intermediate particles CH and C₂. Combinations of glass filters were also used for 435 nm (transmission at maximum 70%, ± 35 nm), 520 nm (transmission at maximum 35%, ± 60 nm), and 590 nm for the line of Na atoms (transmission at maximum 70%, ± 25 nm) in order to establish the features of the appearance in time and space of active intermediate particles and self-heating. This is because the radiation of Na atoms is caused by their thermal excitation [22], which occurs at a flame temperature above 1200 °C [50].

The results of high-speed video filming of the flame penetration of a combustible mixture of 15.4% PG + 30.8% O₂ + 46% CO₂ + 7.8% Kr at an initial pressure of 180 Torr through a flat obstacle 14 cm in diameter with a single hole 25 mm in diameter are demonstrated in Fig. 26. There is also a second flat obstacle with a single hole 25 mm in diameter, covered with a flat mesh (obstacle D §2 of this Chapter), recorded without light filters at a rate of 300 frames/s in comparison with the registration of the CH band (A¹ Δ – X² Π) b) and the C₂ band (A³P_g – X³P_v) (transition 0-0) c), which are registered at the same speed.

It can be seen from Fig. 26 that before the obstacle there is a blue glow in the reactor due to the emission of CH radicals, C₂ radicals in recorded quantities are observed only after the first obstacle.

It is also clearly seen from Fig. 27 where the results of recording the radiation of a propagating flame using glass filters in the wavelength range of 435 nm, 520 nm, and 590 nm are presented, that both the appearance of C₂ radicals in recorded quantities and the main heat release in the process are observed after the first obstacle, i.e. after turbulization of the gas flow.

The obtained result means that the used experimental technique makes it possible to separate in time and space “cold” and “hot” flames in a single experiment. This result is also important for the verification of numerical models of methane combustion.

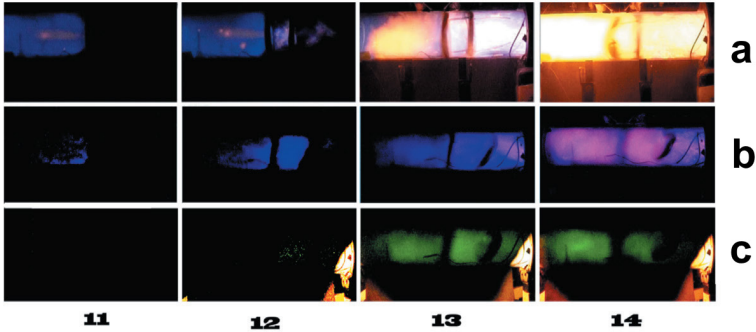


Figure 26. High-speed filming of the propagation of the FF of the combustion of a mixture of 15.4% NG + 30.8% O₂ + 46% CO₂ + 7.8% Kr at an initial pressure of 180 Torr through a combined obstacle consisting of a flat obstacle with a diameter of 14 cm with a single hole 25 mm in diameter. There is a second flat obstacle with a single hole with a diameter of 25 mm, covered with a flat mesh (obstacle D); a) - without filters, b) - interference filter 435 nm, c) - interference filter 520 nm (shooting speed 300 frames/s). The number on the frame corresponds to the sequence number of the frame after the moment of ignition initiation; other position of obstacles after penetration of flame in Fig. 23a and Fig. 23a, b is due to the fact that these are different experiments; Fig. 23b, c were obtained in the same experiment.

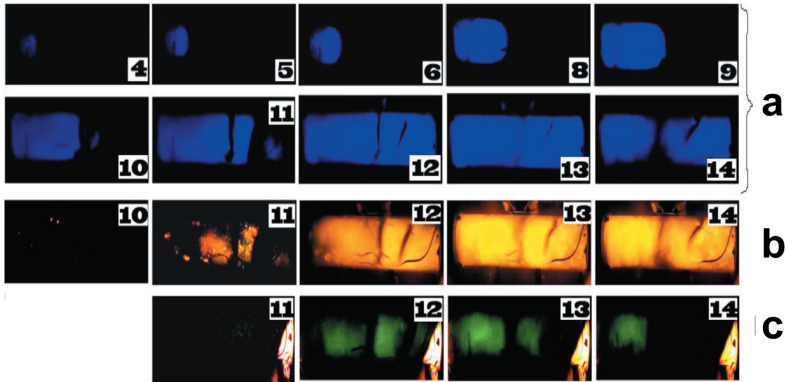


Figure 27. High-speed filming of the propagation of the FF of the combustion of a mixture of 15.4% NG + 30.8% O₂ + 46% CO₂ + 7.8% Kr at an initial pressure of 180 Torr through a combined obstacle consisting of a flat obstacle with a diameter of 14 cm with a single hole 25 mm in diameter. There is a second flat obstacle with a single hole with a diameter of 25 mm, covered with a flat mesh (obstacle D); glass filters are used,

- a) - glass filter in the region of 435 nm (transmission at a maximum of 70%, ± 35 nm),
- b) - a glass filter in the region of 520 nm (transmission at a maximum of 35%, ± 60 nm),
- c) - combined glass filter in the region of 590 nm (transmission at a maximum of 70%, ± 25 nm). The shooting speed is 300 frames/s. The number on the frame corresponds to the sequence number of the frame after the moment of initiation.

Conclusions for Chapter 6

It has been shown experimentally that in the case of flame penetration through an obstacle considered in this Chapter, gas-dynamic factors, for example, flame turbulization, can determine the kinetics of the process, including the transition of low-temperature combustion of hydrocarbons to a high-temperature regime.

It has been established that the flame front after a single obstacle does not arise in the immediate vicinity of the obstacle. The first ignition site can be observed relatively far from the obstacle surface. It is shown that the use of a mesh sphere as an obstacle leads to an increase in the length of the flame "jump" behind the obstacle in comparison with a round hole. It is shown that two or more obstacles, both spherical and flat, noticeably suppress the propagation of the flame, which can be associated with both heat losses from the flame front and with heterogeneous termination of reaction chains at the obstacle. It has been experimentally shown that below the limit of the flame penetration of a dilute methane-oxygen mixture through a flat obstacle with a single hole, for an obstacle in the form of a funnel, the flame does not penetrate from the side of the funnel mouth, but penetrates from the side of the funnel nose. Numerical modeling of the Navier-Stokes equations for a compressible medium in the approximation of a small Mach number with the representation of a chemical process as a single reaction and the simplest chain mechanism made it possible to qualitatively describe the experimental features.

The features of the penetration of the flame front through rectangular holes in comparison with round holes were experimentally investigated by using color filming and visualization of a gas flow. It is shown that the length of the "flame jump" after the hole in the obstacle is mainly determined by the time of occurrence of the laminar-turbulent transition, and not by the ignition delay period.

It was found that C_2 radicals in detectable quantities and the main heat release in the process are observed by using 4D spectroscopy combined with high-speed color filming after the flame passes the first obstacle, i.e. after turbulization of the gas flow. The result obtained means that the technique used allows one to separate in time and space the "cold" and "hot" flames in a single experiment. The result obtained is also important for the verification of numerical models of methane combustion. In addition, the results obtained are important for solving explosion safety problems for volumes with complex geometrical arrangements.

References for Chapter 6

1. Chakraborty S., Mukhopadhyay A., Sen S. Interaction of Lewis Number and Heat Loss Effects for a Laminar Premixed Flame Propagating in a Channel. *International Journal of Thermal Sciences*. 2008. Vol. 47. No. 1. pp. 84-92.
2. Hargrave G. K., Jarvis S. J., Williams T. C. A study of transient flow turbulence generation during flame/wall interactions in explosions. *Meas. Sci. Technol.* 2002. Vol. 13. pp. 1036–1088.
3. Polezhaev V., Nikitin S. Thermoacoustics and heat transfer in an enclosure induced by a wall heating. 16th International Congress on Sound and Vibration. Kraków, Poland. 5–9 July 2009. pp. 2-8.
4. Moen I. O., Donato M., Knystautas R., Lee J. H. Flame acceleration due to turbulence produced by obstacles. *Combustion and Flame*. 1980. Vol. 39. No. 1. pp. 21-32.
5. Ibrahim S. S., Masri A. R. The effects of obstructions on overpressure resulting from premixed flame deflagration. *Journal of Loss Prevention in the Process Industries*. Vol. 14. No. 3. pp. 213-221. ISSN: 0950-4230. DOI: 10.1016/S0950-4230(00)00024-3
6. Salamandra G. D., Bazhenova T. V., Naboko I. M. Formirovaniye detonatsionnoy volny pri gorenii gaza v trubakh (Formation of a detonation wave during gas combustion in pipes). *Zhurnal Technicheskoi fiziki*. 1959. Vol. 29. pp. 1354-1359. (in Russian)
7. Ardey N., Mayinger, F. Highly turbulent hydrogen flames. *Energy and Environment Symposium*. Karadeniz Technical University, Trabson, Turkey. 1996. p. 679.
8. Durst B., Ardey N., Mayinger F. OECD/NEA/CSNI Workshop on the Implementation of Hydrogen Mitigation Techniques, Winnipeg, Manitoba. 1996. AECL-11762. p. 433.
9. Jourdan M., Ardey N., Mayinger F., Carcassi M. Influence of turbulence on the deflagrative flame propagation in lean premixed hydrogen air mixtures. *Heat Transfer. Proceedings of 11th IHTC, Kuongju, Korea*. 1998. Vol. 7. p. 295.
10. Gussak L. A., Turkish M. C. LAG Stratiff. Charge Engines. In: *Proceedings of the First Mechanical Conference Publication*. London. 1976. p. 137.
11. Naboko I. M., Rubtsov N. M., Seplyarsky B. S., Troshin K. Ya., Chernysh V. I. Rezhimy rasprostraneniya plameni pri gorenii bednykh vodorodo-vozdushnykh smesey v prisutstvii dobavok v usloviyakh tsentrpl'nogo initsirovaniya pri atmosfernom davlenii (Modes of flame propagation during combustion of lean hydrogen-air mixtures in the presence of additives under conditions of central initiation at atmospheric pressure). *Physical-Chemical kinetics in gas dynamics*. 2012. Vol. 13. No. 2. <http://chemphys.edu.ru/issues/2012-13-2/articles/311/>

12.. Naboko I. M., Rubtsov N. M., Seplyarskii B. S., Chernysh V. I., Tsvetkov G. I. *Interaction of Spherical Flames of Hydrogen-Air and Methane-Air Mixtures in the Closed Reactor at the Central Spark Initiation with Closed Meshed Obstacles*. *J. Aeronautics & Aerospace Engineering*. 2013. 2:5. <http://dx.doi.org/10.4172/2168-9792.1000127>

13. Rubtsov N. M. *The Modes of Gaseous Combustion*, Springer International Publishing. 2016. 302 p

14. Naboko I. M., Rubtsov N. M., Seplyarskii B.S., Chernysh V. I., Tsvetkov G. I. *Influence of an acoustic resonator on flame propagation regimes in spark initiated H_2 combustion in cylindrical reactor in the vicinity of the lower detonation limit*. *Mendeleev Communications*. 2013. Vol. 24. No. 1. p. 50-52. DOI: 10.1016/j.mencom.2013.12.017

15. Alasard T. *Low Mach number limit of the full Navier-Stokes equations*. *Archive for Rational Mechanics and Analysis*. 2006. *Archive for Rational Mechanics and Analysis*. 180(1):1-73. DOI: 10.1007/s00205-005-0393-21

16. Nicoud F. *Conservative High-Order Finite-Difference Schemes for Low-Mach Number Flows*. *Journal of Computational Physics*. 2000. Vol. 158. No. 1. pp. 71-97. <https://doi.org/10.1006/jcph.1999.6408>

17. Akkerman V., Bychkov V., Peichenko A., Eriksson L.-E, *Flame oscillations in tubes with nonslip at the walls*, *Combustion and Flame*, 2006, V.145. pp. 675-687. *Combustion and Flame*. 2006. Vol. 145. No. 4. pp. 675-687. DOI: 10.1016/j.combustflame.2006.01.013

18. Majda A. *Compressible fluid flow and systems of conservation laws in several space variables*. *Applied Mathematical Sciences*. Springer-Verlag, New York. Vol. 53. 1984. 172 p.

19. Abugov D. I., Bobyle, V. M. *Teoriya i raschet raketnykh dvigatelei tverdogo topliva (The theory and calculation of the solid-propellant rocket engines)*. Moscow, Mashinostroenie. 1987. 272 p. (in Russian)

20. Clavin P. *Premixed combustion and gasdynamics*. *Annual Review of Fluid Mechanics*. 1994. Vol. 26. pp. 321-352.

21. Clanet C., Searby G., Clavin P. *Primary acoustic instability of flames propagating in tubes: cases of spray and premixed gas combustion*. *J. Fluid Mech*. 1999. Vol. 38. pp. 157-197. DOI: 10.1017/S0022112099004231

22. Lewis B., Von Elbe G. *Combustion, Flames and Explosions of Gases*. New York, London. Acad. Press. 1987. p. 66.

23. van Kampen J. F. *Acoustic pressure oscillations induced by confined turbulent premixed natural gas flames*. PhD thesis. University of Twente, Enschede, The Netherlands, March 2006. ISBN 90-365-2277-3. Printed by Febodruk BV, Enschede, The Netherlands. 274 p.

24. Backstrom G. *Simple Fields of Physics by Finite Element Analysis*. (Paperback). GB Publishing. 2005. 324 p.

25. Omar D. Lopez, Robert Moser, Ofodike A. Ezekoye. *High-Order Finite Difference Scheme For The Numerical Solution Of The Low Mach-Number Equations. Conference: ENIEF 2006 XV Congreso sobre Métodos Numéricos y sus. Santa Fe, Argentina Volume: Mecánica Computacional. Vol. XXV. pp. 1127-1137.*

26. Rubtsov N. M., Seplyarskii B.S., Naboko I. M., Chernysh V.I., Tsvetkov G.I., Troshin K. Ya. *Non-steady propagation of single and counter flames in hydrogen–oxygen and natural gas–oxygen mixtures in closed cylindrical vessels with spark initiation in initially motionless gas Mendeleev Communications. 2014. Vol. 24. No. 5. pp. 308-310. DOI: 10.1016/j.mencom.2014.09.021*

27. Griffiths J. F., Barnard J. A. *Flame and Combustion. 3rd Edition. CRC Press. 1995. 328 p.*

28. Abdel-Gayed R. G., Bradley D. *Criteria for turbulent propagation limits of premixed flames. 1985. Combust. Flame. Vol. 62. pp. 61-68. [https://doi.org/10.1016/0010-2180\(85\)90093-8](https://doi.org/10.1016/0010-2180(85)90093-8)*

29. Bradley D., Abdel-Gayed R.G., Lung F.K.-K. *Combustion regimes and the straining of turbulent premixed flames. 1989. Combust. Flame. Vol. 76. pp. 213-218. DOI:10.1016/0010-2180(89)90068-0*

30. Baer M. R., Gross R. J. 2001. *SANDIA REPORT, Sandia National Laboratories Albuquerque, New Mexico 87185 and Livermore, California. 94550. 199.*

31. Rubtsov N.M., Seplyarskii B.S., Troshin K. Ya., Chernysh V. I., Tsvetkov G. I. *Initiation and propagation of laminar spherical flames at atmospheric pressure. // Mendeleev Communications. 2011. Vol. 21. pp. 218-221. <https://doi.org/10.1016/j.mencom.2011.07.016>*

32. Naboko I. M., Rubtsov N.M., Seplyarskii B.S., Chernysh V. I., Tsvetkov G. I. *Vozniknoveniye takusticheskoy neustoychivosti v vodorodo-vozdushnykh smesyakh v zamknutom reaktore pri tsentral'nom initsirovanii iskrovym razryadom (Occurrence of acoustic instability in hydrogen-air mixtures in a closed reactor with central initiation by a spark discharge). Physical-chemical kinetics in gas dynamics. 2011. Vol. 12. <http://www.chemphys.edu.ru/pdf/2011-12-23-002.pdf>*

33. Richardson E. *An experimental study of unconfined hydrogen –oxygen and hydrogen-air explosions. <https://ntrs.nasa.gov/api/citations/20150002596/downloads/20150002596.pdf>*

34. Zeldovich Ya. B. *Companeets A. S. Teoriya detonatsii (Detonation Theory). Moscow: Gostechizdat. 1955. 268 p. (in Russian).*

35. Shepherd J. E. *Detonation in gases. Proceedings of the Combustion Institute. 2009. Vol. 32. pp. 83–98.*

36 Murray S. *Fundamental and Applied Studies of Fuel-Air Detonation - A Quarter Century of Large-Scale Testing at DRDC Suffield (Stephen. Murray @ drdc-rddc.gc.ca), 2010, DRDC Suffield, P.O. Box 4000, Station Main, Medicine Hat, Alberta, Canada T1A 8K6*

37. Orzag S. A., Kellst L. C., *Transition to turbulence in plane Poiseuille and plane Couette flow. Journal of Fluid Mechanics.* 1980. Vol. 96. No. 1. pp. 159 – 205. <https://doi.org/10.1017/S0022112080002066>

38. Saric W S., Reed H. L., Kerschen E. J. *Boundary-layer receptivity to freestream disturbances. Annual review of fluid mechanics.* 2002. Vol. 34. No. 1. pp. 291-319.

39. Ibrahim S. S., Masri A. R. *The effects of obstructions on overpressure resulting from premixed flame deflagration. J. Loss Prev. in the Process Ind.* 2001. Vol. 14. No. 3. p. 213.

40. Clanet C., Searby G. *On the “tulip flame” phenomenon.. Combustion and flame.* 1996. Vol. 105(1-2): pp. 225-238.

41.. Rubtsov N. M, Seplyarskii B. S., Chernysh V. I., Tsvetkov G.I. *International Journal of Chemistry and Materials Research.* 2014. Vol. 2. p. 102. <https://archive.conscientiabeam.com/index.php/64/article/view/1836/2572>

42. Abramovich G. N. *Teoriya turbulentnykh struj (The theory of turbulent flows).* 1960. Moscow. Ekolit, reprint. 2011. <https://www.livelib.ru/book/1000645441-teoriya-turbulentnyh-struj-g-n-abramovich> (in Russian).

43. Lemanov V. V., Terechov V. I, Sharov K. A., Shumei A. A. *Eksperimental'noye issledovaniye zatoplennykh struy pri nizkikh chislakh Reynol'dsa (Experimental Study of Submerged Jets at Low Reynolds Numbers).* JTP Letters. 2013. Vol. 39. pp. 34-41. (in Russian)

44. Durst F., Haddad K., Ertun O. in *Advances in Turbulence ed. Prof. B. Erkkhardt, Proceedings of the 12th Euromech European Turbulence Conference September 7-10. 2009. Marburg Germany, Springer Publishing.* 160.

45. Vinogradov A. N., Egorov V. V., Kalinin A. P., Melnikova E. M., Rodionov A. I., Rodionov I. D. *Lineyka giperspektral'nykh sensorov opticheskogo diapazona (Line of hyperspectral sensors of the optical range).* Preprint of Space Research Institute of RAS. Pr-2176. 2015. 16 p.

46. Rubtsov N. M., Vinogradov A. N., Kalinin A. P., Rodionov A. I., Troshin K. Ya., Tsvetkov G. I. *Ustanovleniye zakonomernostey rasprostraneniya neustoychivogo fronta plameni metodami opticheskoy 3D spektroskopii i tsvetnoy skorostnoy kinos'yomki (Establishing the Regularities of the Propagation of an Unstable Flame Front by the Methods of Optical 3D Spectroscopy and Color High-Speed Filming).* Ishlinsky Institute for Problems in Mechanics RAS. Preprint No. 1097. (in Russian)

47. Rubtsov N.M., Seplyarsky B.S., Troshin K. Ya., Chernysh V.I., Tsvetkov G.I. *Initiation and propagation of laminar spherical flames at atmospheric pressure. Mendelev Communications.* 2011. Vol. 21. No. 4. pp. 218-220. DOI: 10.1016/j.mencom.2011.07.016

48. Coheur P.-F., Bernath P. F., Carleer M., Colin R., Polyansky O. L., Zobov N. F., Shirin S. V., Barber R. J., Tennyson J. A 3000 K laboratory emission spectrum of water. *The Journal of Chemical Physics*. 2005. 122(7): 074307. DOI:10.1063/1.1847571

49. Herzberg G. *Molecular Spectra and Molecular Structure. Vol. 1, Spectra of Diatomic Molecules*. 2nd edn. Van Nostrand. New York. 1950.

50. Kreshkov A. P. *Osnovy analiticheskoy khimii. Teoreticheskiye osnovy. Kolichestvennyy analiz (Fundamentals of analytical chemistry. Theoretical basis. Qualitative analysis)*. M: Publishing house "Khimiya". 1970. Vol. 3. (in Russian)

CHAPTER 7. Study of the combustion of hydrogen-air and hydrogen-hydrocarbon (C_1 - C_6) -air mixtures over the surface of palladium metal with the combined use of a hyperspectral sensor and high-speed color filming

It was found that the temperature of the ignition limit over the palladium surface at 1.75 atm for mixtures of 30% methane + 70% hydrogen + air ($\theta=0.9$, $T=317^\circ\text{C}$) and 30% propane + 70% hydrogen + air ($\theta=1$, 106°C), measured by the "bottom approach" temperature method, decreases during subsequent ignitions. The flammability limit returns to the initial value after the reactor is treated with oxygen or air, i.e. hysteresis takes place. The temperature of the ignition limit of mixtures of 30% (C_2 , C_4 , C_5 , C_6) + 70% H_2 + air ($\theta=0.6$, 1.1, 1.2, 1.2, respectively) over the palladium surface is $19 \div 35^\circ\text{C}$ at 1.75 atm; there is no hysteresis. It is shown that the lean ($\theta=0.6$) mixture of 30 ethane + 70% hydrogen + air has the lowest temperature of the ignition limit: 24°C at 1 atm. The effective activation energy for the ignition of mixtures over palladium is estimated as $\sim 2.4 \pm 1 \text{ kcal/mol}$. It was found that the separation of the CH and Na emission bands in time during the combustion of a mixture of 30% propane + 70% H_2 + air ($\theta=1$) found in this work, is due to the occurrence of hydrodynamic instability of the flame when it touches the end of the cylindrical reactor.

It was found that the ignition temperatures of hydrogen - oxygen and hydrogen - methane - oxygen mixtures under the pressure of heated wires of palladium, platinum, nichrome and kantal (fechral) at a total pressure of 40 Torr increase with a decrease in the hydrogen content in the mixture; only heated palladium wire exhibits a noticeable catalytic effect. A qualitative numerical calculation made it possible to reveal the role of the additional branching reaction $H + HO_2 \rightarrow 2OH$.

Keywords: combustion, ignition, palladium, hysteresis, sensor

It is known that methane and oxygen on a heated platinum wire can release a significant amount of heat in a dark reaction [1]. Interest in catalytic oxidation processes and their mechanisms is constantly growing due to the broad prospects of using this technology in combustion in power generation systems [2-4], to reduce the concentration of methane in the air [5]; in the use of catalytic converters in vehicles to reduce emissions of harmful gases [6]. The issue of ensuring hydrogen safety at nuclear power plants using catalytic afterburners is a topical issue [7]. There is also a great deal of interest in catalytic partial oxidation leading to intermediates that are critical in the synthesis of target industrial compounds.

§ 1. Study of the combustion of hydrogen-air and hydrogen-methane-air mixtures over the surface of palladium metal with the combined use of a hyperspectral sensor and high-speed color filming

The mechanism of the oxidation of hydrogen and hydrocarbons on noble metals has not yet been sufficiently understood. Experiments on isotope exchange [8] have shown that chemisorption of methane on noble metals results in the formation of adsorbed methyl or methylene radicals. Their interaction with adsorbed oxygen can lead either to direct oxidation to carbon dioxide and water or to the formation of adsorbed formaldehyde [9]. Until now, the nature of the active surface is generally unknown. In the case of palladium, oxidation can occur on the metal itself, on the surface of Pd (II) oxide, or even on a surface partially covered with adsorbed oxygen, and at the same time. According to X-ray photoelectron spectroscopy (XPS) data [10], the smaller the size of the palladium crystallites is, the more likely they are to exist in the oxide form. It should be noted that because of a certain degree of conversion of the reagent, a significant amount of heat can be released. This leads to a significant increase in temperature, thus, the stability of the catalyst at high operating temperatures must be known [2]. As the temperature rises, the activation energy of methane oxidation on the Pd catalyst changes sharply. The temperature, at which this transition occurs is a function of the catalyst composition [11]. It should be emphasized that noble metals form oxides, which, depending on their reactivity, determine the rate and mechanism of the catalytic process. This significantly complicates the search for optimal conditions for catalysis. For example, Pd readily transforms into PdO at temperatures lower than 1100 K, but PtO₂ already decomposes at temperatures above 825 K. Due to the greater stability of PdO compared to PtO₂, in the case of a Pd-containing catalyst, the active phase is most likely PdO, in while in the case of a Pt catalyst, the active phase is Pt. The activity of PdO is higher than that of Pt. This allows to achieve higher conversions when using PdO. Controlling the presence of PdO in the gas phase, which is necessary to establish the mechanism of catalysis, is complicated by the fact that the spectroscopic data on PdO are scattered and contradictory [12 - 14]. In [15], the emission spectra of PdO obtained during the pyrolysis of polymer complexes (PtCl₂) upon excitation at a wavelength of 355 nm are presented. Thus, the appearance and participation of a chemically active surface in gas combustion significantly complicate the understanding of the process, not only due to the emergence of new control parameters, but also difficulties in registering catalyst molecules or particles.

It is worth reminding that the hyperspectrometers used in this Chapter and discussed in the previous Chapters are devices that allow remote registration of reflected, scattered and emitted radiation, obtaining its spectrum in a wide wavelength range [16, 17]. The hyperspectrometer makes it possible to study the tem-

poral characteristics of the processes occurring on a narrow strip of the investigated surface. 4D dimension is formed by the x coordinate, the spectral coordinate - by the wavelength λ , the intensity of the spectral line I and the time t . The work [18] demonstrated the possibility of studying combustion and explosion processes using remote hyperspectral sensing.

High-speed filming is also used in this book as a remote study of various processes. In [19, 20], the method of high-speed color cinematography was used to study spark-initiated ignition of hydrogen-air and pentane-air mixtures. This method makes it possible to visualize the propagation of the flame front and reveal the features of combustion processes, in particular, the transition of a smooth flame front into a cellular structure.

This section is devoted to identifying the regularities of the combustion of hydrogen and mixtures of hydrogen with methane over metallic palladium, among them using an optoelectronic complex based on a hyperspectral sensor and high-speed color filming.

Experimental

The experiments were carried out in a heated horizontal cylindrical stainless steel reactor 25 cm in length and 12 cm in diameter, equipped with a tangential gas inlet, collapsible covers, and an optical quartz window in one of the coatings (Fig. 1). In experiments, in which it was required to avoid gas circulation due to the presence of a tangential inlet (Fig. 1), an aluminum ring with an outer diameter of 11.2 cm and an inner diameter of 11 cm was introduced into the reactor perpendicular to the gas flow (see also paragraph 5 of Chapter 3).

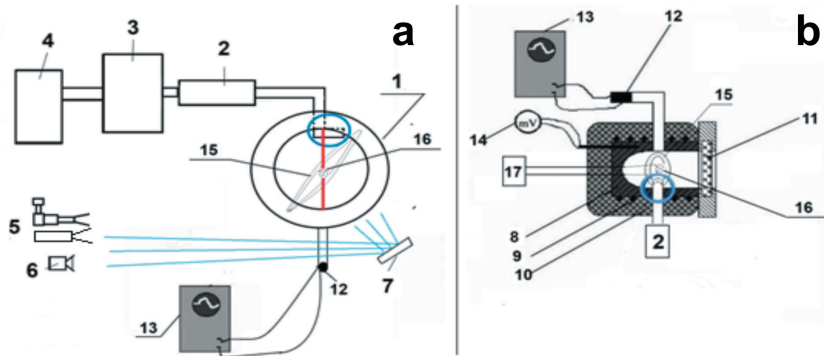


Figure 1. Block diagram of the experimental setup, end view (a) and side view (b). The strip along which the 4D spectral survey was carried out is indicated in red. The width of this strip is about 1 mm

- 1) reactor,
- 2) solenoid valve, 3) buffer volume, 4) gas cylinder,
- 5) hyperspectrometer, 6) digital video camera, 7) folding mirror,
- 8) internal asbestos insulation, 9) heater,
- 10) external asbestos insulation, 11) optical window,
- 12) pressure sensor, 13) ADC converter and computer for receiving and accumulating data, (14) millivoltmeter for taking thermocouple readings,
- 15) aluminum ring to prevent gas circulation, 16) Pd spiral,
- 17) Wheatstone bridge. The unit for tangential gas injection into the reactor is highlighted with the blue circle

The temperature measurement accuracy was 0.3 K. The evacuated and heated to the required temperature reactor was quickly filled with a gas mixture from the high-pressure buffer volume to the required pressure. An electromagnetic valve was used to open and close the gas lines. Due to the sharp pressure drop in the buffer volume and in the reactor, a gas vortex arises in the reactor, leading to a reduction in the time for establishing a uniform temperature distribution. To prevent gas circulation, an aluminum ring was introduced into the reactor perpendicular to the gas flow, as described in the last paragraph of Chapter 3. The pressure during the gas input and combustion process was recorded using a "Karat-DI" tensoresistive sensor, a signal from which was fed through an ADC to a computer. Pd wire (in a number of experiments, Pt wire) 80 mm long and 0.3 mm in diameter in the form of a spiral was placed into the reactor. This wire was used to initiate the ignition of the combustible mixture. Also, the wire was connected as a shoulder of the Wheatstone bridge, which allowed controlling its average temperature. Before each experiment, the reactor was evacuated to 0.1 Torr. The total pressure in the reactor and the pressure in the buffer volume were monitored with a pressure

gauge. We used chemically pure gases and 99.85% Pd.

The registration of the ignition and FF propagation was carried out through the optical window with VID-IK3 hyperspectrometers (see Chapters 2, 4), BIK, as well as a color high-speed film camera Casio Exilim F1 Pro (frame rate - 1200 s⁻¹ at a resolution of 336x96 pixels, 600 frames per second at a resolution of 432x192 pixels or 300 frames per second at a resolution of 512x384 pixels) or PHANTOM (frame rate - 4000 s⁻¹ at a resolution of 1300x800 pixels). The obtained data were written into the computer memory, and then they were processed. We used hyperspectrometers of both the visible and near infrared range (400-970 nm VID-IK3 [5]) and the BIK1 hyperspectrometer in the wavelength range 970-1700 nm.

Optical schemes of VID-IK3 and BIK1 hyperspectrometers are given in Chapters 2 and 4.

It is worth reminding that the optical system of the BIK hyperspectrometer is similar to the optical system of the VID-IK3 hyperspectrometer, only a diffraction grating is used as a spectral splitter. A detailed description of the structure of the hyperspectrometers used and methods for studying combustion and explosion processes, together with the use of high-speed color filming, can be found in Chapter 2.

Results and discussion

The typical results of simultaneous recording of the pressure change (a) and the change in the resistance Pd of the wire (b, c) upon ignition of the mixture of 40% H₂ air at 128 °C at P₀ = 1 atm is shown in Fig. 2a. As seen from Fig. 2a, the total pressure in the reactor reaches 1 atm before ignition, i.e. ignition occurs after the completion of the gas injection. Since palladium wire does not heat up uniformly due to heat dissipation at the soldering points, the dependence of resistance on time is somewhat more inertial than the pressure curve. The vertical segment of this dependence corresponds to the change in resistance at the moment of ignition.

Temperature calibration was performed by changing the temperature of the reactor. However, the temperature measured by means of a Pd wire is the lower limit of the actual temperature of the ignition site [21]. The main result of the experiment is that the temperature of the reactor upon ignition of the mixture of 40% H₂ - air over Pd (108 °C, 1 atm) is at least ~ 160 °C less than above the surface of Pt (260 °C, 1 atm, 40% H₂ - air) [21]. It should be noted that the heating recorded on a Pd wire (360 °C, Fig. 2a) is insufficient for thermal initiation of the ignition of a 40% H₂ - air mixture [21]. Thus, the contribution of surface catalytic reactions to the direct initiation of hydrogen combustion over palladium, in contrast to platinum is very noticeable. It is worth reminding that the role of catalytic processes on a Pt surface is only to heat the surface to the ignition temperature. The role of the emission of active centers from the surface is insignificant.

The spatial development of ignition and flame propagation in a 40% mixture

of H_2 - air and $(80\% \text{H}_2 + 20\% \text{CH}_4)_{\text{stoich}} + \text{air}$ was studied over a Pd wire (Fig. 2b, c). In the same way as in the case of Pt, Pd is heated before and after ignition due to catalytic reactions on the Pd surface. It can be seen that in the presence of a Pd wire, the cellular structure of the flame front is not observed in comparison with the results obtained on the Pt surface [22]. This is due to the greater stability of PdO in comparison with PtO_2 , which decomposes even at 500°C and is a very unstable compound [22].

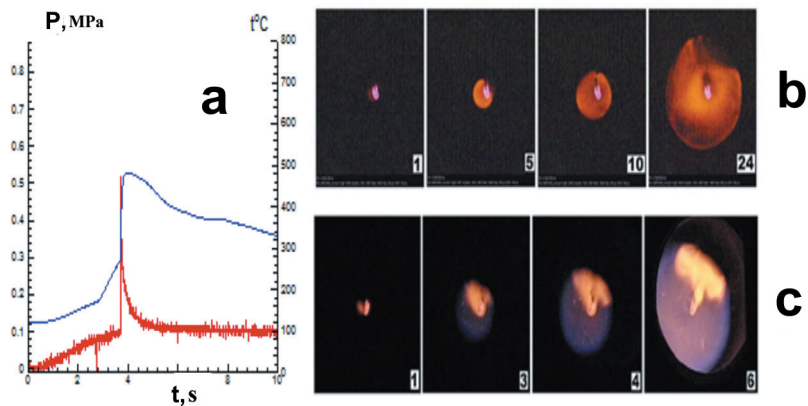


Figure 2.

a) - Simultaneous registration of the heating and average temperature of the Pd coil upon initiation of the ignition of the mixture of 40% H_2 with air over palladium. $T_0 = 128^\circ\text{C}$, $P_0 = 1.08$ atm;

b) - a sequence of video frames of the initiated ignition of the mixture of 40% H_2 with air. $T_0 = 120^\circ\text{C}$, $P_0 = 1.25$ atm, 600 frames/s;

c) - a sequence of video frames of initiated ignition of a stoichiometric mixture $(80\% \text{H}_2 + 20\% \text{CH}_4)_{\text{stoich}} + \text{air}$. $T_0 = 190^\circ\text{C}$, $P_0 = 1.17$ atm, 600 frames/s.

The temperature dependence of the hydrogen concentration at the flammability limit was determined experimentally to reveal the contribution of surface reactions (including those responsible for heating the Pd wire). The ignition limits of stoichiometric mixtures 6-40% $\text{H}_2 + \text{air}$ (indicated by crosses) and $(20\text{-}60\% \text{H}_2 + 80\text{-}40\% \text{CH}_4)_{\text{stoich}} + \text{air}$ are shown in Fig. 3a. As you can see, Pd wire ignites a mixture of 40% H_2 - air in the reactor, which is heated only to 70°C . For comparison, ignition of the same mixture with Pt wire requires heating to 260°C [21]. In addition, as can be seen from the figure, the minimum H_2 concentration at the limit is approximately 5%, which is very close to the concentration limit of H_2 ignition at atmospheric pressure when initiated by a spark [23, 24]. This means that CH_4 in $\text{H}_2 - \text{CH}_4 - \text{air}$ mixtures reacts only in the gas phase and not on the Pd surface.

It should be emphasized also that Pt wire of the same size does not ignite any of the mixtures (20÷60% H₂ + 80÷40% CH₄)_{stoich} + air at reactor temperatures up to 450 °C.

On the contrary, Pd wire ignites mixtures (H₂ 30÷60% + 70÷40% CH₄)_{stoich} + air (circles in Fig. 3a). However, the mixture (20% H₂ + 80% CH₄)_{stoich} + air at temperatures up to 450 °C cannot be ignited with Pd wire, probably because the H₂ concentration in the mixture (2.2%) turned out to be lower than the concentration limit of hydrogen ignition [23, 24].

The temperature dependence of the H₂ fraction in combustible mixtures in Arrhenius coordinates is shown in Fig. 3b. As can be seen from the figure, this dependence can be approximated by a straight line (correlation coefficient 0.98). The data were processed using the Statistica 9 software package (Statsoft).

We can conclude from Fig. 3b, that the dependence for H₂ - CH₄ - air mixtures is determined only by the H₂ fraction in the mixture. We limited ourselves to 40% H₂ in the mixture, because after a further increase in the H₂ content, the hydrogen oxidation reaction slows down [24]. For this reason, the value of the effective activation energy obtained below is only an estimate.

Let's consider the nature of the resulting dependence. For a stoichiometric mixture 2H₂ + O₂, the lower flammable limit (marked with the subscript lim) at low pressures: $2k_2(O_2)_{lim} = k_4$ i.e. $(O_2)_{lim} = 1/2 (H_2)_{lim} = k_4/k_2$, where k_4 – the rate constant of heterogeneous termination of active combustion centers (leanly dependent on temperature) and k_2 is the activated rate constant of branching (16.7 kcal/mol [25]).

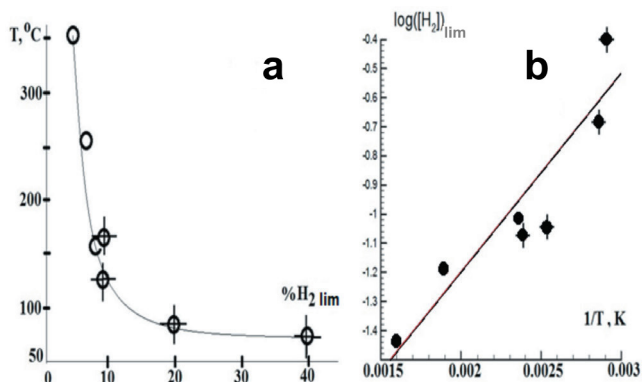


Figure 3.

a) - Experimental dependence of the ignition temperature at the concentration limit on the hydrogen content in the mixture, crosses refer to the hydrogen-air mixture;

b) - Dependence a) in Arrhenius coordinates.

Thus, we obtain the Arrhenius dependence $\ln(H_2)$ lim on $1/T$ with a positive slope. Obviously, the heterogeneous nature of the process on Pd significantly complicates the analysis. However, it can be assumed that in the catalytic oxidation of H_2 , the reaction rate depends mainly on the H_2 concentration, which can be expressed for the steady state as the ratio of some two effective constants [25].

The experimental value of the effective activation energy of the process is $E = 3.5 \pm 1$ kcal/mol, which is typical for surface processes [25]. It should be noted that the value of the effective activation energy is close to the activation energy of adsorption - desorption of hydrogen on Pd [26]. However, in order to ensure ignition, a cycle of reactions must occur, in which branching is realized [24]. The activated ($E = 16.7$ kcal/mol [25]) homogeneous branching reaction $H + O_2 \rightarrow O + OH$ is the slowest elementary reaction of the cycle. Therefore, the activation energy of branching should determine the temperature dependence of the overall process, as it happens for experiments with metallic Pt ([21], see also Chapter 5). This means that in the case of Pd, branching can be of a heterogeneous nature, because the effective activation energy is close to ~ 3.5 kcal/mol. The obtained approximate value of E along with the results presented in Fig. 3a, b, can be used in practical applications to assess the flammability of mixtures $H_2 - CH_4$ - air in the presence of metallic palladium.

It can be seen from Fig. 2b and 2c that, upon initiation with Pd wire, combustion is accompanied by an orange luminescence for both hydrogen and hydrogen-methane mixtures, while this luminescence propagates for the latter mixture non-uniformly and independently on the spherical flame front. An attempt was made to establish the nature of this luminescence using the hyperspectral method. The optical and IR emission spectra of a flame of hydrogen and a mixture (80% H_2 + 20% CH_4)_{stoich} + air, experiments with metallic Pt [21] is shown in Fig. 4a, b, c. This means that in the case of Pd, branching can be of a heterogeneous nature, because the effective activation energy is close to ~ 3.5 kcal/mol.

It can be seen from Fig. 3b, c that, upon initiation with Pd wire, combustion is accompanied by an orange luminescence for both hydrogen and hydrogen-methane mixtures, while for the latter mixture, this luminescence propagates nonuniformly and independently on the spherical flame front. An attempt was made to establish the nature of this luminescence using the hyperspectral method. The optical and IR spectra of radiation from a flame of hydrogen and a mixture (80% H_2 + 20% CH_4)_{stoich} + air, recorded along a vertical strip along the diameter of the optical window (red strip, Fig. 1a) are shown in Fig. 4a, b, c.

Let us preliminarily point out that a hydrogen flame at low pressures is practically invisible, since its radiation is mainly due to the radiation of hydroxyl radicals $OH A^2\Sigma - X^2\Pi$ in the ultraviolet region at 306 nm [24]. In Fig. 14 Chapter 4, the combustion spectrum of a stoichiometric mixture of pentane with air + 10% CO_2 is shown. This spectrum contains intense lines of atoms of alkali metals sodium (581 nm) and potassium (755 nm), inherent in all hot flames [24] and water

vapor bands of water vapor bands in the range 900-970 nm [27, 28]. In the IR spectrum, broad bands of water are observed between $\lambda = 1300$ nm and 1600 nm. A relatively narrow band of the OH* radical is recorded at about 1400 nm [29].

It should be noted that the spectra presented in [28] and in this work were recorded in the same reactor using the same hyperspectral technique. It follows from Fig. 4a, b that the main features of the spectra of the flame of 40% H₂ + air, initiated by palladium in the visible region, in comparison with the optical spectra of the emission of a hydrogen flame initiated by a platinum wire and a spark discharge ([28], Fig. 13a) are:

a) the absence of a system of emission bands in the range of 570 - 650 nm, referred to in [30] as H₂O*. This may be because we used in this paragraph an optical window made of leucosapphire rather than quartz, as in [28]. Leucosapphire, unlike quartz, does not contain active surface OH groups. Thus, the emergence of water bands in the region of 570 - 650 nm may be due to the adsorboluminescence of water on quartz. Such a process is impossible on leucosapphire.

b) increased intensity of water bands in the region 900 - 970 nm in comparison with the intensities of lines of alkali metals.

This indicates the emergence of an additional source of excited H₂O molecules. Earlier, we showed [31] that the catalytic activity of the palladium surface in the hydrogen combustion reaction is higher than that of the platinum surface. In other words, there is a fast catalytic reaction of hydrogen oxidation on the hot Pd surface along with the initiation of gas combustion. This reaction can lead to the formation of an additional amount of excited water molecules.

We summarize the results obtained in this section.

It has been shown experimentally that the ignition temperature of a 40% H₂ - air mixture over metallic Pd (70 °C, 1 atm) is ~ 200 °C lower than over the Pt surface (260 °C, 1 atm). In addition, the Pd wire initiates the ignition of mixtures (H₂ for 30-60% + 70-40% CH₄)_{stoich} + air; Pt wires of the same size cannot ignite these mixtures up to 450 °C. This means that Pd wire is more efficient than Pt wire.

It was shown that the cellular structure of the flame front during ignition on a Pd wire is not observed in comparison with the results obtained on the Pt surface. Therefore, Pd is more applicable for hydrogen recombiners in nuclear power plants, since catalytic particles do not appear in the gas phase, as is the case when using Pt.

The experimental value of the effective activation energy of the process is estimated as 3.5 ± 1 kcal/mol, which is typical for the surface process. This indicates a significant role of the dark reaction of the consumption of H₂ and O₂ on Pd, which is observed directly at low pressures. The presence of this reaction reduces the likelihood of an accidental explosion compared to Pt.

It was found that in the presence of leucosapphire the system of H₂O* emission bands in the region of 570 - 650 nm is missing. A possible explanation of this phenomenon is given. An explanation is proposed for the appearance of an additional source of excited water molecules emitting in the range of 900-970 nm.

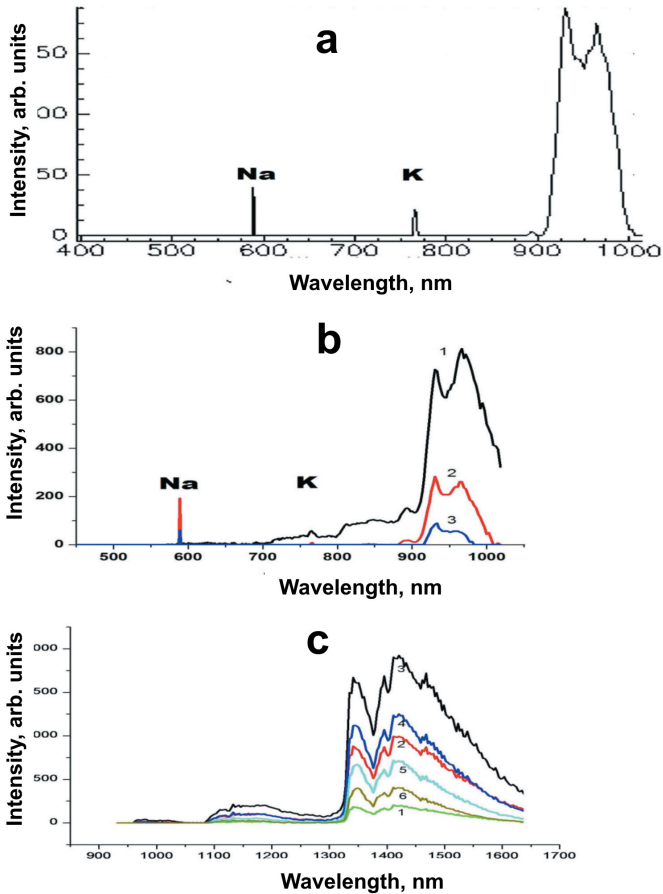


Figure 4.

a) - The emission spectrum of combustion of a mixture of 40% H_2 + air, hyperspectrometer VID-IK-3, 30 frames/s;

b) - Time dependence of the intensity of the emission spectra of the combustion of the mixture (80% H_2 + 20% CH_4)_{stoich} + air, hyperspectrometer VID-IK-3, 300 frames/s;

c) - Time dependence of the intensity of the emission spectra of the combustion of a mixture of 40% H_2 + air, BIK hyperspectrometer, 300 frames/s. The emission spectra of combustion of a 40% H_2 + air mixture in this spectral region do not differ qualitatively.

As the spectrum number increases, time increases.

§ 2. Ignition of hydrogen - hydrocarbon (C_1-C_6) - air mixtures over palladium surface

Hydrogen-hydrocarbon blended fuels are gaining attention as alternative fuels for energy production for two main reasons. The first reason relates to the addition of hydrogen to methane in order to improve performance, expand the range of use and reduce pollutant emissions when using lean mixtures in stationary [32] and mobile [33] systems. The second reason is associated with the prospect of using hydrogen in fuel cells and devices using combustion [34] in the development of hydrogen power engineering.

It is clear that the use of premixed combustion is one of the promising methods to meet the stringent requirements for limiting unwanted NOx emissions from energy production including internal combustion engines [35, 36]. The reduction in combustion temperature that is achieved using lean mixtures can significantly reduce NOx emissions, but more research is needed to address issues that are hindering widespread adoption of this technology. For example, lower combustion temperatures of premixed mixtures can lead to suppression of oxidation reactions, an increase in unwanted CO emissions and a deterioration in the stability of combustion chambers [37].

Natural gases, which are primarily methane, can contain about several percent to 18% of other gases, depending on the field [33, 37]. These impurities are usually C_2 and C_3 hydrocarbons - ethane and propane. Changes in the composition of natural gas can cause changes in combustion chemistry and NOx emissions.

Catalytic ignition can show its main advantages when using lean fuels [38], since the use of a catalyst can initiate combustion of leaner mixtures than a conventional spark plug. At the same time, there are no extinguishing effects during electrical breakdown, as when using spark plug electrodes, the ignition site can be placed in an arbitrary place in the combustion chamber. Catalytic ignition does not require electrodes and an ignition system. Therefore, electrode erosion cannot take place, therefore the operating time of the catalytic ignition system will be significantly longer than for a device using a spark plug.

There is a need to develop catalysts that provide oxidation at low temperatures (<300 °C) for a new generation of highly efficient internal combustion engines [39]. The problems of catalyst stability were studied, for example, in [40]. Palladium alumina catalyst is unstable during methane conversion. The addition of platinum to these catalysts provides significantly higher stability. On the other hand, Pd-Pt catalysts are reversibly poisoned by water vapor, i.e., after the water is removed, their activity is restored. At the same time, a decrease in the activity of Pd/Al₂O₃ is not observed for all fuels, as a result of the combustion of which water vapor is formed. Hydrogen is very stably oxidized to Pd/Al₂O₃. In this case, the degree of conversion of ethane decreases slightly with time, but not to the extent

that is observed during the conversion of methane.

The noble metals Pt and Pd affect the flammability of fuels based on methane and hydrogen in different ways. It was shown that the ignition temperature of a mixture of 40% H₂ - air on palladium (70 °C, 1 atm) is ~ 200 °C lower than on the Pt surface (260 °C, 1 atm) [31, 41]. In addition, Pd ignites stoichiometric mixtures (30 ÷ 60% H₂ + 70 ÷ 40% CH₄) + air ($\theta = 1$, θ is the fraction of fuel mixed with air: $\theta\text{H}_2 + 0.5(\text{O}_2 + 3.76\text{N}_2)$). Metallic Pt does not ignite these mixtures up to 450 °C, i.e. metallic palladium is more efficient than Pt. It was also shown that the cellular structure of the flame front during ignition on the palladium surface is not observed in comparison with the results obtained on the Pt surface. Thus, palladium appears to be more suitable for use in hydrogen recombiners at nuclear power plants, because catalytic particles as ignition centers arising from the thermal decomposition of labile oxide (PtO₂) cannot appear in the gas phase [42].

The experimental value of the effective activation energy for the ignition of hydrogen-air mixtures over the surface of palladium metal is estimated as 3.5 ± 1 kcal/mol, which is typical for surface processes. This indicates a significant role of the dark reaction of hydrogen oxidation observed above the palladium surface at low pressures [31]. Obviously, this reaction behavior reduces the probability of an accidental explosion in comparison with Pt.

The paragraph is devoted to establishing the combustion features of fuels containing hydrogen - hydrocarbon mixtures (C₁ - C₆, namely CH₄, C₂H₆, C₃H₈, C₄H₁₀, C₅H₁₂, C₆H₁₄) with $\theta = 0.6 \div 1.2$ above the palladium surface at a total pressure of 1 ÷ 2 atm. The purpose of this section was both to establish the features of the propagation of the flame front in mixtures and the temperature dependence of the ignition limit over the palladium surface.

Experimental

The experiments were performed with gas mixtures of 30% hydrocarbon (C₁ - C₆) + 70% H₂ + air at $\theta = 0.6 \div 1.2$, and a pressure of 1 ÷ 2 atm. In the experiments, we used a heated cylindrical stainless steel reactor 25 cm long and 14 cm in diameter, equipped with an optical sapphire window in one of the ends (Fig. 5).

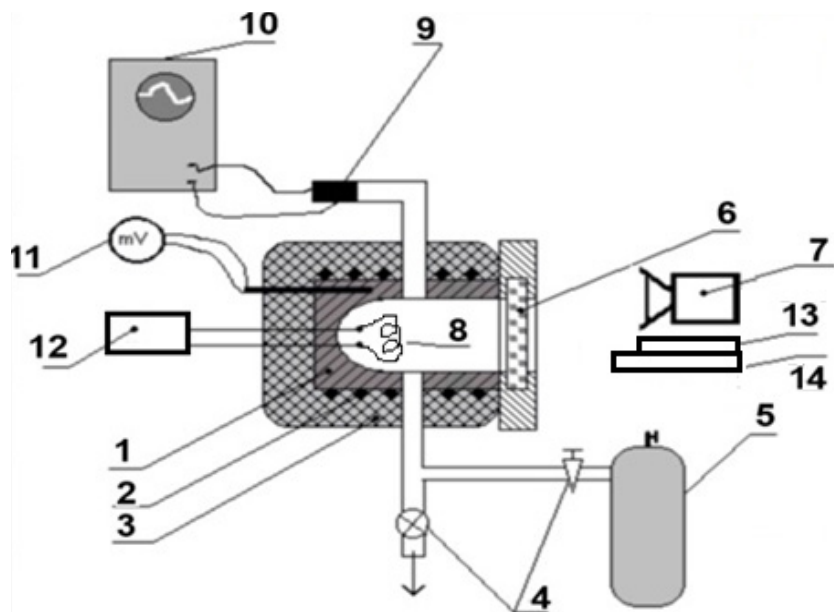


Figure 5. Diagram of the experimental setup:

- 1 - stainless steel reactor, 2 - electric heater, 3 - thermal insulation, 4 - valves,
- 5 - high pressure buffer volume, 6 - optical window, 7 - digital movie camera,
- 8 - palladium coil, 9 - manometer, 10 - registration system,
- 11 - digital millivoltmeter, 12 - Wheatstone bridge,
- 13 - hyperspectrometer 400-1000 nm, 14 - hyperspectrometer 900-1700 nm.

The temperature measurement accuracy was 0.3 K. Ignition registration and flame propagation was carried out using a high-speed color Casio Exilim F1 Pro camera (frame speed 600 s^{-1}). The video file was saved in the computer memory, and then it was processed frame by frame [42]. The evacuated and heated reactor was quickly filled with the test gas mixture from the buffer volume to the required pressure. The flammability limit was determined as the average of two close temperatures at a given pressure. At a higher temperature, ignition occurred, at a lower temperature, there was no ignition. An electromagnetic valve was used to quickly open and close gas lines. A capacitive pressure gauge was used to record the pressure during gas inlet and combustion. A palladium coil made of wire 80 mm long and 0.3 mm in diameter was placed in the reactor. This coil was used both to initiate the ignition of the combustible mixture and to estimate the warming up value of the wire as a shoulder of the bridge circuit. Before each experiment, the reactor was evacuated to 0.01 Torr. After each ignition, the reactor was evacuated for 1.5 hours to remove most of the water vapor. The total pressure in the reactor was

recorded with a vacuum gauge, the pressure in the buffer volume was monitored with a reference manometer. Chemically pure gases and Pd 99.85% were used.

Results and discussion

Typical sequences of video footage of the spatial development of ignition initiated by a palladium wire and flame propagation of preliminarily prepared mixtures of 30% $\text{CH}_4 + 70\% \text{H}_2 + \text{air}$ and 30% $\text{C}_2\text{H}_6 + 70\% \text{H}_2 + \text{air}$ at $\theta = 0.6 \div 0.9$, and a pressure of 1.75 atm are presented in Fig. 6a, b. In the same way as in the case of Pt [31, 41, 42], palladium wire is heated before and after ignition due to catalytic reactions on the surface of palladium metal. As can be seen from the figure, in lean mixtures, a cellular structure of the flame front is observed. The thermal diffusion instability of a fuel-lean flame leads to the appearance of cellular structures [43, 44].

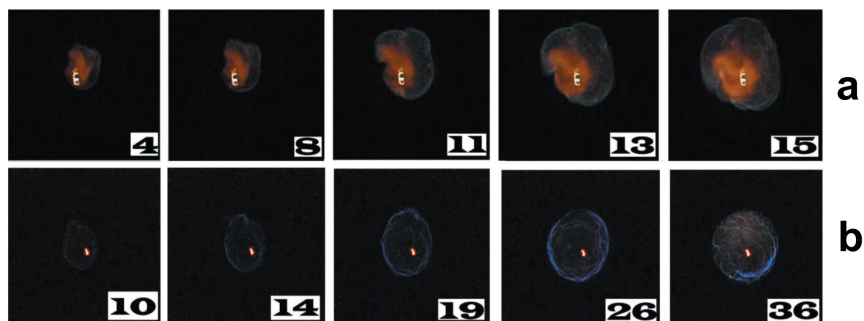


Figure 6 a) High-speed registration of initiation of combustion with a palladium coil and flame propagation in mixtures

a) - 70% $\text{CH}_4 + 30\% \text{H}_2 + \text{air}$, $\phi = 0.7$, $P = 1.75 \text{ atm}$, $270 \text{ }^\circ\text{C}$, 600 s^{-1} ;
 b) - 30% $\text{C}_2\text{H}_6 + 70\% \text{H}_2 + \text{air}$, $\theta = 0.6$, $P = 1.75 \text{ atm}$, $390 \text{ }^\circ\text{C}$, 300 s^{-1} .
 The numbers on each frame correspond to the sequential number of the video image during the ignition.

The results of simultaneous recording of pressure changes and changes in the resistance of a palladium wire (proportional to warming up) during ignition at $P = 1.75 \text{ atm}$ of mixtures a) 30% $\text{C}_2\text{H}_6 + 70\% \text{H}_2 + \text{air}$, $\theta = 0.6$, $39 \text{ }^\circ\text{C}$ and b) 30% $\text{C}_6\text{H}_{14} + 70\% \text{H}_2 + \text{air}$, $\theta = 1.2$, $36 \text{ }^\circ\text{C}$ in Fig. 7. Since the Pd foil is heated nonuniformly [42], the time dependence of the resistance, which represents the relative temperature, is somewhat “delayed” in comparison with filming. A kink in this dependence corresponds to a change in resistance at the moment of ignition. Obviously, the temperature value measured with the palladium resistance is the lower limit of the true temperature of the center of ignition, which initiates the combustion of the gas, since it takes a certain time to heat the entire palladium coil.

The dashed curve in Fig. 7 shows the change in the resistance of the palladium

coil in when a mixture of 30% + 70% H₂ + air is injected into the reactor. Thus, the first maximum in the dependence of the resistance on time during combustion refers not to the ignition process, but to the interaction of hydrogen with the palladium surface.

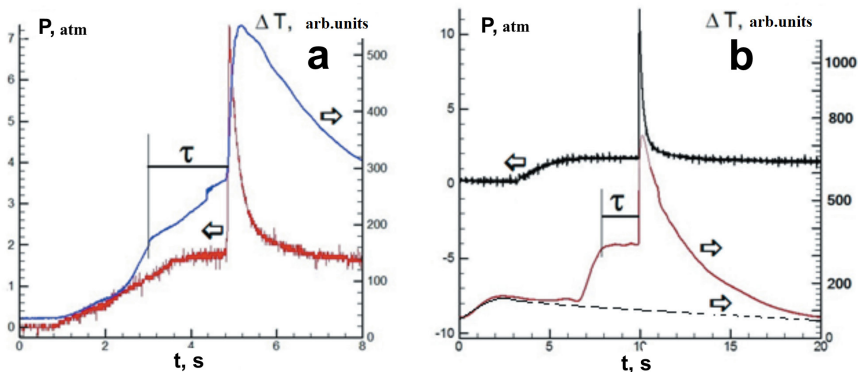


Figure 7. Simultaneous recording of pressure and resistance changes of a palladium coil during ignition

a) - 30% C₂H₆ + 70% H₂ + air, $\theta = 0.6$, P = 1.75 atm, 39 °C

b) - 30% C₆H₁₄ + 70% H₂ + air, $\theta = 1.2$, P = 1.75 atm, 36 °C. The ignition delay is indicated in the figure. The dotted line in Fig. 7b - change in the resistance of the palladium coil when a mixture of 30% Ar + 70% H₂ + air is injected into the reactor up to 1.75 atm.

As can be seen from Fig. 7, the total pressure in the reactor reaches 1.75 atm before the moment of ignition, i.e. ignition occurs after completion of the gas injection in cases a) and b). The ignition delay period τ for a mixture of 30% C₂H₆ + 70% H₂ + air is ~ 2 s; τ is 8 s at 24 °C and P = 1 atm. Thus, the combustion of this fuel can be initiated by a palladium surface at room temperature, without external physical stimulation. In this case, the mixture of 30% C₂H₆ + 70% H₂ + air with $\theta = 0.6$ has the lowest temperature of the ignition limit: 24 °C at 1 atm.

It has been shown that mixtures of 30% CH₄ + 70% H₂ + air and 30% C₃H₈ + 70% H₂ + air exhibit two temperature limits of ignition. A higher value can be achieved with a “bottom” approach by temperature, a lower one is achieved when the reactor is treated with ignitions. The foregoing is illustrated by the dependences of the flammability of mixtures 70% CH₄ + 30% H₂ + air (Fig. 8a) and 30% C₃H₈ + 70% H₂ + air (Fig. 8b) on the number of successive ignitions at P = 1.75 atm.

As can be seen from the figure, the ignition temperature in the “fresh” reactor (“bottom” approach from lower to higher temperature: there were no ignitions in the reactor before) is ~ 315 °C at $\theta = 0.9$. At this temperature, mixtures with $\theta < 0.9$ at the same pressure in the “fresh” reactor do not ignite. However, during

treatment with flames, the flammability limit temperature decreases markedly and amounts to 274 °C at $\theta = 0.7$ after 7 ignitions. It was shown that the process is reversible: after treating the reactor with oxygen (1 atm O_2 for 2 min), the ignition limit returns to its initial value of ~ 315 °C. Similar dependences were also observed in the case of ignition of the mixture of 30% $C_3H_8 + 70\% H_2 +$ air (Fig. 8b).

The ignition limit temperature in the "fresh" reactor is ~ 108 °C at $\theta = 1$. During subsequent ignitions of the same compound, the temperature limit is reduced to 30 °C after 7 ignitions. The process is also reversible: after the reactor is treated with oxygen (1 atm O_2 for 2 min), the ignition limit returns to its initial value of ~ 108 °C.

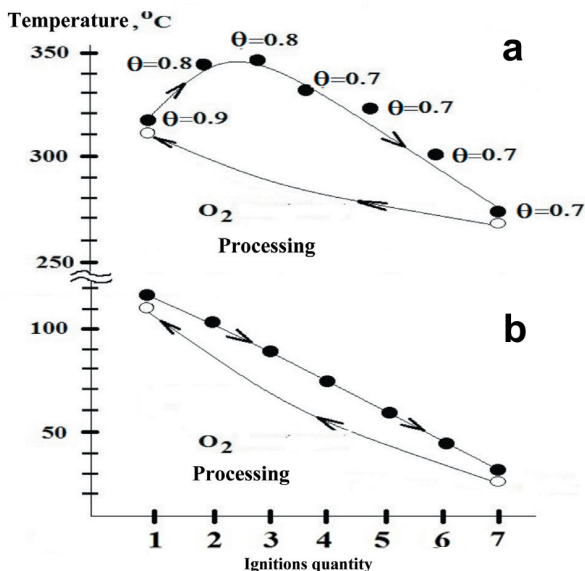


Figure 8. Dependence of the flammability of mixtures

- a) - 30% $CH_4 + 70\% H_2 +$ air,
 b) - 30% $C_3H_8 + 70\% H_2 +$ air $\theta = 1$, from the number of consecutive ignitions.
 P = 1.75 atm. Filled circles refer to ignition, empty circles refer to no ignition.

Thus, the observed phenomenon is hysteresis; it can be caused by reversible changes in the palladium surface and, consequently, in the activity of the catalyst.

It should be noted that reversible changes in the palladium surface are observed only for fuels H_2 - methane and H_2 - propane. For the other mixtures studied, the hysteresis effect is missing. This means that the flammability limit over palladium is also determined by the peculiarities of the kinetic mechanism of hydrocarbon oxidation. The temperatures at the ignition limit for these mixtures at a total pressure of 1.75 atm are presented in Table 5.

Table 5.

Flammable limits for mixtures 70% H₂ + 30% (C₂, C₄-C₆) at 1.75 atm

Fuel	30% C ₂ H ₆ +70% H ₂ θ = 0.6	30% C ₄ H ₁₀ +70% H ₂ θ = 1.1	30% C ₅ H ₁₂ +70% H ₂ θ = 1.2	30% C ₆ H ₁₄ +70% H ₂ θ = 1.2
Temperature at the flammability limit, °C	20	28	24	36

To estimate the effective activation energy of the gross reaction for mixtures that do not exhibit the features associated with reversible changes in the activity of the catalyst, the temperature dependences of the ignition delay times were obtained. The experimental temperature dependences of the ignition delay periods in Arrhenius coordinates for the ignition of mixtures of 30% (C₂H₆, C₄H₁₀, C₅H₁₂, C₆H₁₄) + 70% H₂ + air are shown in Fig. 9.

As seen from Fig. 9, these dependences can be approximated by a straight line (correlation coefficient 0.98). The data were processed using the Statistica 9 software package (Statsoft). The experimental value of the effective activation energy of the gross processes obtained from Fig. 9 is $E = 2.4 \pm 1$ kcal/mol, which is characteristic of the surface process [25].

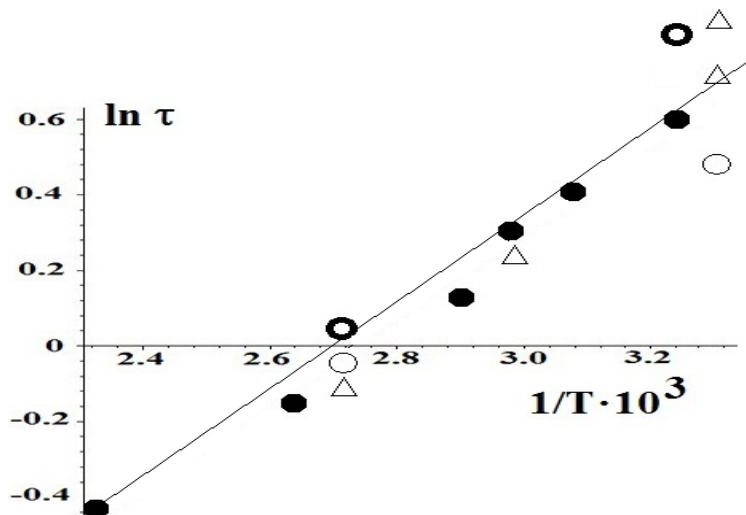


Figure 9. Experimental temperature dependences of ignition delay periods in Arrhenius coordinates at $P = 1.75$

Solid circles - 30% C₂H₆ + 70% H₂ + air, θ = 0.6;

Empty circles - 30% C₄H₁₀ + 70% H₂ + air, θ = 1.1;

Triangles - 30% C₅H₁₂ + 70% H₂ + air, θ = 1.2.

This value is very close to that obtained in the previous paragraph from the dependence of the H_2 content in mixtures H_2 - air and $H_2 + CH_4 +$ air on temperature (3.5 ± 1 kcal/mol). Hence, we can conclude that the temperature dependence for mixtures of 30% (C_2, C_4, C_5, C_6) + 70% $H_2 +$ air is determined only by the content of H_2 in the mixture, as is shown for a mixture of H_2 - air and $H_2 - CH_4 -$ air in [41]. This may mean that the obtained estimates of the effective activation energy refer to the same process, probably the branching reaction [41]. This means that the branching reaction is of a heterogeneous nature. In addition, the lowest temperature of the ignition limit of a hydrogen - air mixture on the surface of palladium is ~ 70 °C for a mixture of 40% $H_2 + 60\%$ air. Since the ignition limit temperature for mixtures of 70% hydrogen + 30% hydrocarbon (C_2 - C_6) + air is ~ 40 °C lower (see Table 5), this indicates an important role of reactions involving hydrocarbon molecules on the palladium surface.

The results of frame-by-frame processing of filming of Pd-initiated ignition of the mixture of 70% $H_2 + 30\%$ $C_3H_8 +$ air ($\theta = 1, P_0 = 1.73$ atm) are shown in Fig. 10. It can be seen from Fig. 10 that when Pd is initiated by the wire until the flame touches the reactor walls (frames 10 - 19). In addition, a spatially inhomogeneous combustion of the combustible mixture occurs, in this case when the flame touches the end wall of the reactor (which is closer to the Pd spiral), there is a sharp increase in the combustion intensity (frames 23 - 26). It can be seen that after the completion of the combustion process in the volume, the afterburning of the combustible mixture on the palladium coil continues.

An attempt was made to establish the nature of this luminescence using the hyperspectral method. The optical and IR emission spectra of the mixture 60% $H_2 + 40\%$ $C_3H_8 +$ air ($\theta = 1$), recorded along the vertical strip along the diameter of the optical window are demonstrated in Fig. 11a, b, c. This corresponds luminescence to the red strip in Fig. 1a.

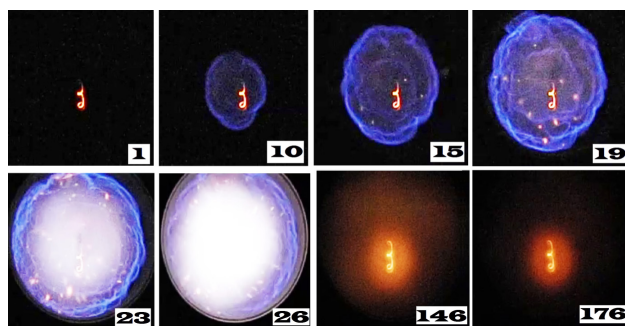


Figure 10. High-speed registration of the process of initiation of combustion with palladium coil and flame propagation in a mixture of 70% C_3H_8 % + 30% $H_2 +$ air, $\theta = 1, P = 1.75$ atm, 35 °C, 600 s^{-1} . The numbers on each frame correspond to the sequential number of the video image during the ignition

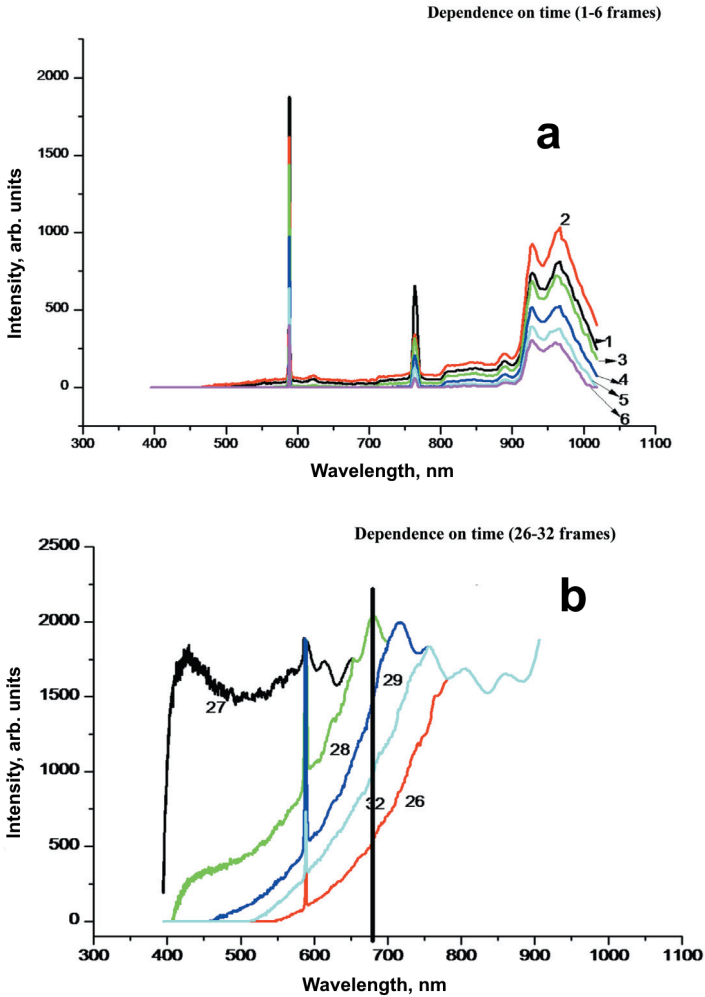


Figure 11.

a) - Dependence of the intensity of the emission spectra of the combustion of a mixture of 60% H_2 + 40% C_3H_8 + air ($\theta = 1$, $P_0 = 1.9$ atm), hyperspectrometer VID-IK3, 70 frames/s;

b) - Dependence of the intensity of the emission spectra of the combustion of a mixture of 60% H_2 + 40% C_3H_8 + air on time ($\theta = 1$, $P_0 = 1.9$ atm), VID-IK3 hyperspectrometer, blue spectrum region, 70 frames/s, black vertical line limits the distortion region spectrum, located on the right and associated with a sharp increase in the sensitivity of the device;

c) - Time dependence of the intensity of the emission spectra of the combustion of a mixture of 40% H_2 + air, BIK1 hyperspectrometer, 300 frames/s. As the spectrum number increases, time increases.

The intense lines of atoms of alkali metals sodium (581 nm) and potassium (755 nm) inherent in all hot flames [24] and water vapor bands of the water vapor band in the range 900–970 nm [27, 28] can be seen in the spectrum in Fig. 11a. In the IR spectrum, broad bands of water are observed between $\lambda = 1300$ nm and 1600 nm. A relatively narrow band of the OH* radical is recorded at about 1400 nm [29] (Fig. 11c). The task was to establish the features of the appearance in time and space of active intermediate CH particles (431 nm [24],) and 590 nm for the line of Na atoms, in order to establish the features of the appearance in time and space of active intermediate particles and self-heating. This is because the radiation of Na atoms is caused by their thermal excitation [24], which is carried out at a flame temperature not lower than 1200 °C [45]. It is seen from Fig. 11b that at the beginning of the process (spectrum 25), a blue CH emission is recorded (the spectral band at 431 nm is not resolved due to collisional broadening at an initial pressure of 1.9 atm [24]). The maximum of the Na line is recorded much later (spectrum 27).

Let us pay attention to the fact that the observed separation of the CH and Na radiation in time is consistent with the results obtained in [46] for penetration of a methane-air flame through a small hole in a flat obstacle when the gas flow is turbulized. It can be seen from Fig. 11 (corresponding to Fig. 5 from [46]) that before the obstacle there is a blue luminescence in the reactor due to the emission of CH radicals, C_2 radicals in recorded quantities are observed only after the first obstacle. When registering the radiation of a propagating flame using glass filters in the wavelength range of 435 nm, 520 nm, and 590 nm, it is clearly seen that both C_2 radicals in recorded quantities and the main heat release in the process of Na luminescence are observed after the first obstacle, i.e. after turbulization of the gas flow (see Chapter 6). We point out that earlier [47] we have experimentally and theoretically established that when the methane-air mixture flame touches the end of a cylindrical reactor (see Chapter 3), there is turbulence of the combustion front caused by the occurrence of hydrodynamic instability. Thus, the time separation of the CH and Na emission bands observed in this work is due to the hydrodynamic instability of the flame when it touches the end of the cylindrical reactor.

This result means that the used experimental technique makes it possible to separate the “cold” and “hot” flames in time and space in a single experiment.

Let us point out the increased intensity of the water bands in the region 900 - 970 nm in comparison with the intensities of the lines of alkali metals, while, according to Fig. 11a, water bands are observed at the end of the combustion process, when the sodium line is practically not observed in the spectrum (Fig. 11a, spectrum 5). As is indicated in the previous paragraph, this radiation can be associated with the catalytic oxidation of unburned hydrogen and, possibly, propane on the hot surface of Pd.

We briefly summarize the results obtained in this section.

It has been experimentally shown that the temperature of the ignition limit over the palladium surface at $P = 1.75$ atm, measured by "bottom" approach from lower to higher temperature, for mixtures of 30% methane + 70% hydrogen + air ($\theta = 0.9$, $T = 317$ °C) and 30% propane + 70% H_2 + air ($\theta = 1$, $T = 106$ °C) noticeably decreases after subsequent ignitions to $T = 270$ °C for H_2 - CH_4 - air and to $T = 32$ °C for a mixture H_2 - C_3H_8 - air. The flammability limit returns to the initial value after the reactor is treated with oxygen or air, i.e. there is a hysteresis phenomenon. The flammability limit of mixtures 30% (C_2 , C_4 , C_5 , C_6) + 70% H_2 + air ($\theta = 0.6, 1.1, 1.2, 1.2$, respectively) over the surface of metallic palladium is $25 \div 35$ °C at $P = 1.75$; there is no hysteresis effect. It was found that a lean mixture of 30% C_2H_6 + 70% H_2 + air ($\theta = 0.6$) has the lowest ignition limit temperature: 24 °C at 1 atm. The estimate of the effective activation energy for the ignition of mixtures over Pd is $\sim 2.4 \pm 1$ kcal/mol, which is typical for the surface process. It is shown that the use of Pd makes it possible to ignite combustible 30% hydrocarbon + 70% H_2 at 1–2 atm at the initial room temperature without using external energy sources. It was found that the separation of the CH and Na emission bands in time during the combustion of a mixture of 30% propane + 70% H_2 + air ($\theta = 1$), found in this work, is due to the occurrence of hydrodynamic instability of the flame when it touches the end of the cylindrical reactor.

§ 3. Ignition of hydrogen-oxygen and hydrogen-methane-oxygen mixtures with heated wires at low pressure

Hydrogen is a renewable energy source for the future, combustion products of which do not pollute the environment. However, before the widespread use of hydrogen, the issues of explosion safety of production, transportation and storage of hydrogen must be resolved. Accidental ignition is one of the largest hazards, as hydrogen has much wider flammability limits than conventional fuels [48].

By analyzing the risk of accidental ignition in the event of an uncontrolled hydrogen leak, as can occur during a vehicle collision or pipeline breakdown, the most likely ignition source is a hot surface. Therefore, it is important to be able to predict and thus prevent a situation, in which ignition can occur when a flammable mixture is in contact with a hot surface.

The use of hydrogen as a fuel requires the ability to ignite it predictably. The problem with refueling spark ignition engines with hydrogen is that the hydrogen-air mixture entering the combustion chamber can be ignited immediately upon contact with a hot surface, such as an intake valve. In diesel engines with direct fuel injection, the pre-ignition problem does not arise. However, hydrogen is difficult to ignite when compressed, an additional device is required such as a glow plug and some ignition helps, usually a glow plug [49]. Therefore, the design of both spark ignition and diesel engines should be based on the analysis of hot sur-

face ignition information.

Many experimental works [50] are devoted to the investigation of hydrogen ignition by a hot surface. Most measurements were carried out for gas mixtures at atmospheric pressure. Measurements of the surface temperature required to initiate the ignition of hydrogen (T_{ign}) in air or oxygen at 1 atm, as a rule, were in the range from 640 °C [48] to 930 °C [51]. The value $T_{\text{ign}} \sim 70$ °C was observed for a mixture of 40% hydrogen -60% air over the palladium surface, i.e. with a significant catalytic effect [52, 53, see § 1]. In addition, in some works, there is practically no dependence of T_{ign} on H_2 content [50, 54]. However, in other works, for example, [55], this dependence is observed.

We showed earlier that T_{ign} at 40 Torr on a heated palladium foil is ~ 100 °C lower than on a heated platinum foil [31]. For thermal ignition, it was found that at pressures up to 180 Torr at 288 °C, the catalytic activity of the palladium surface is higher than that of the Pt surface [31]. We showed in [41] that the dependence of T_{ign} on the hydrogen content for H_2 - CH_4 - air mixtures is determined only by the H_2 content in the mixture. Thus the dependence of T_{ign} on $[\text{H}_2]$ exists. The wide range of measured values also shows that the hot surface temperature required for the ignition is not only a property of the gas, but also depends on a number of factors such as mixture composition and pressure, the nature and state of the surface as determined by the surface history, etc.

This section is devoted to the establishment of the regularities of the ignition of mixtures of hydrogen - oxygen and hydrogen - methane - oxygen at low pressures with heated wires of Pd, Pt, nichrome and kanthal (fechral), in order to detect the dependence of the ignition temperature on the fuel concentration and assess the contribution of the catalytic properties of the materials used.

Experiments were carried out with stoichiometric gas mixtures $2\text{H}_2 + \text{O}_2$, $(20\% \text{H}_2 + 80\% \text{CH}_4)_{\text{stoich}} + \text{O}_2$, $(40\% \text{H}_2 + 50\% \text{CH}_4)_{\text{stoich}} + \text{O}_2$, $(50\% \text{H}_2 + 50\% \text{CH}_4)_{\text{stoich}} + \text{O}_2$, $(60\% \text{H}_2 + 40\% \text{CH}_4)_{\text{stoich}} + \text{O}_2$, $(80\% \text{H}_2 + 20\% \text{CH}_4)_{\text{stoich}} + \text{O}_2$. In a number of experiments CH_4 was replaced with N_2 nitrogen. The reactor was a quartz cylinder 12 cm high and 8 cm in diameter, equipped with a replaceable window CsI on the generatrix of the cylinder, inlet holes for gas injection, pumping and electrodes, on which an igniting wire was located (Fig. 12). The quartz reactor was used to study initiated ignition, which was provided by heating polished wires Pd, Pt, nichrome and kanthal (0.3 mm in diameter and 80 mm long). The optical window CsI (40 mm in diameter and 5 mm thick) withstands only 5-6 ignitions at an initial pressure of 40 Torr, after which it was changed to a new one. The Flir 60 infrared camera (60 frames/s, 320x240 pix, sensitivity range 8-14 mm) was used to determine the ignition temperature T_{ign} wires during ignition.

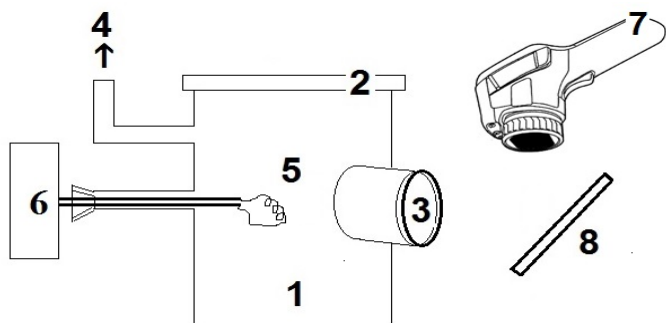


Figure 12. Experimental setup for investigation of initiated ignition

- 1 - quartz cylinder 12 cm high and 8 cm in diameter,
- 2 - quartz vacuum lid, 3 - CsI window, 4 - to the pump, 5 - Pt or Pd spiral,
- 6 - heater, 7 - IR thermal imager Flir 60, 8 - rotary mirror.

Video recording was turned on at arbitrary time before initiation. The video file was stored in the computer's memory and processed frame-by-frame. The evacuated reactor was filled with a gas mixture from the buffer volume to the required pressure. The wires were quickly heated to initiate ignition of the gas mixture. Before each experiment, the reactor was evacuated to 10^{-2} Torr. The total pressure in the reactor was monitored with a VIT-2 vacuum gauge, the pressure in the buffer volume was recorded with a manometer. We used chemically pure gases, 99.99% Pt and 98.5% Pd, commercial nichrome and kanthal.

The ignition temperatures of the mixtures under study with heated wires were measured. It was previously shown that replacing methane with nitrogen does not significantly affect the T_{ign} value, in agreement with [41]. Typical results of IR video recording at a total initial pressure of 40 Torr are shown in Fig. 13. The temperature presentation by the Flir 60 camera lags somewhat behind in time due to the inertia of the temperature sensor; therefore, the maximum temperature $T_{\text{exp}} = 306$ °C (shown in the upper left corner of each frame) in the 3rd and 4th frames of Fig. 13 corresponds to the temperature of the wire immediately before ignition. The temperature on the 5th frame ($T_{\text{exp}} = 380$ °C) corresponds to the temperature of the wire heated by the flame. This temperature is underestimated because the ignition is fast, but the temperature during the ignition delay can be measured accurately and reproducibly. The emissivity was set 0.95 in these experiments (close to a black body).

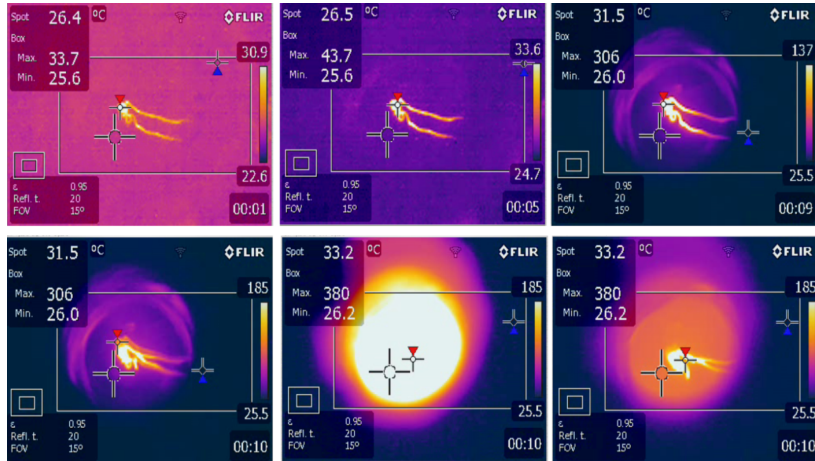


Figure 13. IR - filming of initiated ignition with a heated Pd wire. 60 frames/s, $T_0 = 20^\circ\text{C}$. A mixture (60% H_2 - 40% methane)_{stoich} - oxygen. $P_0 = 40$ Torr. The time in seconds is given on the bottom right of each frame. The red triangle shows the maximum temperature in the rectangle. The blue triangle shows the minimum temperature in the rectangle, the cross indicates the temperature at the point. Emissivity is set to 0.95 (lower left corner of the frame)

The recommended emissivity in the range of 8-14 mm for polished palladium wire is $\varepsilon \sim 0.07$ (<http://www.zaoeuromix.ru/>) and $\varepsilon \sim 0.07-0.1$ (<http://www.thermalinfo.ru/>) for Pt wire. The value $\varepsilon \sim 0.1$ for Pt and Pd wires, $\varepsilon \sim 0.1$ for kanthal and $\varepsilon \sim 0.15$ for nichrome wire was accepted (<http://www.thermalinfo.ru/>). The actual ignition temperature on the wire immediately before the explosion at 40 Torr can be estimated from the Stefan-Boltzmann law: $0.95T_{\text{exp}}^4 \approx \varepsilon 0.07T_{\text{ign}}^4$. The results are shown in Fig. 14. As can be seen from the Figure, the dependence of T_{ign} on $[\text{H}_2]$ takes place; Pd shows the highest catalytic activity (T_{ign} values are the lowest) according to [31].

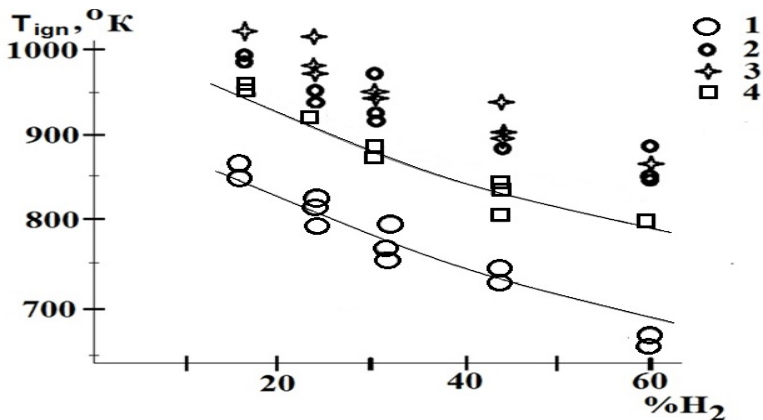
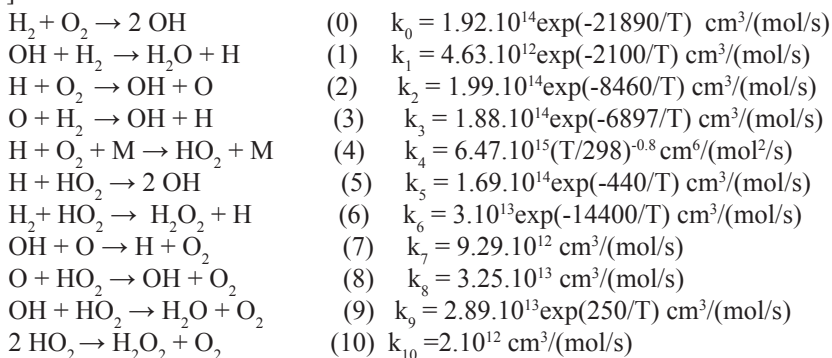


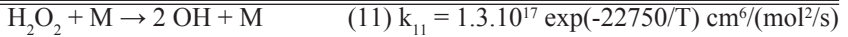
Figure 14. Experimental dependences of T_{ign} on wires on the H_2 content in the mixture,

1 - Pd, 2 - Pt, 3 - nichrome, 4 - kanthal, 5 - crosses - calculations with the values $k_{ocat} = 4.10^{12} \exp(-3500/T) \text{ cm}^3/(\text{mol}/\text{s})$ for initiation by the heated Pd surface (lower curve), and $k_{ocat} = 2.10^{15} \exp(-5000/T) \text{ cm}^3/(\text{mol}/\text{s})$ for Pt (upper curve)

The purpose of the numerical calculation was to establish the limiting ignition conditions in temperature at a wall temperature of 300 K, depending on the H_2 content in the combustible mixture. The model reflects the experimental fact that at the initial stages of the combustion process, the development of the primary heating source leads to the propagation of the flame front [42] with a velocity U .

The surface chain initiation reaction (generation of active combustion centers) was also taken into account, as well as the peculiarities of the mechanism of branched-chain hydrogen oxidation. The reduced kinetic mechanism of hydrogen oxidation in the region of the upper ignition limit can be represented as follows [42]:





A two-dimensional problem was studied. The characteristic scales of the process were chosen as follows: $t_0 = 1/(k_1^0 [\text{H}_2]_0)$, $x_0 = (D_3/k_1^0 [\text{H}_2]_0)^{1/2}$, $U_0 = x_0/t_0 = (D_3 k_1^0 [\text{H}_2]_0)^{1/2}$ (scales of time, length and velocity, respectively, D_3 is the diffusion coefficient of H_2). We define dimensionless variables and parameters $\tau = t/t_0$, $\xi = x/x_0$, $\eta = y/y_0$, $\varpi = U/U_0$, $Y_i = [\text{concentration of the } i\text{th component}] / [\text{H}_2]_0$, $\delta_i = D_i/D_3$ (D_i is the diffusion coefficient of the i th component). The velocity and coordinates of the propagating flame front were determined through D_3 : $\varpi = U/(D_3 k_1^0 [\text{H}_2]_0)^{1/2}$, $\xi = x/(D_3/k_1^0 [\text{H}_2]_0)^{1/2}$, $\eta = y/(D_3/k_1^0 [\text{H}_2]_0)^{1/2}$. Here U , x and y are the corresponding dimensional quantities, k_1^0 is the preexponential factor of reaction (1). Diffusion coefficients (D_i/D_3 , $i=0-6$) $\delta_0, \delta_1, \delta_2, \delta_3=1, \delta_4, \delta_5, \delta_6$ in a hydrogen-oxygen mixture refer to $\text{OH}, \text{O}, \text{H}, \text{H}_2, \text{O}_2, \text{HO}_2, \text{H}_2\text{O}_2$, respectively. The system of equations for the above reaction mechanism takes the form ($m, n = 0 \div 6$ refer to the reacting particles $\text{OH}, \text{O}, \text{H}, \text{H}_2, \text{O}_2, \text{HO}_2, \text{H}_2\text{O}_2$, respectively):

$$\begin{aligned} \partial Y_i / \partial \tau &= \delta_i (\partial^2 Y_i / \partial \xi^2 + \partial^2 Y_i / \partial \eta^2) + \sum_{\substack{m \neq i, n \\ m=i, n}} k_n Y_m Y_n - \sum_{m=i, n} k_n Y_m Y_n \\ \partial T / \partial \tau &= \delta_7 (\partial^2 T / \partial \xi^2 + \partial^2 T / \partial \eta^2) + 1/(C_p \rho) \sum_{m, n} Q_n k_n Y_m Y_n \end{aligned} \quad (I)$$

The rate of heat release in the component of the reaction chain [42] is given by the last equation of system (I). Here C_p is the average specific heat at constant pressure, $\delta_7 \approx \delta_3$ is the thermal diffusivity for near-stoichiometric mixtures, and $\delta_7 \approx \delta_4$ for lean mixtures [42], T is the temperature (K), ρ is the mixture density g/cm^3 , taken from [56]. Specific heat Q_i and diffusion coefficients were taken from [42]. f is the molar fraction of the initial component.

The reaction-diffusion equation for O atoms is shown below as an example:

$$\partial Y_1 / \partial \tau = \delta_1 (\partial^2 Y_1 / \partial \xi^2 + \partial^2 Y_1 / \partial \eta^2) + k_2 Y_2 Y_4 - k_3 Y_1 Y_3 - k_7 Y_0 Y_1 - k_8 Y_1 Y_5$$

The solutions of system (I) satisfy the following boundary conditions for flame propagation from right to left (L is the dimensionless distance between the reactor axis and the reactor wall, symmetry conditions are established on the axis):

$$Y_i(\xi, \eta) \rightarrow 0 \quad (i \neq 3, 4), \quad T(\xi, \eta) \rightarrow 300 \text{ K}, \quad \xi \rightarrow \pm \infty \quad Y_3(\xi, \eta) \rightarrow f_{\text{H}_2}, \quad Y_4(\xi, \eta) \rightarrow f_{\text{O}_2},$$

$$\xi \rightarrow -\infty; \quad \partial Y_3(\xi, \eta) / \partial \eta \rightarrow 0, \quad \partial Y_4(\xi, \eta) / \partial \eta \rightarrow 0, \quad \xi \rightarrow +\infty$$

$$(\partial Y_i(\xi, \eta) / \partial \eta)_{L=0} = 0; \quad T(\xi, L) = 300 \text{ K}$$

When solving system (I), the initial fronts of the initial components Y_3 [H_2] and Y_4 [O_2] in the coordinate zero time were determined according to the composition of the mixture. For the numerical solution, a finite-difference approximation of system (I) on a uniform grid of Cartesian coordinates was used. The two-step implicit scheme provided the second order of approximation of system (I) in spatial and temporal variables [57]. The distribution of the initial components in

sections parallel to the central plane of the channel was approximated as follows $Y_3 = 1/2 - 1/\pi(\arctg(\xi+\eta))$, $Y_4 = 1/2 - 1/\pi(\arctg(\xi-\eta))$, the initial temperature front was defined as $T = T_{ign} \exp((\xi+\eta)^2/50)$ [42], where T_{ign} is an a priori (trial) estimate. These initial fronts correspond essentially to the initiation of flame propagation by an external source. In the calculations, we used 500 partition points along the ξ and 70÷350 points of division along η coordinate. The Laplace operator was approximated according to the "cross" scheme. The boundary conditions on the wall and the plane of symmetry were also approximated with a second order accuracy, while the partial derivatives with respect to time were approximated by one-sided differences, providing first-order accuracy. The calculations used such values of steps in spatial and temporal coordinates, which did not change the solution of the original problem with a further decrease in the step. Integration was performed according to an explicit scheme using the "predictor-corrector" procedure. The change in the concentration and temperature distribution was displayed on the screen, which made it possible to control the calculated parameters during the computation and determine the time of its completion in the dialogue mode. In the course of integration, either the regime of propagation of all the fronts of the Y_i concentrations at the same velocity was achieved, or the process of chemical transformation was faded away. It was believed that the traveling wave mode was achieved when the average value of the velocity did not change at a distance of 100 characteristic dimensions of the flame front, which was defined as the distance on the central plane of the channel where the dimensionless concentration of hydrogen atoms decreased by a factor of e ($e = 2.71828 \dots$). If it was necessary to carry out long-term calculations (near the limits of flame propagation), the following procedure was used. Because the propagating wave with the values of the governing parameters used in the calculations occupied no more than 50 grid nodes, then when the wave approached the left boundary of the computational domain, when all changes in concentration and temperature occurred at 100 left grid nodes (there were only zero values on the right), the Y_i values from the left half of the net were transferred to the right half and the calculation was continued. The reliability of this calculation method was quantitatively verified in [58].

Obviously, to ensure ignition, a cycle of reactions must occur, in which branching occurs (an increase in the number of active centers) [59]. To lower T_{ign} , namely, the flammability limit, the branching rate must increase [59], for example, due to the implementation of an additional branching reaction. Under the conditions of our experiment, this step can be reaction (5), in which a relatively inactive HO_2 radical is converted into active OH, i.e. branching occurs additionally to the reaction (2). As is shown in [59], taking into account reaction (5) makes it possible to explain the expansion of the ignition region in the presence of H atoms generated by an external source. In our case, the source of atoms is the chain initiation reaction (0), because $k_0(a, E)$ increases in the presence of a hot catalyst. This rate is defined below as k_{0cat} (a is the preexponent, E is the activation energy). The higher

the catalytic activity of the metal is, the greater the value of $k_{0\text{cat}}$ is. The numerical experiment consisted in the fact that the value of the value $k_{0\text{cat}}$ ($k_{0\text{cat}} \gg k_0$) for all experimental points of each curve in Fig. 14 was sought by means of paired linear regression analysis [60] with parameters a and E , so that the calculated curve was the closest to the experimental one. The experimental points on each curve were the average of the experimental temperatures, above which combustion occurred and below which there was no combustion. The calculated profiles of the chemical temperature of the components and the flame velocity U for one of the experimental points are shown in Fig. 15.

In Fig. 15, the shade of green determines the spatial distribution of Y_i concentrations. While the boundaries between the shades are isoconcentration (for the temperature distribution by isotherms), a darker color corresponds to a higher concentration (temperature) value within the range of variation between isoconcentration lines (isotherms). The interval between adjacent isoconcentration (isothermal) lines corresponds to a change in concentration (temperature) by 30%. In each of the given two-dimensional distributions, the top of the “frame” is the channel wall, and the bottom of the “frame” is the central plane. The calculation results are shown in Fig. 14 (crosses).

As can be seen from Fig. 14, taking into account the elementary reaction $\text{H} + \text{HO}_2 \rightarrow 2\text{OH}$ (5) allows one to explain the experimentally discovered dependence of T_{ign} on the H_2 concentration. It also allows one to obtain satisfactory agreement with experimental data at $k_{0\text{cat}}$ (a , E) values for catalytic materials: $k_{0\text{cat}} = 4.10^{12} \exp(-3500/T) \text{ cm}^3/(\text{mol}/\text{s})$ for palladium and $k_{0\text{cat}} = 2.10^{15} \exp(-5000/T) \text{ cm}^3/(\text{mol}/\text{s})$ for platinum.

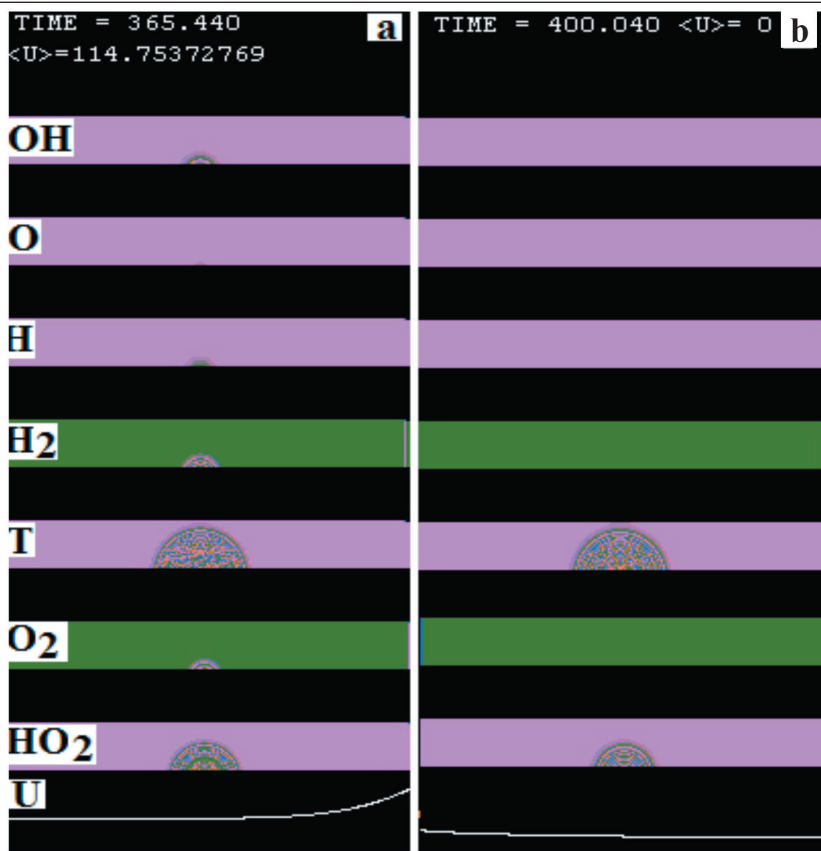


Figure 17. Calculated profiles of chemical components and temperature at a given point in time (when it is clear whether the reaction has started or not) above (a) and below (b) T_{ign} . The top of each frame is the reactor wall; bottom - the axis of the reactor. The front of the flame moves from the center to both sides. $P = 40$ Torr, wall temperature - 300 K

a) - Initial $T = 680$ K, ignition occurs;

b) - Initial $T = 670$ K, no ignition. U - flame velocity, arbitrary units.

It should be noted that the activation energy of the gross process for a hot palladium surface (~ 7 kcal/mol) is higher than for a cold palladium surface (2.4 kcal/mol), while for a hot platinum surface (~ 10 kcal/mol). It is lower than for the cold platinum surface (19 ± 4 kcal/mol), which may be due to both the use of the reduced hydrogen combustion mechanism and errors in temperature measurement. Establishing the nature of this discrepancy requires further research.

Conclusions for Chapter 7

It was experimentally established that the temperature of the ignition limit above the palladium surface at $P = 1.75$ atm, measured bottom approach by temperature, for mixtures of 30% methane + 70% hydrogen + air ($\theta = 0.9$, $T = 317$ °C) and 30% propane + 70 % H_2 + air ($\theta = 1$, $T = 106$ °C) noticeably decreases after subsequent ignitions to $T = 270$ °C for $H_2 - CH_4$ - air and to $T = 32$ °C for a mixture $H_2 - C_3H_8$ - air. The flammability limit returns to the initial value after the reactor is treated with oxygen or air, i.e. there is a hysteresis phenomenon. The ignition limit of mixtures 30% (C_2 , C_4 , C_5 , C_6) + 70% H_2 + air ($\theta = 0.6, 1.1, 1.2, 1.2$, respectively) over the surface of metallic palladium is $25 \div 35$ °C at $P = 1.75$. There is no hysteresis effect. It was found that a lean mixture of 30% C_2H_6 + 70% H_2 + air ($\theta = 0.6$) has the lowest ignition temperature: 24 °C at 1 atm. The estimate of the effective activation energy for the ignition of mixtures over Pd is $\sim 2.4 \pm 1$ kcal/mol, which is typical for the surface process. It is shown that the use of Pd makes it possible to ignite combustible 30% hydrocarbon + 70% H_2 at 1÷2 atm at the initial room temperature without using external energy sources. It was observed that the separation of the CH and Na emission bands in time during the combustion of a mixture of 30% propane + 70% H_2 + air ($\theta = 1$), found in this work, is due to the occurrence of hydrodynamic instability of the flame when it touches the end of the cylindrical reactor.

It was found that the ignition temperatures of hydrogen - oxygen and hydrogen - methane - oxygen mixtures using heated wires of palladium, platinum, nichrome and kanthal (fechral) at a total pressure of 40 Torr increase with a decrease in the hydrogen content in the mixture. Only heated palladium wire has a noticeable catalytic effect. A qualitative numerical calculation made it possible to reveal the role of the additional branching reaction $H + HO_2 \rightarrow 2OH$ in the process of ignition initiation by a heated wire.

References for Chapter 7

1. Davy H. *Some new experiments and observations on the combustion of gaseous mixtures with an account of a method of preserving a continuous light in mixtures of inflammable gases and air without flame. 1817. Phil. Trans. R. Soc. London A. Vol. 107. pp.77-100.*
2. Lee J., Trimm D. L. *Catalytic combustion of methane. Fuel Processing Technology. 1995. Vol. 42. pp. 339-355.*
3. Deutschmann O., Maier L. I., Riedel. U. et al. *Hydrogen assisted catalytic combustion of methane on platinum. Catalysis Today. 2000. Vol. 59. pp.141-165.*
4. Lyubovsky M., Karim H., Menacherry P. et al. *Complete and partial catalytic oxidation of methane over substrates with enhanced transport properties. Catalysis Today. 2003. Vol. 83. pp. 183-201.*

5. Salomons S., Hayes R. E., Poirier M. et al. Flow reversal reactor for the catalytic combustion of lean methane mixtures. *Catalysis Today*. 2003. Vol. 83. pp. 59-75.

6. Lampert J. K., Kazia M. S., and Farrauto R. J. Palladium catalyst performance for methane emissions abatement from lean burn natural gas vehicles. *Applied catalysis B: Environmental*. 1997. Vol. 14. pp. 211-230.

7. IAEA SAFETY STANDARDS SERIES. Design of Reactor Containment Systems for Nuclear Power Plants SAFETY GUIDE. No. NS-G-1.10. 2004. 127 p.

8. Frennet A. Chemisorption and exchange with deuterium of methane on metals. *Catal. Rev.- Sci. Eng.* 1974. Vol. 10. pp. 37-51.

9. Cullis C. F., Willatt B. M. Oxidation of methane over supported precious metal catalysts. *Journal of Catalysis*. 1983. Vol. 83. pp. 267-281.

10. Hicks R. F., Qi H., Young M. L., Lee R. G. Structure sensitivity of methane oxidation over platinum and palladium. *Journal of Catalysis*. 1990. Vol. 122. pp. 280-291.

11. Hayes R. E., Kolaczowski S., Lib P., Awdryb S., The palladium catalyzed oxidation of methane: reaction kinetics and the effect of diffusion barriers. *Chemical Engineering Science*. 2001. Vol. 56. pp. 4815-4830.

12. Choudhury S., Sasikala R., Saxena V., Kumar-Aswalb D., Bhattacharyac D. A new route for the fabrication of an ultrathin film of a PdO–TiO₂ composite photocatalyst. *Dalton Trans*. 2012. Vol. 41. pp. 12090-12095.

13. Nilsson P. O., Shivaraman M. S. Optical properties of PdO in the range of 0.5–5.4 eV. *J. Phys. C: Solid State Phys.* 1979. Vol. 12. pp. 1423-1427.

14. Ling F., Chika Anthony O., Xiong Q., Luo M., Pan X., Jia L., Huang J., Sun D., Li Q. PdO/LaCoO₃ heterojunction photocatalysts for highly hydrogen production from formaldehyde aqueous solution under visible light. *International journal of hydrogen energy*. 2016. Vol. 41. pp. 6115-6122. DOI: 10.1016/j.ijhydene.2015.10.036

15. Diaz C., Valenzuela M. L., Rios C., Segovia M. Oxidation facility by a temperature dependence on the noble metals nanostructured M^o/M_xO_y phase products using a solid state method: the case of Pd. *Journal of the Chilean Chemical Society*. 2016. Vol. 61. No. 4. <http://dx.doi.org/10.4067/S0717-97072016000400024>

16. Rodionov I. D., Rodionov A. I.; Vedeshin L. A., Vinogradov A. N., Egorov V.V., Kalinin A. P. Airborne hyperspectral systems for solving remote sensing problems. *Izvestiya Atmospheric and Oceanic Physics*. 2014. Vol. 50. No. 9. pp. 989-1003. DOI: 10.1134/S0001433814090175

17. Vinogradov A. N., Egorov V. V., Kalinin A. P., Rodionov A. I., Rodionov I. D. A line of aviation hyperspectrometers in the UV, visible, and near-IR ranges. *Journal of Optical Technology*. 2016. Vol. 83. No. 4. pp. 237-243. <https://doi.org/10.1364/JOT.83.000237>

18. Kalinin A. P., Orlov A. G., Rodionov A. I., Troshin K. Ya. *Demonstraciya vozmozhnosti izucheniya processov goreniya i v zryva s pomoshch'yu distancionnogo giperspektral'nogo zondirovaniya (Demonstration of the possibilities to study combustion and explosion processes on the base of hyperspectral remote sensing). Physical-Chemical Kinetics in Gas Dynamics. 2009. Vol. 8. http://physics.nist.gov/PhysRefData/ASD/lines_form.html (in Russian)*

19. Rubtsov N. M., Seplyarskii B. S., Troshin K. Ya., Chernysh V. I., Tsvetkov G. I. *Investigation into Spontaneous Ignition of Hydrogen–air Mixtures in a Heated Reactor at Atmospheric Pressure by High-speed Cinematography. Mendeleev Communications. 2012. Vol. 22. No. 4. pp. 222-224. DOI: 10.1016/j.mencom.2012.07.001*

20. Rubtsov N. M., Seplyarskii B. S., Troshin K. Ya., Tsvetkov G. I., Chernysh V. I. *High-speed color cinematography of the spontaneous ignition of propane–air and n-pentane–air mixtures. Mendeleev Communications. 2011. Vol. 21. No. 3. pp. 31-33. DOI: 10.1016/j.mencom.2011.01.013*

21. Rubtsov N. M., Chernysh V. I., Tsvetkov G. I., Troshin K. Ya., Shamshin I. O. *Ignition of hydrogen–air mixtures over Pt at atmospheric pressure. Mendeleev Communications. 2017. Vol. 27. No. 3. pp. 307-309. <https://doi.org/10.1016/j.mencom.2017.05.031>*

22. Rubtsov N.M., Vinogradov A.N., Kalinin A.P., Rodionov A. I., Chernysh V.I. *Cellular combustion and delay periods of ignition of a nearly stoichiometric H₂–air mixture over a platinum surface. Mendeleev Communications. 2016. Vol. 26. No. 2. pp. 160-162. DOI: 10.1016/j.mencom.2016.03.027*

23. Cashdollar K. L., Zlochower I. A., Green G. M., Thomas R. A., Hertzberg M. *Flammability of Methane Propane and Hydrogen Gases. Journal of Loss Prevention in the Process Industries. 2000. Vol. 13. No. 3. pp. 327-340. DOI: 10.1016/S0950-4230(99)00037-6*

24. Lewis B., Von Elbe G. *Combustion, Explosions and Flame in Gases. New York, London. Acad. Press. 1987.*

25. Repinski S.M. *Vvedenie v himicheskuyu fiziku poverhnosti tvordych tel (Introduction into chemical physics of the surface of solids). Novosibirsk: Nauka, Sibir publishing company. 1993. (in Russian)*

26. Kristinsdóttir L; Skúlason E. *A systematic DFT study of hydrogen diffusion on transition metal surfaces Surface Science. 2012. Vol. 606. No. 17-18. pp. 1400-1404. DOI: 10.1016/j.susc.2012.04.028*

27. Rothman L. S., Gordon I. E., Babikov Y., Barbe A., Chris Benner D., et al. *The HITRAN 2012 Molecular Spectroscopic Database. Journal of Quantitative Spectroscopy & Radiative Transfer. 2013. 130. pp. 4-50.*

28. Rubtsov N. M., Vinogradov A. N., Kalinin A. P., Rodionov A. I., Rodionov I. D., Troshin K. Ya., Tsvetkov G. I., Chernysh V. I. *Ispol'zovaniye vysokoskorostnoy opticheskoy mnogomernoy metodiki dlya ustanovleniya osobennostey vosplamneniya i goreniya smesi 40% H₂ – vozdukh v prisutstviy metallicheskey platiny (High Speed Multidimensional Optical Complex in Research of ignition and combustion features of 40% H₂ – air mix in the presence of platinum). Physical-Chemical Kinetics in Gas Dynamics. 2016. Vol. 17. No. 1. <http://chemphys.edu.ru/issues/2016-17-1/articles/615/>*

29. Stützer R. G., Kraus S., Oschwald M. *Characterization of Light Deflection on Hot Exhaust Gas for a LIDAR Feasibility Study. Conference 4th Space Propulsion. 2014. <https://www.researchgate.net/publication/263586493>.*

30. Icitaga T. *Emission spectrum of the oxy-hydrogen flame and its reaction mechanism. (1) Formation of the Activated Water Molecule in Higher Vibrational States. The Review of Physical Chemistry of Japan. 1939. Vol. 13f. No. 2. pp. 96–107.*

31. Rubtsov N. M., Chernysh V. I., Tsvetkov G. I., Troshin K. Ya, Shamshin I. O., Kalinin A.P. *The features of hydrogen ignition over Pt and Pd foils at low pressure. Mendeleev Communications. 2018. Vol. 28. Vol. 2. pp. 216-218. <https://doi.org/10.1016/j.mencom.2017.05.031>*

32. Tang C., Zhang Y., Huang Z., *Progress in combustion investigations of hydrogen enriched hydrocarbons. Renewable and Sustainable Energy Reviews. 201. Vol. 30. pp. 195–216.*

33. Knyazkov D. A., Shvartsberg V. M., Dmitriev A. M., Osipova K. N., Shmakov A. G., Korobeinichev O.P., Burluka, A. *Combustion Chemistry of Ternary Blends of Hydrogen and C1–C4 Hydrocarbons at Atmospheric Pressure. Combustion, Explosion, and Shock Waves. 2017. Vol. 53. No. 5. pp. 491–499. DOI: 10.1134/S001050821705001X*

34. Biswas S., Tanvir S., Wang H., Qiao, L. *On ignition mechanisms of premixed CH₄/air and H₂/air using a hot turbulent jet generated by pre-chamber combustion. Applied Thermal Engineering. 2016. Vol. 106. pp. 925–937. DOI: 10.1016/j.applthermaleng.2016.06.070*

35. Cho E.-S., Chung S. H. *Improvement of flame stability and NO_x reduction in hydrogen-added ultralean premixed combustion. Journal of Mechanical Science and Technology. 2009. Vol. 23. No. 3. pp. 650-658. DOI: 10.1007/s12206-008-1223-x*

36. Razali H., Sopia, K., Mat S. *Green fuel: 34% reduction of hydrocarbons via hydrogen (AL+HCl) blended with gasoline at maximum torque for motorcycle operation. ARPN Journal of Engineering and Applied Sciences. 2015. Vol. 10. No. 17. pp. 7780-7783.*

37. Flores R. M., McDonnell V. G., Samuelsen G. S. *Impact of Ethane and Propane Variation in Natural Gas on Performance of a Model Gas Turbine Combustor*. *J. Eng. Gas Turbines Power*. 2003. Vol. 125. No. 3. pp. 701–708. <https://doi.org/10.1115/1.1584480>
38. Hassan H., Khandelwa, B. *Reforming Technologies to Improve the Performance of Combustion Systems*. *Aerospace*. 2014. Vol. 1. pp. 67–96. DOI: 10.3390/aerospace1020067
39. Xiong H., Wiebenga M. H., Carrillo C., Gaudet J. R., Pham H. N., Kunwar D. et. al. *Design considerations for low-temperature hydrocarbon oxidation reactions on Pd based catalysts*. *Applied Catalysis B: Environmental*. 2018. Vol. 236. No. 15. pp. 436–444. DOI: 10.1016/j.apcatb.2018.05.049
40. Persson K., Pfeifferle L. D., Schwartz W., Ersson A., Jaras S.G. *Stability of palladium-based catalysts during catalytic combustion of methane: The influence of water*, *Applied Catalysis B: Environmental*. 2007. Vol. 74. pp. 242–250. DOI: 10.1016/j.apcatb.2007.02.015
41. Rubtsov N. M., Chernysh V. I., Tsvetkov G. I., Troshin K. Ya., Shamshin I.O. *Ignition of hydrogen-methane-air mixtures over Pd foil at atmospheric pressure*. *Mendelev Communications*. 2019. Vol. 29. No. 4. pp. 469–471. DOI: 10.1016/j.mencom.2019.07.039
42. Rubtsov N. M. *The Modes of Gaseous Combustion*, Cham, Switzerland, Springer International Publishing, 2016. DOI: 10.1007/978-3-319-25933-8
43. Markstein G. H. *Cell structure of propane flames burning in tubes*. *The Journal of Chemical Physics*. 1949. Vol. 17. p. 428. <https://doi.org/10.1063/1.1747278>
44. Zeldovich. Ya. B. *Teoriya gorennya i detonatsii gazov (Theory of Combustion and Detonation of Gases)*. Moscow, Acad. Sci. USSR. 1944. (in Russian)
45. Kreshkov A. P. *Osnovy analiticheskoy khimii. Teoreticheskiye osnovy. Kolichestvennyy analiz (Fundamentals of analytical chemistry. Theoretical basis. Qualitative analysis)*. M: Publishing house "Khimiya". 1970. Vol. 3. (in Russian)
46. Rubtsov M. N., Vinogradov A. N., Kalinin A. P., Rodionov A. I., Troshin K. Ya., Tsvetkov G. I., Chernysh V. I. *Gas dynamics and kinetics of the penetration of methane–oxygen flames through complex obstacles, as studied by 3D spectroscopy and high-speed cinematography*. *Mendelev Communications*. 2017. Vol. 27. No. 2. pp. 192–194. <https://doi.org/10.1016/j.mencom.2017.03.029>
47. Naboko I. M., Rubtso N. M., Seplyarskii B. S., Troshin K. Ya., Tsvetkov G. I., Chernysh V. I. *Cellular combustion at the transition of a spherical flame front to a flat front at the initiated ignition of methane–air, methane–oxygen and n-pentane–air mixtures*. *Mendelev Communications*. 2013. Vol. 23. No. 6. pp. 358–360. DOI: 10.1016/j.mencom.2013.11.020
48. Fisher M. *Safety aspects of hydrogen combustion in hydrogen energy systems*. *Int. J. Hydrogen Energy*. 1986. Vol. 11. pp. 593–601.

49. Welch A. B., Wallace J. S. *Performance Characteristics of a Hydrogen-Fueled Diesel Engine with Ignition Assist*. SAE Paper 902070. 1990. DOI:10.4271/902070

50. Kumar R. K. *Ignition of hydrogen-oxygen- diluent mixtures adjacent to a hot, non-reactive surface*. *Combustion and Flame*. 1989. Vol. 75. pp. 197-215.

51. Silver R. S. *The Ignition of Gaseous Mixtures by Hot Particles*. *The Philosophical Magazine and Journal of Science*. 1937. 23(156). pp. 633-657.

52. Brady K. B. *Ignition Propensity of hydrogen/air mixtures in the presence of heated platinum surfaces*. Master of Science Thesis. Department of Mechanical and Aerospace Engineering. Case Western Reserve University. January 2010.

53. Rinnemo, M., Deutschmann O., Behrendt F., Kasemo B. *Experimental and numerical investigation of the catalytic ignition of mixtures of hydrogen and oxygen on platinum*. *Combustion and Flame*. 1997. 111. pp. 312-326. DOI:10.1016/S0010-2180(97)00002-3

54. Menon S. K., Boettcher P.A., Ventura B., Blanquart G., Shepherd J.E. *Investigation of hot surface ignition of a flammable mixture*. Western States Section of the Combustion Institute (WSSCI). Arizona University, Tempe, Paper # 12S-39. 2012.

55. Dong-Joon Kim *Ignition Temperature of Hydrogen/Air Mixture by Hot Wire in Pipeline*. *Fire Science and Engineering*. 2014. Vol. 28. No. 4. pp. 8-13. DOI: 10.7731/KIFSE.2014.28.4.008

56. *Tables of Physical Values. Handbook (Tablitsy fizicheskikh velichin. Spravochnik)*. ed. Kikoin I. K. Atomizdat. Moscow. 1976. 1007 p. (in Russian)

57. Marchuk G. I. *Metody vychislitel'noy matematiki (Methods of computational mathematics)*. Moscow: Nauka. 1989. 608 p. (in Russian)

58. Rubtsov N. M., Kotelkin V. D., Karpov V. P. *Perekhod rasprostraneniya plameni iz izotermicheskogo rezhima v rezhim tsepnnykh protsessov s nelineynym razvetvleniyem tsepey (The transition of flame propagation from isothermal mode to the mode of chain processes with non-linear chain branching)*. *Kinetics and Catalysis*. 2004. Vol. 45. No. 1. pp. 3-11.

59. Semenov N. N. *O nekotorykh problemakh khimicheskoi kinetiki i reaktsionnoi sposobnosti (On some problems of chemical kinetics and initiative reactivity)*. 2nd edn., Moscow: Izdatel'stvo AN SSSR. 1958. 686 p. (in Russian)

60. Montgomery D. C., Peck E. A., Vining G. *Introduction to linear regression analysis*. 5th ed. John Wiley & Sons Inc., Wiley Series in probability and statistics, Hoboken, New Jersey, US. 2012. 659 p.

CHAPTER 8. Determination of the features of combustion of nanopowders and their compacted samples by the methods of visible and infrared filming

Copper nanopowders are obtained by the method of hydrogen reduction (chemical-metallurgical method) and thermal decomposition of copper citrate and formate. It was shown that copper nanopowder synthesized from copper citrate is not pyrophoric. Combustion of this copper nanopowder can be initiated by an external source, with the combustion wave velocity being 1.3 ± 0.3 mm/s. The nanopowder has a ~ 4 times larger specific surface area than the nanopowder obtained by the chemical-metallurgical method. It practically does not contain oxides and is stable in atmospheric air. Copper nanopowder obtained by the chemical-metallurgical method is pyrophoric and therefore requires passivation, but its passivation leads to the formation of noticeable amounts of copper oxides. The burning rates of passivated and non-passivated copper nanopowder obtained by the chemical-metallurgical method are the same.

Tungsten nanopowders are synthesized by reduction of tungsten trioxide with hydrogen (chemical metallurgical method) at $440\div 640$ °C from samples with different specific surface. It is shown that the W nanopowder synthesized at 640 °C for all three precursors used is non-pyrophoric α - W . Its combustion can be initiated by an external source. Combustion develops in a spatially non-uniform regime. Nanopowder synthesized at 480 °C from tungsten oxide of grades 1 and 2 is a mixture of α - W , β - W u $WO_{2.9}$. This powder is pyrophoric. It was found that the passivated W nanopowder synthesized at 480 °C from grade 3 tungsten oxide at 480 °C is β - W with traces of WO_3 and $WO_{2.9}$. The temperature range of synthesis β - W , obtained in the work is very narrow: $470\div 490$ °C. The specific surface area of α - W nanopowders is 10 ± 2 m²/g. It is 18 ± 1 m²/g for the β - W mixture with traces of WO_3 and $WO_{2.9}$. The dynamics of temperature fields during the ignition and combustion of tungsten nanopowders obtained at different temperatures has been studied. Preliminary experimental studies of the combustion features of compact samples made of non-passivated iron nanopowders and the effect of the porosity of these compact samples on the dynamics of their heating in air have been carried out. The aim was to establish the temperature range, at which it is possible to carry out technological operations with compact samples of non-passivated iron nanopowders safely.

Keywords: *combustion mode, nanopowders, pyrophoricity, compacting, infrared video camera.*

Metal nanopowders are pyrophoric, i.e. are capable of spontaneously igniting on contact with air due to their high chemical activity and large specific surface area. There are two main ways to ensure fire and explosion safety of technological

processes: passive engineering, based on warning systems of undesirable changes in the process, and scientific and technological, involving such a change in the technological process or materials used in the process, which leads to the fact that the technological the process becomes less dangerous or safer. In order to make the process of further processing of nanopowders into products safe, they are passivated. Passivation consists in creating a thin protective film on the surface of nanoparticles, which prevents spontaneous combustion of metal nanopowders. Passivation lasts tens of hours, which is a limiting factor in increasing the production of nanopowders. We have previously formulated a model of the passivation of a pyrophoric nanopowder layer and analyzed it by analytical and numerical methods [1-3]. Assuming the limiting role of oxidant diffusion in the mechanism of propagation of the passivation wave, the dependence of the temperature in the heat release zone on the governing parameters is obtained. It is shown that for the maximum temperature in the nanopowder layer there is an intermediate asymptotic behavior when the temperature does not change with time. An approximate formula for calculating the minimum time of full passivation for a sample of arbitrary thickness is obtained on the basis of experimental data for a specific sample. The applicability of theoretical approaches of the classical macroscopic theory of thermal explosion to explain the phenomena of ignition in macroscopic objects consisting of iron and nickel nanoparticles is shown. The results of recent work with the participation of the authors of this book are demonstrated below. Along with the establishment of the features of the combustion of copper and tungsten nanopowders, preliminary experimental studies of the features of the combustion of compact samples of non-passivated iron nanopowders and the effect of the porosity of these compact samples on the dynamics of their heating in air are described. The goal is to develop new highly efficient methods for producing compact products from nanopowders, which make it possible to provide the required level of fire and explosion safety both in the processing of nanopowders and products made of them.

§ 1. Combustion of copper nanopowders

Copper nanoparticles have attracted considerable attention in recent years due to their wide possible application in photochemical catalysis, in bio- and electrochemical sensors, photovoltaic energy converters, and medicine [4-11].

The synthesis of copper nanoparticles is carried out by methods of chemical reduction [8], thermal decomposition of precursors [12], explosion of thin wires, etc. [13-18].

Copper nanoparticles can be pyrophoric, therefore, in order to make possible subsequent processing of nanopowders in atmospheric air, they must either be stored under an inert liquid or protected. Protection (passivation) means obtaining a thin oxide film on the surface of nanoparticles, which prevents the oxidation of

nanoparticles and ensures the preservation of their unique properties [19] during or after synthesis.

The purpose of this section is to identify the thermal regimes and dynamics of ignition and combustion of copper nanopowders obtained by the chemical-metallurgical method and the method of thermal decomposition of copper salts, to establish the conditions for their passivation to prevent ignition and subsequent oxidation. A number of characteristics of synthesized copper nanopowders have been determined using X-ray phase analysis, BET and scanning electron microscopy methods.

For experimental studies, we used copper nanopowders obtained both by the chemical-metallurgical method and by thermal decomposition of copper citrate and formate salts. The main stages of the synthesis by the chemical-metallurgical method are the preparation of a precipitate of metal hydroxide, its drying, reduction and passivation. The synthesis of copper hydroxide was carried out by heterophase interaction of CuCl_2 with an alkali solution. After precipitation of hydroxide, it was washed with water in a Buchner funnel to $\text{pH} = 7$ and dried in air until dusting. A quartz boat with copper hydroxide powder was installed inside a quartz reactor and placed in an oven heated to $80\text{ }^\circ\text{C}$ for 1 h while blowing hydrogen through the reactor. Then the reactor with the boat was removed from the furnace and cooled to $20\text{ }^\circ\text{C}$ in an argon flow through the reactor. Then the reactor was placed on a subject table for video recording, and a quartz boat with copper nanopowder was removed from the reactor and placed next to it. Then the boat with copper nanopowder and the reactor were either blown with air using a fan, or the air fan was turned off. In some experiments, copper nanopowder was passivated in an argon flow containing 0.6% oxygen for 30 min and only then was removed from the reactor.

Thermal decomposition of copper citrate $\text{Cu}_3(\text{C}_6\text{H}_5\text{O}_7)_2$ (at $350\text{ }^\circ\text{C}$) and copper formate ($\text{C}_2\text{H}_2\text{CuO}_4$) (at $250\text{ }^\circ\text{C}$) was carried out in the same reactor, in vacuum with continuous pumping out of the gas released during the decomposition of salts using a forevacuum (2NVR-5D) and diffusion (H1) pumps. When the salt was heated, an increase in pressure was first recorded from 10^{-4} Torr to $> 10^{-1}$ Torr. The decomposition was considered complete when the pressure in the reactor became less than 10^{-2} Torr. Then the reactor was removed from the furnace and cooled with continuous evacuation of gas. After cooling to $20\text{ }^\circ\text{C}$, argon was admitted to the reactor to atmospheric pressure, and only then the quartz boat with copper nanopowder was removed from the reactor and placed on a subject table for video recording. The process of removing the boat and placing it on the table took about 5 s.

Casio Exilim F1 PRO high-speed color video camera (60-1200 frames per second) and Flir 60 infrared camera (shooting speed 60 frames/s, resolution 320x240 pix, sensitivity interval 8-14 μm) were used to study the ignition and combustion modes of copper nanopowder. The phase composition of the obtained samples was studied using a DRON 3M X-ray diffractometer with a coordinate-sensitive

sensor. The specific surface area was measured using a Sorbi-M analyzer by the BET method. The microstructure of the powders was studied using an ultrahigh-resolution scanning electron microscope Zeiss Ultra Plus (Germany) equipped with an INCA 350 Oxford Instruments X-ray microanalyzer.

Combustion in air of a copper nanopowder obtained by the chemical-metallurgical method by holding it in a furnace for 1 h at 80 °C and blowing hydrogen through a reactor (a 2-millimeter-thick sample) is shown in Fig. 1a. Self-ignition, leading to combustion of the sample, occurs only when it is blown with air. Spontaneous combustion is not observed without blowing. The propagation velocity of the combustion front over the sample surface, estimated as the average velocity over three points selected at different parts of the front, is 0.3 ± 0.02 mm/s. The sequential frames of initiated combustion in air of copper nanopowder (2 mm layer thickness) obtained under the same conditions by the chemical-metallurgical method in the absence of blowing are shown in Fig. 1b. Filming was carried out with a Flir 60 infrared camera.

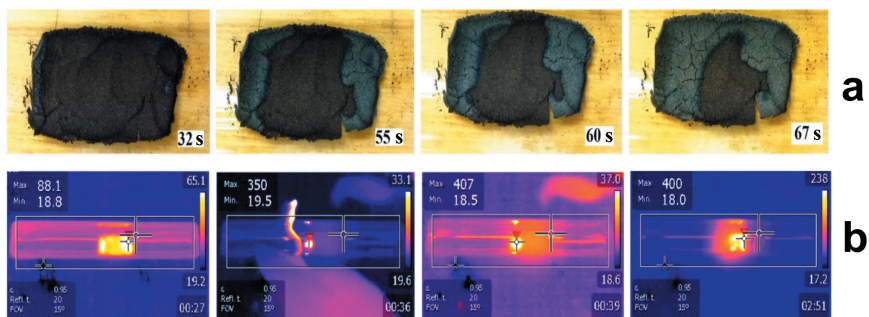


Figure 1. Combustion of copper nanopowder in a stream of air

a) chemical-metallurgical method (sample of 2 mm thickness). At the bottom of each frame on the right is the time in seconds after the boat with the nanopowder was removed from the reactor. Initial powder temperature is 20 °C. The shooting speed is 60 frames per second.

b) A sequence of frames of infrared video recording of the combustion of copper nanopowder (2 mm layer thickness) obtained by the method of chemical metallurgy. There is no air flow. The initial temperature of the powder is 20 °C. The shooting speed is 60 frames per second. The left frame shows the temperature distribution on the sample surface at the moment of maximum self-heating. The three right frames show the initiation and combustion of the same sample of copper nanopowder with a heated wire (the front propagates from left to right).

The time in minutes is indicated at the bottom of each frame on the right: seconds after being removed from the reactor.

In case of visual analysis of infrared video data, one should take into account the peculiarities of image processing with the Flir 60 infrared camera: the area with the maximum temperature value at a given time has the same brightness for all frames. The real values of the maximum and minimum temperatures at a given time are shown near the left border of each frame. The larger cross on each frame indicates the selected point, at which the temperature is measured. The smaller cross with a red flag automatically points to the point with the maximum temperature in the frame, and the smaller cross with a blue flag to the point with the minimum temperature in the frame. The left frame in Fig. 1b shows the temperature distribution over the sample surface at the moment of maximum self-heating, which is 88 °C. This local heating in the center of the sample did not lead to the propagation of the reaction front, but after cooling, it turned out to be possible to initiate combustion with a heated wire of the same sample of copper nanopowder in air (the next three frames in Fig. 1b). The maximum combustion temperature reaches 407 °C, and the reaction front velocity is 0.3 ± 0.04 mm/s and is consistent with the experiment shown in Fig. 1a. Therefore, if the sample is blown, then the air freely reaches the surface of the powder, and the self-ignition occurs. In the absence of blowing, residual argon flows out of the reactor near the boat and makes it difficult to supply oxygen from the atmosphere to the sample. Therefore, self-ignition is missing. Since such a slight change in the experimental conditions leads to qualitative changes in the modes of interaction of the copper nanopowder with air, this indicates the high sensitivity of the copper nanopowder to the conditions of the experiments. Measurements of the specific surface area of a non-passivated nanopowder (obtained without blowing) and passivated for 30 min in an argon flow containing 0.6% mass of oxygen at 20 °C showed that they are 13 ± 2 m²/g and 10 ± 2 m²/g, respectively. The value of the average diameter of nanoparticles can be estimated by the formula $d = 6 / (\rho s)$, where s is the specific surface area, $\rho = 8.92$ g/cm³ is the copper density. For non-passivated and passivated nanopowders, calculation by the formula gives the value of the average diameter of copper nanoparticles $d = 47$ nm and $d = 61$ nm, respectively.

Consequently, passivation does not lead to a qualitative change in the specific surface area of a copper nanopowder and nanoparticle sizes.

The modes of combustion of copper nanopowders obtained by decomposition of salts is demonstrated in Fig. 2. Hot-wire-initiated combustion of copper nanopowder (2-mm layer thickness) in air (without blowing) obtained from copper citrate at 350 °C is shown in Fig. 2a. The velocity of the combustion front of copper nanopowder obtained from copper citrate is 1.3 ± 0.3 mm/s. It turned out that only the surface layer is oxidized in the combustion wave, while the inner part of the sample remains combustible. Indeed, if the continuity of the oxide layer is violated, the powder inside ignites (see frames 182, 259). The specific surface of the nanopowder after synthesis, determined by the BET method, is 45 ± 5 m²/g, and the average diameter of copper nanoparticles is $d = 14.6$ nm.

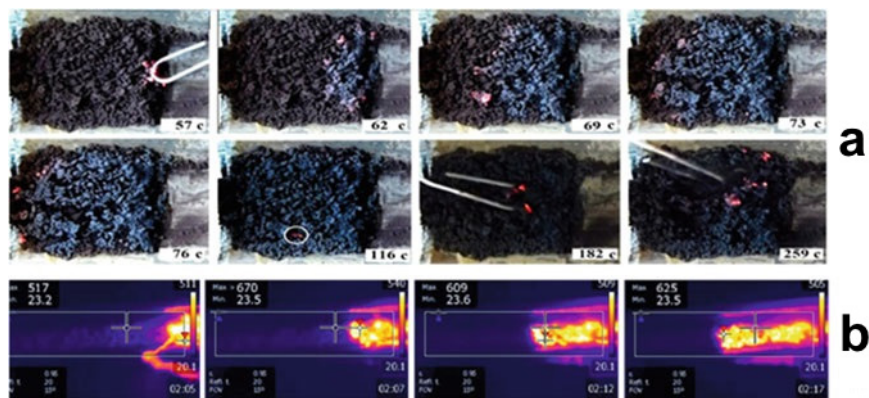


Figure 2.

a) - Sequences of video footage of initiated combustion in air of copper nanopowder (2 mm layer thickness) obtained from copper citrate at 350 °C. At the bottom of each frame on the right is the time in seconds after the boat with the powder was removed from the reactor.

b) - Sequences of frames of infrared video recording of initiated combustion in air of copper nanopowder (2 mm layer thickness) obtained from copper citrate at 350 °C. At the bottom of each frame on the right is the time in minutes - seconds after the boat with the powder was removed from the reactor.

Despite such a high specific surface area, we were unable to obtain self-ignition of the sample, even if the residual pressure in the reactor after the decomposition of copper citrate was $5 \cdot 10^{-5}$ Torr. This is inconsistent with the results of [20], in which the copper powder obtained by the decomposition of copper citrate ignited spontaneously in air at a pressure in the reactor after the completion of decomposition equal to 10^{-3} Torr.

Thus, the regimes of combustion of a copper nanopowder layer could be realized only when it is initiated by a heated wire.

The frames of infrared video recording of copper nanopowder (two-millimeter layer thickness), initiated by a heated wire combustion in air, obtained from copper citrate at 350 °C in Fig. 2b. It can be seen that the combustion front propagates over the sample surface initially, and the bulk of the nanopowder continues to react when the surface combustion front has already passed. This is evidenced by the long (tens of seconds) retention of a high temperature in the region of the sample where the combustion front passed, and the movement of the temperature maximum (the location of the smaller cross with a red flag) in the opposite direction: from the left end of the sample to the central part (see Fig. 2). The maximum temperature in the combustion front reaches 611 °C. Based on the data

obtained (large specific surface area, high velocity and temperature of the combustion front), it could be expected that copper nanopowder synthesized from copper citrate will be pyrophoric. However, copper nanopowder obtained from copper citrate does not self-ignite, i.e. is not initially pyrophoric. The stability of this non-pyrophoric nanopowder can be associated with the “poisoning” of copper with CO [21], which is formed during the thermal decomposition of citrate.

It should be noted that, during the decomposition of copper formate, along with copper powder, a copper foil is formed on the inner surface of the boat. Copper powder contains relatively large crystallites. In contrast to the methods for producing copper powders described above, self-sustaining combustion was not possible even when it was initiated with a heated wire. The combustion process dies out starting near the spiral. The results obtained allow us to conclude that the thermal decomposition of copper formate is not a promising method for producing copper nanopowder.

The photographs of Cu nanopowders synthesized by the chemical-metallurgical method and passivated for 30 min with a mixture of 0.6% air with argon at 20 °C (a) and thermal decomposition of copper citrate (b), obtained by scanning electron microscopy (Zeiss Ultra Plus / INCA 350 Oxford Instruments) are shown in Fig. 3a, b. As can be seen from the figure, sample (a) consists of sintered agglomerates. Particles with a size of 100-200 μm and less than 20 μm are present. However, they are all sintered agglomerates of smaller particles.

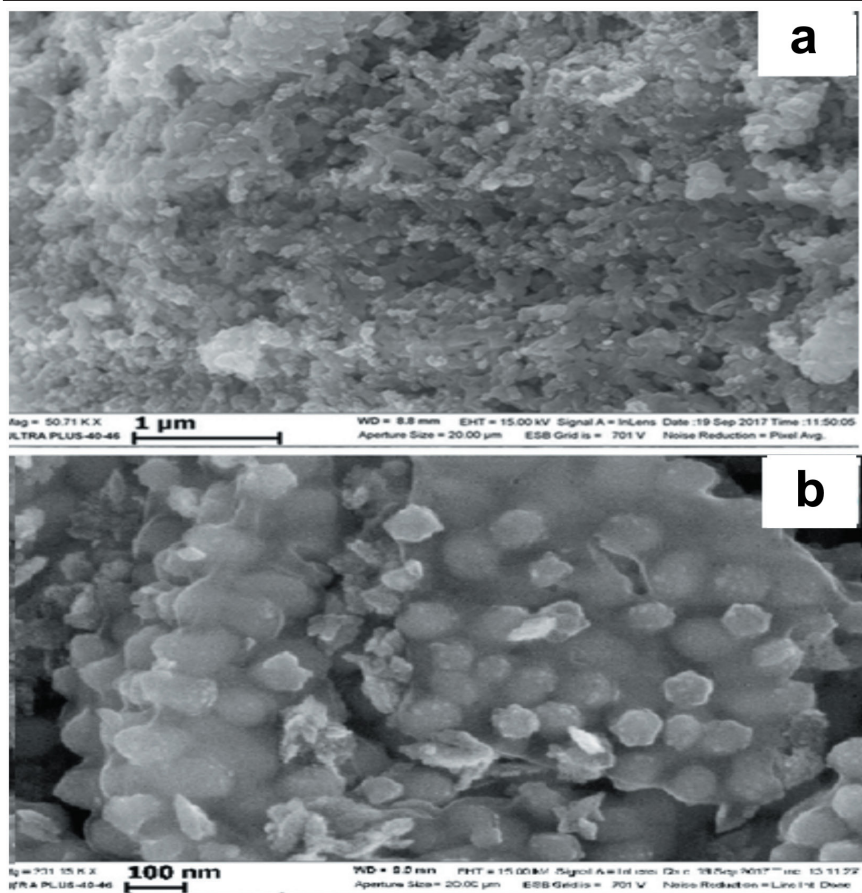


Figure 3. Microphotographs of copper nanopowders obtained by
a) - chemical-metallurgical method (passivation for 30 minutes) and
b) - thermal decomposition of copper citrate

Sample (b) is uniform in particle size about 10-30 μm. These particles are agglomerates of particles with a size of about 100 nm, located in a matrix, which is visible in the photograph as a "binding glue" between the particles. The hierarchy of the structure is well traced. Particles less than 100 nm in size stick together into structures with a size of 1-2 μm, which in turn form separate agglomerated particles with a size of 10-30 μm (not shown in the figure). On particles less than 100 nm in size, particles of even smaller size (less than 10 nm) are also observed, but it is not entirely clear whether 100 nm particles consist of 10 nm objects, or just 10 nm particles cover 100 nanometer particles.

X-ray phase analysis of copper nanopowders obtained by a) chemical-metallurgical method (sample 2 mm thick, passivation for 30 min); b) from copper citrate (circles - Cu, rhombuses - Cu_2O , squares - CuO) is shown in Fig. 4. As can be seen from the Figure, even passivated copper nanopowder obtained by chemical metallurgy contains noticeable amounts of Cu_2O and CuO . In this case, the nanopowder obtained from copper citrate contains only traces of CuO , i.e. the production of copper nanopowder by the thermal decomposition of salts is more promising since the signal of copper oxides is practically practically missing.

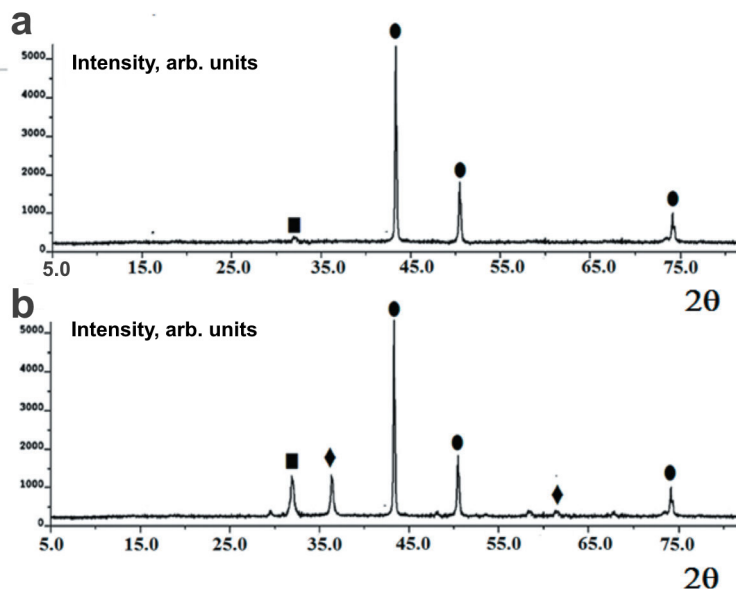


Figure 4. Data of X-ray phase analysis of copper nanopowders obtained a) - from copper citrate, b) - by the method of chemical metallurgy (2 mm thick sample, passivation for 30 min). Circles - Cu, rhombuses - Cu_2O , squares - CuO

We briefly list the results of this section. Copper nanopowders are obtained by the method of hydrogen reduction (chemical-metallurgical method) and thermal decomposition of copper citrate and formate. It was shown that copper nanopowder synthesized from copper citrate is not pyrophoric. Combustion of this copper nanopowder can be initiated by an external source, with the combustion wave velocity being 1.3 ± 0.3 mm/s. The nanopowder has a ~ 4 times larger specific surface (45 ± 5 m^2/g) than the nanopowder obtained by the chemical-metallurgical method, practically does not contain oxides and is stable in atmospheric air.

Copper nanopowder obtained by the chemical-metallurgical method is pyrophoric and therefore requires passivation, but its passivation leads to the formation of noticeable amounts of copper oxides. The combustion velocities of passivated and non-passivated copper nanopowder obtained by the chemical-metallurgical method are the same and amount to 0.3 ± 0.04 mm/s. The dynamics of temperature fields during the ignition and combustion of copper nanopowders obtained by various methods has been studied.

§ 2. Combustion of tungsten nanopowders

Tungsten-based nanomaterials have advantages as electron emitters. Elements of photocopiers, laser printers and air cleaners, chargers, nanodevices with chemical sensors, biomedical sensors, antistatic coatings can be made from nanoscale powders including tungsten.

Tungsten-based nanomaterials are used in cathode-ray tubes, displays, X-ray anodes, klystrons, magnetrons for microwave ovens [22]. This section presents the results of studying the temperature regimes of synthesis of tungsten nanopowder with different crystal structures, determining the optimal passivation regimes and studying the regularities of the ignition and combustion of nanopowder obtained under various conditions [23].

The stable crystal structure of tungsten (α -W) is face-centered cubic. There is a metastable form of tungsten (β -W), which has a cubic crystal structure A-15, containing eight atoms per unit cell [24]. Tungsten (β -W) has a giant spin Hall effect, which makes this material very promising in spin electronics. This is a branch of quantum electronics dealing with the study of spin current transfer (spin-polarized transport) in solids, where, along with the charge, the electron spin is an active element for storing and transmitting information, forming integral and functional microcircuits, designing new magneto-optoelectronic devices [25 - 27]. The spin Hall effect is considered as a promising mechanism for generating spin-polarized current, which does not require the use of a magnetic field or ferromagnetic materials [28]. β -W with its giant spin Hall effect, is among the materials with the highest efficiency in converting electric current into spin current, which is accepted as a prototype in the design of spin electronics devices [29, 30].

Although β -W was discovered more than 60 years ago [31], there was no understanding of the mechanism of β -W formation. It has been shown that β -W formation is sensitive to synthesis parameters such as inert gas pressure and the presence of oxygen impurities. However, there are no empirical models that could describe the relationship between the β -W formation mechanism and deposition parameters. In particular, the role of oxygen impurity is still being discussed [29, 30], since it is assumed that β -W is a nonstoichiometric oxide with the formula W_3O , while it is known that oxygen in β -W films has zero valence, i.e. β -W is an allotrope of α -W [32].

The purpose of this section is to establish the modes of combustion and passivation of tungsten nanopowders, as well as the modes of synthesis of nanopowders by the method of chemical metallurgy [33] in order to determine the temperature ranges of formation of α -W and β -W. Partial characterization of the synthesized nanopowders W was carried out. In the experiments, we used WO_3 samples with different specific surface: 2 m^2/g (WO_3 (1, ISMAN)), 11 m^2/g (WO_3 (2)), Novosibirsk, <http://rare.metal.ru>), 0.8 m^2/g (WO_3 (3)), UK Cat No.B1188).

A quartz boat with tungsten trioxide powder WO_3 1-3 mm thick was installed inside a cylindrical quartz reactor and placed in a furnace heated to $450 \div 650$ °C for 2-5 h while blowing hydrogen through the reactor (Fig. 5).

The quartz boat was equipped with a chromel - alumel thermocouple (diameter 0.3 mm), placed in a powder. The thermocouple was not touching the walls of the boat. In a number of experiments, after synthesis and cooling to room temperature, the reactor was placed in an external bath of a HAAKE-Q cryostat (Germany), cooled to 0 – -35 °C in an argon flow using ethyl alcohol as a refrigerant [34]. After reaching the required temperature, the argon flow was replaced with a dry air flow to passivate the nanopowder. For drying, air was passed through a column with solid alkali (KOH) 0.6 m long and turns of a flexible hose placed in the inner bath of the cryostat. The heating of the powder after replacing the gas streams indicated the beginning of the process of interaction with air.

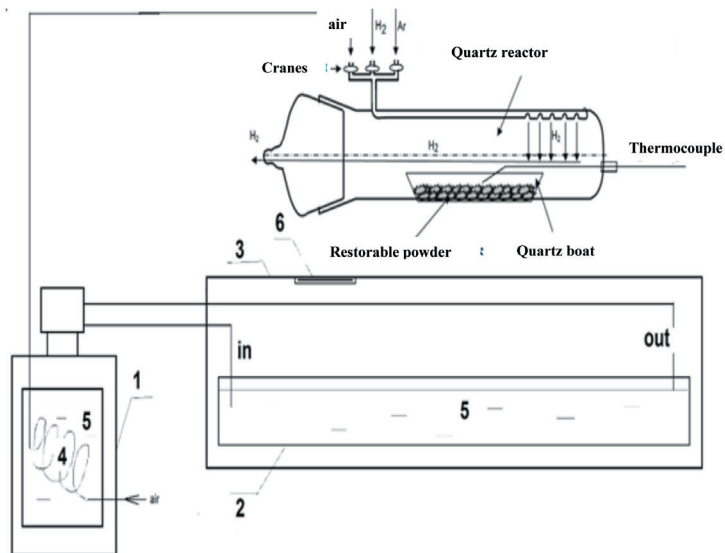


Figure 5. Diagram of the experimental setup,

- 1 - HAAKE-Q cryostat, 2 - external cooling bath, 3 - thermal insulation, 4 - loop of a flexible hose for air drying, 5 - ethyl alcohol, 6 - hole for filming.

If ignition occurred, the sample surface changed color from black to yellow-green (WO_3 is yellow-green). If there was no ignition within 30 minutes, the air flow was replaced with an argon flow and the reactor was heated to room temperature. Then the quartz boat with the passivated powder was removed from the reactor and immediately placed on a nickel foil to avoid ignition. Then, a nickel foil with nanopowder was placed on a stage for video recording. The process of removing the boat and placing the nanopowder on the table took about 5 s.

In another series of experiments, the W nanopowder was passivated at 20 °C for 1 hour in an argon flow containing 3% air.

To establish the combustion modes of W nanopowders, a Nikon 1 color video camera (30 frames per second) and a Flir 60 infrared camera (30 frames per second, 320x240 pix, sensitivity interval 8 - 14 μm) were used. The phase composition of the obtained samples was studied using a DRON 3M X-ray diffractometer (Russia) with a coordinate-sensitive detector. The specific surface area was measured using a Sorbi-M analyzer by the BET method.

Nanopowders obtained by chemical metallurgy at 480 °C from all three starting WO_3 powders used are pyrophoric. Typical sequences of video frames of self-ignition and combustion in air of a synthesized nanopowder from (WO_3 (1), 2-mm layer thickness) are shown in Fig. 6a. A sequence of IR video frames of a nanopowder burning in air (initial WO_3 powder (1), 2 mm thick) obtained under the same conditions is showed in Fig. 6b. As seen from Fig. 6, the combustion front appears at the edge of the samples and spreads to the center of the backfill. The maximum combustion temperature exceeds 670 °C. The powders obtained from samples WO_3 (2) and WO_3 (3) burn in the same way.

Nanopowders α -W obtained at 640 °C from all used initial WO_3 powders are not pyrophoric, because at temperature of 20 °C in air, they do not ignite spontaneously. Self-heating of the samples taken from the reactor immediately after synthesis does not lead to the propagation of the flame front. However, after the completion of the stage of self-heating and cooling of the samples to room temperature, the combustion of each sample of W nanopowder can be initiated with a heated wire. Upon initiation by heated wire, the combustion mode of the α -W nanopowder, as can be seen from Fig. 7a, is finger-like. A sequence of frames of infrared video recording of self-heating in air for samples of α -W nanopowder (initial temperature 20 °C) of various thickness (1, 2.3 mm, from left to right) obtained by the method of chemical metallurgy at 640 °C is shown in Fig. 7b (2 left frames).

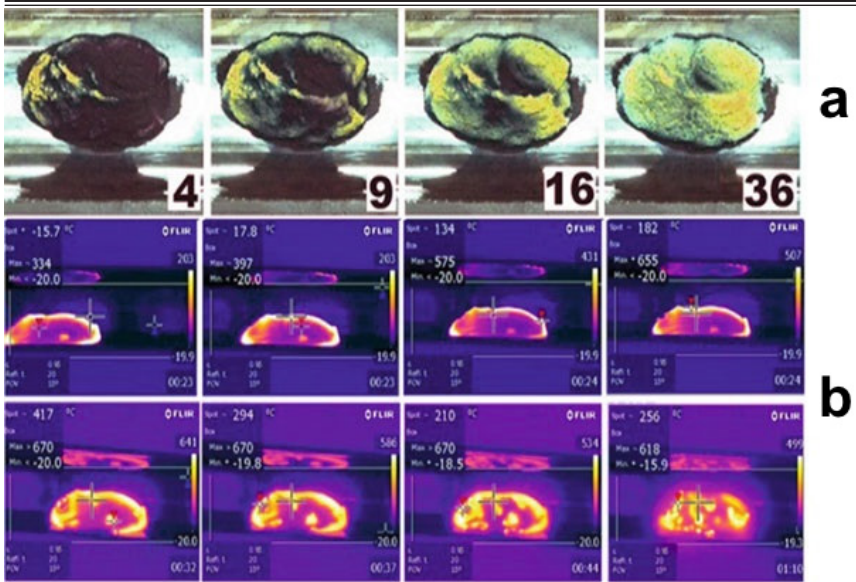


Figure 6.

a) - Combustion in air of nanopowder obtained by chemical metallurgy at 480 °C (sample 1, 2 mm thick); 20 °C, 30 frames per second. On each frame bottom right is the time in seconds after the video mode was turned on..

b) - A sequence of frames of infrared video recording of a nanopowder burning in air (sample 1, 2 mm thick) obtained by the method of chemical metallurgy at 480 °C, initial temperature 20 °C, 30 frames per second. On each frame bottom right is the time (minutes-seconds) after the video mode was turned on.

Self-heating of the samples removed from the reactor immediately after synthesis (Fig. 7b, 2 left frames) does not lead to the propagation of the flame front. However, after the completion of the stage of self-heating and cooling of the samples to room temperature, combustion of any sample of nanopowder W can be initiated with a heated wire (two right frames in Fig. 7b). As seen from Fig. 7b, the initiated sample burns nonuniformly, the maximum temperature of the sample at the “tip” of the “finger” exceeds 670 °C.

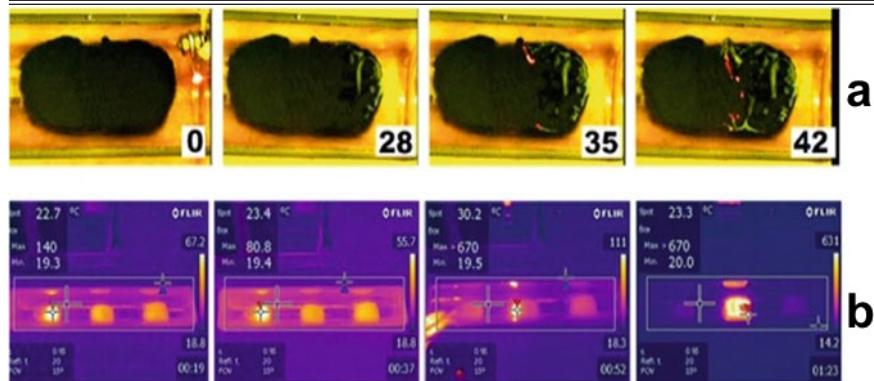


Figure 7.

a) - Initiated combustion in air of W nanopowder (initial powder of grade (1)) obtained by chemical metallurgy at 640 °C (sample 2 mm thick). Initial temperature 20 °C. On each frame bottom right, the time in seconds after initiation is shown.

b) - A sequence of frames of infrared video recording of self-heating in air for samples of α -W (initial temperature 20 °C) of various thickness (1.2.3 mm, from left to right) obtained by the method of chemical metallurgy at 640 °C (two left frames). The two right frames show the initiated combustion of the central sample, 2 mm thick. On each frame bottom right the time (minutes - seconds) after turning on the video recording mode is shown.

The time dependences of heating W nanopowder obtained at 480 °C from grade 1 tungsten oxide on time during passivation in a dry air flow at initial temperatures of -34 °C (squares), -30 °C (bold circles), and -24 °C (circles) are shown in Fig. 8. Zero time corresponds to the moment of replacing the argon flow with a passivating dry air flow. As can be seen from the figure, the maximum heating at the initial passivation temperature - 24 °C is 170 °C. In this case the color of the sample changes to yellow. Heating at -30 °C is ~ 20 °C, heating at -35 °C is ~ 0 °C. In both cases, the samples do not change color.

The relatively small values of heating at $T_0 = - 30$ °C are probably associated with the release of heat during the passivation of tungsten nanoparticles. However, unlike iron and nickel nanopowders, this method of processing of the obtained nanopowders did not provide passivation of the W nanopowder, since the sample ignites spontaneously on contact with air. The ignition of the nanopowder was avoided if it was placed on a nickel foil immediately after being removed from the reactor. Thus, passivation at temperatures below zero proved to be ineffective without additional heat removal into the metal foil. Therefore, in the main series of experiments, passivation was carried out at room temperature for 1 hour

in an argon flow containing 3% air. This procedure excluded self-ignition of the nanopowder upon contact with air.

For all three precursors used, the specific surface areas of nanopowders, determined by the BET method, both for those obtained at 480 °C (passivated) and at 640 °C (not passivated), were 15 ± 3 m²/g and 9 ± 3 m²/g, respectively. For all three precursors used, X-ray phase analysis of W nanopowders obtained at 640 °C showed that they contain only α -W (Fig. 9a). Passivated nanopowders obtained at 500 °C from tungsten oxide grades 1 and 2 contain α -W, β -W and WO_{2,9} (Fig. 9b).

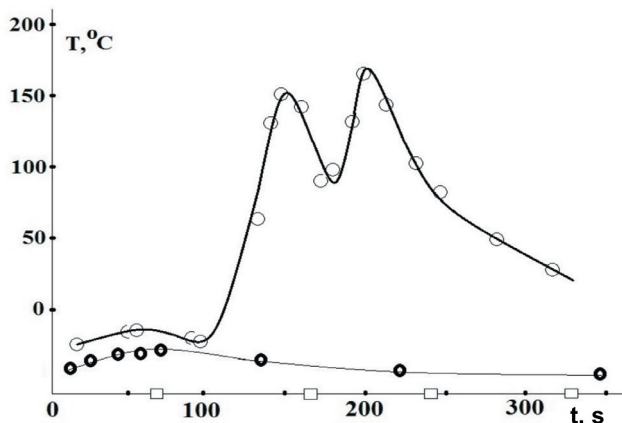


Figure 8. Time dependence of sample heating during passivation at - 34 °C (squares), - 30 °C (bold circles) - 24 °C (circles). Zero time corresponds to the moment of replacing the argon flow with a dry air flow

A sample of W nanopowder obtained from grade 3 tungsten oxide at 480 °C contains only β -W and traces of WO_{2,9} and WO₃ (Fig. 9d), the presence of which is obviously associated with the passivation procedure. It should be noted that the temperature range of β -W synthesis obtained in this work is very narrow: 470 ÷ 490 °C, while in [24] the optimal temperature was 500 °C. For comparison, the XRD analysis of a nanopowder obtained from grade 2 tungsten oxide at 480 °C is shown in Fig. 9c. It can be seen that this nanopowder is a mixture of α -W, β -W, WO₃ and WO_{2,9}. Above 640 °C, only α -W is obtained.

Here are the main results of this section. Tungsten nanopowders are synthesized by reduction of tungsten trioxide with hydrogen (chemical metallurgy method) at 440 ÷ 640 °C from samples with different specific surface: 2 m²/g (1), 11 m²/g (2), 0.8 m²/g (3). It is shown that the W nanopowder synthesized at 640 °C for all three precursors used is non-pyrophoric.

Its combustion can be initiated by an external source. Combustion develops in a spatially non-uniform regime. Nanopowder synthesized at 480 °C from tungsten

oxide grades 1 and 2 is a mixture of α -W, β -W and $WO_{2.9}$; this powder is pyrophoric. It was found that the passivated W nanopowder synthesized at 480 °C from grade 3 tungsten oxide is β -W with traces of WO_3 and $WO_{2.9}$. Temperature range of synthesis β -W, obtained in the work is very narrow: 470–490 °C.

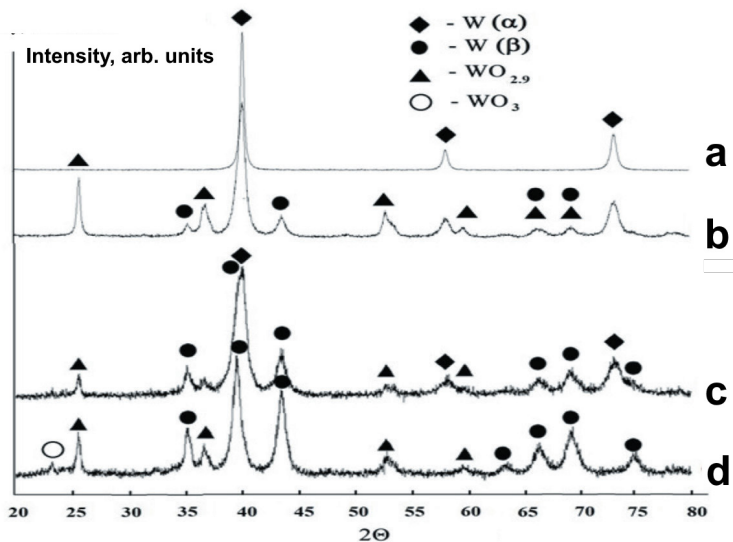


Figure 9.

a) - X-ray phase analysis of W nanopowder obtained at 640 °C and passivated in an argon flow containing 3% air at a temperature of 20 °C (starting powder of grade (1)).

b) - X-ray phase analysis of nanopowder obtained at 500 °C and passivated in an argon flow containing 3% air at a temperature of 20 °C (original powder of grade (2)).

c) - X-ray phase analysis of a nanopowder obtained at 480 °C and passivated in an argon flow containing 3% air at a temperature of 20 °C (original powder of grade (2)).

d) - X-ray phase analysis of W nanopowder obtained at 480 °C and passivated in an argon flow containing 3% air at a temperature of 20 °C (original powder of grade (3)).

The specific surface area of α -W nanopowders is 10 ± 2 m²/g; for the β -W mixture with traces of WO_3 and $WO_{2.9}$ it is 18 ± 1 m²/g. The dynamics of temperature fields during the ignition and combustion of tungsten nanopowders obtained at different temperatures has been studied.

§ 3. *Combustion of compacted samples of iron nanopowders*

Literature data on the preparation and properties of compact samples from nanopowders are rather limited. In [35], the features of flame propagation over tablets made of mixtures of Al/CuO nanopowders (so-called nanothermites) were studied as a function of the density during laser initiation of combustion. It was found that less dense samples (porosity 90%) ignite faster and the velocity of flame propagation in them is an order of magnitude higher than in denser samples (porosity 50%). According to the authors, these results indicate a change in the combustion mechanism with an increase in the density of the compacted sample from convective to diffusion one. Similar measurements described in monograph [36] were carried out with samples of Al/MoO₃ nanopowders, and the results obtained for this nanothermite are qualitatively the same. It should be noted that there are no data in the literature on the regularities of spontaneous ignition and self-heating of compacted samples.

This section describes the experimental establishment of the combustion features of compact samples of non-passivated iron nanopowders and the effect of the porosity of these compact samples on the dynamics of their heating in air.

Experimental

In this work, for experimental studies of the processes of ignition and passivation, iron nanopowders obtained by the chemical-metallurgical method were used. The main stages in the synthesis of metal nanopowder are the deposition of metal hydroxide, drying, and reduction [37]. The synthesis of iron hydroxide was carried out by heterophase interaction of a solid metal salt with an alkali solution. After precipitation of iron hydroxide, it was first washed in a Buchner funnel to pH = 7 and then dried in air until dusting. To obtain a metal nanopowder, iron hydroxide powder was reduced in a furnace for 1 h at 400 °C in a hydrogen flow in a reactor (the reactor is schematically shown in Fig. 5). Then the reactor was removed from the furnace and cooled in air to 20 °C in an argon flow. Then a quartz boat 19 cm long and 3 cm wide with nanopowder was transferred from the reactor to a portable quartz vessel filled with argon at atmospheric pressure. In a separate series of experiments, a quartz boat with nanopowder was removed from the reactor and placed on a stage for filming using a Flir 60 infrared camera (60 frames/s, 320x240 pix, sensitivity interval 8–14 μm).

The compaction of nanopowders was carried out in an original installation equipped with a heated mould (Fig. 10). The installation includes a sealed box with scales, a press, a gateway, and electrical inputs for connecting heating, initiation and measurement devices, as well as a heated mould, into which the required amount of non-passivated iron nanopowder was placed. The installation makes

it possible to obtain compact products even from pyrophoric (non-passivated) nanopowders, because all operations with nanopowders, from opening vessels with nanopowders, weighing and pressing them to heating the samples, are carried out in a sealed box filled with an inert gas (argon) and equipped with a gateway for changing powders and samples. Cylindrical compact samples with a diameter of 5 mm, a length of 7.7–11.8 mm, and a density of 2.55–3.84 g/cm³ were obtained from iron nanopowder [37] and also studied.

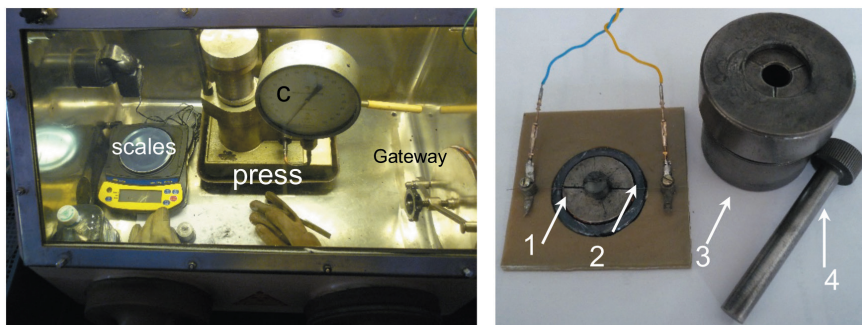


Figure 10. General view of the installation (a sealed box with scales, a press, a sluice and electrical inputs for connecting heating, initiation, measuring devices) and a mould

The peculiarity of the mould is the possibility of programmed heating of samples pressed from metal powders in an inert gas atmosphere. To control the heating temperature in the lower punch of the mold (1) there is a slot for installing a U-shaped thermocouple 50-100 μm thick (2), isolated from the punch (1), the mould (3) and the upper punch (4). To reduce heat loss, the powder being pressed is separated from the punches by heat-insulating gaskets. The signal from the thermocouple is recorded to a computer through an analog-to-digital converter with a frequency of 1 kHz. A Flir 60 infrared camera and a SONY - FDR - AX - 33 video camera were used to study the change in the temperature distribution over the sample surface over time and to determine the maximum temperature at each time point. The temperature of the upper end of the sample was recorded with an infrared camera.

Results and discussion

The typical results of optical filming of the combustion of cylindrical samples made of iron nanopowder a) 7.7 mm high and 3.84 g/cm³ and b) 9.5 mm high and 3.22 g/cm³ are shown in Fig. 11. It should be noted that self-ignition of the sample (there is no external initiation) begins from the top end, which is least screened from the oxidizer, and, as will be shown below, the self-ignition occurs almost

immediately on the entire end surface. As is seen in Fig. 11, a combustion wave propagates downward from the upper end of the sample at an approximately constant velocity.

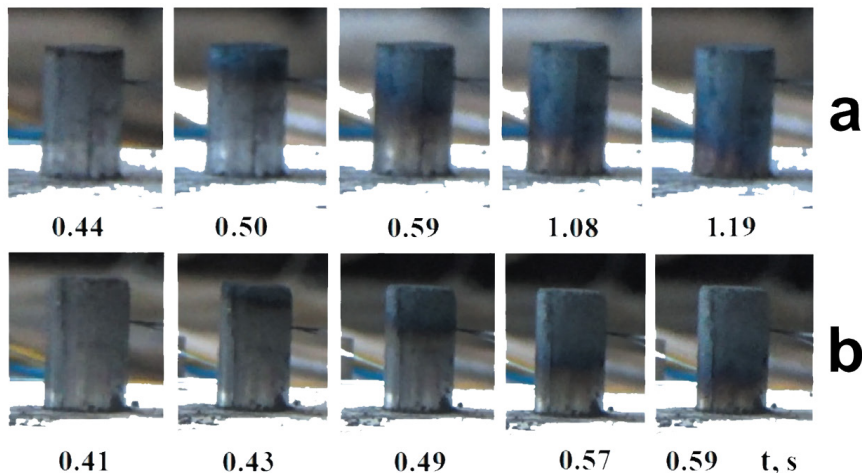


Figure 11. Results of optical filming of the combustion of cylindrical samples made of iron nanopowder

- a) - in height of 7.7 mm and density of 3.84 g/cm^3
- b) - in height of 9.5 mm and density of 3.22 g/cm^3 .

Estimations of the combustion velocity V , determined from three points on the combustion front, which is visualized very clearly in the form of a horizontal dark stripe, give for the sample a) $V \approx 0,019 \text{ cm/s}$, and for the sample b) $V \approx 0,047 \text{ cm/s}$. This means that the velocity of flame propagation in a less dense sample a) is noticeably higher than in a denser sample b), that is, the process of transfer of the oxidant into the sample plays an important role in the combustion of compacted samples of iron nanopowders. This result is similar to the results obtained in [35, 36] for the initiated combustion of nanothermites.

Let us consider the change in the combustion temperatures of the samples of different density during the self-ignition. Typical frames of self-ignition and combustion of samples of iron nanopowder 1 mm thick (on the left in each frame) and 4 mm (on the right in each frame) immediately after extraction from the reactor into atmospheric air are shown in Fig. 12. It can be seen that a thinner sample heats up more leanly due to a more intense heat dissipation. A red triangle indicating the maximum temperature is located on a sample 4 mm thick in all frames.

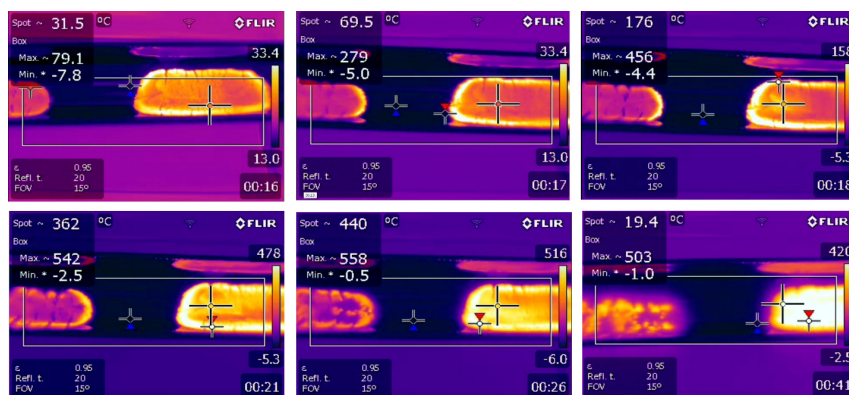


Figure 12. Typical frames of the self-ignition and combustion of samples of iron nanopowder 1 mm thick (on the left in each frame) and 4 mm (on the right in each frame) immediately after being removed from the reactor

It can be seen from Fig. 12 that the maximum combustion temperature of the bulk iron nanopowder sample is 560 °C (5th frame at 26 s). With an increase in the density of compacted samples, the maximum combustion temperature decreases. For example, typical frames of the combustion of a compacted sample of iron nanopowder with a density of 2.91 g/cm³ are shown in Fig. 13.

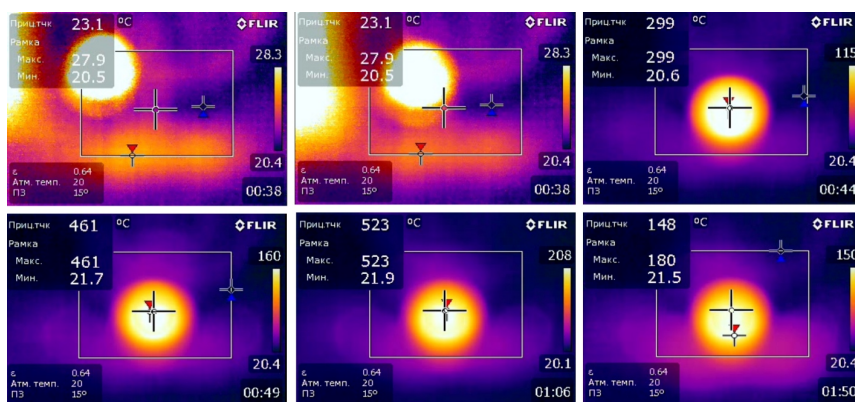


Figure 13. Typical frames of combustion of a compacted sample of iron nanopowder with a density of 2.91 g/cm³. The first two frames (top left) show the transfer of the sample from the compaction unit to the stage for filming

It can be seen (5th frame at 1 min 6 s) that the maximum combustion temperature of the compacted sample is less than the maximum temperature reached

during the combustion of the sample (see Fig. 12). With an increase in the compact density, the maximum combustion temperature decreases. This is illustrated in Fig. 14, which shows the dependences of the maximum combustion temperature on time for compacted samples of different densities.

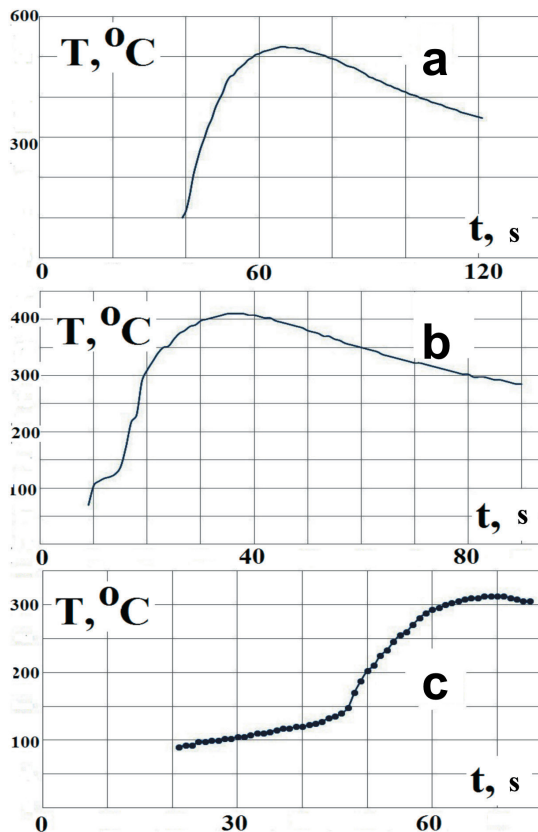


Figure 14. Dependences of the maximum combustion temperature on time for compacted samples of different densities:

a) - 2.91 g/cm^3 , b) - 3.37 g/cm^3 , c) - 3.84 g/cm^3

The results obtained mean that the propagation velocity of the combustion front and the maximum combustion temperature of compacted samples made of non-passivated iron nanopowders decrease with increasing compact density. Recently similar regularities were observed for the initiated combustion of nanothermites ($\text{Al} + \text{CuO}$, $\text{Al} + \text{MoO}_3$) [35, 36], it can be assumed that these regularities are general for combustible or pyrophoric nanosystems.

Conclusions for Chapter 8

Copper nanopowders are obtained by the method of hydrogen reduction (chemical-metallurgical method) and thermal decomposition of copper citrate and formate. It was shown that copper nanopowder synthesized from copper citrate is not pyrophoric. Combustion of this copper nanopowder can be initiated by an external source, with the combustion wave velocity being 1.3 ± 0.3 mm/s. The nanopowder has a ~ 4 times larger specific surface area than the nanopowder obtained by the chemical-metallurgical method. It practically does not contain oxides and is stable in atmospheric air. Copper nanopowder obtained by the chemical-metallurgical method is pyrophoric and therefore requires passivation, but its passivation leads to the formation of noticeable amounts of copper oxides. The burning velocities of passivated and non-passivated copper nanopowder obtained by the chemical-metallurgical method are the same.

Tungsten nanopowders are synthesized by reduction of tungsten trioxide with hydrogen (chemical metallurgy method) at $440 \div 640$ °C from samples with different specific surface. It is shown that the W nanopowder synthesized at 640 °C for all three precursors used is non-pyrophoric α -W. Its combustion can be initiated by an external source. Combustion continues in a spatially non-uniform regime. Nanopowder synthesized at 480 °C from tungsten oxide of grades 1 and 2 is a mixture of α -W, β -W and $WO_{2.9}$. This powder is pyrophoric. It was found that the passivated W nanopowder synthesized at 480 °C of grade 3 tungsten oxide is β -W with traces of WO_3 and $WO_{2.9}$. Temperature range of synthesis β -W, obtained in the work is very narrow: $470 \div 490$ °C. The specific surface area of α -W nanopowders is 10 ± 2 m²/g; for the β -W mixture with traces of WO_3 and $WO_{2.9}$, it is 18 ± 1 m²/g. The dynamics of temperature fields during the ignition and combustion of tungsten nanopowders obtained at different temperatures has been studied. Preliminary experimental studies of the combustion features of compact samples made of non-passivated iron nanopowders and the effect of the porosity of these compact samples on the dynamics of their heating in air have been carried out. The aim is to determine the temperature range, at which it is possible to carry out safely technological operations with compact samples of non-passivated iron nanopowders safely. It was found that the propagation velocity of the combustion front and the maximum combustion temperature of compacted samples made of non-passivated iron nanopowders decrease with increasing compact density.

References for Chapter 8

1. Rubtsov N. M., Seplyarsky B. S., Alymov M. I. *Kriticheskiye yavleniya i razmernyye efekty v avtovolnovykh protsessakh s ekzotermicheskimi reaktsiyami (Critical Phenomena and Dimensional Effects in Autowave Processes with Exothermic Reactions)*. Saratov: Publishing House "KUBiK". 2019. 338 p. ISBN 978-5-91818-595-7
2. Seplyarsky B.S., Ivleva T. P., Alymov M. I. *Makrokineticheskiy analiz protsessy passivatsii pirofornykh poroshkov (Macrokinetic analysis of the process of passivation of pyrophoric powders)*. *Doklady Academy of Sciences. Physical chemistry*. 2018. Vol. 478. No. 3. pp. 310-314. (in Russian)
3. Alymov M. I., Rubtsov N. M., Seplyarskii B. S., Zelensky V. A., Ankudinov A. B. et al. *Synthesis of Ni nanoparticles with controlled pyrophoricity and mean size*. *Doklady Chemistry*. 2019. Vol. 484. No. 1. pp. 19-23. DOI: 10.31857/S0869-5652484148-51
5. Kamyshny A., Steinke J., Magdassi S. *Metal-based inkjet inks for printed electronics*. *The Open Applied Physics Journal*. 2011. Vol. 411. No.19. pp. 19-36. DOI: 10.2174/1874183501104010019
6. Gréget R., Nealon G. L., Vileno B. et al. *Magnetic properties of gold nanoparticles: A room-temperature quantum effect*. *ChemPhysChem*. 2012. Vol. 13. No. 13. pp. 3092-3097. <https://doi.org/10.1002/cphc.201200394>
7. Letfullin R. R., Iversen C. B., George T. F. *Modeling nanophotothermal therapy: kinetics of thermal ablation of healthy and cancerous cell organelles and gold nanoparticles*, *Nanomedicine: Nanotech. Bio. and Med*. 2011. Vol. 7. pp. 137-145.
8. Wei Y., Chen S.; Kowalczyk B. Huda S. Gray T. P. Grzybowski B. A. *Synthesis of stable, low-dispersity copper nanoparticles and nanorods and their antifungal and catalytic properties*, *J. Phys. Chem. C*. 2010. Vol. 114. No. 37. pp. 15612-15616. <https://doi.org/10.1021/jp1055683>
9. Ramyadevi J., Jeyasubramanian K., Marikani A., Rajakumar G., Rahuman A. A. *Synthesis and antimicrobial activity of copper nanoparticles*. *Mater. Lett*. 2012. Vol. 71. pp. 114-116.
10. Dhas N. A., Ra C. P., Gedanken A. *Synthesis, Characterization, and Properties of Metallic Copper Nanoparticles*. *Chem. Mater*. 1998. Vol. 10. No. 5. pp. 1446-1452. <https://doi.org/10.1021/cm9708269>
11. Hashemipour H., Zadeh M. E., Pourakbari R., Rahimi P. *Investigation on synthesis and size control of copper nanoparticle via electrochemical and chemical reduction method*. *Inter. J. of Physical Sciences*. 2011. Vol. 6. No. 18. pp. 4331-4336.
12. Salavati-Niasari M., Davar F. *Synthesis of copper and copper (I) oxide nanoparticles by thermal decomposition of a new precursor*. *Materials Letters*. 2009. Vol. 63. No. 3-4. pp. 441-443. DOI: 10.1016/j.matlet.2008.11.023

13. Park B. K., Kim D., Jeong S., Moon J., Kim J. S. Direct writing of copper conductive patterns by ink-jet printing. *Thin Solid Films*. 2007. Vol. 515. No. 19. pp. 7706-7711.

14. Egorova E., Revina A., Synthesis of metallic nanoparticles in reverse micelles in the presence of quercetin, *Colloids and Surfaces A: Physicochem. and Eng. Aspects*. 2000. Vol. 168. No. 1. pp. 87-96. DOI: 10.1016/S0927-7757(99)00513-0

15. Noemi Jardón-Maximino, Perez Alvarez M., Rubén Sierra-Ávila et al. Oxidation of Copper Nanoparticles Protected with Different Coatings and Stored under Ambient Conditions. *Journal of Nanomaterials* 2018:1-8. DOI: 10.1155/2018/9512768

16. Solanki J. N., Sengupta R., Murthy Z. Synthesis of Copper Nanoparticles, *Solid State Sciences*. 2010. Vol. 12. No. 9. pp. 1560-1566. DOI: 10.1016/j.solidstatesciences.2010.06.021

17. Francis L., Nair A. S., Jose R., Ramakrishna S., Thavasi V., Marsano E. Fabrication and characterization of dye-sensitized solar cells from rutile nanofibers and nanorods. *Energy*. 2011. Vol. 36. No. 1. pp. 627-632.

18. Stankova M, Vilanova X, Calderer J, Llobet E, Brezmes J, Gràcia I, Cané C, Correig X. Sensitivity and selectivity improvement of rf sputtered WO₃ microhotplate gas sensors. *Sensors Actuators B Chemical*. 2006. Vol. 113. No. 1. pp. 241–248. DOI: 10.1016/j.snb.2005.02.056

19. Alymov M. I., Rubtsov N. M., Septyarskii B. S., Zelensky V. A., Ankudinov A. B. Temporal characteristics of ignition and combustion of iron nanopowders in the air. *Mendeleev Communications*. 2016. Vol. 26. No. 5. pp. 452-454. DOI: 10.1016/j.mencom.2016.09.030

20. Gorrie T. M., Kopf P. W., Toby S. Kinetics of the reaction of some pyrophoric metals with oxygen. *J. Phys. Chem*. 1967. Vol. 71. No. 12. p. 3842-3845. <https://doi.org/10.1021/j100871a019>

21. Sharma B. K. *Objective Question Bank in Chemistry*. Krishns Prakashan Media Ltd., India. 2009. 488 p.

22. <https://www.nanoshel.com/topics/nanoshel-llc-news/>

23. Gnedovets A. G., Ankudinov A. B., Zelenskii V. A. et al. Synthesis of micron particles with Fe–Fe₄N core–shell structure at low-temperature gaseous nitriding of iron powder in a stream of ammonia. *Inorganic Materials: Applied Research*. 2016. Vol. 7. No. 2. pp. 303-309. DOI: 10.1134/S2075113316020106

24. Morcom W. R., Worrell W. L., Sell H. G., Kaplan H. I. The preparation and characterization of beta-tungsten, a metastable tungsten phase. *Metallurgical Transactions*. 1974. Vol. 5. No.1. pp. 155-161.

25. Žutić I., Fabian J., Das Sarma S. Spintronics: Fundamentals and Applications. *Rev. Mod. Phys*. 2004. Vol. 76. pp .323-410. DOI: <https://doi.org/10.1103/RevModPhys.76.323>

26. Wolf S. A., Awschalom D. D., Buhrman R. A, et al. *Spintronics: A Spin-Based Electronics Vision for the Future*. Science. Vol. 294. No. 5546. pp. 1488-1495. doi: 10.1126/science.1065389
27. Johnson M., Silsbee H. *Interfacial Charge-Spin Coupling: Injection and Detection of Spin Magnetization in Metals*. Phys. Rev. Lett. 1985. Vol. 55. pp. 1790-1793.
28. Jungwirth T., Wunderlich J., Olejnik K. *Spin Hall Effect Devices*, Nat. Mater. Vol. 11. No. 5. pp. 382-390. doi: 10.1038/nmat3279
29. Pai C. F., Liu L., Li Y. et al. *Spin Transfer Torque Devices Utilizing the Giant Spin Hall Effect of Tungsten*. Appl. Phys. Lett. 2012. 101, 122404. <https://doi.org/10.1063/1.4753947>
30. Hao Q., Chen W., Xiao G. *Beta (β) Tungsten Thin Films: Structure, Electron Transport, and Giant Spin Hall Effect*. Appl. Phys. Lett. 2015. Vol. 106. No. 18. 182403. DOI: 10.1063/1.4919867
31. Hägg G., Schönberg N. *' β -Tungsten' as a Tungsten Oxide*. Acta Crystallogr. 1954. Vol. 7. No. 4. pp. 351-354.
32. Petroff P., Sheng T. T., Sinha A. K., Rozgonyi G. A., Alexander F. B. *Microstructure, Growth, Resistivity, and Stresses in Thin Tungsten Films Deposited by RF Sputtering*. J. Appl. Phys. 1973. Vol. 44. pp. 2545. <https://doi.org/10.1063/1.1662611>
33. Lassner E., Schubert W.-D. *Tungsten Properties, Chemistry, Technology of the Element, Alloys, and Chemical Compounds*. 1998. Kluwer Academic / Plenum Publishers New York, Boston, Dordrecht, London, Moscow. 447 p.
34. Alymov M. I., Rubtsov N. M., Seplyarskii B. S., Zelensky V. A., Ankudinov A. B. *Passivation of iron nanoparticles at subzero temperatures*. Mendeleev Communications. 2017. Vol. 27. No. 5. pp. 482-484. DOI: 10.1016/j.mencom.2017.09.017
35. Saceleanu F., Idir M., Chaumeix N., Wen J. Z. *Combustion Characteristics of Physically Mixed 40 nm Aluminum/Copper Oxide Nanothermites Using Laser Ignition*. Frontiers in Chemistry. 2018. Vol. 6. doi: 10.3389/fchem.2018.00465
36. *Metal Nanopowders: Production, Characterization, and Energetic Applications* (ed. by Gromov A. A., Teipel U.). John Wiley & Sons. 2014. 417 p. DOI: 10.22226/2410-3535-2021-1-39-44
37. Rubtsov N. M., Seplyarskii B. S., Michail I. Alymov M. I. *Initiation and Flame Propagation in Combustion of Gases and Pyrophoric Metal Nanostructures*. 2021. Springer Nature Switzerland AG, Cham, Switzerland. <https://doi.org/10.1007/978-3-030-57891-6>

CONCLUSIONS

The method of multispectral analysis of remote sensing data is considered and the assessment of the capabilities of multisensor imagery performed in a wide range of wavelengths from ultraviolet to infrared is carried out. Various combinations of data made it possible to georeference images, to reveal the detailed structure of the analyzed scene, to study the spectral composition of the radiation of objects and to distinguish point sources by it, which is especially important, for example, for detecting fire centers and determining their coordinates. One of the very promising optoelectronic devices is a hyperspectrometer. The relevance of the work carried out in Russia on the creation of new types of hyperspectral modules is determined by their ability to extract the maximum information from optical radiation ascending from remotely sounded objects, as well as by the lagging of domestic developments outlined in the 90s of the last century from developments carried out abroad. The hyperspectral modules developed at "RDC "Reagent", JSC are not inferior in their technical characteristics and even surpass modern foreign aviation imaging spectrometers. In particular, this concerns the spatial resolution and the number of spectral channels of the modules. "RDC "Reagent", JSC has mastered the industrial production of hyperspectral modules in the UV, visible and near-infrared range. Full-scale tests of the developed and manufactured devices confirmed the correctness of the design solutions incorporated in them and the ability to confidently determine the type and state of probed natural and anthropogenic objects based on hyperspectral sensing data in the interests of solving many scientific, industrial and other problems. In particular, it is shown that the joint analysis of data from different sensors allows a significant synergistic effect to be achieved. This book examines some hyperspectrometers developed at "RDC "Reagent", JSC, as well as a very interesting development - the UV sensor. Most of the book is devoted to describing the results of remote sensing of combustion and explosion processes in laboratory conditions.

It has been experimentally established that spherical flames of lean (6-15% H₂) hydrogen-air mixtures have a cellular structure. In mixtures containing 6-10% H₂, the flames at the initial stage near the lower concentration limit propagate spherically symmetrically. Then the gravity field distorts the shape of the combustion front. Flames of mixtures containing 10-15% H₂ propagate spherically symmetrically. It is shown that the Boussinesq approximation is applicable to obtain cells with H₂ < 10%, taking into account the force of gravity. Calculations by the Boussinesq model in the absence of gravity do not give the formation of cells. The use of the Navier-Stokes equations for a compressible medium makes it possible to describe the spherically symmetric mode of propagation of a cellular flame under microgravity conditions. It is shown that the analysis of experimental data on flame propagation in lean mixtures does not make it possible to take apart the

calculation results using a two-dimensional model with and without convection. It has been shown experimentally that additives of isobutene C_4H_8 in amounts below the lower concentration limit (up to 1.5%) lead to an increase, and additives of CO_2 to 15% to a decrease in the flame propagation velocity in lean hydrogen-air mixtures. The reasons for the acceleration of combustion in the presence of a hydrocarbon additive are considered.

Using the combustion of hydrogen-air mixtures (30% and 15% H_2) as an example, it is shown that the detected light emission inhomogeneities can be associated with the presence of acoustic waves. It was found that the flame propagation velocities in a stoichiometric hydrogen-air mixture with central spark initiation do not depend on the material of the inner surface of the reactor (stainless steel, TiO_2 , Ta, Pt) but depend on the shape of the inner surface of the reactor.

It is shown that spark-initiated flames of lean hydrogen mixtures (8% -15% H_2 in air) pass through aluminum mesh spheres with a cell size of 0.04-0.1 mm², while the flame of a mixture of 15% H_2 in air accelerates after passing through an obstacle. In the presence of an obstacle during the propagation of flame in mixtures of 10% and 15% H_2 , acoustic oscillations of the gas arise in the reactor. The onset of oscillations occurs earlier in time in the presence of a sphere of a smaller diameter. The flame of a mixture of 7.5% H_2 in air does not pass through the mesh spheres. It was found that the flame of a mixture of 8% natural gas with air passes through the mesh spheres. However, after the obstacle, the flame velocity remains the same, while acoustic oscillations are not observed. It is shown that the active centers of combustion of methane and hydrogen, which determine the propagation of the flame, have a different chemical nature.

In a static bypass installation with a tangential inlet of the mixture under study, the effect of thermal ignition of combustible mixtures at reactor temperatures significantly lower than the thermal ignition temperature was experimentally discovered. In this case, the difference between the temperature of the reactor and the temperature of thermal ignition can reach more than 150 K. This effect is caused primarily by the presence of centripetal forces, which inevitably arise during the formation of a vortex gas flow. The result of the action of these forces on the flow is the radial stratification of the gas in terms of density and, therefore, in terms of temperatures. In the central region, the hottest and least mobile gas is formed and, in addition, it is well insulated from the walls of the reactor. The possibility of mixing it with fresh cold masses of gas is excluded. The pressure increase in the reactor caused by the mixture admission leads to adiabatic compression and additional heating of the gas. The centripetal forces contribute to the fact that the heat, which begins to release with the onset of a chemical reaction, accumulates in the central region of the reactor, thus creating favorable conditions for thermal ignition.

By the example of combustion of stoichiometric mixtures of n-pentane (C_5H_{12}) with air, diluted with carbon dioxide (CO_2) and argon (Ar), at a total atmospheric

pressure, it is shown that when the propagation of the FF flame front from spherical to propagation in a tube occurs, phenomena arise, caused by the instability of a flat flame. It is shown that, upon deceleration of the FF near the end wall of the reactor, a smooth FF acquires a cellular structure. It is shown that qualitative modeling of the results obtained is possible when analyzing the Navier-Stokes equations for a compressible medium in the approximation of a small Mach number. In this book, using the methods of 4D optical spectroscopy and color high-speed filming, the features of combustion in flame cells caused by hydrodynamic instability are experimentally established for the first time.

In addition, as a result of direct experimental verification of Landau's hypothesis about the hydrodynamic instability of a flat flame front, the relationship was established between the main factors responsible for the instability of hydrodynamic and acoustic flames. This means that in the cell of the combustion front, caused by an instability of any nature (thermodiffusion, hydrodynamic, thermoacoustic), a complete cycle of transformations is carried out, which is characteristic of a given combustion process. It is shown that any combustion cell is essentially a separate "chemical reactor", in each of which the process of complete chemical transformation is carried out. The results obtained on the spectral study and visualization of the propagation of fronts of unstable flames are important in solving the issues of explosion safety for volumes of complex geometry.

A cellular mode of combustion of a 40% mixture of hydrogen with air in the presence of platinum wire and foil in the range of 270-350 °C at atmospheric pressure was found. Using the methods of routine and 4D optical spectroscopy, which allows registering the intensity of the optical spectrum simultaneously depending on the wavelength, time and coordinate, and color high-speed filming, combustion cells caused by catalytic instability have been experimentally detected for the first time. It was found that the cellular mode is determined by the catalytic combustion of hydrogen on Pt - containing particles formed during the decomposition of unstable platinum oxide in the gas phase. It is shown that the temperature dependence of the delays of hydrogen ignition on a platinum wire and foil in both stationary and rotating gases corresponds to an activation energy of 19 ± 3 kcal/mol, which is close to the activation energy of branching of the reaction chains of hydrogen oxidation. The impurity origin of the 552 nm emitting band, which is often recorded during the combustion of gas and heterogeneous mixtures, has been established. The results obtained are of immediate importance for the development of Catalytic Stabilization (CS) technology and the development of catalysts with increased activity. The results are also important for verification of theoretical concepts of the propagation of dust and gas flames.

It has been shown experimentally that in the case of flame penetration through an obstacle, gas-dynamic factors, for example, flame turbulization, can determine the kinetics of the process, including the transition of low-temperature combustion of a hydrocarbon to a high-temperature regime.

It has been established that the flame front after a single obstacle does not arise in the immediate vicinity of the obstacle. The first ignition site can be observed relatively far from the obstacle surface. It is shown that the use of a mesh sphere as an obstacle leads to an increase in the length of the flame "jump" behind the obstacle in comparison with a round hole. It has been shown that two or more obstacles, both spherical and planar, noticeably suppress the propagation of the flame, which can be associated with both heat losses from the flame front and with heterogeneous termination of reaction chains at the obstacle. It has been experimentally shown that below the limit of penetration of a flame of a dilute methane-oxygen mixture through a flat obstacle with a single hole, for an obstacle in the form of a funnel, the flame does not penetrate from the side of the confuser, but penetrates from the side of the diffuser. Numerical modeling of the Navier-Stokes equations for a compressible medium in the approximation of a small Mach number with the representation of a chemical process as a single reaction and the simplest chain mechanism made it possible to describe qualitatively the experimental features. Within the framework of an approximate consideration using the Navier-Stokes equations in a compressible reacting medium, the features of flame propagation through a conical obstacle with additional holes on the converging generatrix are described qualitatively. In other words, the flame does not penetrate through the central hole of the converging tube, but only penetrates through the central hole of the diffuser, even if there are holes in the generatrix of the cone. The simulation carried out in small volumes suggests that in the event of an emergency situation, the flame will not penetrate through the open valve located in the center of the confuser located in the pipe. In this case, the most effective double-sided flame arrester in the pipe can be a system of two confusers, the funnels of which are located on the pipe axis along the gas flow and against it, since an emergency situation can occur before and after the obstacle. A hole or valve can be located in the middle.

The features of the penetration of the flame front through rectangular holes in comparison with round holes were experimentally studied using color filming and visualization of a gas flow. It is shown that the length of the "flame jump" after the hole in the obstacle is mainly determined by the time of occurrence of the laminar-turbulent transition, and not by the ignition delay period.

It was found that C_2 radicals in detectable amounts and the main heat release in the process are observed after the flame passes the first obstacle by using 4D spectroscopy combined with high-speed color filming, i.e. after turbulization of the gas flow. The obtained result means that the used experimental technique makes it possible to separate in time and space "cold" and "hot" flames in one experiment. The result obtained is also important for the verification of numerical models of methane combustion. In addition, the results obtained are important for solving explosion safety problems for volumes with complex geometrical arrangement.

It was found that the ignition temperature of a 40% H_2 - air mixture in the pres-

ence of metallic palladium (70 °C, 1 atm) is ~ 200 °C lower than over the platinum surface (260 °C, 1 atm). In addition, Pd initiates the ignition of mixtures (30÷60% H₂ + 70÷40% CH₄)_{stoich} + air; Pt foil does not initiate combustion of these mixtures up to 450 °C. The effective activation energy of ignition over Pd is estimated as ~ 3.5 kcal/mol.

It was found that the temperature of the ignition limit above the palladium surface at 1.75 atm for mixtures of 30% methane + 70% hydrogen + air ($\theta=0.9$, T=317 °C) and 30% propane + 70% hydrogen + air ($\theta=1$, 106 °C), measured by the “approach from below” method by temperature, decreases during subsequent ignitions and is 270 °C for a mixture containing hydrogen - methane and 32 °C for a mixture containing hydrogen and propane. The flammability limit returns to the initial value after the reactor is treated with oxygen or air, i.e. hysteresis takes place. The temperature of the ignition limit of mixtures 30% (C₂, C₄, C₅, C₆) + 70% H₂ + air ($\theta=0.6, 1.1, 1.2, 1.2$, respectively) over the palladium surface is 19÷35 °C at 1,75 atm. There is no hysteresis. It is shown that the lean ($\theta=0.6$) mixture of 30% ethane + 70% hydrogen + air has the lowest temperature of the ignition limit: 24 °C at 1 atm. The effective activation energy for the ignition of mixtures over palladium is estimated as ~ 2.4 ± 1 kcal/mol. It was found that the separation of the CH and Na emission bands in time during the combustion of a mixture of 30% propane + 70% H₂ + air ($\theta=1$), found in this work, is due to the occurrence of hydrodynamic instability of the flame when it touches the end of the cylindrical reactor.

It was found that the ignition temperatures of hydrogen - oxygen and hydrogen - methane - oxygen mixtures under the pressure of heated wires of palladium, platinum, nichrome and kanthal (fechral) at a total pressure of 40 Torr increase with a decrease in the hydrogen content in the mixture. Only heated palladium wire has a noticeable catalytic effect. A qualitative numerical calculation made it possible to reveal the role of the additional branching reaction $H + HO_2 \rightarrow 2OH$ in the process of ignition initiation by a heated wire.

Copper nanopowders are obtained by the method of hydrogen reduction (chemical-metallurgical method) and thermal decomposition of copper citrate and formate. It was shown that copper nanopowder synthesized from copper citrate is not pyrophoric. Combustion of this copper nanopowder can be initiated by an external source, with the combustion wave velocity 1.3 ± 0.3 mm/s. The nanopowder has a ~ 4 times larger specific surface (45 ± 5 m²/g) than the nanopowder obtained by the chemical-metallurgical method. It practically does not contain oxides and is stable in atmospheric air. Copper nanopowder obtained by the chemical-metallurgical method is pyrophoric and therefore requires passivation, but its passivation leads to the formation of noticeable amounts of copper oxides. The combustion rates of passivated and non-passivated copper nanopowder obtained by the chemical-metallurgical method are the same and amount to 0.3 ± 0.04 mm/s. The dynamics of temperature fields during the ignition and combustion of copper nanopowders obtained by various methods has been studied.

Tungsten nanopowders are synthesized by reduction of tungsten trioxide with hydrogen (chemical metallurgy method) at $440 \div 640$ °C from samples with different specific surface: $2 \text{ m}^2/\text{g}$ (1), $11 \text{ m}^2/\text{g}$ (2), $0.8 \text{ m}^2/\text{g}$ (3). It is shown that the W nanopowder synthesized at 640 °C for all three precursors used is non-pyrophoric α -W. Its combustion can be initiated by an external source. Combustion develops in a spatially non-uniform regime. Nanopowder synthesized at 480 °C from tungsten oxide of grades 1 and 2 is a mixture of α -W, β -W and $\text{WO}_{2,9}$. This powder is pyrophoric. It was found that the passivated W nanopowder synthesized at 480 °C of grade 3 tungsten oxide is β -W with traces of WO_3 and $\text{WO}_{2,9}$. Temperature range of synthesis β -W, obtained in the work is very narrow: $470 \div 490$ °C. The specific surface area of α -W is $10 \pm 2 \text{ m}^2/\text{g}$. For the β -W mixture with traces of WO_3 and $\text{WO}_{2,9}$ it is $18 \pm 1 \text{ m}^2/\text{g}$. The dynamics of temperature fields during the ignition and combustion of tungsten nanopowders obtained at different temperatures has been studied.

An experimental determination of the features of combustion of compact samples made of non-passivated iron nanopowders and the effect of the porosity of these compact samples on the dynamics of their heating in air are described. It is shown that the propagation velocity of the combustion front and the maximum combustion temperature of compacted samples made of non-passivated iron nanopowders decrease with increasing compact density.

Acknowledgment

Dr. of Sci. in Tech. E. F. Lebedev, Dr. of Phys.-Math. Sci. A. V. Gavrikov, Dr. of Eng. Sci. V. A. Zeigarnik (Joint Institute for High Temperatures RAS), Cand. of Phys.-Math. Sci. B. S. Seplyarsky, Cand. Phys.-Math. Sci. S. G. Vadchenko, Cand. of Tech. Sci. R. A. Kochetkov, postgraduate student N.I. Abzalov, Cand. of Phys.-Math. Sci. V. I. Chernysh, Dr. of Sci. in Tech. V. A. Zelensky, leading engineer G. I. Tsvetkov (Merzhanov Institute of Structural Macrokinetics and Materials Science, RAS), Dr. of Sci. in Tech. V. V. Egorov (Space Research Institute RAS), engineer A. B. Ankudinov (A.A. Baikov Institute of Metallurgy and Materials Science, RAS), for their continuous support. In terms of studying combustion using high-speed color filming, the work was carried out within the framework of state orders AAAA-A17-117011910011-09, AAAA-A17-117040610346-5 and AAAA-A19-119010990034-5 and the ISMAN State Assignment. In terms of the use of hyperspectral surveys and subsequent analysis, the work was carried out within the framework of state orders AAAA-A20-120011690135-5 and AAAA-A19-119010990034-5.

The research described in Chapter 8 was supported by a grant from the Russian Science Foundation (project no. 16-13-00013).

N. M. Rubtsov, M. I. Alymov, A. P. Kalinin,
A. N. Vinogradov, A. I. Rodionov, K. Ya. Troshin

Remote studies of combustion and explosion processes based on optoelectronic methods

Monograph

Signed in print 25.01.2022 r. 60x84/16.
Ed. No. 1. Circulation of 500 copies.
AUS PUBLISHERS, 2022.



Rubtsov Nickolai Mikhailovich,
Dr. of Chem. Sci., Merzhanov Institute of
Structural Macrokinetics and Materials
Science Russian academy of science, Joint
Institute for High Temperatures Russian
academy of science



Alymov Mikhail Ivanovich,
Full Professor, Corr. Mem. Russian academy
of science, Merzhanov Institute of Structural
Macrokinetics and Materials Science Russian
academy of science



Kalinin Alexander Petrovich,
Dr. of Phys.-Math.,
Ishlinsky Institute for Problems in
Mechanics Russian academy of science



Vinogradov Alexey Nikolaevich,
Cand. of Phys.-Math. Sci.,
"Reagent" Research & Development center,
Joint-stock company



Rodionov Alexey Igorevich,
Cand. of Phys.-Math. Sci.,
N.N. Semenov Federal Research Center for
Chemical Physics RAS



Troshin Kirill Yakovlevich,
Dr. of Phys.-Math. Sci.,
N.N. Semenov Federal Research Center for
Chemical Physics RAS